Exploring novel physics and applications with high-resolution silicon nanofabrication

Albrechtsen, Marcus

Publication date:
2023

Document Version
Publisher's PDF, also known as Version of record

Citation (APA):
Albrechtsen, M. (2023). *Exploring novel physics and applications with high-resolution silicon nanofabrication*. Technical University of Denmark.

DTU ELECTRO
Department of Electrical and Photonics Engineering

Exploring novel physics and applications with high-resolution silicon nanofabrication

Marcus Albrechtsen

DTU ELECTRO
Department of Electrical and Photonics Engineering
Technical University of Denmark

Exploring novel physics and applications with high-resolution silicon nanofabrication

Marcus Albrechtsen
March 5, 2023

Revised version submitted April 1, 2023.

A dissertation submitted to the
Department of Electrical and Photonics Engineering
at the Technical University of Denmark
in partial fulfillment of the requirements
for the degree philosophiae doctor.

Cover image: An artist's impression of a new nanocavity where light is concentrated at the center to a volume deep below the diffraction limit using a bowtie structure.
— Design by Ella Maru Studio.

I wish to thank Asst. Prof. Babak Vosoughi Lahijani for insightful discussions and valuable supervision.

"Navigare necesse est ..."
It is necessary to navigate ...
— Plutarch.

DTU Electro
Department of Electrical and Photonics Engineering
Technical University of Denmark
Ørsteds Plads
Building 343
DK-2800 Kgs. Lyngby
Denmark

This thesis is typeset in 10 pt Latin Modern using XƎLaTeX.

Preface

This thesis reports the results of a PhD conducted over the three years from March 1, 2020 to March 5, 2023 in the Nanophotonics section at the Department of Electrical and Photonics Engineering at the Technical University of Denmark. The month between October 21, 2022 and November 21, 2022 was carried at the Phononic and Photonic Nanostructures group led by Prof. Clivia M. Sotomayor Torres at the Catalan Institute of Nanoscience and Nanotechnology (ICN2, UAB).

The project was originally titled ”Chip-scale nanoelectromechanical spectrometers”, however, several factors affected the project, and the scope was redefined to the present title.

First, the initial national lockdown due to the covid-19 pandemic struck within 10 days. However, I became critical staff from the start, and therefore continued as one of the only researchers who could carry out experimental work, including nanofabrication and optical characterization. I got involved in a variety of other projects, both doing nanofabrication but also some characterization. Even though these projects were not at the core of my project, I have remained involved in many of them since then – primarily my contributions have been nanofabrication and within design-of-experiments. Example includes the investigation of photonic topological insulators and attempts to directly measure and quantify the ubiquitous surface-forces that affects nanostructures with nanometer-scale separations, e.g., the Casimir force. I have also contributed significantly to the natural follow-up work of using these nanoscale forces for constructive self-assembly. Here, the objective is to resolve features well below the resolution of the nanofabrication processes.

Second, the research team that I was a part of received a considerable grant to develop chip-scale spectrometers, which included a number of PhD and postdoc positions with specific tasks spanning the scope of my original project. This means that a number of projects where I initiated or carried out the early parts of the work has since been expanded into more ambitious and complete projects of which I only constitute a part. Here, my contributions are primarily within the early stages, i.e., to the conception of the ideas, projects and scope as well as, in some cases, to supervision. This includes the development of grating couplers where my contributions have been major and within packaging, where my contributions have primarily been to the conception of the ideas. This further motivated the purchase of new double-side polished silicon-on-insulator wafers as well as an electronic-optical probe station with access to both the front and the back of the device-under-test. Following the lockdown and a rapid expansion of the research group, I have further spent considerable time transferring knowledge, e.g., by training colleagues in cleanroom processes as well as optical characterization.

Third, the advances within high-resolution silicon nanofabrication documented in Part I of this thesis were originally developed with the objective to achieve low-loss slot-mode waveguides, but it has spawned a number of collaborations to explore novel physics with silicon nanostructures. Most prominently, the dielectric bowtie nanocavities presented in Part II, which now also form a central part of this thesis. While this project has led to a number of further unpublished studies, and natural avenues for additional experiments, I have retained a focus on my original project towards the development of a low-cost and scalable chip-scale spectrometer, where applications is at the very heart and the current state is presented in Part III of this thesis. I nevertheless remain deeply excited about the on-going nanocavity-efforts on extreme dielectric confinement – and I look forward to following the continued work of many excellent colleagues!

Marcus Albrechtsen

Marcus Albrechtsen
April 1, 2023
Copenhagen, Denmark

Acknowledgements

This work is the result of 3 years intensive work, and despite covid-19 doing its best to isolate us, I have had the great fortune to still meet a large number of new highly skilled and inspiring people – many of whom I today consider friends. I have had the opportunity to travel and meet researchers from all over the world, and so I wish to extend my gratitude, thanks and acknowledgements to a number of friends and colleagues throughout this journey!

I started my PhD as part of the research group of Jesper Mørk, which is established, hospitable and mature. I want to thank Jesper for scientific discussions and input, as well as acknowledge his support. Back then, I was part a small research team and in this context I want to thank Babak Vosoughi Lahijani for his supervision and support. He has always had an open door, time for more discussions, and importantly, I have shared many a beer and good times with him. Another of the original spectrometer-musketeers is Konstantinos Tsoukalas. In my Master's thesis I thanked him for "quirky discussions" – after three more years I have to say that these have not become less obscure, but fortunately, they have remained as enjoyable and full of brilliant insight as ever: There is no limit! I also want to thank Christian Rosiek, whom I have now known as a good friend and long-time co-student, and I continue to appreciate his scientific rigor, dedication and deep understanding. I also wish to acknowledge his patience for not just working together but also sharing an apartment with me throughout several of our PhD-years – even during the lockdowns, where we have had endless chances to discuss science.

Half-way through my PhD the spectrometer-team broke out of the group of Jesper Mørk, and I wish to express my gratitude towards the many past and present members of what—as of the time of writing—is called the Photonic Nanotechnology group, but has changed its name so frequently that the Git-repositories rarely could stay up to date. I wish to thank Morten Mechlenborg and Chirag Patil for welcoming me to the mix. I also want to thank fellow PhD-students in the group: Christian, Ali Babar, Konstantinos, Thor Weis, Søren Hansen and Anastasiia Vladimirova. I have very much enjoyed working with them, being at conferences and going to the cleanroom or labs – but I have also enjoyed sharing a beer and having a chat over a board game. I would like to especially highlight Ali and Konstantinos for joining me on a successful ride on the hardmask-bus in the cleanroom. I want to also thank the senior member beyond Babak, i.e., the postdoc Guillermo Arregui for many a good time and wonderful discussions.

I wish to thank a number of students and student assistants who has passed through or to the group. I have had the pleasure of working with 4 student assistants

over the years to develop on a mask-making software, called Swordfish: Mathias Korsgaard, Mikkel Horn, Mathias Sutherland and Søren Hansen. In particular I want to highlight Mathias Korsgaard, it has always been a pleasure and meetings with him has the unique effects of leaving me with more energy afterwards – thanks! It has been exciting supervising a range of fun student projects and I want to say thanks to all these students for their energy, challenging questions and of course their hard work: Thor Weis, Jesper Sand, Nikolaj Houghs, Kristian Knudsen, Mathias Sutherland, Jacob Svane-Petersen, Sune Nielsen, Nicholei Hansen and Andreas Nymand. In particular, I want to highlight Jesper Sand for providing experimental data used in this thesis, highlighted explicitly when used. I also want to acknowledge a number of additional students who have carried out projects around me solving problems for the greater good, myself included: Mikkel Horn, Rasmus Lindtrup and Bjarke Frederiksen.

Finally, I feel obliged to acknowledge the partial funding to my PhD provided by Søren Stobbe (Villum Foundation Young Investigator Program, grant no. 13170). I would also like to acknowledge a number of interesting discussions, primarily in the early parts of the project, and of course his technical input at the later stages.

I want to thank the many excellent members of the NanoPhoton research-center for introducing me to exciting new physics and for inviting me along on joyous events. In particular, I wish to thank Philip Kristensen. He is a great scientist. His rigor and decency has been an inspiration for me, and I have come to deeply respect his intuition – I must also highlight that Philip has introduced me to a whole new world with quasi-normal modes. I also want to acknowledge Ole Sigmund, Nicolas Stenger, Rasmus Christiansen, Mikkel Heuck, and Kresten Yvind and thank them for their support, supervision, guidance and input during my PhD. Of course, I must also highlight a number of less senior, albeit no less important, colleagues within the center for stimulating scientific discussions, eventful Friday bars and more generally, making the stressful time of a PhD great. In particular, I want to mention Moritz Fischer, Göktuğ Işıklar, Laura Casses, Ayman Kamel, Frederik Schröder, Evangelos Dimopoulos, Benjamin Gøtzsche, George Kountouris and Meng Xiong. Lastly, I want to thank Yueguang Zhou with whom I shared an office during this PhD.

I wish to extend my gratitude towards the numerous people at DTU Nanolab – the National Centre for Nano Fabrication and Characterization, i.e., the cleanroom. Most prominently, I want to thank Henri Jansen, who accelerated my interest in technology – and in particular dry-etching. Meetings were always fun with time for anecdotes and more often than not occurred spontaneously inside the cleanroom. I want to also explicitly thank Rune Christensen, Evgeniy Shkondin, Roy Cork, Jonas Michael-Lindhard, Berit Herstrøm, Leif Johansen, Peixiong Shi, Lean Pedersen, Vy Nguyen, Karen Birkelund and Jens Hemmingsen for help with and across a variety of processes. Often with short notice and sometimes just for an extended chat to understand what is going on.

I want to acknowledge the external teams contributing to the spectromter project, i.e., STS Elionix, Beamfox Technologies, Ibsen Photonics and Foss Analytics – and in particular: Taichi Suhara, Brian Reynolds and Lukas Stampfer from STS Elionix;

Leonardo Midolo, Anders Esbensen, Lasse Frølich and Bjarke Frederiksen from Beamfox; Toke Lund-Hansen and Aslı Uğurlu from Foss for insightful discussions on data analysis within Fourier transform spectroscopy; as well as Bjarke Rose and Morten Mechlenborg from Ibsen.

During my PhD I spent 1 month in the laboratories of Clivia M. Sotomayor Torres at the Catalan Institute of Nanoscience and Nanotechnology (ICN2, UAB), and I want to express my gratitude for hosting me. In this context I also want to highlight in particular Guilhem Madiot for day-to-day supervision, and I want to thank Guilhem, Omar Florez, Martin Poblet and Francisco Cespedes for inviting me along for a number of fun and exciting events! It has been great meeting them – thanks for making me feel welcome during the stay!

I wish to explicitly thank those who have contributed with constructive feedback on various chapters of this thesis. First and foremost, thanks to Babak for helping me construct an outline from the somewhat nonlinear journey through fabrication, physics and applications! I want to thank Moritz for valuable feedback on a number of sections as well as Philip, Jonas, Ali, Guillermo, Rune and Guilhem for valuable comments on specific chapters – most of it within a short time-span yet of high quality: Thanks!

Finally, I want to thanks family and friends, and in particular, my parents, two sisters and my friends Anton and Andreas. For always supporting me, and for listening to endless rants of problem when things have been less easy as well as to the endless rants whenever I got new results.

Summary

The interaction between light and matter is feeble, but optical cavities can enhance it by focusing and storing the light. Previous approaches have used dielectric materials to improve the temporal storage, i.e., the quality factor, Q. However, improvement to the spatial confinement, i.e., the mode volume, V, have so far relied on plasmonics, where Ohmic absorption losses are a problem for many applications. This thesis presents the recent demonstration of a dielectric bowtie nanocavity that focuses the light to well below the so-called diffraction limit in a dielectric material that is free from absorption losses. This is achieved through a combination of multiple advances. It is shown that V depends sensitively on the smallest feature-size that can be fabricated, and the first part of this thesis presents the developments and advances within nanofabrication technologies towards high-resolution silicon nanofabrication. Specifically, within electron-beam lithography and silicon dry-etching. The fabrication method is carefully characterized and the fabrication-tolerances are directly included in the state-of-the-art deterministic inverse design algorithm, topology optimization. The objective is to maximize the local density of states (i.e., indirectly the Q/V ratio) in the center of the domain, and the result is a novel and exotic – but importantly, realistic – nanocavity design that features a bowtie structure. Calculations show that it confines light to a mode volume, $V = 3 \cdot 10^{-4}\,\lambda^3$, and simultaneously achieves $Q = 1100$ in a compact $4\,\lambda^2$ area for telecom photons with a wavelength, $\lambda \sim 1550\,\mathrm{nm}$. Since the cavity design takes into account fabrication-tolerances it can be fabricated with high precision, and optical measurements in the far-field confirm the high optical quality factors. Moreover, near-field measurements corroborate the mode volume deep below the diffraction limit, which is enabled by the only 8 nm wide silicon bowtie-bridge, which is etched vertically into a 240 nm thick silicon membrane. This extreme dielectric confinement of light paves the way for broadband enhancement of the light-matter interaction, i.e., interaction with broadband pulses, which is important for many applications including optical nonlinearities.

This high-resolution silicon nanofabrication method further enables a range of studies from fundamental physics to novel applications. This includes the experimental demonstration of hypersonic phonon-circuits and cavity optomechanics in the gigahertz. Moreover, specific applications include integrated nano-electro-mechanical photonics systems such as comb-drive–controlled optical waveguides that can be used for, e.g., optical switching and programmable photonics. These systems are then combined to demonstrate a chip-scale spectrometer, which is based on slot-mode waveguides that can be used to construct optical delay-lines. Finally, the emerging challenges towards packaging and commercialization are discussed.

Resumé

Interaktionen mellem lys og stof er fra naturens hånd svag, men optiske kaviteter kan fokusere og opbevare lys, så interaktionen bliver stærkere. Denne afhandling dokumenterer nylige resultater, hvor lys fokuseres til et mode volumen, V, dybt under den såkaldte diffraktionsgrænse i et dielektrisk materiale – altså et materiale, som ikke absorberer lyset, og dermed åbner muligheder for en lang række nye anvendelser. Blandt andet muliggør det en stærkere interaktion med bredbåndet lys, altså optiske pulser, hvilket er vigtigt for fx optiske ikke-lineariteter. Dette er muliggjort af en kombination af flere ting. Det vises, at V hænger direkte sammen med den mindste dimension, som kan fabrikeres, og første del af afhandlingen præsenterer udvikling og fremskridt i nanofabrikations-metoder af den dielektriske halvleder silicium, med særligt fokus på højoplsnings elektronstråle-litografi og plasmaætsning. Denne metode karakteriseres metodisk, og produktions-tolerancerne kodes direkte ind i en algoritme, som laver deterministisk inverst design, nemlig topologi-optimering, og lys-stof vekselvirkningen i strukturens centrum optimeres direkte. Det resulterer i en ny og eksotisk — men dog realistisk — nanokavitet, og udregninger viser, at den opnår $V = 3 \cdot 10^{-4}\,\lambda^3$ samt en optisk kvalitetsfaktor $Q = 1100$ på et kompakt $4\,\lambda^2$ område for telekommunikations-fotoner med $\lambda \sim 1550\,\mathrm{nm}$. Da kaviteten er designet sådan, at den tager højde for fabrikations-tolerancerne, kan den fabrikeres med stor nøjagtighed, og optiske fjernfeltsmålinger verificerer kvalitetsfaktoren. Dernæst udføres nærfeltsmålinger, som understøtter et V dybt under diffraktionsgrænsen. Det er muliggjort af den kun 8 nm brede butterfly-formede bro, som er ætset vertikalt gennem en 240 nm tyk silicium-membran.

Den nyudviklede nanofabrikations-teknologi muliggør derudover en lang række studier fra fundamental fysik til applikationer. Det gælder blandt andet hypersoniske fonon-kredsløb og optomekanik med kaviteter. Derudover præsenteres konkrete anvendelser med et fokus på fotoniske nano-elektro-mekaniske systemer, såsom kamdrevskoblede bølgeledere som kan bruges til at konstruere optiske switches samt faseskiftere. Der bygges videre slot-mode bølgeledere til justerbare forsinkelseslinjer, hvilket er en kritisk komponent for skalerbare chip-baserede spektrometre. Slutteligt diskuteres anvendelser, næste skridt samt udfordringer i forbindelse med pakning og kommercialisering af et sådant spektrometer.

List of publications

This thesis has resulted in 9 papers: 4 publications, 2 accepted papers, 2 publicly available preprints and 1 submitted manuscript. Two of the publications have been highlighted in the *News and Views*–sections of *Nat. Nanotechnol.* and *Nat. Photon.*, respectively. One of them has been featured in the popular-science magazine Laser Focus World as well as was chosen for its January 2023 cover as indicated below.

1. **M. Albrechtsen**, B. Vosoughi Lahijani, S. Stobbe, ”Two regimes of confinement in photonic nanocavities: bulk confinement versus lightning rods,” *Opt. Express* **30**, 15458–15469 (Apr. 2022), doi:10.1364/OE.448929.

2. O. Florez, G. Arregui, **M. Albrechtsen**, R.C. Ng, J. Gomis-Bresco, S. Stobbe, C.M. Sotomayor-Torres, P.D. García, ”Engineering nanoscale hypersonic phonon transport,” *Nat. Nanotechnol.* **17**, 947–951 (Aug. 2022), doi:10.1038/s41565-022-01178-1.
    - Highlighted in *News and Views* of Nat. Nanotechnol. (Aug. 2022).

3. **M. Albrechtsen**, B. Vosoughi Lahijani, R.E. Christiansen, V.T.H. Nguyen, L.N. Casses, S.E. Hansen, N. Stenger, O. Sigmund, H. Jansen, J. Mørk, S. Stobbe, ”Nanometer-scale photon confinement in topology-optimized dielectric cavities,” *Nat. Commun.* **13**, 6281 (Oct. 2022), doi:10.1038/s41467-022-33874-w.
    - Highlighted in *News and Views* of Nat. Photon. (Dec. 2022).
    - Featured in the popular-science magazine Laser Focus World (Nov. 2022).
    - Selected for the January 2023 cover of the printed magazine.

4. G. Arregui, R.C. Ng, **M. Albrechtsen**, S. Stobbe, C.M. Sotomayor-Torres, P.D. García, ”Cavity optomechanics with Anderson-localized optical modes,” *Phys. Rev. Lett.* **130**, 043802 (2023), doi:10.1103/PhysRevLett.130.043802.

5. G. Madiot, R.C. Ng, G. Arregui, O. Florez, **M. Albrechtsen**, S. Stobbe, P.D. García, C.M. Sotomayor-Torres, ”Optomechanical generation of coherent GHz vibrations in a phononic waveguide,” arXiv:2206.06913 (2022). Accepted in *Phys. Rev. Lett.*

6. C.A. Rosiek, G. Arregui, A. Vladimirova, **M. Albrechtsen**, B. Vosoughi Lahijani, R.E. Christiansen, S. Stobbe, ”Observation of strong backscattering in valley-Hall topological interface modes,” arXiv:2206.11741 (2022). Accepted in *Nat. Photon.*

7. B. Vosoughi Lahijani, **M. Albrechtsen**, R.E. Christiansen, C.A. Rosiek, K. Tsoukalas, M.T. Sutherland, S. Stobbe, "Electronic-photonic circuit crossings," arXiv:2204.14257 (2022). *In Review.*

8. R.C. Ng, P. Nizet, D. Navarro-Urrios, G. Arregui, **M. Albrechtsen**, P.D. García, S. Stobbe, C.M. Sotomayor-Torres, G. Madiot, "Frequency comb modulation in bimodal optomechanical phonon laser," arXiv:2210.16370 (2022). *In Review.*

9. S.E. Hansen, G. Arregui, A.N. Babar, **M. Albrechtsen**, B. Vosoughi Lahijani, R.E. Christiansen, S. Stobbe, "Efficient vertical coupling into fully etched suspended silicon photonic circuits via a low back-reflection free-space grating coupler," (2023). *In Review.*

The author of this thesis have presented at 5 international conferences.

1. **M. Albrechtsen**, B. Vosoughi Lahijani, R.E. Christiansen, V.T.H. Nguyen, O. Sigmund, H. Jansen, J. Mørk, S. Stobbe, "Fabrication and Characterization of Topology-Optimized Photonic Cavities with Deep Subwavelength Confinement," in Integrated Photonics Research, Silicon and Nanophotonics (Optical Society of America, 2020), paper IM4A.4 (oral, virtual, 2020), doi:10.1364/IPRSN.2020.IM4A.4.

2. **M. Albrechtsen**, B. Vosoughi Lahijani, R.E. Christiansen, V.T.H. Nguyen, L.N. Casses, S.E. Hansen, P.T. Kristensen, N. Stenger, O. Sigmund, H. Jansen, J. Mørk, S. Stobbe, "Shot-filling effects in nanometer-scale electron-beam lithography," 47th Micro and Nano Engineering Conference (oral, 2021), Turin, Italy.

3. **M. Albrechtsen**, B. Vosoughi Lahijani, R.E. Christiansen, V.T.H. Nguyen, L.N. Casses, S.E. Hansen, N. Stenger, O. Sigmund, H. Jansen, J. Mørk, S. Stobbe, "Effects of shot-filling in electron-beam lithography," Nordic Nanolab User Meeting (poster, 2022), Gothemburg, Sweden.

4. **M. Albrechtsen**, B. Vosoughi Lahijani, R.E. Christiansen, V.T.H. Nguyen, L.N. Casses, S.E. Hansen, N. Stenger, O. Sigmund, H. Jansen, J. Mørk, S. Stobbe, "Nanometer-scale photon confinement inside dielectric cavities," NanoPhoton conference (poster, 2022), Rungsted, Denmark.

5. **M. Albrechtsen**, A.N. Babar, B. Vosoughi Lahijani, E. Shkondin, G. Arregui, J. Sand, H. Jansen, S. Stobbe, "Tailoring a nanometer-scale fabrication process for silicon photonics," 48th Micro and Nano Engineering Conference (poster, 2022), Leuven, Belgium.

The author of this thesis has contributed to 24 international conferences listed chronologically below. The name of the presenting author is underlined.

1. O. Florez, **M. Albrechtsen**, G. Arregui, J. Gomis-Bresco, C.M. Sotomayor-Torres, S. Stobbe, P.D. Garcia, ”Brillouin detection of a full mechanical band gap in the GHz regime,” Workshop on Optomechanics and Brillouin Scattering (2021).
2. O. Florez, G. Arregui, J. Gomis-Bresco, **M. Albrechtsen**, S. Stobbe, C.M. Sotomayor Torres, P.D. Garcia, ”Brillouin Detection of a Complete GHz Mechanical Band Gap,” CLEO (2021).
3. A.N. Babar, **M. Albrechtsen**, B. Vosoughi Lahijani, R.E. Christiansen, J. Mørk, H. Jansen, S. Stobbe, ”High-resolution etching of nanophotonic cavities using a chromium hard mask,” MNE (2021).
4. C.A. Rosiek, **M. Albrechtsen**, A. Vladimirova, H. Jansen, S. Stobbe, ”Measuring propagation losses of edge modes in photonic topological insulators,” MNE (2021).
5. G. Arregui, R.C. Ng, **M. Albrechtsen**, C.M. Sotomayor-Torres, S. Stobbe, P.D. García, ”Anderson light localization in slotted photonic crystal waveguides,” MNE (2021).
6. S.E. Hansen, B. Vosoughi Lahijani, **M. Albrechtsen**, P.T. Kristensen, J. Mørk, S. Stobbe, ”Optical nonlinearities in photonic nanocavities with extreme subwavelength confinement,” MNE (2021).
7. T.A.S. Weis, **M. Albrechtsen**, K. Tsoukalas, A.N. Babar, S. Stobbe, ”Measurements of attracting surface forces in nanoelectromechanical systems,” MNE (2021).
8. A.N. Babar, **M. Albrechtsen**, B. Vosoughi Lahijani, R.E. Christiansen, J. Mørk, H. Jansen, S. Stobbe, ”Fabrication and characterization of silicon bowtie nanocavities,” Nordic Nanolab User Meeting (2022).
9. C.A. Rosiek, R.E. Christiansen, **M. Albrechtsen**, B. Vosoughi Lahijani, S. Stobbe, ”Topology optimization of mechanical suspension system for photonic circuits,” Nordic Nanolab User Meeting (2022).
10. N.B. Hougs, K.S. Knudsen, **M. Albrechtsen**, T. Suhara2, C.A. Rosiek, S. Stobbe, ”Experimental measurements of point-spread functions for 150 keV electron-beam lithography,” Nordic Nanolab User Meeting (2022).
11. T.A.S. Weis, **M. Albrechtsen**, K. Tsoukalas, A.N. Babar, S. Stobbe, ”Nanomechanical platforms for characterization of surface forces,” Nordic Nanolab User Meeting (2022).
12. A.N. Babar, **M. Albrechtsen**, B. Vosoughi Lahijani, R.E. Christiansen, J. Mørk, H. Jansen, S. Stobbe, ”Fabrication and characterization of silicon bowtie nanocavities,” NanoPhoton (2022).

13. B. Vosoughi Lahijani, **M. Albrechtsen**, R.E. Christiansen, C.A. Rosiek, K. Tsoukalas, M.T. Sutherland, S. Stobbe, ”Electronic-photonic circuit crossings,” NanoPhoton (2022).

14. R.C. Ng, G. Arregui, G. Madiot, **M. Albrechtsen**, O. Florez, S. Stobbe, C.M. Sotomayor-Torres, P.D. García, ”A cavity optomechanical platform for GHz phonon launching via Anderson-localized optical modes,” SPIE (2022).

15. C.A. Rosiek, R.E. Christiansen, **M. Albrechtsen**, B. Vosoughi Lahijani, S. Stobbe, ”Topology optimization for suspended nanophotonic circuits,” MNE (2022).

16. B.A. Frederiksen, B. Vosoughi Lahijani, **M. Albrechtsen**, C.A. Rosiek, K. Tsoukalas, T.A.S. Weis, S. Stobbe, ”Compact nanoelectromechanical optical phase shifters,” MNE (2022).

17. O. Florez, G. Arregui, J. Gomis-Bresco, **M. Albrechtsen**, S. Stobbe, C.M. Sotomayor Torres, P.D. Garcia, ”GHz phonon waveguides in nanopatterned silicon,” IEEE Nano (2021).

18. C.M. Sotomayor Torres, D. Navarro-Urrios, M.F. Colombano, G. Arregui, G. Madiot, A. Pitanti, T. Makkonen, A. Griol, A. Martinez, O. Florez, R.C. Ng, **M. Albrechtsen**, S. Stobbe, P.D. Garcia, J. Ahopelto, ”A platform for GHz Si phononics: Sources, waveguides and circuits,” TNT (2022).

19. C.A. Rosiek, G. Arregui, A. Vladimirova, **M. Albrechtsen**, B. Vosoughi Lahijani, R.E. Christiansen, S. Stobbe, ”Propagation Losses in Photonic Topological Insulators,” Foremost Photonics (2022).

20. G. Arregui, R.C. Ng, G. Madiot, **M. Albrechtsen**, C.M. Sotomayor-Torres, S. Stobbe, P.D. García, ”Exploiting fabrication disorder in cavity optomechanics,” Foremost Photonics (2022).

21. P. Nizet, R.C. Ng, D. Navarro-Urrios, G. Arregui, **M. Albrechtsen**, P.D. García, S. Stobbe, C.M. Sotomayor Torres, G. Madiot, ”Broadband gigahertz frequency comb via mechanical-optical-mechanical multimode lasing,” Foremost Photonics (2022).

22. G. Arregui, C.A. Rosiek, A. Vladimirova, **M. Albrechtsen**, B. Vosoughi Lahijani, R.E. Christiansen, S. Stobbe ”Backscattering in slow-light valley-Hall photonic topological waveguides,” *submitted to* CLEO Europe (2023).

23. C.A. Rosiek, G. Arregui, A. Vladimirova, **M. Albrechtsen**, B. Vosoughi Lahijani, R.E. Christiansen, S. Stobbe, ”Measuring Propagation Loss in Slow-light Valley-Hall Photonic Topological Waveguides,” *submitted to* CLEO (2023).

24. G. Madiot, M. Poblet, R.C. Ng, G. Arregui, **M. Albrechtsen**, S. Stobbe, C.M. Sotomayor Torres, ”Waveguides and sources for topological phononics,” *submitted to* TMC (2023).

The author of this thesis have co-supervised 9 student projects overlapping with content of this thesis. All these projects are listed below, and contributions are acknowledged explicitly where applicable throughout this thesis. The name of the senior supervisor is underlined.

1. Mathias T. Sutherland, ”Vapor phase etching of SiO_2,” F. Jensen, R.K.D. Christensen, **M. Albrechtsen**. Special course (5 ECTS), Aug. 2020.
2. Mathias T. Sutherland, ”Fabrication and characterization of locally doped silicon electronic-photonic devices,” S. Stobbe, **M. Albrechtsen**. BSc thesis (20 ECTS), Sep. 2020–Feb. 2021.
3. Thor A.S. Weis, ”Design and fabrication of silicon nanostructures using quantum vacuum forces,” S. Stobbe, **M. Albrechtsen**, K. Tsoukalas. MSc thesis (30 ECTS), Sep. 2020–Feb. 2021.
4. Kristian S. Knudsen, Nikolaj B. Hougs, ”Experiments on point spread functions for electron beam lithography,” S. Stobbe, **M. Albrechtsen**. BSc thesis (15 ECTS), Feb. 2021–Jun. 2021.
5. Jesper L. Sand, ”Near-infrared spectroscopy for continuous quality control of oil,” S. Stobbe, S.E. Hansen, **M. Albrechtsen**, C.F. Nørgaard, C.S. Pedersen. BSc thesis (20 ECTS), Feb. 2021–Jun. 2021.
6. Sune V. Nielsen, Jacob Svane-Petersen, Nicholei S. Hansen, Andreas Nymand, ”Modelling, fabrication, and characterization of photonic crystal nanocavities: Impact of surface roughness on quality factor statistics,” S. Stobbe, **M. Albrechtsen**, T.A.S. Weis. Special course (10 ECTS), Sep. 2021–Dec. 2021.
7. Nikolaj B. Hougs, ”Numerical and experimental characterization of photonic nanobeam cavities,” S. Stobbe, **M. Albrechtsen**. Special course (5 ECTS), Sep. 2021–Dec. 2021.
8. Nikolaj B. Hougs, ”Experimental investigation of the impact of electron-beam lithography on nanocavities,” S. Stobbe, **M. Albrechtsen**. Special course (5 ECTS), Feb. 2022–Jun. 2022.
9. Jesper L. Sand, ”Characterization of nano-electro-mechanical systems,” S. Stobbe, **M. Albrechtsen**, B. Vosoughi Lahijani. Special course (5 ECTS), Feb. 2021–Jun. 2021.

Contents

CHAPTER 1

Introduction

The technological revolution of the 20th century originates from a number of breakthroughs – some of which stand out. The invention of the transistor in 1948 by Bardeen and Brattain [1]—awarded with the Nobel Prize in Physics in 1956 together with Shockley—enabled classical computing and has been key to the information age. The laser (light-amplification by stimulated emission of radiation) has had ramifications for communications, and although it was predicted by Einstein in 1917 – it took almost half a century to realize it experimentally due to a multitude of technological challenges. Initially, it was achieved with microwaves (MASERs) but in 1960 the first laser in the infrared/visible regime was demonstrated by Maiman [2], after which development accelerated. The next application was demonstrated only a year later by Franken *et al.* [3], namely second-harmonic generation where one color of light is converted to another. Moreover, the laser was immediately adopted in popular culture with its inclusion in the 1964 James Bond–movie: *Goldfinger*.

Following these initial demonstrations the race was on towards scalability within electronic and photonic nanotechnology: reducing cost and footprint while improving capabilities. A promising technological platform was microfabrication of integrated circuits (IC) on silicon wafers, where thin slices (wafers) are cut from a cylinder of a crystalline semiconductor, and a sequence of fabrication steps produce a stack of stratified media. This forms an array of nominally identical complex devices on the wafer, such as an array of central processing units (CPUs), which can then be cut into individual chips. Each fabrication step involves, in principle, a lithography step where a two-dimensional (2D) pattern is defined in a compliant material (called the resist, and could be a plastic polymer), followed by a pattern-transfer step where the features are etched into the semiconductor or metals are deposited onto it. The resist is then removed, a new resist is deposited and a new step is performed in order to form complex three-dimensional complimentary metal-oxide-semiconductor (CMOS) structures. By improving the fabrication methods to make features ever-smaller, more transistors were crammed onto less chips-space. In 1965 Moore predicted that the number of transistors per integrated function would double every two year in what is today known as Moore's law [4]. In the early days, this was achieved by improvements in the resolution of lithography, but quickly isotropic etching limited the number of features. Anisotropic profiles were achieved with plasma etching [5], or dry-etching, additionally offering savings in chemical consumption compared to wet etching. Today, state-of-the-art CMOS-processes are carried out in multi-billion–dollar robotic cleanroom foundries, devoid of human interaction and purged of particles that can cause a drop in yield. These processes can include hundreds of steps as shown in Fig. 1.1 [6], and the most recent international roadmap for devices and systems (IRDS) on lithography from 2022 describes wafer-wide nanometer-scale feature sizes and high-aspect–ratio (HAR) contact-holes down to few tens of nanometers [7]. In short, semiconductor fabrication methods have enabled scalability – and thereby low-cost and widespread accessibility. Notably, the popular-name of the technology nodes [7]—such as the current ”3 nm”–node—which refer to the capabilities for a corresponding foundry or fabrication technology, are only marketing names that no longer correspond directly to the achievable minimum feature size [8, 9] – currently $\gg 10\,\mathrm{nm}$.

Using silicon has numerous advantages [10]: It is abundant ($\sim 27.7\%$ of the Earth's crust) and non-toxic. It is a semiconductor so transistors can be manufactured in it by controlling the number of carries, and its native oxide SiO_2 (glass) is one of the best electrically insulating materials in the world. This native oxidation is self-limited and stops after a few nanometers [11], thereby protecting the chip from erosion. This is in contrast to for example iron and silver that needs protective coatings. Silicon has a band-gap energy, $E = 1.12\,\mathrm{eV} = 1100\,\mathrm{nm}$, which enable low-loss optical waveguides at telecommunication wavelengths, $\lambda = 1550\,\mathrm{nm}$, where glass-fibers provide minimal optical losses for long-distance communications. Silicon also absorb light in the visible spectrum, enabling solar cells and low-cost photodetectors there. However, the band gap is indirect, so emission of photons from an electrical signal is prohibitively inefficient. Consequently, silicon is the material-of-choice for all electrical matters, but when optical sources are required other materials are employed, e.g., through heterogeneous integration or flip-chip integration. A rich variety of exotic and exciting materials are being explored. Examples include indium phosphide (InP), galium

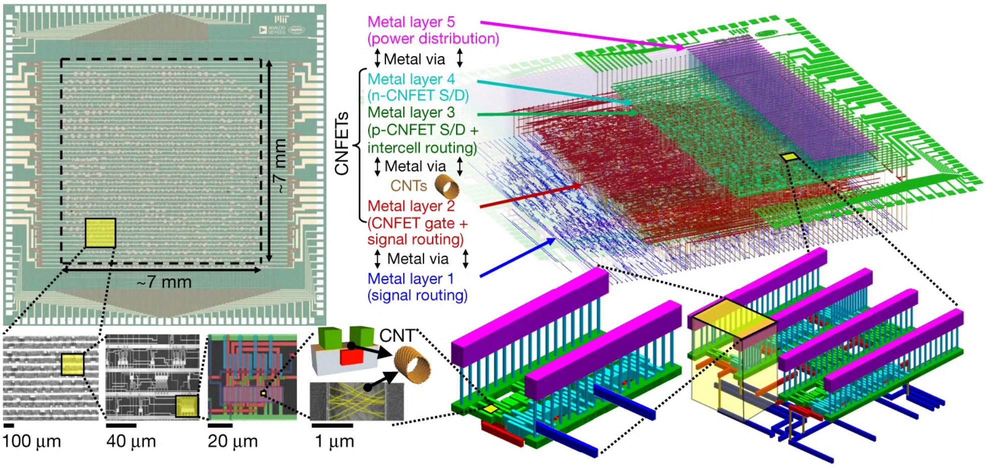

Figure 1.1. Example of a complex modern integrated circuit. More than 100 steps are used to manufacture this carbon-nanotube–based microprocessor. The insets illustrate the depth of complexity of the structures forming three-dimensional circuits. Figure reproduced with permission from Springer Nature (Ref. [6], license no. 5478961400598).

arsenide (GaAs), diamond (C), silicon carbide (SiC), silicon nitride (Si_3N_4), lithium niobate ($LiNbO_3$) and many more. They have various advantages over silicon, such as faster response, stronger nonlinearities or direct band gaps [10].

The CMOS-industry achieves unrivaled scalability with high up-front costs but almost no additional per-device cost. This is enabled by the parallel processing where circuits are transferred to a 2D disc, called a wafer, which typically is circular with diameters of 50, 100, 150, 200 and 300 mm. Larger wafers enable faster production and less wasted material at the edges (which scale linearly with the radius) compared to the area of the wafer (which scale quadratically with the radius). However, it also requires larger and more expensive equipment. Smaller wafers are more suited for prototyping – especially for expensive materials. Often a wafer is 0.3–1 mm thick to offer sufficient mechanical stability. In order to pattern small insulated materials it is instead desirable to have a thin slice (e.g., 220 nm) bonded to the handle wafer. This thin layer must be separated by a sacrificial layer, which can be etched away or that naturally insulates, such as a buried oxide (BOX). A number of materials can be provided on-insulator with the most common being silicon-on-insulator (SOI) [12].

Industrial applications require high throughput and speed. Therefore, ultra violet (UV)–or more recently, deep UV (DUV) and extreme UV (EUV) [13]–exposures are employed in which a mask is transferred to the entire wafer in one step from a ”master” mask. Similarly, nano-imprint lithography (NIL) [14, 15] can transfer a master without the diffraction limit–restriction of optical methods, and while there are still challenges to the yield of NIL it is now on the lithography roadmap [7]. Common to all these methods: They rely on a maskless method to define the master-mask – and typically the method-of-choice is electron-beam lithography (EBL). Here, a beam of electron is directed to a series of points with nanometer-scale spatial resolution, thereby defining a pattern without a mask. The problem is that this is a serial rather than parallel exposure technique, and hence, low-speed. Nevertheless, it is often employed directly in research and prototyping due to the large flexibility, precision and maturity it offers [16]. In this context it is also worth highlighting that the lithography roadmap considers EBL also for industrial use as a direct-write approach—complimentary to conventional optical lithography—with applications such as embedding unique security information into a chip as well as for some low-volume or low-density applications [7].

1.1 Thesis structure

This thesis explores novel physics and applications at the deep nanoscale by utilizing high-resolution silicon nanofabrication methods on the silicon-on-insulator platform. A central objective is to develop a nanofabrication process that is not only competitive with state-of-the-art industrial processes – but even ahead in terms of resolution and disorder, albeit at the price of throughput and yield [16], such that developments will become realistic in the coming years [7]. The thesis is structured in three parts as detailed below.

The first part discuss the nanofabrication methods, with Ch. 2 describing standard fabrication methods developed and used during this project and serves to provide an introduction to the nomenclature related to silicon nanofabrication techniques, including local diffusion-doping, metalization to form bonding pads and physical vapor deposition. Chapters 3 and 4 presents the development of high-resolution silicon nanofabrication processing based on novel methodologies within patterning using electron-beam lithography (Ch. 3) and pattern transfer with state-of-the-art plasma dry-etching (Ch. 4).

The second part focuses on results of fundamental physics interest. Chapter 5 covers the principles of light-matter interactions and the theoretical framework around dielectric bowties, parts of which is discussed in Ref. [17]. Chapter 6 presents the experimental demonstration of nanometer-scale photon confinement in dielectric bowtie cavities and is loosely based on Ref. [16]. Chapter 7 builds upon four publications within gigahertz-phononics (i.e., hypersonic mechanical vibrations) [18], cavity optomechanics [19], phonon lasing [20] and a GHz-phonon frequency comb [21] resulting from collaborations during this PhD project. It presents some new results on an engineered mechanical-optical-mechanical system on two closely spaced GHz-modes investigated during an external stay in the group of Prof. Clivia M. Sotomayor Torres.

The third part of this thesis considers novel applications, first in Ch. 8 on photonic nano-electro-mechanical systems (NEMS), which enables a strong nonlinear optical response in silicon on-chip waveguides required for compact phase-shifters and optical delay-lines, further enabling low-cost applications such as spectrometers [22], optical switches [23, 24] and photonic computing [25, 26] in a readily-scalable material platform. Chapter 9 presents work on developing a chip-scale NEMS spectrometer and further discusses the challenges relevant to commercialization, considering aspects such as electrical and photonic packaging, which has seen substantial activity and progress in recent years [27]. Finally, a outlook is provided by presenting and discussing a schematic of a next-generation spectrometer-design taking the knowledge gained from the design, fabrication, and experimental characterization during this thesis into account.

Lastly, the central conclusions are summarized, and an outlook towards future perspectives and further fundamental studies are suggested.

Part I

High-resolution silicon nanofabrication

CHAPTER 2

Nanofabrication methods

This chapter introduces common micro- and nanofabrication methods as well as describes and documents a number of specific processes used and referred to in this thesis. The thesis focus on new developments within high-resolution nanofabrication of silicon, specifically commercial silicon-on-insulator (SOI) prepared with the smart-cut technique [12]. Two SOI-stacks are used, both have a (100) silicon device-layer, the buried oxide (BOX) is grown by thermal (wet) oxidation, which also oxidizes the backside of the wafer, and both are prime-quality Soitec wafers. Wafer type 1 is 150 mm in diameter with nominal layer-thicknesses, $t_{\mathrm{dev}} = 250\,\mathrm{nm}$ and $t_{\mathrm{BOX}} = 3\,\mu\mathrm{m}$. The device layer has some variation across the surface and the thickness of the device layer of most chips used in this project from these wafers are measured using variable-angle ellipsometric spectroscopy [16, 28] to be $t_{\mathrm{dev}} = 240\,\mathrm{nm}$. The backside of the wafers are back-side damaged, i.e., rough. Wafer type 2 is 300 mm state-of-the-art wafers with little variation in dimensions across the surface and has layer-thicknesses $t_{\mathrm{dev}} = 220\,\mathrm{nm}$ and $t_{\mathrm{BOX}} = 2\,\mu\mathrm{m}$. The wafers are double-side polished. To accommodate the available sample holders for the tools used, the wafers are cut into 24-by-24 mm chips before processing.

The following four sections covers the principles of lithography (Sec. 2.1) followed by deposition techniques and lift-off (Sec. 2.2). Section 2.3 presents a process for local diffusion-doping and an IV-characterization to quantify the contact resistance, sheet resistance and carrier concentration of the doped and undoped device-layer of wafer type 2. This thesis presents work that requires the structures to be suspended, i.e., the BOX must be underetched to release the device-layer silicon membrane both to enable nano-mechanical manipulation of the structures but also to protect optical modes from leakage. Section 2.4 explains methods to etch SiO_2 under the silicon both using wet chemistry, i.e., hydrofluoric acid (HF), but also using temperature- and pressure-controlled HF in vapor-phase to control the amount of water in the process, and thereby, the associated stiction due to capillary forces [29–32]. While all of these subjects can be improved, this thesis does not seek to advance the state-of-the-art within these subjects. Rather, established processes are calibrated to the specific applications studied and this chapter serves both to document these processes and to introduce the nomenclature required to appreciate the subsequent chapters of this part on novel nanofabrication methods within high-resolution silicon nanofabrication. Appendix A summarizes the process flow for the fabrication of suspended nanostructures.

2.1 Principles of lithography

Figure 2.1 shows a cross-section schematic of a typical fabrication flow. The first step is to spin-coat a resist (Fig. 2.1**b**), which is a layer that can be easily patterned [10, 33]. Many resists are polymers (i.e., plastics) but does not have to be, e.g., hydrogen silsesquioxane (HSQ) is a resist that turns glass-like upon development and consequently it is much more resilient to, e.g., etching. The resist is dissolved in a solvent and deposited onto the sample, which is then spun at a few thousand rotations per minute (rpm) for, e.g., a minute to leave a homogeneous film of resist-solution. The sample is then soft-baked to evaporate the solvent but without damaging the resist, typically with temperatures, $T =$60–200 °C. The resulting resist will be thicker at the edges, an effect named edge-beads, and particles or defects on the sample will throw a shadow of thickness variation behind it, radially from the center of rotation during spin-coating, an effect called comets. Due to the change in which wavelengths will destructively or constructively interfere nanometer-scale thickness-variations can be identified by eye and if regions of varying thickness is used care must be taken to adjust the subsequent process accordingly.

The resist should be sensitive to irradiation with electrons or light of specific wavelengths, or malleable in the case of nano-imprint lithography [14, 15], such that high-resolution features can be defined in it fast. Ultra violet exposures can be carried out using a mask or as maskless lithography, where mask-based lithography normally involves a transparent quartz mask with the pattern defined with a thin chromium layer, which reflects the light. This enables the exposure of a full wafer in a matter of seconds, and this high throughput makes it a prime tool for industrial production. However, it requires the manufacturing of the mask and does not offer customization of the pattern during each exposure, which is convenient in research. On the other hand, maskless optical lithography relies on a powerful light-source shining on an array of micro-mechanical mirrors, which can switch the light on/off for each pixel, enabling a flexible exposure of custom patterns, however at the price of a reduced throughput. A smaller wavelength will enable a higher spatial resolution, and the optical i-line with a $\lambda = 365\,\mathrm{nm}$ wavelength is commonly used to pattern UV-sensitive resists with micrometer-scale dimensions. In this thesis maskless-UV exposures are carried out using three different maskless UV tools with laser sources at 365 nm, 375 nm and 405 nm. The last one is available at considerably higher power but does not activate all resists, the 375 nm tool uses an objective with higher numerical aperture (NA) and is able to achieve higher resolution. Additionally, the two latter tools offers back-side alignment. Once the resist has been exposed it is developed by submerging it in an appropriate solvent or base. In this thesis a 2.38 % pre-diluted solution (AZ MIF-726) composed of the base tetramethylammonium hydroxide (TMAH) in de-ionized water (DIW) is used. For a positive (negative) tone resist this dissolves the exposed (unexposed) parts.

In this thesis two resists are used, the positive tone resists (AZ) MiR701 and (AZ) 5214E as well as the negative tone (AZ) nLOF2020; strictly, the 5214E can be

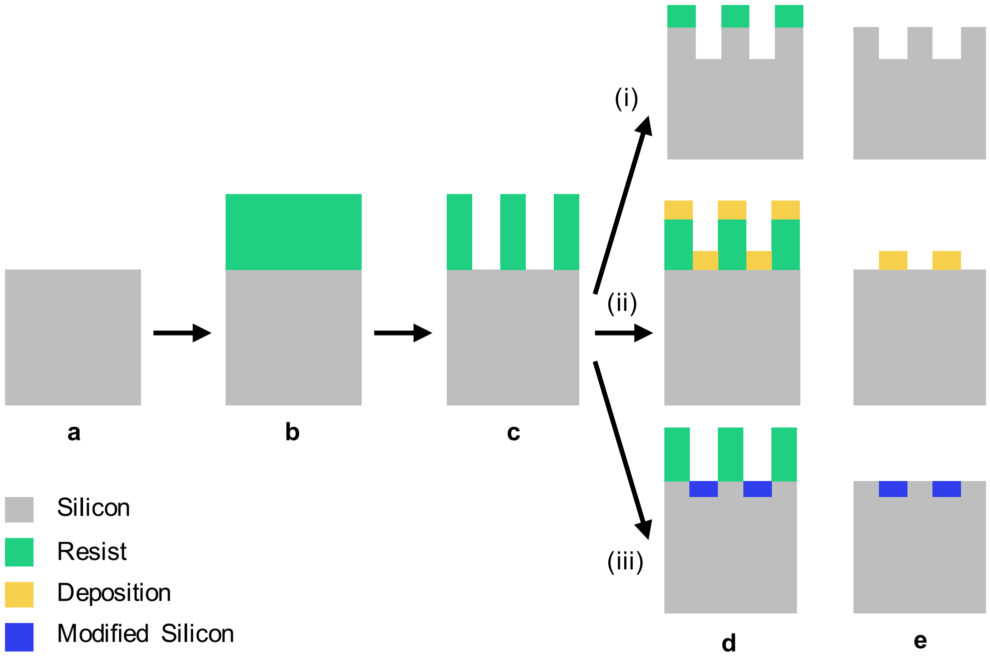

Figure 2.1. Cross-section schematic of standard fabrication processes. **a**, Unpatterned silicon, **b** resist is spin-coated onto the substrate, and **c** a pattern is lithographically defined by an exposure and subsequent development. **d**, Three types of pattern transfers where the pattern is (i) etched into the silicon also partially etching the mask, (ii) a material is deposited onto the substrate and resist and is disconnected due to the high aspect-ratio features in the resist, (iii) the substrate is altered locally using the mask. **e**, The resist is removed—leaving etched, deposited or altered features—and the process can be repeated starting from **b**.

used both as a positive- and negative-tone resist but is only used in the former case. Both positive resists can be exposed with the 405 nm–tool at a speed of $\sim 5\,\mathrm{min}$ for a $\sim 20\,\mathrm{cm}^2$ pattern, using a dose of $200\,\mathrm{mJ/cm}^2$ and $320\,\mathrm{mJ/cm}^2$ for 5214E and MiR701, respectively. For comparison, the older 365 nm–tool can expose $\sim 4\,\mathrm{cm}^2$ pattern in $\sim 10\,\mathrm{min}$, i.e., 10 times slower, but it can also activate nLOF2020. All 3 resists are developed by submersion in MIF-726 for 60 s, however, prior to development yet after the exposure MiR701 is baked at 110 °C for 60 s and nLOF2020 is baked at 100 °C also for 60 s. This baking step is called the post-exposure bake (PEB) and is needed to fully activate the resist-chains; baking of 5214E reverses it to use it as a negative-tone resist. By adjusting the temperature and duration of the PEB, as well as the dose and development time, the sidewall profile of the resist can be tuned, which is useful to obtain a negative sidewall in nLOF2020 for lift-off [34], i.e., where the feature-size becomes wider close to the substrate.

Figure 2.1**c** shows a patterned resist with vertical sidewalls. Depending on the application it can be advantageous to adjust the angle of the resist. Figure 2.1**d**(i)-(iii) illustrates etching of the pattern into the underlying substrate of interest, deposition of a new material such as a metal, and altering of the underlying substrate such as ion-implantation or doping [10]. Anisotrpic etching will be discussed extensively in Ch. 4 and the following two sections will discuss deposition and diffusion doping, respectively. Section 2.4 will discuss isotropic etching.

2.2 Material deposition including metalization by lift-off

Deposition as shown in Fig. 2.1(ii) can be achieved with multiple techniques for different purposes and applications [10]. This section will discuss some different techniques used in this thesis briefly and document one method, metalization by lift-off, specifically, which is used to create bonding pad. In addition to spin-coating, the techniques includes chemical vapor deposition (CVD), including plasma-enhanced CVD (PECVD) where gases can be mixed to control and tune the deposited film, e.g., to deposit doped glass. Additionally, if chemicals that react self-limited are used atomic layer deposition (ALD) can be achieved by switching the gases. Moreover, material can be deposited using physical vapor deposition (PVD) where a target material is released in a vacuum chamber and re-deposited on the substrate, and specific examples includes plasma sputtering where, e.g., an argon plasma is used to sputter the target. Other types of PVD includes electron-beam evaporation (EBPVD) and thermal evaporation (TPVD), where the target is heated either by a beam of electrons or by resistive-heating. These techniques have different advantages, for example ALD can deposit on the sidewall of features, i.e., it is independent of aspect ratio but relies on specific chemistries, and therefore is only applicable to certain materials. On the other hand PVD techniques such as EBPVD deposits highly directional and therefore can be defined lithographically, however electrically or thermally insulating materials are inefficient to deposit with EBPVD and TPVD and instead sputtering can be used. Thermal processes, such as oxidation, is not used here since it sacrifices the device-layer of the SOI-stack; however, the buried oxide in the stack has been defined by a thermal (wet) process.

Metalization, i.e., definition of bonding pads, is achieved by first spin-coating 2 µm nLOF2020, which is a negative resist, and patterning it with maskless UV lithography by exposing everywhere except the bonding pads, and finally developing the pattern. Then, without breaking vacuum (base pressure $\leq 10^{-6}$mTorr), three steps are carried out in sequence in an e-beam evaporation chamber (Ferrotec Temescal FC-2000), first an argon-ion–gun is used for 10 min to remove the native oxide that naturally forms on the silicon surface when exposed to the atmosphere. Next 5 nm (0.05 kÅ) chromium is deposited at a rate $5\,\text{Å}\,\text{s}^{-1}$ immediately followed by 200 nm (2 kÅ) gold deposited at a rate $2\,\text{Å}\,\text{s}^{-1}$. The thin chromium layer provides sufficient adhesion for the gold layer and the gold enables good electrical contact. The lift-off is achieved by submerging the sample in N-Methyl-2-pyrrolidone (NMP, 1165 Remover), which dissolves the nLOF under the chromium/gold layer, leaving the deposited metal only on the exposed and opened features. Mild ultrasound can be applied to speed up the lift-off, however, this can damage some fragile structures [28]. Finally, the sample is cleaned in 2-propanol (IPA) and dried with dry N_2. The above process is described with minor adjustments in Ref. [24].

A larger bonding pad has a higher capacitance, C, but a lower resistance, R, since it contacts more area. The response time (also called the RC-time), $t = (RC)^{-1}$, and so bonding pads should be large enough to contact efficiently but not too large to become slow. Typically, the size is determined by packaging-constraints or by the size of the electrical probes used to contact the pads, i.e., $\sim 100\,\mu\text{m}$-by-$100\,\mu\text{m}$. In this thesis only a thin layer is required to contact the structures using electrical probes, as shown in Ref. [24] where only 20 nm gold is used; however, to ensure adhesion and stability the thicker 200 nm layer is preferred. To reduce the RC-time further, the device-layer can be doped under the bonding pad to reduce the electrical resistance [10], however, this must be done locally and around the optical systems to keep Ohmic losses low in the dielectric waveguides.

2.3 Local diffusion-doping

The sample fabrication discussed in this section was carried out primarily by Mathias T. Sutherland as part of his BSc thesis [35].

Crystalline silicon is a semiconductor with a band gap of 1.12 eV arranged in a diamond lattice with lattice constant, $a = 5.43\,\text{Å}$, and there is approximately $5 \cdot 10^{22}$ silicon atoms in one cubic centimeter. At room temperature ($T = 20\,°\text{C}$) the thermal energy is 25 meV and consequently silicon behaves as an insulator unless a bias is applied [10]. However, it is possible to introduce defects that add carriers of electrical current, either by providing additional electrons in the conduction band (n-type) or by providing vacancies (holes) in the valence band (p-type). This is called doping when small amounts of defects are added ($\ll 1\,\%$) and alloying when substantial fraction of the lattice is replaced. Adding for example phosphor (P) to silicon results in n-type doping while adding boron (B) results in p-type doping. Typical undoped electron-grade silicon wafers have a resistivity of $\rho =$1–20 Ω cm while the device-layer of the highest-quality SOI-wafer considered in this thesis, type 2 with a 220 nm device layer, has a specification-sheet resistivity (p-type, boron), $\rho =$10–15 Ω cm, with a radial gradient.

Doping can be achieved by ion-implantation, which has excellent control of the spatial degree of freedom but relies on more complex tools, which is not available at the cleanroom facility used for the work of this thesis. An alternative method is diffusion doping where a material rich in the defect-of-interest is deposited and subsequently driven into the substrate by annealing. Since the silicon is already doped with low levels of boron (p-type) it is desirable to increase the doping levels with more boron. Additionally, by utilizing the different diffusion speeds of boron in silicon and glass [10] it is possible to mask parts of the silicon to only achieve

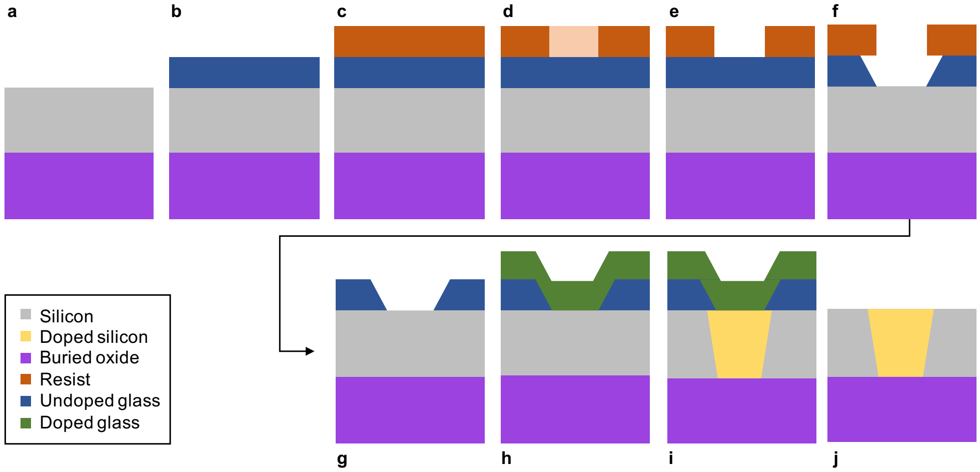

Figure 2.2. Outline of diffusion-doping process. a, Clean silicon substrate. **b**, PECVD deposition of undoped glass to function as a hardmask. **c**–**e**, Lithography defining doping regions: spin-coat (**c**), exposure (**d**) and development (**e**). **f**, Transfer softmask in resist to glass hardmask. **g**, Strip softmask and clean. **h**, Deposit doped glass. **i**, Anneal to transfer dopants into silicon substrate. Diffusion stops at buried oxide. **j**, Strip glass layers by submersion in hydrofluoric acid.

local doping. Figure 2.2 outlines the fabrication steps to achieve local doping of the device-layer of an SOI-chip, and further illustrates the various types of patterning and transfer processes shown in Fig. 2.1.

First, an undoped glass hardmask is deposited by PECVD as shown in Fig. 2.2**b**. Second, a $\sim 2\,\mu\text{m}$ UV-sensitive resist is spin-coated, patterned, post-exposure baked and developed (Fig. 2.2**c**–**e**) to define the regions to be doped, and the sample is submerged in buffered HF (BHF, 12.5 %) for 2 min, which etches the pattern into the SiO_2-hardmask (Fig. 2.2**f**). Hydrofluoric acid etches glass isotropically [10] and therefore results in some undercut. Precise control of the spatial dimension was beyond the scope of the project, however, a thinner hardmask results in less undercut so this should be as thin as possible while still functioning as a diffusion–stop-layer, and it is found that $\geq 75\,\text{nm}$ suffices [35]. Moreover, etching the hardmask with an anisotropic etch could further improve the spatial resolution. The UV-sensitive softmask is stripped and the sample is cleaned (Fig. 2.2**g**) by submersion for 10 min in piranha (1 part H_2SO_4 added to 4 parts H_2O) [36]. Next, a 375 nm layer of boron-doped glass is deposited with PECVD (Fig. 2.2**h**) by including a diborane (B_2H_6) gas flow of 130 sccm. The sample is then annealed (Fig. 2.2**i**) for 20 min at 1000 °C to diffuse the dopants into the silicon-layer. The diffusion stops at the buried oxide, however, diffusion will also occur laterally [10] further restricting the spatial resolution. Finally, both the doped and undoped PECVD-oxides are removed by submersion into BHF (12.5 %) [37]. If the chips are unpatterned a long strip can be carried out [35], however, if the chips are already patterned and the buried oxide is removed care should be taken. The 12.5 % BHF has an approximate etch rate of 100 nm/min in the buried oxide [36]. By tuning the relative diborane–gas flow the B-concentration of the doped oxide, and therefore the final dopant concentration in the silicon device-layer, can be tuned. By adjusting the time and temperature of the anneal, the speed and depth reached by the dopants can be adjusted [10].

Due to cleanliness and cross-contamination compatibility requirements of the tools used, the experiment reported here was carried out using less contamination-free equipment and on-going work has adjusted the process parameters to comply with a clean process flow. Specifically, an RCA-clean [36] should be carried out before both PECVD-deposition steps, replacing the piranha clean. The RCA clean is a 3-step chemical cleaning process with submersion first in standard clean 1 (SC-1): 5 parts H_2O, 1 part NH_4OH(25–29 %) and 1 part H_2O_2(30 %), followed by standard clean 2 (SC-2): 5 parts H_2O, 1 part HCl(37 %) and 1 part H_2O_2(30 %). Both SC-1 and SC-2 are carried out at T =70–80 °C. Finally, the sample is submerged in HF (5 %) to remove oxide generated in SC-1 and SC-2. The sample is submerged in water before, between and after each of the steps, and the HF-step must be skipped during the second RCA-clean to protect the glass hardmask.

2.3.1 Characterization of doped and undoped samples

A rectangular island (MESA) is defined lithographically by patterning an isolation trench around it and etching down to the buried oxide to electrically isolate the MESA. Then a series of 200 nm gold bonding pads are defined by lift-off, each separated by different distances, L, to allow a transmission-line measurement (TLM) [10]. The

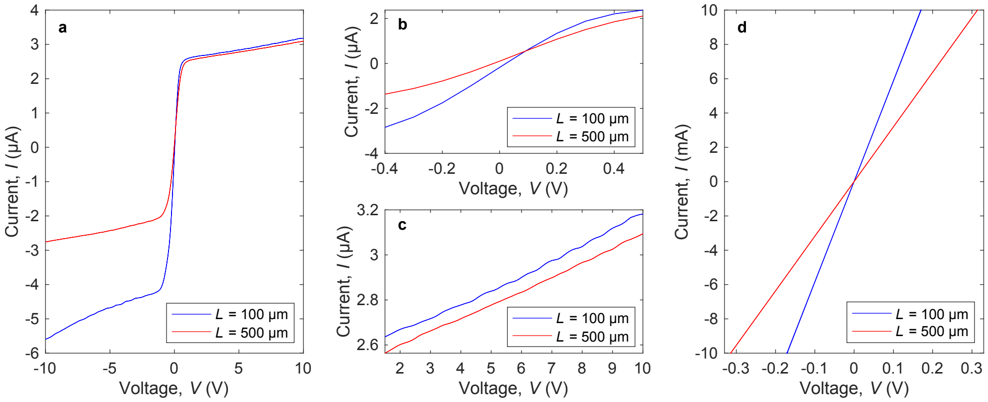

Figure 2.3. Electrical measurements of doped and undoped silicon-on-insulator. The bonding pads are 1000-by-200 μm on a MESA-TLM and L implies their separation. **a**, IV-characterization of undoped SOI with insets of low (high) voltage linear regimes in **b** (**c**). **d**, IV-characterization of doped SOI reaching the current-limit at a few hundred mV.

bonding pads are 1 mm wide and 200 µm tall resulting in a large capacitance. The doped and undoped MESA-TLMs are characterized by applying a voltage between two bonding pads and measuring the current (IV-measurement), the slope yields the resistance following Ohm's law [10],

$$U = RI. \tag{2.1}$$

Figure 2.3**a** shows an IV-measurement of two pads separated by 100 µm and 500 µm on undoped SOI, with a zoom-in around low (high) voltages shown in Fig. 2.3**b** (**c**), with the slope corresponding to resistances, $R = 0.22\,\mathrm{M\Omega}$ ($16\,\mathrm{M\Omega}$) for $L = 100\,\mu\mathrm{m}$ and $R = 0.34\,\mathrm{M\Omega}$ ($17\,\mathrm{M\Omega}$) for $L = 500\,\mu\mathrm{m}$. Figure 2.3**d** shows IV curves for the doped substrate, notably the y-axis is in units of mA, already at a few hundred mV the current reaches the 10 mA–limit set on the source-measure unit (SMU) to avoid damaging the chip. The slopes corresponds to resistances, $R = 17.0\,\Omega$ and $31.4\,\Omega$ for $L = 100\,\mu\mathrm{m}$ and $500\,\mu\mathrm{m}$, respectively.

This measured resistance is a combination of twice the contact resistance, R_c, representing the resistance between the SMU output and the sample, which is practice is dominated by the resistance between the bonding pad and the semiconductor due to the miss-match of their Fermi-levels [10]. Further assuming a linear dependence of resistance and distance, one can write the measured resistance,

$$R = 2R_c + LR_s, \tag{2.2}$$

with R_s the sheet resistance [10],

$$R_s = \frac{\rho}{t}. \tag{2.3}$$

Here, $t = 220\,\mathrm{nm}$ is the thickness of the device layer and ρ the resistivity. The resistance is then

$$R = \rho\frac{L}{Wt} = R_s\frac{L}{W}, \tag{2.4}$$

with $W = 1\,\mathrm{mm}$ the width of the channel. A linear fit to Eq. (2.2) enables quantifying the contact resistances as half the intercept, and the sheet resistance ($R_s = mW$), square resistance ($R_\square$) and resistivity ($\rho = tR_s$) can be estimated from the slope, m. The square resistance is an intuitive number, which allows the estimation of the resistance of a path on a semiconductor from its aspect ratio, and further avoids ambiguity with bulk resistance [10]. Lastly, by assuming the mobility of holes in silicon, $\mu_h = 1000\,\mathrm{cm}^2/\mathrm{Vs}$, the concentration of holes can be estimated [10],

$$N_h = \frac{1}{\mathrm{e}\mu_h\rho}, \tag{2.5}$$

with $\mathrm{e} = 1.602 \cdot 10^{-19}\mathrm{C}$ the charge of the electron. The results are displayed in in Tabel 2.1, and the undoped values, $\rho \sim 10\,\Omega\,\mathrm{cm}$, fits well with the specification-sheet value, $\rho =$10–15 $\Omega\,\mathrm{cm}$.

To verify the linear scaling with distance, the IV-characterization is carried out on two nominally identical copies of MESA TLMs on an undoped sample with square

Type	$\boldsymbol{R_c}$	$\boldsymbol{R_s}$ ($\boldsymbol{R_\square}$)	$\boldsymbol{\rho}$ ($\boldsymbol{\Omega}$ **cm**)	$\boldsymbol{N_h}$ (**cm**$^{-3}$)
Doped	$6.7\,\Omega$	$36\,\Omega$ ($/\square$)	$7.9 \cdot 10^{-4}$	$7.9 \cdot 10^{18}$
Undoped ($\lvert V\rvert < 0.3\,\mathrm{V}$)	$0.95\,\mathrm{M\Omega}$	$0.3\,\mathrm{M\Omega}$ ($/\square$)	6.6	$9.5 \cdot 10^{14}$
Undoped ($V > 1.6\,\mathrm{V}$)	$7.4\,\mathrm{M\Omega}$	$2.5\,\mathrm{M\Omega}$ ($/\square$)	55	$1.1 \cdot 10^{14}$

Table 2.1. Results of electrical measurements. Contact, sheet and square resistances as well as resistivity and hole concentration of doped and undoped silicon.

bonding pads of $W = 100\,\mu\mathrm{m}$, i.e., a 20-fold reduction in size compared to the previous measurements. The structures are characterized as part of project by Jesper Sand [38] and his electrical measurements are reproduced in Fig. 2.4. This confirms the electrical scaling as linear. Each nominally identical copy is measured multiple times both inside a dark enclosure and out as well as with light on and off around the setup, which results in minor fluctuations – however, as can be seen by comparing the two nominally identical copies the fluctuations between two MESAs a few hundred micrometers apart is substantially larger than the fluctuations incurred by varying the conditions and in any case the variations are small. The fits in Fig. 2.4**b** results in slopes of $0.72\,\mathrm{k\Omega/mm}$ and $0.69\,\mathrm{M\Omega/mm}$ for copies 1 and 2, respectively, and a contact resistance, $R_c \sim 400\,\mathrm{k\Omega}$.

With the exception of this section, all other experiments reported in this thesis considers undoped silicon and the high-resistances of the undoped silicon is not an issue for the electrostatic nano-electro-mechanical systems (NEMS) considered in this

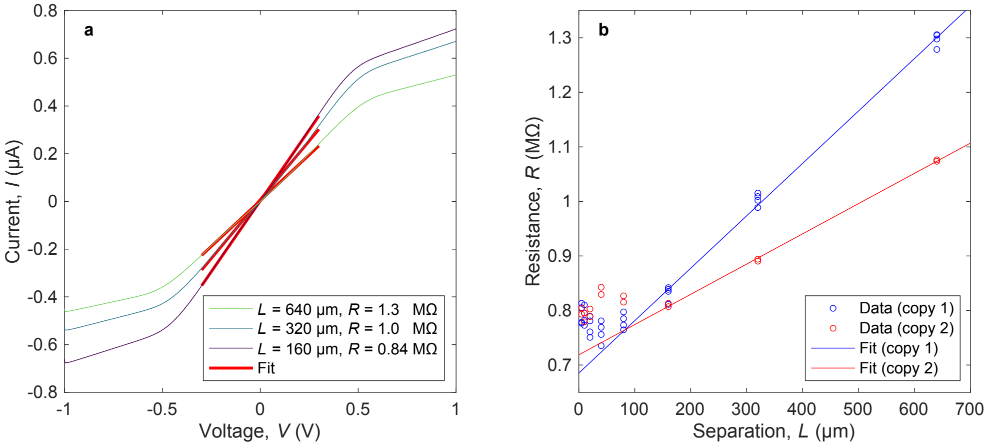

Figure 2.4. Measured resistances of two nominally identical MESA TLMs. a, Illustrates 3 IV-curves of copy 1 with $160\,\mu\mathrm{m}$, $320\,\mu\mathrm{m}$ and $640\,\mu\mathrm{m}$ separation between the bonding pads and linear fit to obtain the corresponding resistances. **b**, The resistance obtained for separations, L, of both copies as well as linear fits. Figure adapted from data in Ref. [38] with permission.

theses, and hence, the actuation reported in Ch. 8 and 9 are low-speed direct-current (DC). Nevertheless, the local doping process reported here could increase the response time of the NEMS considered without introducing optical losses at the waveguides. A recent study of the response time of the undoped structures discussed in this thesis was carried out in Ref. [24].

2.4 Vapor-phase hydrofluoric acid release-etch

The final fabrication-step to realize suspended structures are the underetching in which the buried oxide is etched to release the silicon membrane. Hydrofluoric acid does not etch silicon but can etch $\mathrm{SiO_2}$ through the reaction [10, 31],

$$\mathrm{SiO_2(s) + 4HF(aq) \rightarrow SiF_4(ads) + 2H_2O(aq)}. \tag{2.6}$$

Silicon tetrafluoride is volatile, and hence, is desorbed and dissolved in the water. Typically, low concentrations of HF (e.g., 12.5 %) is used with a buffer to stabilize the etch rate and a wetting agent to enable the liquid to penetrate through narrow features otherwise restricted by strong capillary forces. While this works well for mechanically stable structures, fragile systems such as NEMS are susceptible to collapse due to capillary forces when the sample is dried [39]. One alternative is to dry the sample using critical-point drying, in which the water is first substituted by isopropanol (IPA), which again is exchanged for liquid $\mathrm{CO_2}$ under high pressure. The $\mathrm{CO_2}$ can then be turned into gas through its supercritical point, thus avoiding capillary forces. However, this process is cumbersome and requires substantial handling of the samples, which can cause errors.

In this thesis HF is used in vapor-phase [29–32] in a temperature- and pressure-controlled chamber, further substituting the water with ethanol as a catalyst in a commercially available tool [30]. Figure 2.5 shows a tilted cross-section scanning electron microscope (SEM) image of 3.5 µm wide opening in the 220 nm silicon device-layer enabling a 1.67 µm isotropic etch into the 2 µm buried oxide in 800 s = 13 min 20 s corresponding to an etch rate of $125\,\mathrm{nm\,s^{-1}}$. The tool was installed at the start of the work leading to this thesis, following initial testing by the same author [28], and this section documents the processes used. The author further wishes to explicitly acknowledge valuable discussions with Rune Christiansen and Claus Nielsen.

The system is a vacuum chamber with three gas inputs using ALD-regulated $\mathrm{N_2}$- and HF-valves as well as a low dead-volume liquid valve to supply ethanol. The $\mathrm{N_2}$ supply carries the ethanol through a heated vaporizer before it is mixed with the HF and input to the chamber from one side and the gas is purged through a needle-valve–controlled line to the pump. The output-valve has a manual Vernier scale and the system measures the pressure at a given time as well as the mean pressure during the process. The chamber and sample is normally heated with resistive elements and PID control to 45 °C, the temperature should be at least 40 °C to avoid condensation [31] and $< 50\,^\circ\mathrm{C}$ to keep an appreciable etching speed. The combination of temperature and pressure controls the rate of desorption of the water produced by the etching

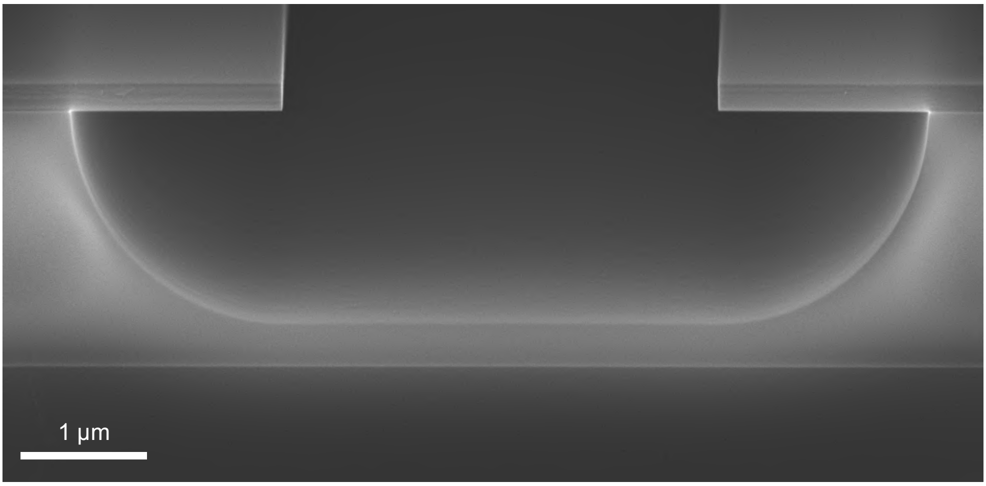

Figure 2.5. Cross-section scanning electron micrograph of underetched silicon membrane. Using one cycle of Recipe 3 over 800 s, 1670 nm is etched isotropically corresponding to an etch rate of $125\,\mathrm{nm\,s^{-1}}$. The process-pressure was 122.3 Torr.

as well as the etch rate. Therefore, a trade-off exists between total etching time and stiction-tolerance of the released structures. Release-processes are described for stable structures such as cavities in Ref. [16] and more fragile NEMS in Ref. [24]. The operating pressures is 50–150 Torr (atmospheric pressure is 760 Torr). At 150 Torr water will form and already beyond 130 Torr caution should be exhibited. Typically, the process-pressure fluctuates around the mean value within a couple of Torr and the mean process-pressure drifts over time, so the manual valve should be adjusted every few months to ensure reproducibility. The target pressure of all processes is 125 Torr, which is the highest pressure (and therefore speed) that maintains a practically water-free underetch.

The tool comes with 5 standard recipes but only recipes 1 and 3 are used extensively in this thesis. The process-information for all 5 recipes are listed in Table 2.2. Notably, the total gas flow is kept roughly constant, such that the target gas pressure 125 Torr can be obtained without adjusting the valve. Reducing the pressure below 100 Torr will greatly slow down the etch rate. Rather than adjusting the pressure, the process is run as a number of cycles and the chamber is pumped to base-pressure between each cycle. By running more and shorter cycles it is possible to reduce the risk of stiction. Whenever possible process times of each cycle should be in the range 10–20 min to ensure a stable etch rate, however, shorter times can be used if the precise etched depth gained is not important and rather the amount of stiction is. This can for example be the case in a multi-process etch, where the first step releases a fragile membrane and the second step deep-etches the buried oxide several micrometers around photonic components to protect the optical modes from leakage into the substrate [24], i.e., the structures should be separated by at least an optical wavelength, which for telecom photons imply, $\lambda \sim 1550\,\text{nm}$.

Recipe	**N_2 (sccm)**	**C_2H_6O (sccm)**	**HF (sccm)**	**Etch rate (nm/min)**
1	1425	210	190	17
2	1250	350	310	45
3	1000	400	525	125
4	910	400	600	$150^{\dagger}$
5	880	325	720	350

Table 2.2. The 5 standard recipes for vapor-phase HF etching. The total gas flow is 1925 sccm for all processes except recipe 1 with 1825 sccm. Recipes 1 and 3 have primarily been used in this thesis and it found that the etch rate varies 125–140 nm/min with average process pressures 122–130 Torr for Recipe 1 and the value given here is for the 122.3 Torr–run presented in Fig. 2.5. The value for Recipe 1 is given for a 124.0 Torr–run. † The rate for recipe 4 was measured on a different SiO_2.

The tool uses anhydrous hydrofluoric acid (99.995 %) as a source [16], which in principle enables a water-free etch, since the tool can also be used to etch other materials [32], however a standard oxide-etch cannot be anhydrous as the etch itself produces water. An interesting feature of vapor-phase HF is that it does not etch aluminium, aluminium oxide and steel, which is otherwise normally etched by liquid HF [36], due to the lack of water present – the latter is relevant as it allows the tool and exhaust systems to be constructed out of stainless steel, while the former two materials are interesting as hardmask-options and stops the HF etch by fluorinating the aluminium surface forming AlF. Aluminium is low-cost, can be easily deposited with standard lift-off processes and it is widely used to form bonding pads for these two reasons. Aluminium bonding pads are rapidly oxidized so to establish proper electrical contact, probes must be scratched through this oxide-film, which shortens the lift-span of contacts. However, for packaged, scaled-up solutions it has many advantages over the Cr/Au bonding pads used in this thesis. Alumina (Al_2O_3) can be deposited with PVD, e.g., sputtering, but it can also be efficiently deposited using atomic-layer deposition (ALD) as previously discussed, which enables deposition of high-quality films that uniformly covers the exposed surfaces, and therefore, provides an excellent mask. Both aluminium and alumina can be easily stripped with a dip in liquid HF or using hydrochloric acid, such as in the SC-2 step of the RCA clean previously described, which does not etch silicon or silicon dioxide [36].

The etching tool used, a PrimaxX uEtch, is a single-wafer system with a 200 mm–chamber with three pins that holds the wafer suspended in the center such that the gases will pass both above and below the wafer. The pins are spaced to allow substrates down to 4”-wafers (i.e., diameter of 100 mm), so to underetch a chip this should be placed on a carrier-wafer, which in turn disallow a free gas-flow to the back of the chip. It is possible to place the chip on small pieces—or even use a dedicated carrier wafer with etched trenches—to expose some of the back, however, the oxide on the back of an SOI-chip should in general be expected to remain. This has three consequences. First, since the lattice constant of silicon and silicon dioxide is different, the chip will experience tensile stress if the oxide is removed on the back but left on the front, which will normally be the case when etching the sample using wet HF. Indeed, this is the reason it is left there in the first place on the SOI wafer: to avoid the wafer bending by maintaining a similar stress on both sides of the wafer; it is primarily the oxide closest to the interface that contributes the most to this effect as this is where the lattice–miss-match occurs. Second, protecting the oxide on the back of the chip further enables maintaining patterns in this oxide. Third, the oxide electrically insulates the silicon-handle layer, which is therefore not easily grounded by simply placing the chip on a chuck. Instead, the potential of the substrate is in principle floating, and for NEMS systems care should be taken to take this into account. Ideally, the substrate potential must be controlled, e.g., by covering the backside in a conductive material such as silver paint or by providing a dedicated bonding pad for ground-access to the substrate as discussed in Sec. 9.4. Finally, the inherent stress due to the miss-match between silicon and silicon dioxide further causes the released silicon structures to deform after the release. Practically, this must be taken into account by including stress-release structures to absorb the stress in a controlled fashion, thus avoiding device failure. Interestingly, such stress-release does not have to be destructive – in fact, by tuning the film-stress in silicon nitride (Si_3N_4) Grutter *et al.* [40] demonstrated constructive self-assembly, manufacturing structures deep below the resolution otherwise obtainable with the nanofabrication methods directly.

CHAPTER 3

High-resolution electron-beam lithography

Electron-beam lithography (EBL) is a versatile and widespread tool used to define nanostructures. This results from the ease-of-access to electron sources combined with the low wavelength of electrons – which enables focusing electron beams to nanometer-scale spot-sizes using high acceleration-voltages [10, 41, 42]. However, the high-energy electrons have a low-mass and scatter far in the substrates [43–45], delivering a proximity dose many microns from the intended site in an effective dose distribution characterized by a point-spread function (PSF), Ψ [43, 46–50]]. The PSF in turn can be used to predict the result of a given exposure as well as to modify the exposure mask to obtain the desired result using proximity effect corrections (PEC) [51–58].

This chapter will first introduce the principles of EBL, and then provide experimental results to obtain the dose to clear in a self-consistent manner as well as present direct measurements of the point-spread function. Finally, high-resolution lithography is discussed including hardware-specific challenges such as fracturing and shot-filling, which become critical to take into account.

3.1 Principles of electron-beam lithography

In electron-beam lithography a beam of electrons is generated and accelerated by a potential, V, that further directs it into a column. It is filtered by a pinhole to improve the directionallity to tune the current, I, coarsely. Since there is a nonlinear dependence on pinhole size and the size of the focused beam a number of pinholes are typically available in dedicated EBL-systems. The beam is then focused by a series of electromagnetic coils providing a nonlinear field across the cross-section of the column. It is desirable to focus the beam to smaller spots since this enables higher resolution, and reducing the current enables smaller spot-sizes. However, the exposure time of a pattern is directly proportional to the current and so an optimum exists. Alternatively, multi-current exposures can be carried out in which coarse features (e.g., bonding pads and isolation trenches) are patterned with a higher current, while fine features (e.g., optical components) can be added with a lower current. Increasing the acceleration voltage further enables focusing the beam to smaller sizes [43, 50, 59, 60], however, higher-energy electrons are less likely to interact and therefore provide the necessary dose to activate the resist, i.e., the exposure dose required is also increasing.

Modern dedicated EBL-systems provide a current $I = 0.1$–$100\,\mathrm{nA}$ with acceleration voltages, $V = 50$–$150\,\mathrm{kV}$. This enables spot-sizes down to a few nanometers for the smallest currents and tens of nanometers for the higher currents [10]. Dedicated mask-writing tools for industrial manufacturing often use $V = 50\,\mathrm{kV}$ to achieve higher throughput. Recently, STS-Elionix has developed a 1 µA, 50 kV tool for high throughput. This is limited to spot-sizes of several tens of nanometers but is competitive in terms of speed and flexibility for low-volume, low pattern-densities or few customizable layers, as previously mentioned is predicted in the lithography roadmap [7]. Both JEOL and Elionix EBL-systems are so-called direct-write tools where the beam is deflected by an electric field to individual spots sequentially. An alternative methods are fixed-beam–moving-stage (FBMS)—commonly used by Raith tools [42]—where the mechanical stage with the sample is moved instead. Finally, fast exposures can be carried out with shape-exposure tools (e.g., Vistec) where a flood-exposure is masked by a combination of multiple shaped pinholes resulting in complex shapes.

In this thesis, all exposures of structures are carried out on a 100 keV dedicated JEOL-JBX 9500FSZ system [62]. Some tests are carried out using an STS-Elionix F125 (125 keV) and using a state-of-the-art F150 (150 keV). The JEOL system is the main focus with some comparisons drawn to the Elionix tools. It achieves a theoretical minimal spot-size–diameter, $d = 3.3\,\mathrm{nm}$, for $I \sim 0.2\,\mathrm{nA}$ using a 40 µm circular aperture [41]; in order to go to lower currents, an asymmetric aperture must be used, which distorts the beam. The electron charge, $\mathrm{e} = 1.602 \cdot 10^{-19}\mathrm{C}$, and so this current corresponds to 1.25 electrons per nanosecond. Additionally, the tool can dynamically adjust depth-of-focus (DOF) across the sample [41], however, the DOF depends on the size of the aperture used – and typically will be $\gg 10\,\mu\mathrm{m}$ for high-resolution exposures based on low-current through small apertures [63]. Instead,

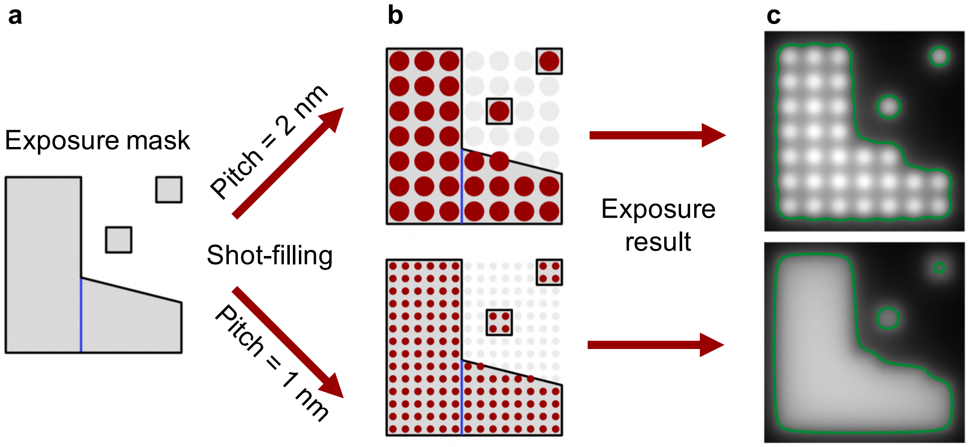

Figure 3.1. Exposure flow of direct-write electron-beam lithography. **a**, A mask is fractured into primitives of the pattern-generator, and **b**, each primitive is filled with discrete shots. **c**, The resulting exposure is a convolution between the electron point-spread function and the discrete shot-sites and the resists that receives a dose above the threshold-dose is developed. Figure adapted from [61].

since height variations across a chip are typically within a few micrometers, the focus is set to the mean height of the sample surface and exposure speed is prioritized. All exposures are direct-write and the exposure flow is outline in Fig. 3.1. The patterns-to-be-exposed are provided as a list of two-dimensional (2D) polygons, P, in a mask, $M(x, y)$, prepared in the database format `Calma GDS II` using an in-house–developed software-library [28]. The mask is fractured into basic primitives allowed by the specific EBL-system (blue line in Fig. 3.1**a**). The JEOL tool allows only trapezoids with all inner angles $\geq 30°$ and the two parallel sides aligned to either the x- or y-axis and triangles can be defined by letting two points be identical on the short side. This allows a fast pattern generator [64] but is somewhat restrictive and should be carefully considered when designing masks [16]. Contrary to this, Elionix tools offers a wide range of primitives – notably the circle, which is relevant to the photonic crystal (PhC)-community [65, 66].

The system has a 100 MHz pattern-generator, which enables it to move the beam once every 10 ns or slower – albeit not faster. Figure 3.1**b** shows the fractured primitives discretized into shots [44, 48, 61],

$$S(i, j) = \sum_{i,j} \int M(x, y)\delta(x - ip_x)\delta(y - jp_y)dxdy, \tag{3.1}$$

with S a 2D matrix describing which of the discrete sites should be exposed, and p_x and p_y being the pitch, i.e., separation between the shots, which can be different along x and y on Elionix tools but are equal on JEOL. In practice the current is not changed dynamically and so the dose delivered to a shot is controlled by a dwell time, τ, weighted by the pitch, $p^2 = p_x p_y$, and the base charge dose density of the exposure, D_0, often called the dose to clear, and the dwell time can be written as,

$$\tau(i, j) = \frac{p^2 D_0}{I} S(i, j). \tag{3.2}$$

For a dose of $200\,\mu\mathrm{C\,cm^{-2}} = 2\,\mathrm{aC\,nm^{-2}}$, a current $I = 0.2\,\mathrm{nA}$ and the minimum pitch of 1 nm, the dwell time becomes 10 ns, which is the limit of a 100 MHz e-beam writer, i.e., a lower dose requires a correspondingly lower current or a larger pitch. This typical limit corresponds to 12.5 electrons per shot, which is clearly shot-noise limited. Additionally, it can be seen that a smaller pitch results in a better pattern-fidelity due to the better shot-filling.

The mass of the electron is $511\,\mathrm{keV/c^2}$ [67] and the energy-ranges in electron-beam lithography are therefore non-relativistic. The scattering cross-section of electrons in a stack of stratified media, and therefore the expected dose to clear, scales as $\sqrt{V}$ [44], i.e., few direct scattering events will occur and rather the main contribution of the resist exposure is through local secondary electrons generated from the primary scattering event. The likelihood of a primary scattering event is low but linearly proportional with the thickness of the resists so this further implies that the required dose to clear the resist does not depend strongly on the resist thickness for relatively thin resists (thickness, $t < 200\,\mathrm{nm}$) and high voltage ($V > 50\,\mathrm{kV}$). While the number of electrons delivered to each shot is shot-noise limited, it is important to remember that the shot pitch is also much lower than the size of the focused electron beam and so a smooth exposure is generally obtained. This is shown in Fig. 3.1**c** illustrating the resulting effective dose, D_{eff}, from exposing a series of discrete shots by performing a convolution between the array of discrete shots and the point-spread function (PSF) [68], $\Psi(r)$, which is a density function describing the fraction of energy deposited a distance r from the target position that further obeys azimuthal symmetry [28],

$$D_{\text{eff}}(x, y) = \sum_{i,j} \tau(i, j) * \Psi(r). \tag{3.3}$$

The green outline in Fig. 3.1**c** shows the threshold (which in general is a smooth transition) for clearing the resists [28, 48], i.e., $D_{\text{eff}}(x, y) \geq D_0$, with D_0 the dose to clear. Notably this outline is less rough for a smaller shot-pitch since a smaller pitch results in a better pattern fidelity as well as a more uniform exposure [54].

3.2 The dose to clear

The dose to clear is a key parameter to a successful exposure [28, 43, 44, 48, 61] – yet often it is defined inconsistently or specific to a pattern, which easily can be motivated from hardware-specific quirks but may cause confusion in terminology. The definitions and lack of clarity are closely related to the concept of proximity effect correction (PEC); and thereby the PSF. This section will provide the intuitive description of the dose to clear commonly used, and then—as has been done before in, e.g., Refs. [28, 43, 44, 48, 61]—define it more rigorously in the context of the PSF. Finally, measurements of the dose to clear are presented and discussed.

The term "dose to clear" can be taken as the *base* charge-dose–density, D_0, that sufficiently breaks down (cross-links) the polymer in the positive (negative) resist and the developer will dissolve the exposed (unexposed) features. The EBL system delivers a dose (energy) per unit volume (typically in $\text{eV}\,\mu\text{m}^{-3}$) in the entire stack, however, since the resist is generally thin, the out-of-plane variation (along z) and the threshold energy to active the resist can be factored out

$$\Psi(r) = \Psi(x, y) = \frac{\Psi(x, y, z)}{\int\int dx dx \Psi(x, y, z)}, \tag{3.4}$$

thus defining a 2D density function (typically in μm^{-2}) [28]. In the context of PEC with a 100 kV exposure in a (substantially) silicon substrate, only the long-range part of the PSF is taken into account and it can be approximated as a Gaussian with variance $\beta \approx 30\,\mu\text{m}$ [18]. This implies that dense and connected features, such as the 50-by-50 µm crystal in Ref. [18], affect their neighbours with background dose, and PEC should be applied to adjust $\tau(i, j)$ spatially [51, 53, 57, 58]. However, small and isolated features, such as the cavity in Ref. [16], will have a uniform dose within each feature – they can be exposed without dose-modulation (often miss-interpreted as exposed without PEC) albeit the uniform dose will still be given by the PEC [57], and notably, it results in a dose density that is larger than D_0. Large periodic or uniform features where only the central part is of relevance can be exposed with a uniform dose. Examples include phononic crystal waveguides with many periods of mirrors in the ends [20, 21] or lines to be cleaved somewhere in the middle for cross-section analysis.

The pattern-specific dose-density is sometimes also confused with the base dose-density to clear for a couple of reasons – although this practice should be avoided to avoid ambiguity. First, it is common to expose an array of the desired mask (or a representative subset of its content) with various doses and from an analysis of the outcome decide a dose density for the actual exposure [69]; sometimes this is done to "avoid" PEC, although this practice represents an experimental trial-and-error approach instead of solving the inverse problem [51] before the exposure numerically [57] and scaling it with D_0 [44, 48, 51, 53, 54, 70]. Second, while the physical parameters of EBL is the dwell time and the current, the JEOL systems for example specify τ only indirectly. Instead, the pitch, current and dose density are specified and before the exposure commences it is verified that $p^2 D/I > \tau_{\mathrm{min}}$ with $\tau_{\mathrm{min}} = 10\,\mathrm{ns} = 1/100\,\mathrm{MHz}$ limited by the pattern-generator of the hardware. Since increasing the current speeds up the exposure and reducing the pitch improves the rasterization and exposure results, it is desirable to make D (called the "RESIST" in JEOL terminology) as large as possible, i.e., D_0 is scaled by the smallest dose-modulation applied and all dose-modulations are re-scaled to this relative dose. This is peculiar, since it is rare that one needs to expose huge dense features with high-resolution electron-beam lithography and more often fine features are needed and so the dose and dwell times are naturally boosted. It now also becomes clear that since the smallest pitch possible (1 nm on the JEOL tool) is desirable in order to improve the quality of the exposure [16] and since D is simply a re-scaled version of D_0 to satisfy a virtual process of the hardware, the speed of the pattern generator and the speed of the exposure (i.e., the current) are linearly proportional. Recently, a high-throughput Elionix tool offers a pattern generator up to 400 MHz, however, 100 MHz is still considered state-of-the-art and much-lower values, $\sim 10\,\mathrm{MHz}$, are still prevalent.

With this in mind a dose to clear can be defined that is unique to the material stack, the resist, the development process and the EBL system used (i.e., the voltage scaling the dose to clear as $D_0 \propto V^{-1/2}$ [44]). If a dense pattern much larger than the longest-range component of the PSF (i.e., $\gg \beta$) is exposed with a uniform dose the central region out to $\sim \beta$ from the edge will receive a uniform dose, the base charge-dose–density to clear. Figure 3.2**a**–**b** shows a schematic of an array of of large squares each receiving a different uniform dose. Figure 3.2**c** shows an optical microscope image of a 4-by-8 array of 200-by-200 µm squares with different uniform doses. The patterns are exposed in 180 nm chemically semi-amplified resist (CSAR 6200.09) [33, 71, 72] spin-coated on a silicon wafer and developed in amyl acetate (AR 600-546) in a single puddle for 60 s. The development is carried out using an automatic Laurell EDC 650 puddle, which dispenses the chemical, consistently and reproducibly agitates the sample during the development and exchanges the developer for isopropanol (IPA)

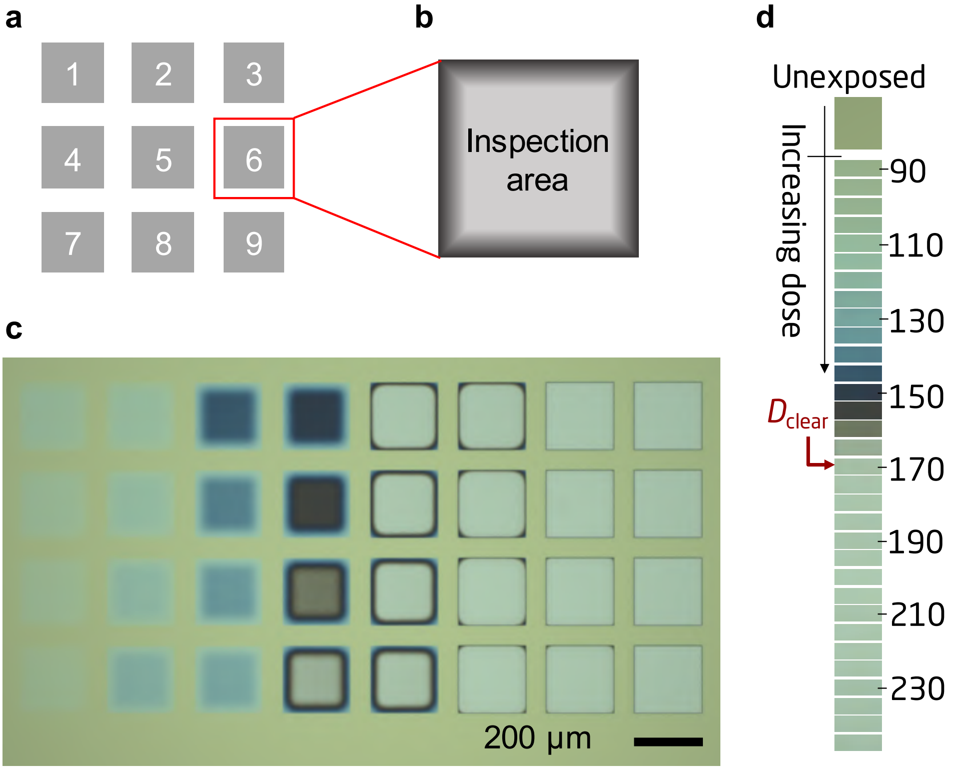

Figure 3.2. Dose test for electron-beam lithograghy. a, Array of large squares such that the central inspection area (**b**) of each receives a uniform dose. **c**, Optical microscope image of dose test performed in 180 nm CSAR resist on a silicon substrate. **d**, the centers of each square next to one another to illustrate that the dose to clear is the smallest value that fully clears the center, in this case $(170 \pm 5)\,\mu\mathrm{C\,cm^{-2}}$.

to stop the development immediately after 60 s has transpired. Finally, it dries the sample with dry N_2. The edges of the squares shows the dose-variation due to the PSF [58] and enables identifying when the resist is fully cleared in the center, i.e., when the color stops changing. Fig. 3.2**d** shows a cut-out of the centers of each square put next to each other to show that the dose to clear is $(170 \pm 5)\,\mu\mathrm{C\,cm^{-2}}$. A dose test carried out for the same resit thickness and development procedure but using an SOI chip instead results in a dose to clear 145–150 $\mu\mathrm{C\,cm^{-2}}$ [18, 28, 68].

It is advantageous to reduce the thickness of the resist in order to improve the spatial resolution, since a challenge from the resolution–point-of-view is the aspect ratio [16]. However, a thinner resist comes at the price of reduced etching selectivity (i.e., the mask is eroded and consequently it is harder to etch as deep). The resolution can therefore be traded for roughness as described in Ref. [16] or the thicker resist

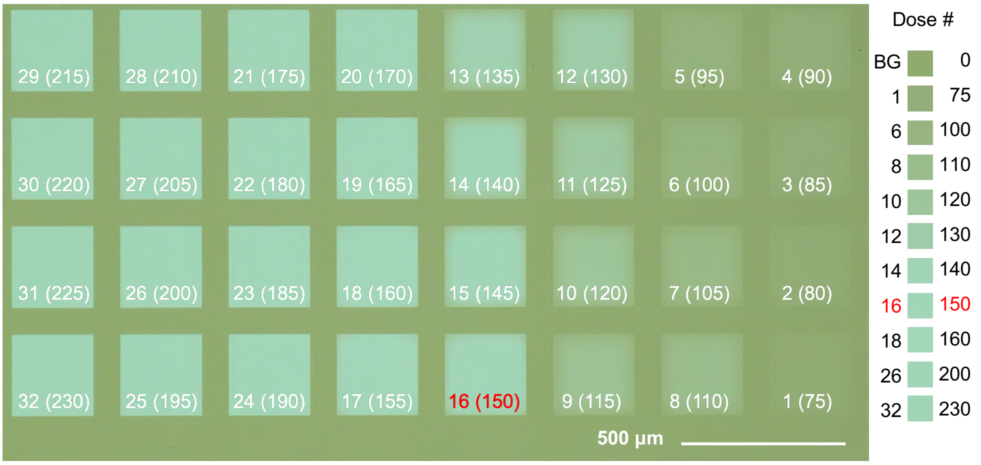

Figure 3.3. Dose test for 65 nm CSAR on SOI. The thin CSAR reduces the contrast in optical microscopy, however, the dose to clear can be determined to be 150 µC cm^{-2}. The dose test is carried out on a 240 nm silicon on 3 µm buried oxide SOI chip and the development is performed with amyl acetate (AR 600 546). The experiment presented in this figure is carried out in collaboration with Christian A. Rosiek.

can be used to maintain a low roughness as described in Ref. [18]. The importance of aspect ratio as well as the trade-offs with selectivity and other figures of merits will be discussed in detail in Ch. 4. Figure 3.3 shows a dose test carried out on 65 nm CSAR on a 240 nm silicon on 3 µm buried oxide SOI chip (i.e., type 1) in collaboration with Christian A. Rosiek, and the dose to clear of 150 µC cm^{-2} is consistent with [28, 68] as well as the thicker CSAR resist on the same substrate [18] but notably lower than the all-silicon substrate. This corroborates that the dose is largely independent of the thickness of the resist as long as it is reasonably thin; however, it does depend on the stack materials [43].

To investigate the effects of shot-filling in nanostructures explicitly, Fig. 3.4**a**–**c** illustrates 3 sets of two dose tests with three different shot pitches p = 12.5 nm, 15 nm and 8 nm, respectively. The dose test is carried out on SOI-stack 2 with 50 nm CSAR (6200.09, i.e., 9 % CSAR concentration diluted 1:1 to 4.5 %) and a multi-layer hardmask stack (10 nm chromium and 10 nm poly-crystalline silicon), which will be discussed and motivated in Sec. 4.3. The development is carried out using amyl acetate (Zeon N-50) for 60 s. As previously mentioned, JEOL and Elionix EBL systems deflect the incident beam to define patterns, however, this deflection cause a deterioration in the exposure quality farther from the center; and hence, is limited to 1 mm on the JEOL JBX-9500FSZ, called a writefield and the e-beam stage is only moved when patterns are larger than this by stitching together writefields – this can cause errors at the writefield interfaces called ”stitching-errors.” In addition, to maintain a high-fidelity, so-called subfields are employed in which the write-fields

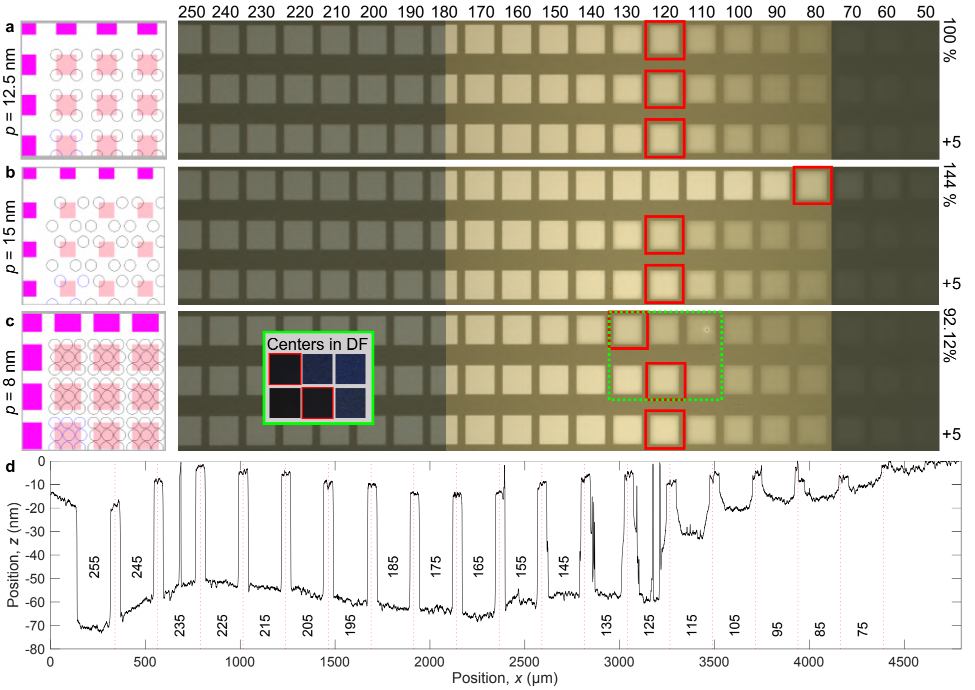

Figure 3.4. Dose tests to probe the effects of shot-filling. All tests on multi-layer hardmask stack on SOI (stack 2) with 50 nm CSAR and development with amyl acetate (Z-N50), 60 s. **a**–**c**, The pitch is varied to p = 12.5 nm, 15 nm and 8 nm, respectively, and 3 rows of 180-by-180 µm squares are exposed using each pitch with doses 50–255 µC cm^{-2}. The top row in each set is manually fractured to 25-by-25 nm squares (7200^2 squares) with comparable dimensions to the pitch to illustrate the shot-filling. The left panels shows the shot-filling as it appears on the JEOL 9500FSZ pattern-generator. The bottom rows are offset +5 µC cm^{-2} compared to the middle row where the squares are fractured to 4-by-4 µm to eliminate shot-filling errors. The red squares highlight the dose to clear estimated from each row and the inset in **c** shows the centers with dark-field optical microscopy, which is sensitive to small amounts of residue, thus illustrating that the dose to clear is higher due to the shot-filling only delivering 92.12 % of the desired dose. **b**, The top row shows that 144 % of the intended dose is delivered. The darker sides on the right and left sides are from a 2.5x magnification bright-field optical micrograph while the brighter central parts are stitched in and obtained using 5x bright-field optical microscopy. The contrast and brightness is not manipulated from the raw images. **d**, Profilometer-scan along the bottom-row of **c** illustrating that the resist is ∼ 50 nm thick and that the dose to clear is 120 µC cm^{-2}.

are deflected in two stages, first a course deflector moves the beam to 4-by-4 µm ”subfields” and then the subfield-generator moves it on a 0.25 nm grid within the subfield. Before the exposure is carried out—and ideally periodically during it—the dose shift and gain due to the deflection is calibrated by deflecting the beam and measuring the variation in dose deposited, however, only a mean compensation can be applied and therefore, to ensure that the dose test is correct, the mask is defined as a single 180-by-180 µm square and the stage is then forced to move to its center before exposing it with a uniform dose. The middle row of the dose tests are swept with uniform doses 50–250 $\mu\mathrm{C\,cm^{-2}}$ in steps of 10 $\mu\mathrm{C\,cm^{-2}}$, and the bottom row of each test from 55–255 $\mu\mathrm{C\,cm^{-2}}$ to establish the dose to clear with high precision. These squares are fractured into 4-by-4 µm squares, which are much larger than all three shot-pitches considered, and hence, they achieve the same result of a 120 $\mu\mathrm{C\,cm^{-2}}$ dose to clear. While it is hard to analyze the low-contrast bright-field optical microscope images, the inset in Fig. 3.4**c** shows the centers of the squares inspected by dark-field optical microscopy, which is much more sensitive to low levels of resist residues, thus, confirming the dose to clear. To further corroborate the dose to clear, a profilometer-scan of the bottom-row of Fig. 3.4**c** is shown in Fig. 3.4**d**. This also enables identifying that the resist is $\sim 50\,\mathrm{nm}$ thick after development.

However, in the top row of each dose test the 180 µm–squares are fractured into a 7200-by-7200 array of 25 nm–squares, which are compatible with the pitches considered [61]. The left panel of Fig. 3.4**a**–**c** shows the pattern-generator–output for such an array of touching 25 nm–squares. Interestingly, for the 3 pitches considered it corresponds to an actual delivered dose of 100 %, 144 % and 92.12 %, respectively, i.e., a correct exposure, an overexposure and an underexposure. This also manifests in the dose test where the dose to clear for the three exposures are 120 $\mu\mathrm{C\,cm^{-2}}$, 80 $\mu\mathrm{C\,cm^{-2}}$ and 130 $\mu\mathrm{C\,cm^{-2}}$, consistent with the prediction from the shot-filling. This uncertainty is huge compared to any other parameter in the exposure process—usually the dose is controlled to within sub-percentage–precision—and implies that great care must be taken whenever polygons are fractured to dimensions comparable to the pitch [16, 61]. In the figures from the pattern generator, the size of the circles represents the simulated diameter of the focused electron-beam (i.e., the full-width half-maximum of a Gaussian spot).

Another interesting point is how the shot-filling is carried out. Manifestly, the pattern is uniformly shrunk by half the pitch and shots are distributed starting from the top-left point and with integer-multiples of the pitch. When the pitch is an integer multiple of the fractured polygon-size (Fig. 3.4**a**) this goes well and the exposure is uniform and clean. However when it is not, every second row is offset by a further half of error, $(w - p) \mod p$, for a feature width, $w = 25\,\mathrm{nm}$. Seemingly, this is done to reduce dose-inhomogeneity resulting from polygon-interfaces at the price of added line-edge roughness at the overall polygon boundary. This may be desirable for fabrication of electrical circuits where establishing a connection is key, however, the added roughness to the edge can be detrimental to optical structures causing increased scattering of the light, i.e., larger propagation losses or lower optical quality factors. Figures 3.4**b**) and **c** both shows that the shot-filling–method is not robust and actually does not results in a very uniform exposure even at the centers of the original polygons due to the errors at fracture-interfaces. Curiously, the resulting dose can be both an underexposure but also an overexposure and it may be hard to gauge when which will occur in more complex structures, such as a smooth waveguide bend. Here, an alternative is the approach taken by, e.g., Elionix in which the shot-filling is always carried out from the top-left corner of the original polygon and spaced by integer pitches horizontally and vertically; the error is then transferred to the right and bottom sides of each of the fractured polygons causing a systematic error, which is not necessarily better albeit at least predictable. The shot-sites and pitches are controlled by an analogue signal (specifically, the discretization is done with an analogue-to-digital converter (ADC) and then the voltages of the beam deflectors are set through a digital-to-analogue converter (DAC)), and so shot-filling errors are not intrinsically needed but rather implemented because it is widely not considered a big problem. In any case, the solution is to ensure that the chosen pitch matches the mask [16] and Ch. 6 gives an example how this can be ensured already at the design stage.

Finally, it should be noted that the dose to clear measured here is substantially lower than previously. Multiple factors have changed; there is a hardmask between the SOI-stack and the resist, the resist is thinner, and the developer is changed. Previously, it was demonstrated that the thickness of the resist does not substantially affect the dose to clear, and for parts of this project the developers have been used interchangeably due to involvement in different projects, and while the results with Zeon Z-N50 seems more reproducible the dose to clear does not seem to fluctuate. This implies that the change is caused by the hardmask-stack, which may in-part be due to the chromium layer, which is conductive such that the deposited electrons can be dispersed to ground from the resist, and therefore not affecting the subsequent incident electrons. It must be noted that it is known that the e-beam current affects the dose to clear, both due to the restrictions on the pitch imposed by the pattern-generator–speed, but also due to transient effects; however, the currents for these experiments are kept constant ($I = 2.005\,\mathrm{nA}$) well below the limits where this should affect the exposure.

3.3 The point-spread function

The measurements of the PSF reported in this section has been carried out in collaboration with Christian A. Rosiek. The base charge dose to clear, D_0, further serves as the normalization constant of the PSF and by exposing a single isolated shot with a given charge dose, q, and measuring the radius of the resulting developed circle, $r_{\mathrm{clear}}(q)$, the PSF can be measured experimentally [28, 48, 49, 54, 68],

$$\Psi(r_{\mathrm{clear}}) = \frac{D_0}{q}. \tag{3.5}$$

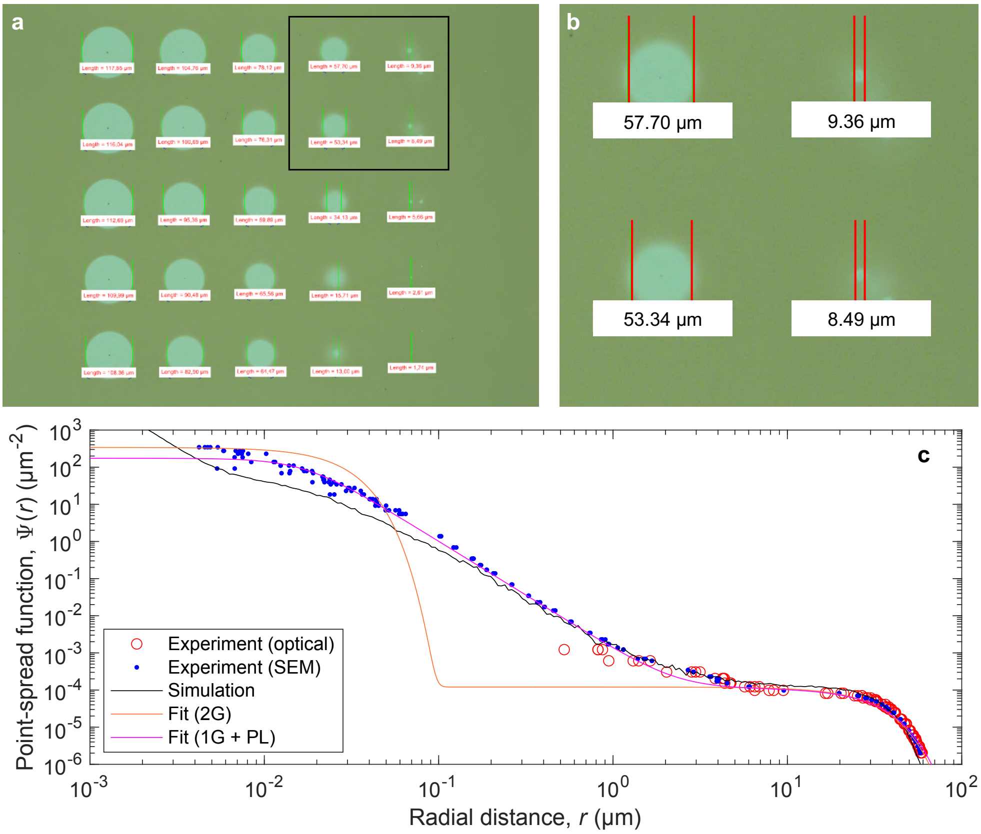

Figure 3.5. Measurement of the point-spread function. **a**, Optical microscope image to measure the size of developed holes with a zoom-in of the inset in **b**. **c**, Measurements by optical microscopy and scanning electron microscopy, numerical Monte-Carlo simulations, and fits using both the conventional double-Gaussian model as well as a power-law model as discussed in the text. The measurements are carried out in collaboration with Christian A. Rosiek.

Figure 3.5**a** shows a bright-field optical microscope image of an array with 25 circles resulting from single-shot exposures with doses, q =0.5625–337.5 nC, exposed with $I = 12.2\,\text{nA}$, i.e., the dwell times ranges from sub-second to minutes. It is important that the circle are well-spaced to avoid cross-talk, such that the size can be measured directly as shown in Fig. 3.5**b**. In addition to these large doses a range of lower doses from 0.25 fC–4 nC are exposed with $I = 211\,\text{pA}$ and inspected with a scanning electron microscope (SEM) and the measurements are shown in Fig. 3.5**c**. The small overlap in the ranges are to confirm that the PSF-measurement is not affected by the currents used. Figure 3.5**c** additionally shows the results of a numerical Monte-Carlo (MC) simulation [46] of the electron scattering in the stack, which agrees reasonably with the measurements. Notably, the MC simulation assumes a point-source of electrons and should be convoluted with, e.g., the beam-spot size, which would make it more closely resemble the measurements at very short distances. Moreover, the measurements includes the development process and therefore deviates slightly for the short ranges, which further are at the limit of the resolution obtainable with standard top-view SEM [49]. In practice measuring the PSF for the full process would be desirable to accurately take it into account for PEC [73, 74]. The radius of the circle represents the point where $D_{\text{eff}} = D_0$, however, the effective dose will be much larger inside the circle. A small solid spot can be seen inside the larger circles, which results from the resist cross-linking again at $D_{\text{eff}} > 490D_0$ [28].

Historically, the PSF has been described by a double-Gaussian (2G) model [47],

$$\Psi(r) = \frac{1}{\pi(1+\eta)} \left(\frac{1}{\alpha^2} \mathrm{e}^{-(r/\alpha)^2} + \frac{\eta}{\beta^2} \mathrm{e}^{-(r/\beta)^2} \right), \tag{3.6}$$

with a shot-range term to describe the size of the focused beam, α, and a long-range term to describe the scattering in the material stack over a length captured by β and a relative weight, η. The use of higher voltages combined with improvements to the EBL-systems has resulted in α being reduced to a few nanometers while β has increased to tens of micrometers. To solve the PEC-problem only the long-range effect is normally taken into account [57, 70] by considering the PSF as [18],

$$\Psi(r) = \frac{1}{\pi(1+\eta)} \left(\pi + \frac{\eta}{\beta^2} \mathrm{e}^{-(r/\beta)^2} \right), \tag{3.7}$$

and the resulting dose becomes dependent on the pattern density, ρ, on a length-scale of β, while the dose-scaling depends on η [43, 69, 70], $\rho(1+\eta)^{-1}$. The PSF spans many orders of magnitudes: In the case reported here the radius spans 4 orders of magnitudes while the PSF spans 8. Moreover, the PSF has azimuthal symmetry so it has a square-dependence on the radius which should also be taken into account when performing the fit in order to avoid that the fit is dominated by local effect [44, 48]. Occasionally, α is simply put to the specification-sheet number of the hardware as it in any case is not used in practice. It is commonly known that this model does not fit the data well and a number of solutions to describe a larger part of the PSF has been proposed such as adding additional Gaussian [75] or exponential [48] terms—even to the extend of naming the processes associated with each additional term—e.g., ”fogging” electrons and ”blur” [69, 76].

While Gaussian terms are efficient to compute and remains valid for practical PEC [58], they do not offer substantial new intuition or understanding. It still appears that the long-range Gaussian captures an effect reasonably, however, with increasing voltages [50, 60] there appears to be an intermediate-region scaling as a power-law, motivating a new model [28, 68],

$$\Psi(r) = \frac{1}{\pi(1+\eta)}\left(\frac{\nu^{-2}}{1+(r/\gamma)^{\sigma}} + \frac{\eta}{\beta^2}\mathrm{e}^{-(r/\beta)^2}\right). \tag{3.8}$$

Where σ controls the slope of the power-law, γ replaces α to describe the beam-size and ν is a normalization constant, which should not be included directly in a fit as it depends on σ and γ. Both models are fitted to the experimental data resulting in the double-Gaussian parameters ($\alpha = 25\,\mathrm{nm}, \beta = 29.7\,\mu\mathrm{m}, \eta = 0.5$), and the power-law results in ($\gamma = 17\,\mathrm{nm}, \sigma = 2.9, \nu = 35\,\mathrm{nm}, \beta = 30.9\,\mu\mathrm{m}, \eta = 0.5$). Notably, considerable care should be taken when performing a power-law fit [77] and further studies might find a more physics-based model. In this context it is worth highlighting that the PSF falls off faster than a Gaussian at long-range, but the Gaussian captures the accumulated energy reasonably and therefore remains suitable for PEC. Possibly, a trigonometric function could be derived following the scattering cross-section described by the Lewis-equation used for MC simulations [44]. The scattering depends on the atomic number, and here only light atoms are considered, i.e., silicon, oxygen, carbon and hydrogen (including the polymeric mask), however, the large deviation between the 2G-model and measurements where first observed for GaAs [48]. Possibly, a Gaussian-like term should be included for each (substantially different and largely present) atomic weight in the stack, e.g., two Gaussian functions might be appropriate to describe InP. If the material is provided as a thin film ($\ll 1\,\mu\mathrm{m}$) on a substantially-silicon–substrate, however, likely the PSF will not deviate substantially from the PSF reported here.

For practical purposes of PEC, estimating η accurately is in fact the most important, which can be done already from the fast microscope test and measurements shown in Fig. 3.5**a**–**b**, and combined with the dose to clear this provides a pattern-independent framework to assign an appropriate exposure dose. Attempts to include short-range effects have great promise for improving the quality of high-resolution EBL [74], however, care must be taken not to simply use the Gaussian model based on simulated α [41] but instead accurately represent the PSF, either by a smoothed version of the experimental data, such as a many-Gaussian model [78] or using a model similar to Eq. (3.8).

3.4 High-resolution lithography

This section illustrates the principles derived in the previous sections by considering a slotted phononic-crystal waveguide (sPnC) shown in Fig. 3.6**a** similar to the structure

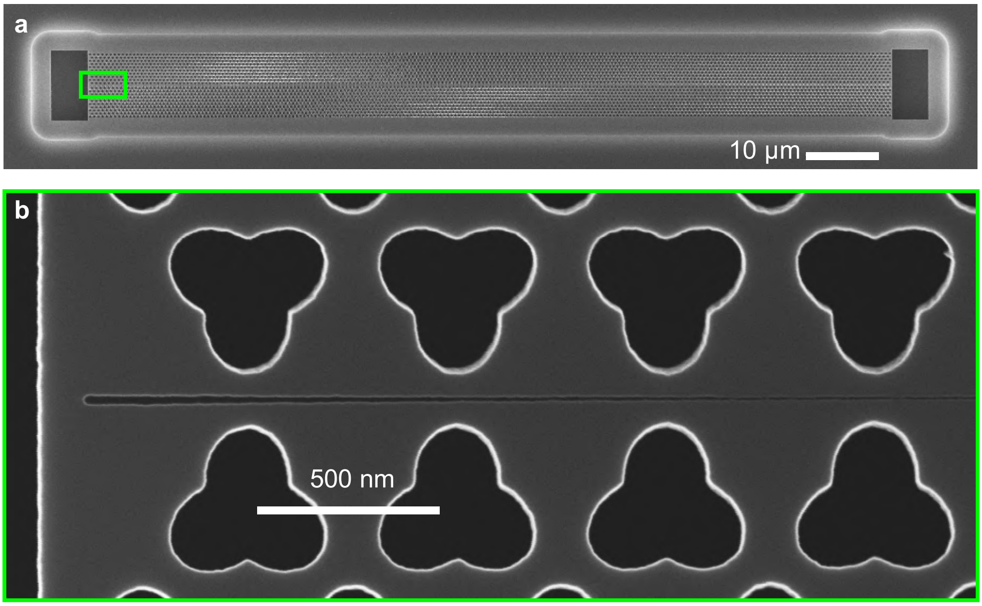

Figure 3.6. Slotted phonon-waveguide without proximity-effect correction. a, A phonon waveguide with an optomechanical interface similar to Ref. [20] with a large air-opening in the end. **b**, Zoom-in at the end of the waveguide where the width of the slot in the center varies and is larger close to the large open feature in the ends and shrinks as it gets farther away due to the change in D_{eff} from the uncompensated background-dose.

in Ref. [20]. The physics of these optomechanical systems will be discussed further in Ch. 7. From a fabrication–point-of-view the system is a long (compared to β) periodic structure with large exposed areas at each end. The structure is composed of large blobs—clover-shaped so-called shamrocks [18]—placed symmetrically around a narrow slot and with an area density $\sim 60\,\%$. The large exposed rectangles at the edges of the system are interesting because they deposit a large background-dose around them, which falls off scaling as the PSF, i.e., over the first many micrometers. Figure 3.6**b** shows a zoom-in around the edge where the slot width veries visibly, changing in size since the background dose-gradient is not compensated by adjusting the dose of the features close to and far from the edges. This error also manifests in the size of the shamrocks, however, this is much less clear from the images at is is only a comparatively small modification in the outline.

Although it illustrates the general need to take proximity effects into account, the first $\sim 4\,\mu\mathrm{m}$ from the edges of the system are in fact less important, as they simply cause a mirror (phonon shield) to establish a cavity [20]. Instead, it is important that the features are similar to each other in the center as the uniformity ensures that it is a proper periodic system that can guide modes – if the system is perturbed slowly a cavity can be engineered as discussed in Sec. 7.3, however, that is not the

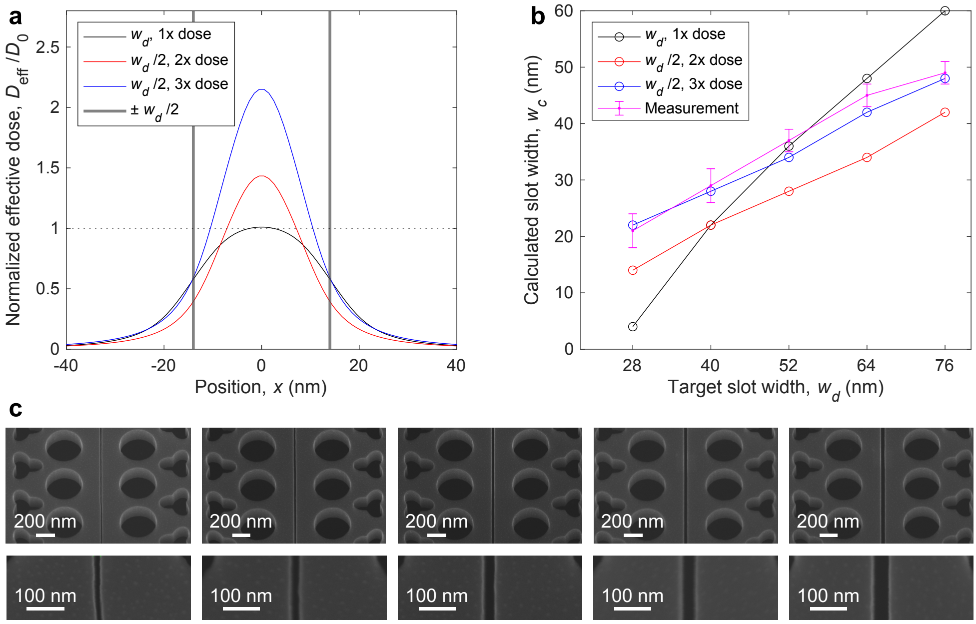

Figure 3.7. Slotted phonon-waveguide with shape and dose corrections. The width of the central slot in a long phonon-waveguide can be accurately calculated, w_c, by reducing the width of the slot in the exposure mask, w_m, from the target slot-width in the design, w_d, and instead increasing its dose. **a**, Convolution between different mask-widths and -doses improving the exposure latitude. **b**, Calculated (and measured) slot width resulting from the predictions in **a**. **c**, Scanning electron micrographs and insets of 5 different slot-sizes resulting from exposing half the slot-width with a 3 times higher dose.

aim of this particular structure. It can be seen in Fig. 3.6**b** that the slot becomes vanishingly small towards the center of the waveguide, since the uniform dose density is estimated using the long-range effect only, which is $\sim$ 6 orders of magnitudes different from the PSF at a few tens of nanometers (Fig. 3.5**c**). However, since the system is periodic along its length the mask of the slot can be adjusted such that the result better resembles the intended design. Figure 3.7**a** shows a convolution between the measured PSF (the fit to Eq. (3.8)). By exposing the nominal width with the same dose as the shamrocks it can be seen that it barely clears the resist in the very center, consistent with the fabricated slot-width vanishing in Fig. 3.6**b**. One method to resolve this is to provide a constant background "flood" exposure to shift the dose to clear until the target and realized dimensions matches. This PEC-method was commercialized as GHOST [54, 58] and can resolve the issues when the mask only contains features with similar size and density, such as the exposure UV-masks for transistors. However, it does not work when size or density varies such as here, since shifting the dose to clear also would cause the shamrocks to change dimensions. In addition it suffers from a small exposure latitude, i.e., the contrast between exposed and unexposed regions [33, 69, 72, 79, 80] is low due to the small slope of D_{eff} across the boundary. This in turn translates to partial development of the mask, which will erode more quickly and can cause increased roughness along the feature-outlines; so-called line-edge roughness (LER).

Instead, the exposure mask is modified using the principle of over-dose–under-size (ODUS), where shape and dose have been adjusted jointly to achieve PEC and normalized to the base dose to clear, i.e., D_{eff}/D_0. This results in a substantially higher exposure contrast and tunable dimensions. Figure 3.7**b** shows the corresponding predicted widths of the fabricated features for the different ODUS-combinations, and Fig. 3.7**c** shows titled SEM images of the slots in the center of fabricated structures where the mask of the slot is reduced to half of its target width and exposed three times (i.e., the dwell time τ is increased 3-fold and in principle can be continuously adjusted). The measured dimensions fits well with the theoretically predicted dimensions using a convolution with the PSF as shown by the blue and magenta lines in Fig. 3.7**b**. Rather than reducing the dimensions by half, a better approach is to shrink the feature-sizes by $\sim\gamma$ from Eq. (3.8), i.e., the point at which the slope of the PSF rapidly increases such that the interface of the developed feature has the highest-possible exposure contrast. The dose should then be increased until the feature-sizes match the design, which is a non-trivial inverse problem [51, 70, 73, 74].

CHAPTER 4

Nanoscale silicon dry-etching

This chapter introduces and discusses the principles of dry-etching, i.e. cold-plasma etching, first in general (Sec. 4.1) and then applies the principles to motivate the recent clear-oxidize-remove-etch (CORE) process (Sec. 4.2) developed in a series of four papers by Nguyen *et al.*, starting with Ref. [11] and expanded in following works to cover black-silicon on-demand [81], using hardmasks defined by lift-off [82] as well as hardmasks defined in-situ within the same reactor [83]. This last process is fine-tuned for nanostructures and this is covered in Sec. 4.3. These CORE-processes have a number of interesting and remarkable features enabling state-of-the-art silicon nanofabrication and the softmask-process [11] has been tailored for specific applications to explore novel physics and applications including extreme resolution at the cost of sidewall roughness [16] and high-resolution with low roughness [18]. The hardmask-processes have been further developed and tuned to maintain the ability to etch small features with high-aspect ratio (HAR) and simultaneously achieve low roughness (Sec. 4.3), demonstrated in Refs. [19–21, 84]. Finally, Sec. 4.4 documents recent work to improve the stability of the process as well as discusses some of the remaining challenges. This chapter focuses on the technology of dry-etching and is motivated by the needs of subsequent applications in Parts II and III.

Silicon dry-etching has been quintessential to the technological advances over the last half-a-century. During the span of this thesis, the author has become passionate about plasma etching—and wishes for the reader to be excited as well—and consequently, wants to motivate this chapter with a quote from the introductory lines of the now 10-year old review in Ref. [5]. While this may seem exaggerated at first, it is crucial to recall that without plasma etching pattern-transfer is limited to isotropic processes (some chemicals can etch preferentially along specific crystal-planes in particular materials [36] but this is not generally the case). Therefore, in order to have many components in a single (small) chip, HAR-anisotropic profiles are a necessity. Lastly, the author would like to highlight and acknowledge Prof. Henri Jansen as well as Vy T. H. Nguyen, Roy Cork and Jonas Michael-Lindhard for insightful discussions about the etching processes.

> *Plasmas have been used to etch fine features in silicon integrated circuits for nearly 40 years. Without this technology, we would be stuck in the 1970s listening through tinny headphones to disco music on our ”small” portable cassette tape player. Carrying laptops around would be more for fitness than for convenience and mobile “smart” phones would require wheels. Today, instead we take these marvelous devices for granted.*
>
> Donnelly and Kornblit (2013). Reprinted with permission. Copyright 2013, American Vacuum Society (Ref. [5]), license no. 5500700902869.

4.1 Principles of reactive-ion etching

Figure 4.1**a** shows a schematic of a Reinberg-reactor [85] in which a chamber is filled with gas to a certain pressure, p, and a radio-frequency (RF) auxiliary power, P, is supplied between two electrodes, the power is delivered to the bottom-electrode, called the platen or the chuck and on which a sample is mounted, and the top-electrode is grounded along with the rest of the chamber side-walls. The power ignites a cold plasma, primarily driven by inelastic scattering (i.e., no heating), through a dissociation process [86],

$$\mathrm{AB} + \mathrm{e}^- \rightarrow \mathrm{A} + \mathrm{B}^* + \mathrm{e}^-, \tag{4.1}$$

where an electron hits the molecule – for example SF_6, which breaks into reactive species F^*, and further becomes charged ions through an ionization process,

$$\mathrm{A} + \mathrm{e}^- \rightarrow \mathrm{A}^+ + 2\mathrm{e}^-. \tag{4.2}$$

The electrons are drained to the ground leaving the plasma positively charged to the plasma potential, V_p, indicated in Fig. 4.1**b**. The sample is mounted on a chuck, which is connected to the RF-source via a blocking capacitor with capacitance, C, forming a capacitively-coupled plasma (CCP) [86] along with the grounded chamber side walls and, in particular, the top electrode. The RF power-supply line is matched such that the supplied power is dissipated in the plasma, the so-called forward power, F, rather than reflected back into the power-supply, R. In this thesis, when discussing

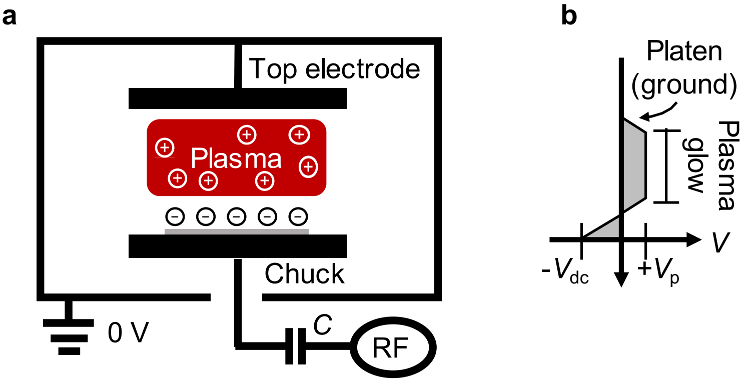

Figure 4.1. Schematic of a capacitive-coupled reactive-ion etching (RIE) system. **a**, A radio-frequency (RF) power is supplied to a bottom-electrode, called the platen or the chuck, and the top-electrode is grounded along with the rest of the chamber walls. This power strikes a plasma. Electrons are drained to ground from the plasma, leaving it at a positive potential, V_p, but build up on the sample surface since its access to ground is blocked with a capacitor, leading to the negative direct-current (DC) bias, V_{dc}. **b**, Schematic of the bias-profile along the height of the reactor.

plasma-power it is implied that it is the forward power, and that the circuit is well matched such that the reflected power is only a negligible fraction of the supply.

As the charges moves a restoring force pull them back resulting in an oscillation at frequency [86],

$$\omega = \sqrt{\frac{n_i q^2}{m\varepsilon_0}} = \frac{v_e}{\lambda_D}, \tag{4.3}$$

where n_i is the number of ions in the plasma, q and m are the charge and mass of the particle and $\varepsilon_0 = 8.854\,\mathrm{pF/m}$ is the vacuum permittivity. For $\mathrm{SF_6}$ and $n_i = 10^{10}\mathrm{cm}^{-3}$, $\omega_{\mathrm{electron}} \sim 1\,\mathrm{GHz}$ and $\omega_{ion} \sim 2\,\mathrm{MHz}$. Typically, the plasma is driven in the Federal Communications Commission (FCC)–allotted band, $\omega = (13.56 \pm 0.01)\mathrm{MHz}$, which keeps the heavier ions relatively motionless but allows the electrons to move, thereby driving the plasma. The characteristic breakdown-voltage of a plasma, $V_{\mathrm{bd}} \sim 1\,\mathrm{kV}$, and the typical power considered in this thesis is $F \sim 10\,\mathrm{W}$ corresponding to a current of $\sim 6 \cdot 10^{16}$ electrons per second. At a pressure $n_i = 10^9$–$10^{11}\mathrm{cm}^{-3}$ This obtains a weakly ionized glow-discharge plasma [86]. The degree of plasma ionization is defined as, $\alpha = n_i/N = n_i/(n_i + n_n)$, and for CCP typical values are $\alpha \sim 10^{-6}$–10^{-4}. It is possible to increase $n_i \sim 10^{12}\mathrm{cm}^{-3}$—and therefore α—using inductively-coupled plasma (ICP) or transformer-coupled plasma (TCP), which can increase the etch rate and is valuable particularly for high-throughput etching-tools used in industry, however, this thesis rather focus on accuracy at the nanoscale with low-power processes using CCP. The processes discussed later in this chapter have been demonstrated also to work with the ICP-source at higher rates in Refs. [11, 83]. Since fluorine has a high electron affinity, attachment is likely, i.e., $\mathrm{A} + \mathrm{e}^- \to \mathrm{A}^-$, and the charged reactive ions can interact with the silicon forming the volatile $\mathrm{SiF_4}$ thereby etching the silicon [87].

The Debye sheet—sometimes called the ion sheet—balances the total charge of the plasma and spans a characteristic length, the Debye length [86],

$$\lambda_D = \left(\frac{\varepsilon_0 k_B T_{\mathrm{e}}}{nq^2}\right)^{1/2}, \tag{4.4}$$

which for $n_i \sim 10^9$–$10^{12}\mathrm{cm}^{-3}$ at room temperature corresponds to $\lambda_D =$0.01–0.1 mm. This is notably much smaller than the dimensions of the chamber of a typical reactor. The region between the wafer and the plasma is called the dark space, since it is drained of electrons (or rather the electrons are slowed down) leading to less collisions that result in the emission of light [86]. The electrons go to ground, however, the blocking capacitor shown in Fig. 4.1**a** ensures an RC time-constant much slower than the frequency of the RF-source. Therefore, electrons build up on the sample surface in a steady-state leaving it on a negative potential called the DC-bias, V_{dc}, as shown in Fig. 4.1**b**, which is a measureable quantity that controls the energy of the ions. In fact, a key reason for using ICP and TCP is that it enables increasing the ion density, n_i, and therefore the etch rate, without affecting the DC-bias, and therefore the etching physics [5, 11, 86]. As electrons build up on the sample surface the electrons are repelled further, thus increasing the dark-space above the wafer compared to between the plasma and the grounded platen and sidewalls.

The ions obtain a kinetic energy from moving through the, $V_E = V_p - V_{dc}$, potential [86],

$$E_{\mathrm{rms}} = \frac{1}{2} m_e v_{\mathrm{rms}}^2 = \frac{1}{2} k_B T_e, \tag{4.5}$$

with $k_B = 1.38 \cdot 10^{-23}\,\mathrm{J/K}$ the Boltzmann constant. The resulting ion-sheath thickness is

$$d = \frac{2}{3} \left(\frac{\varepsilon_0}{j_i} \right)^{1/2} \left(\frac{2\mathrm{e}}{m_i} \right)^{1/4} (V_p - V_{dc})^(3/4), \tag{4.6}$$

where j_i is the ion current density and m_i is the ion mass. The cross-section describes the probability of collisions [10, 86], $\sigma_e = 100 a_0^2 = 2.800 \times 10^{-18}\,\mathrm{m}^2$, and the mean free path is given as

$$\lambda_e = \frac{\nu_{\mathrm{avg}}}{F_{\mathrm{eg}}} = \frac{k_B T}{\sigma p}. \tag{4.7}$$

At room temperature ($T = 20\,°\mathrm{C}$) this becomes $\lambda_e = 10.8\,\mathrm{cm}/p(\mathrm{mTorr})$, which is large compared to the dark space at low-power plasmas, i.e., when the pressure is below 1 mTorr collisions are unlikely. This will make the etch highly directional, i.e. anisotropic, and reduce the ion-angle distribution (IAD), thus avoiding degradation of the etched sidewalls. The IAD is further reduced by increasing the plasma bias, however, this also erodes the mask faster [11]. On the other hand, when the pressure is increased well above 1 mTorr, collisions become likely and the etch becomes more isotropic. The lateral distance etched compared to the vertical etch-depth gained is therefore controlled by a combination between pressure and DC-bias (and to some extend the plasma potential).

Figure 4.2 shows a schematic of the reactor used in this thesis, where the platen has a diameter, $d = 150\,\mathrm{mm}$, corresponding to an area, $A = 700\,\mathrm{cm}^2$ (the chuck on which a sample can be placed is lager, $\sim 200\,\mathrm{mm}$). The schematic is simplified and more details on the reactor design are available in Ref. [88]. The distance between the two electrodes is 13.5 cm and so the volume, $V \sim 10^4\mathrm{cm}^3$. The ICP-coil is driven at RF and have only few windings, however, the inner and outer electromagnetic (EM) coils are operated in DC at 800 W with water cooling and confines the plasma ions for the ICP to increase the degree of ionization by reducing the the electrons lost to the sidewalls. The EM-coils are found to have little effect when the tool is run only with CCP, where permanent magnets employed around the main reactor suffice to contain the plasma. These magnets are related to the field of magnetically-enhanced reactive-ion etching (MERIE) where the etch rate is enhanced while the bias is reduced for CCP-plasma [5]. Another important consideration is the condition of the chamber, as deposition of, e.g., polymer-films on the aluminium chamber-sidewalls will affect the ability to evacuate electrons to ground through the sidewalls and therefore affect the plasma chemistry. For this reason it is possible to control the temperature of the various sections of the reactor, including 4 sets of heaters across the sidewalls, as the temperature affects how readily different polymers will deposit.

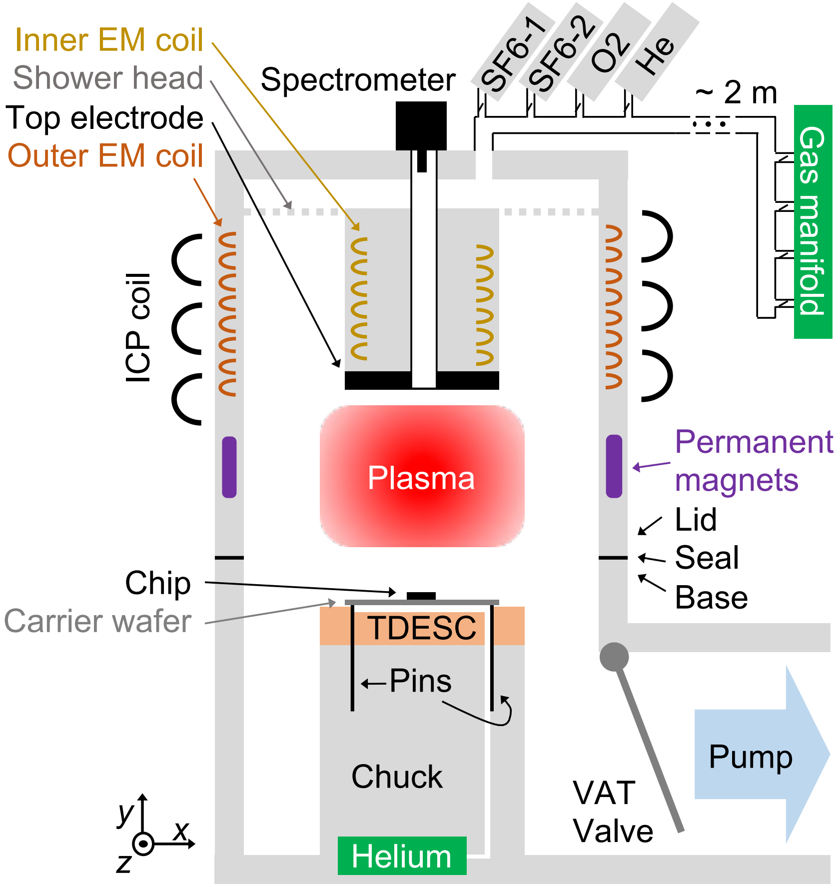

Figure 4.2. Schematic of the central features of the dry-etching tool used. The chuck includes further complexity to allow, e.g., cooling and heating of the sample as well as a lift to change the height of the chuck; the height combined with the platen size must be large enough to avoid effects of fringing fields. The sidewall also includes heaters around the permanent magnets, however, in this thesis processes are run at room temperature without the need for heating and cooling.

Many processes rely on fluorocarbon gases [5], e.g. C_4F_8, which will form polymers on the sidewalls and further require regular cleaning processes with, e.g., oxygen-plasmas to etch away these polymers, and to ensure a reproducible process the chamber should be preconditioned to ensure it has the same start at every process. The 4 gas-ports shown explicitly are controlled by so-called fast mass-flow controllers (MFCs), which provides a needle-valve to adjust the gas flow into the reactor $\sim 10\,\mathrm{Hz}$. Other gases are adjusted from the gas-manifold and it will typically take $\sim 1\,\mathrm{s}$ for the system to respond to changes there. The chuck-schematic is simplified, it includes a lift to adjust the distance between the electrodes (maximum 13.5 cm is used throughout this thesis), or rather the distance from the platen to the ICP coil, as well as 5 metal pins that can lift the substrate using during loading of the sample from the load-lock [88]. The thick dielectric electrostatic chuck (TDESC) is the brand-name of a ceramic block between the chuck and the wafer with an O-ring matching a 6” (i.e., 150 mm diameter) wafer, and 6 kV can be applied across it to electrostatically clamp the substrate. Helium can then be flushed to the backside of the wafer to provide sufficient thermal conduction to heat or cool it as desired. Finally, the pump is a 2500 L/s turbo-pump mounted on the side of and below the chuck, and one could expect some level of asymmetry in the gas flow and etch uniformity, however, this is not observed—and certainly not within the central $\sim 5\,\mathrm{cm}$ radius of the carrier wafer, on which the chip-of-interest is placed. The pump is separated from the reactor-chamber by a VAT throttle-valve, which is a 200 mm-diameter aluminium disc mounted on a pendulum-arm and capable of moving to expose 0–100 % of the throttle within $\sim 0.5\,\mathrm{s}$ with 0.1 % accuracy. By varying this position it is possible to control the pumping speed and thereby the pressure in the chamber.

4.2 The clear-oxidize-remove-etch (CORE)-process

Silicon can be etched with a number of chemicals, fluorine forms the volatile SiF_4 enabling a chemical etch with low bias (i.e., low sputtering), while bromine and chlorine do not etch silicon spontaneously but instead as ion-induced etching, which needs simultaneous ion bombardment to gain etched depth [5, 86]. The strong ion bombardment further achieves high anisotropy, which is desirable, and such etching is typical for most materials, including many III-V materials. Conventionally, the etch can be made directional by mixing gases that provide different radicals, that either form volatile products, e.g., fluorine forming SiF_4 thereby etching silicon – or which form a passivation-layer that shields the substrate from etching, e.g., oxygen forming SiOx which is not fluorinated. This passivation layer is instead removed by high-energy impacts, i.e. sputtering, resulting from a large DC bias. Since the high DC-bias also reduces the IAD the passivation is primarily removed at the bottom of the trenches thereby making the direction anisotropic [5, 86, 89].

In 1993 Laermer and Schilp of Bosch GmbH filed a patent on anisotropic etching of silicon using a switched process [90], now commonly known as the Bosch process [5, 88]. By separating the passivation (deposition) process from the etching process

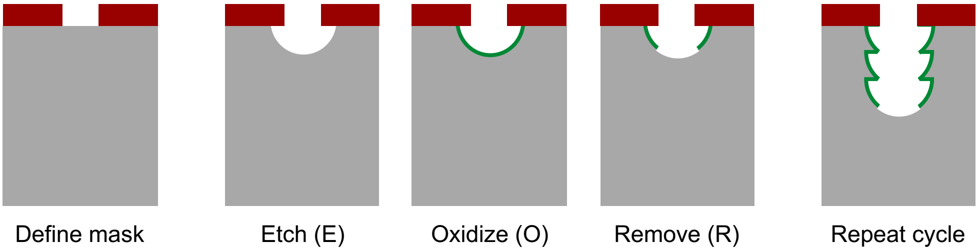

Figure 4.3. Cyclic clear-oxidize-remove-etch (CORE) process. Three steps are carried out in order to transfer a mask into silicon, and the steps are separated by the clear (C) step to prime the reactor for the next cycle. The etch step (E) chemically etches silicon, the oxidation step (O) is a self-limited passivation forming SiOx on all exposed silicon surfaces and the bottom remove step (R) sputters the formed SiOx only through the mask, exposing silicon for the E-step to etch. The reactor clearing (C), passivation (O), bottom removal (R) and etch (E) steps form a cycle, which is repeated multiple times to etch anisotropically.

it is possible to achieve high-aspect ratio structures with much less degradation of the resist, since the high bias is only needed during the etch step – and importantly, the process becomes much more stable and flexible to adjust. Figure 4.3 shows a schematic of the switched process, known also as deep reactive-ion etching (DRIE). Such a switched process rather than a continuous process [91] exhibits characteristic scallops [5], which is periodic roughness on the sidewall of etched features. The size of this roughness may be controlled by the duration of the etching step, i.e., how many cycles are used to etch a given depth, as well as the anisotropy of the etching step [16, 18]. More recently the etch step has been further split into two parts, a high-pressure, low-bias chemical etching step and a low-pressure, high-bias bottom removal step, called deposit-remove-etch many times (DREM) [92]. This enables only eroding the resist during the removal step, which is low-pressure and therefore erodes slowly compared to the high-pressure, high-power combined etch step. The DREM process relies on fluorocarbon deposition with the C_4F_8 gas, which grows a passivation layer much faster than the oxidation process, in part because oxidation is a self-limited process [11]. However, since it is not self-limited, clogging [11] can occur in which the opening of a deep trench closes since more polymer is deposited there than in the bottom; this led to the addition of an ash-step forming the DREAM-process [92]. Ashing is oxygen plasma, which etch-back the polymer, and if the amount of deposited polymer matches the amount of lost resist/polymer from a cycle this process can achieve, in principle, infinite selectivity, i.e., the ratio between the etched depth and the original mask-thickness [92]. Moreover, such switched processes enable three-dimensional (3D) etching [11, 93] needed for the next generation more-than-Moore transistors [7, 94].

The 4-step DREAM process is a substantial improvement from the conventional 2-step Bosch process and continues to offer high etch rates. However, the deposition

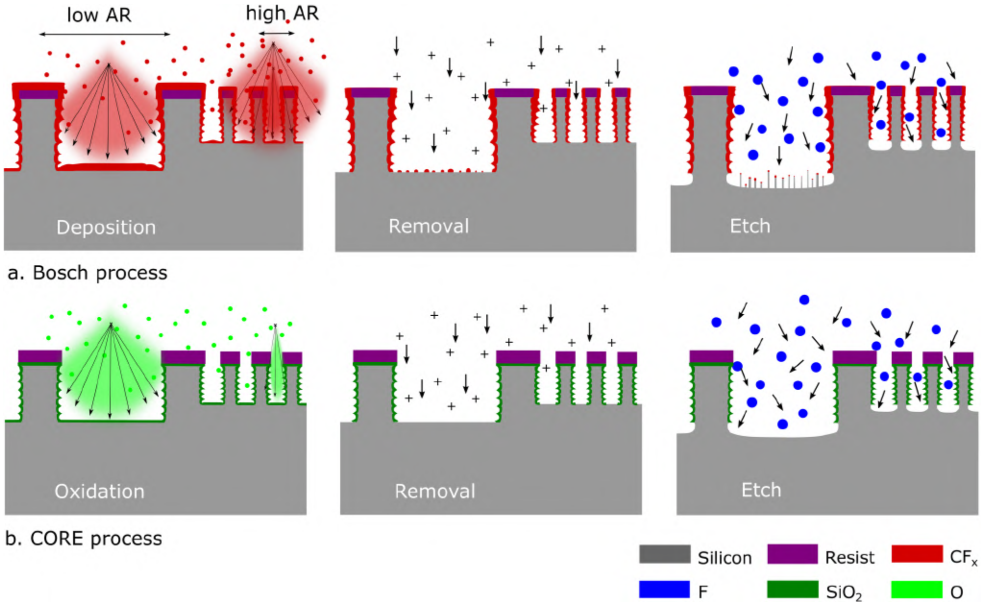

Figure 4.4. Comparison between Bosch and CORE processes. a, Deposit-remove-etch many times (DREM) method, which is a development on the conventional Bosch method. The polymer is deposited unevenly and consequently it is difficult to tune the removal step appropriately for different aspect ratio-features; this further translates into roughness in the bottom, known as grass or black silicon due to its anti-reflective nature. **b**, Oxidation of silicon is self-limited and therefore the same thickness of passivation can be achieved independent of aspect ratio. The removal step is largely free of loading due to the long mean-free path so even high-aspect ratio trenches can be cleared efficiently. Figure reprinted with permission. Copyright 2020, American Vacuum Society (Ref. [81], license no. 5487870544584).

of polymers continues not to be uniform as shown in Fig. 4.4**a**, in particular the deposition depends sensitively on the aspect ratio (AR). Normally, high AR (HAR) and low AR (LAR) features can be fabricated independently with multiple aligned steps, however, this introduces the risk of errors due to missalignment and defects and so it is preferable to have an etching process, which is independent of the AR. In photonics and phononics, the aspect ratio of neighbouring features readily varies from $\ll 1$ to > 10, such as the slotted phononic crystal shown in Figs. 3.7 and 3.6, the physics of which will be discussed further in Ch. 7. To avoid dependence of aspect ratio it is desirable to increase the mean free path, such that ions that sputter the passivation in the bottom can move all the way down a HAR trench without hitting the sidewall, thus removing the protection there without eroding the passivation in the top of the trench. This is a central reason to split the etch-step of the Bosch process into a low-density sputtering step and a high pressure etching step in the

DREM process [92]. This leads to the introduction of the CORE process, which was introduced in 2020 by Nguyen *et al.* [11] and illustrated in Fig. 4.4**b**. Here the R- and E-steps are maintained but the deposit is exchanged for a self-limited oxidation process. Notably, the oxidation is done with oxygen plasma, which is similar to the ash-step of the DREAM-process [92]. This continuously cleans the reactor, such that time-consuming preconditioning is not needed and further alleviates the need for heating of the chamber side-walls, while the process remains reproducible and even stable over long time – e.g., Ref. [82] demonstrated a stable etch lasting 16 h. The CORE process runs at room temperature, since a higher temperature results in faster oxidation; this is simpler and therefore cheaper to implement compared to cryogenic processes often employed with fluorocarbon processes [88].

As discussed in Ch. 3, reducing the softmask thickness results in higher spatial resolution. However, this stresses the process to achieve a higher selectivity, and in Refs. [16] and [18] the CORE process is adjusted to work with thin electron-beam lithographic softmasks to etch only their thin, crystalline (100) 240 nm and 220 nm silicon device layers, respectively. Moreover, the etching process naturally stops when it reaches the buried oxide, as fluorine does not etch SiO_2 – similarly to the oxidized, and therefore passivated, sidewalls. Still, the bottom-removal step may slowly progress a few nanometers into the BOX for large, open features if the process is continued for long after reaching the bottom. The oxidation process is fast (few seconds) and to avoid carry-over effects from the etch step of the preceding cycle the VAT valve is fully opened, the SF_6 input valves closed and the O_2 values opened to supply 100 sccm, such that the reactor is cleared (C-step), which results in a pressure, $p = 1\,\mathrm{mTorr}$ [11]. The unit sccm is standard cubic centimeters per minute, which is the common way to specify gas flows. The gas flow is kept at 100 sccm during the O-step, the plasma is ignited and the VAT valve is swung to be only 1 % open, such that the pressure builds up and the bias is kept low.

Figure 4.5**a** shows an SEM cross-section image of different AR trenches etching into silicon using a variation of the hardmask process in Sec. 4.4. The process is run for 75 cycles with a 5 s O-step and the E-time is ramped from 65–89 s to keep the scallops similar-sized as the aspect ratio increases to compensate the effect of microloading [88, 91]. Figure 4.5**b** shows a plot of the measured width and depth, illustrating the commonly known RIE-lag—and the fit confirms its canonical logarithmic scaling [5, 86, 91, 95]—in which the etch rate depends sensitively on on the aspect ratio. More narrow trenches become HAR faster and the etch rate consequently slows down. Microloading does not occur when limited by bombardment but rather when limited by the available number of reactive species [87, 91], and since the passivation is self-limited, mainly the R- and E-steps are of concern and to reduce the microloading, the bias should be increased, the pressure should be reduced or the gas flow can be increased. Changing the pressure will also affect the bias, and so it is not a desirable method to reduce loading in the E-step where instead the supply-gas flow should be increased. On the other hand, reducing the pressure is the best way to improve the R-step, however, this is limited by the available mass-flow controllers and pumping capabilities of the system; instead the platen power must be increased. Strictly, more

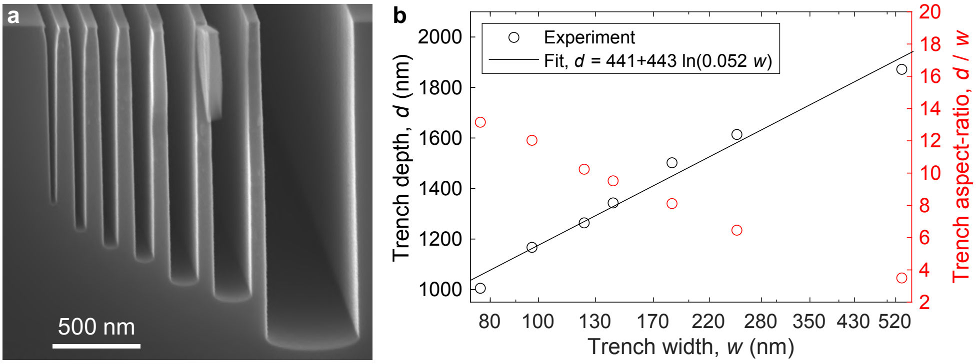

Figure 4.5. Lagging in reactive-ion etching (RIE) due to aspect-ratio dependent etch rate. a, Scanning electron micrograph of 7 trenches etched 1–2 µm depending on their width. A deviation from a vertical sidewall can be observed as well. **b**, Semi-logarithmic graph of measured trench depth against trench width including a fit. The red points show the corresponding aspect ratio, illustrating the RIE-lag are mostly pronounced for high aspect ratios.

reactive species could also be created in the E-step by, e.g., using the ICP source. The sidewall angle can be observed to change for the most narrow trenches in Fig. 4.5**a**, where the profile becomes so-called positively tapered and narrows with etched depth gained. More precisely, due to the high bias to keep the loading-levels low, and since the process is optimized for many fewer cycles to etch only 220 nm, the selectivity drops and faceting [5, 87] can be observed, where the trenches are widened around the openings (undercut). This should be countered by more passivation, strictly only for the later parts of the etch, that is the passivation should be ramped. To still fully clear the bottom of the trenches, the time of the remove step should be increased. Changing the time does not affect other parameters and must simply balance the amount of passivation until no black silicon forms [89].

Ref. [89] gives an introduction on how to adjust etching parameters for a given process, with an SF_6/O_2 chemistry in a continuous flow operation, and refs. [11, 81–83, 87] contain substantial input and discussions on how to adjust the parameters of the CORE process to resolve different issues on the profile. Importantly, since the passivation is self-limited and the physical effects of the different steps are separated, many effects can be adjusted without simultaneously affecting other parts of the etching, which greatly can save time during process development and optimization.

In Ref. [16] the O-step is increased to 4 s (from 3 s in Ref. [11]) and the pressure is measured to ramp from 1–32.4 mTorr during this time. The pressure during the R-step (which lasts 20 s) is stably at (0.33 ± 3)mTorr and during the 72 s E-step, the pressure again ramps up and stabilizes at (14.16 ± 0.02)mTorr over the first ~ 20 s. Importantly, the pressure of the R-step corresponds to a mean free path, $\lambda_e = 32.4$ cm, which is much greater than the width of the dark space, and the pressure, $p \gg 1$ mTorr, for both the O- and E-steps, hence, resulting in less sputtering. However, the SF_6 flow was reduced from 15 sccm [11] to 10 sccm [16] to achieve a lower pressure and therefore make the etch more anisotropic. This results in the very elongated scallops, since the 240 nm device layer is etched in only 8 cycles (10 cycles are used to ensure also the smaller features are etched correctly). In Ref. [18], however, the aspect ratio is uniform and much lower in the periodic crystals are etched. Therefore, 14 cycles are used with $p \approx 50\,\mathrm{mTorr}$ during the E-step to reduce the roughness of the sidewalls. Importantly, the aspect ratio in these discussions concerns only the void features, since the main challenge is for the R-step to reach the bottom of the HAR trenches to clear the passivation there. To reach further, higher power (and therefore DC bias) can be used or alternatively, the pressure can be reduced.

4.3 The CORE-process with a hardmask

A 50 mTorr O_2-plasma at 30 W etches CSAR at a rate of 50 nm/min, measured by etching 7 samples with unexposed, yet developed, CSAR for 0–150 s and measuring the resulting thickness with variable-angle ellipsometric spectroscopy (VASE). This implies that the oxidation step in the CORE sequence etches the resist isotropically, both eroding it from the top but also causing the mask to retract laterally. The etch-step of Fig. 4.3 shows that a certain undercut is produced, where the etching etches underneath the mask. If the mask retracts beyond the undercut, faceting will manifest on the silicon features etched, which results in substantial roughness at the top of the etched structures. This puts a fundamental limit on the amount of roughness from the scallop-size that can be tolerated and the total number of cycles, i.e., the etched depth, due to the limit on the amount of oxygen plasma the resist can sustain. Instead, a hardmask can be used, which is neither eroded by O_2 nor SF_6 plasma. Chromium, nikkel and aluminia (Al_2O_3) are excellent materials for such masks, and Ref. [82] demonstrates ultrahigh aspect-ratio etches using a chromium mask deposited by lift-off, which enables AR$>$ 50 with $> 10\,\mu\mathrm{m}$ deep features. However, lift-off has restrictions in terms of resolution and line-edge roughness and instead an etched mask is preferred. The problem is that the hardmasks mentioned typically requires, e.g., chlorine to be etched.

In 2021 chromium etching with a fluorine-chemistry (i.e., without chlorine or bromine) was demonstrated by Nguyen *et al.* [83] using very specific combinations of oxygen and fluorine. Notably, this was done in the same reactor as used for all other processes discussed in this thesis. Chromium etching exploits that chromyl fluoride (CrO_2F_2) is volatile (similar to the established way of etching it by forming chromyl chloride). Therefore, fluorine with sufficient bias will etch chromium oxide (CrOx), however, flourine on pure chromium will form chromium fluoride, which passivates and stops the oxidation. Therefore, to etch chromium an oxygen plasma with a small fraction (0.5–5 %) of fluorine can etch chromium, while oxygen and fluorine alone will not, nor will mixtures with large fractions of fluorine etch chromium [83]. Therefore, a continuous oxygen plasma is sustained (50 mTorr, 100 sccm) at 40 W and every 10 s

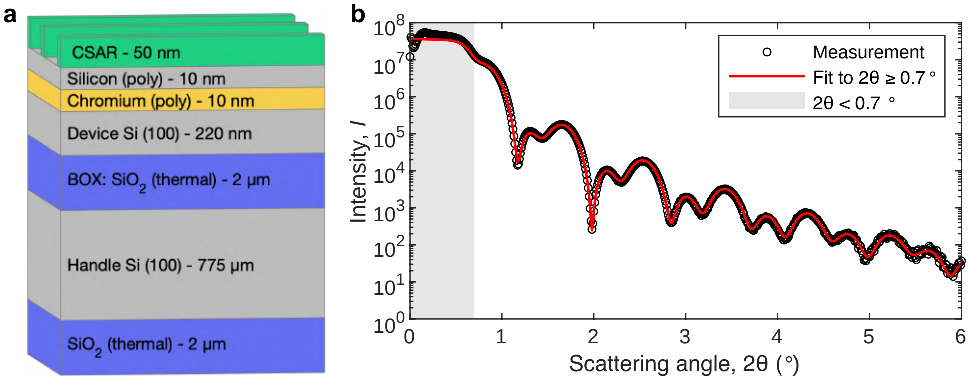

Figure 4.6. Multilayered soft- and hardmask silicon-on-insulator stack. a, Schematic of the target stack dimensions. The double-layer hardmask targets a 10 nm poly-crystalline chromium and 10 nm poly-crystalline silicon deposited using sputtering. 50 nm electron-beam sensitive resist (CSAR) is spin-coated, exposed, and developed to define the patterns. **b**, X-ray reflectivity (XRR) measurement of the hardmask stack on a silicon reference wafer. The fit yields a stack with thickness (roughness) of native oxide on substrate: 0.49 (0.35) nm, chromium: 9.1 (0.18) nm, chromium oxide: 0.17 (0.76) nm, silicon: 9.9 (0.51) nm, native oxide on poly-Si: 0.46 (0.34) nm, and 0.2 (0.4) nm water adsorbed to the surface at room temperature and pressure. Figure and caption reproduced from Ref. [96].

a small amount of SF_6 (6 sccm) is entered for 1 s. This achieves an atomic-layer–like etch with an etch rate $\sim$ 1 nanometer per cycle.

From the resist point-of-view this is essentially a more powerful version of the ashing process (same pressure but higher power) and instead a hardmask that is insensitive to oxygen plasma must be used – silicon comes to mind [83]. Since patterned chromium can be transferred into silicon with high selectivity using this method, and patterned silicon can be transferred into chromium with high selectivity, the required thickness of both silicon and chromium masks must simply be sufficient to avoid defects (i.e., pinholes) in the mask-layers. Refs. [19–21, 84] employ various combinations of thin hardmasks, e.g., 30 nm silicon on 30 nm chromium and 12 nm silicon on 30 nm chromium. However, it is found that thicknesses down to 10 nm of both offers sufficient protection reproducibly – Fig. 4.6**a** shows this hardmask stack on SOI used and Fig. 4.6**b** shows an X-ray reflection (XRR) measurement of the 2-layer hardmask on a silicon substrate, which enables extracting the precise dimensions of the deposited layers. Both hardmask layers are deposited using sputtering and without breaking vacuum in order to keep the amount of native oxide formed on the chromium layer at a minimum. This is important, since any native oxide in the interface will be etched by fluorine [83]. Both the deposited chromium and silicon layers are strictly speaking poly-crystalline, however, the chromium is deposited with a high rate of 60 nm/min, to keep the level of crystallinity at a minimum. Moreover, such thin layers offer little support to form the poly-crystalline regions and so the layers will be almost amorphous. This keeps the levels of line-edge roughness low.

Being back at etching silicon with a softmask may seem counter-productive at first, however, since it is only 10 nm thick, the aspect ratio of HAR final patterns are vastly reduced, and now the softmask can be transferred using a 2 min continuous etch with 5 sccm O_2 and 5 sccm SF_6 at 30 W platen power and the VAT throttle fully opened. This results in a pressure of ~ 0.2 mTorr and an etch rate of 8 nm/s, i.e., the 2 min is an over-etch ensuring that all features are fully etched. Notably, this step is very similar to the remove step. Refs. [19–21, 84] employ variations of a switched process to etch the 12 nm and 30 nm silicon hardmask-layers, however, this is not ideal since a cycles readily etches > 6 nm and the undercut from a DRIE-style process is not a valuable trade-off when etching such low aspect-ratio features.

Figure 4.7 outlines the fabrication processes for the single lithography-layer fabrication of suspended silicon structures in an SOI substrate used to explore applications of etching technology in the later parts of this thesis. It consists of 11 sub-steps, of which 3 are lithography (spin-coating, exposure and development) and 5 are carried out within the same plasma reactor to sequentially transfer the patterns from the softmask and into the multi-layer hardmask stack. The chromium etching process can also be used to strip the chromium hardmask, and it is verified with optical experiments that the chromium is fully gone [38]. The resist is stripped using a 3 min oxygen plasma (50 mTorr, 30 W), to ensure that there is not resist present in the beginning of the chromium etching step, which could affect the number of reactive ions consumed, however, strictly this step might be superfluous as the resist is so thin and is likely etched already within the first few cycles of the chromium etch (which is 15 cycles and includes a 50 % over-etch to ensure that all features are etched to maintain a high yield). Figure 4.8 shows cross-section SEM images from the central etching steps illustrating the high performance of this process, where the etched features are vertical and free of notching [97].

4.4 Self-regulating CORE-process

The processes discussed in the previous sections relied on a number of particularities restricted by software-limitations of the particular reactor-system used (SPTS Pegasus, MP0641). In particular, since the turbo pump has an immense speed of $2.5\,\mathrm{m}^3/\mathrm{s}$ so a large gas flow is needed to achieve a high pressure, which is needed for both the O- and E-steps. This larger gas flow is then wasted and simply pumped through the system. Most gasses used in plasma dry-etching are potent perfluorocarbon (PFC) greenhouse-gases (GHG) [98–100]. Notably, SF_6 is one of the worst with a global warming potential (GWP-100) of 23800 CO_2-equivalent (per mass) over the first 100 year and a lifetime of 1278 year [101], recently up-adjusted from a GWP-100 of 22800 [99]. Already the substitution of C_4F_8 into O_2 is substantial since C_4F_8 has a GWP-100 of 10300 [99], however, there is no denying that SF_6 remains problematic and abatement is the only valid option. Therefore, 100 sccm of helium—which is inert—is added to the 20 sccm SF_6 in the E-step to quickly raise the pressure.

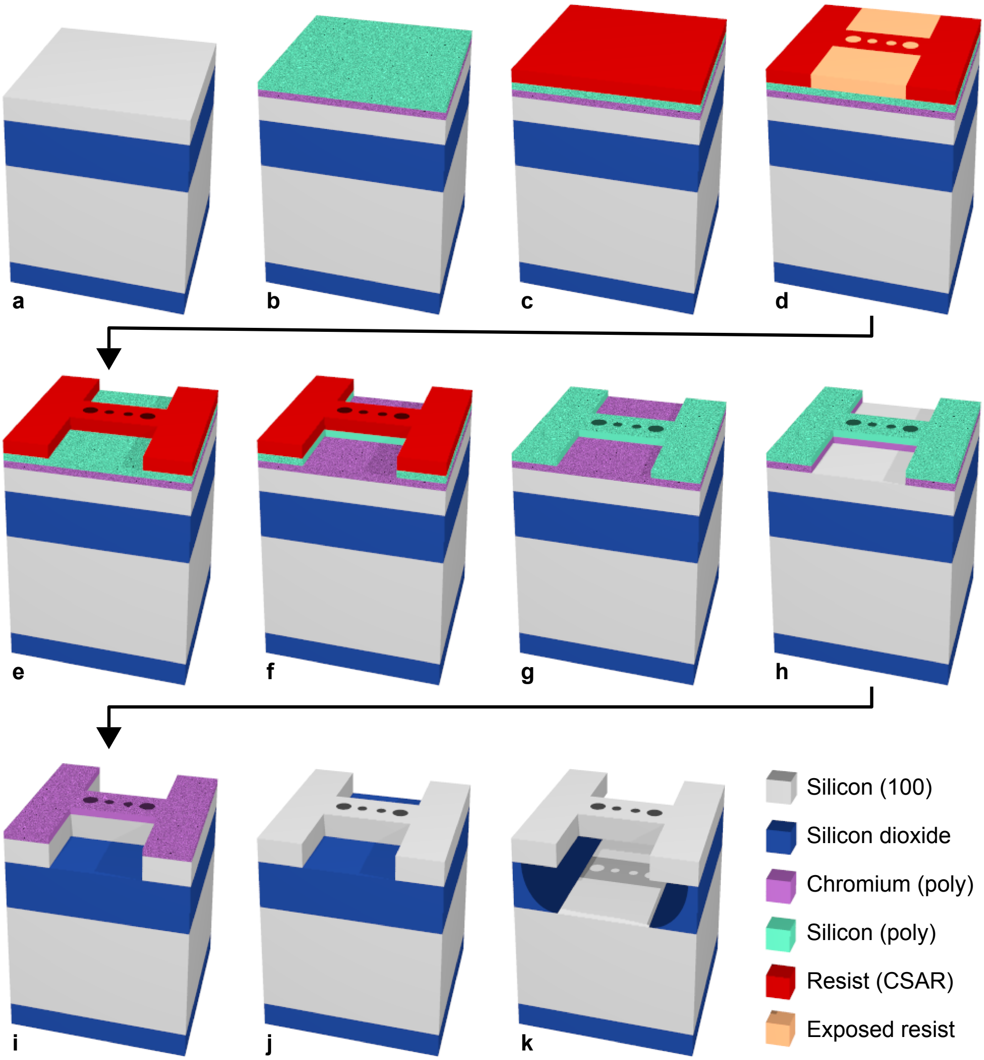

Figure 4.7. Process outline for fabrication of high-resolution suspended structures in silicon-on-insulator substrates with a double-layer hardmask. **a**, Silicon-on-insulator sample. **b**, Deposition of double-layer hardmask (10 nm chromium first, followed by 10 nm poly-crystalline silicon on the top). **c**–**e**, Lithography step with spin-coating of 50 nm CSAR (**c**), exposure with electron-beam lithography (**d**) and development with amyl acetate (Zeon N-50, **e**). **f**–**j**, Pattern-transfer step using 5 plasma dry-etching processes in sequence within the same reactor: (i) continuous poly-silicon–etch with SF_6/O_2 (**f**), (ii) softmask strip with O_2 (**g**), (iii) switched chromium etch with SF_6/O_2(**h**), (iv) switched (100)-silicon CORE-etch with SF_6/O_2 (**i**) and (v) chromium-hardmask–strip by repeating step (iii) (**j**). **k**, Membranization to form suspended silicon-structures by underetching the buried oxide with temperature- and pressure-controlled hydrofluoric acid vapors.

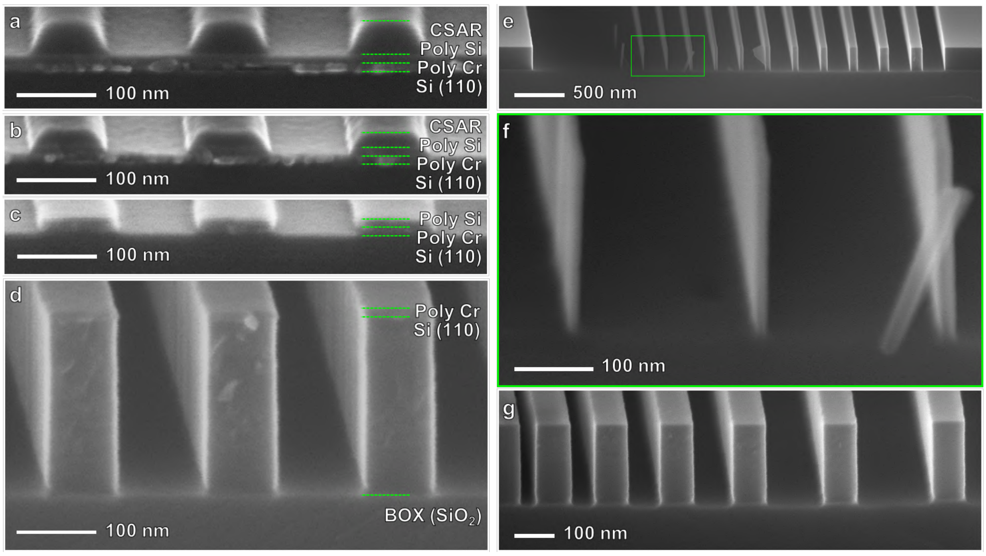

Figure 4.8. Scanning electron micrographs (SEMs) of cross-sections during the process. a-d, Grating structure with 200 nm pitch and 50 % loading after development (**a**), poly-silicon etch (**b**), resist strip and chromium etch (**c**), and main device-layer etch (**d**) with the chromium mask still present, and virtually untouched, enabling ultra-high selectivity as well as flexibility in the process optimization. **e**, Sparse line patterns demonstrating high resolution and low roughness with zoom-in in **f**, confirming a vertical sidewall and high aspect-ratio (HAR) features with nanometer-scale linewidths $\sim$ 10 nm and no notching. **g**, Etching of HAR slits down to $\sim$ 40 nm (i.e., AR = 5.5) showing that the sidewall angle remains vertical and that the etching stops at the buried oxide for the wider features. Figure and caption adapted from Ref. [96].

The high gas flows enables the tool to run all steps of the the processes in so-called pressure-control mode, i.e., where the VAT moves to adjust the pressure in the reactor rather than by moving to a specific position as was the case with previous CORE processes. This allows the process to perform consistent over time and greatly improves the stability of the process.

Another important change has to do with the programming of the process. The SPTS Pegasus systems are designed for a 2-step Bosch process, however, with both the deposition and etch steps having two pre-steps, the delay- and boost-steps. From factory settings it is required that the power is on during the two main steps and the delay- and boost-steps are time-limited to 10 seconds. In this way the R-step was programmed into both pre-steps of the etch step, resulting in a time-limitation of 20 s and instead the power has been increased to ensure a proper performance [11, 16, 18–21, 81–84]. By changing this time limitation, it is possible to encode the R-step purely into the boost-step of the etch phase and instead use its delay-step to fully separate the O- and the R-steps without power, i.e., a second clear-step is added. This is particularly germane as this switch formerly implied that the VAT would move from almost fully closed to fully open with a purely oxygen chemistry in the reactor from the O-step while the SF_6 valve is opened for the R-step, leading to a brief moment of substantially oxygen with a small fraction of SF_6. Additionally, the power would be increased for the R-step, i.e., the reactor state would match exactly the conditions for etching chromium. This put a strict limitation on the reasonable powers as otherwise the chemistry-switch would cause a rapid deterioration of the chromium hardmask. The clear step is carried out using the delay-step of the Deposition-phase and runs with 100 sccm O_2 and the VAT fully open until it is confirmed that no more SF_6 remains in the chamber ($\sim$ 4 s). Next, the boost-step of the Deposition-phase is used to stabilize the chamber pressure to 25 mTorr with oxygen, which enables the O-step to run for very short time-spans consistently. Similarly, by adding the substantial helium flow to the E-step the pressure stabilizes to 50 mTorr immediately, rather than in previous CORE-processes, wherein the first 15–30 s would be spent to reach the desired pressure (and the reached value would drift over time), i.e., the transition from R-step to E-step would be smooth and slow; hence, the steps could be hard to control independently. Finally, the VAT-settings was altered historically to make it respond faster and move to fixed positions as fast as possible, however, when run in pressure control this becomes unstable and the VAT can start oscillating. Therefore, it was slowed down again to dampen its response and keep the tool operating in a stable fashion.

Figure 4.2 shows the schematic of the etcher and notably, there are two fast-switched mass-flow controllers for SF_6; SF6-1 is a 600 sccm-limit port and SF6-2 is 55 sccm-limit port. The latter is exclusively used for these processes, however, the higher-flow MFC could be used instead of helium for simplicity in the chemistry or to reach higher pressures to further reduce the DC bias of the E-step. Indeed, the ICP-source could be used to entirely avoid the DC bias and only rely on the plasma potential. In this context another limitation is worth highlighting. The tool is unable

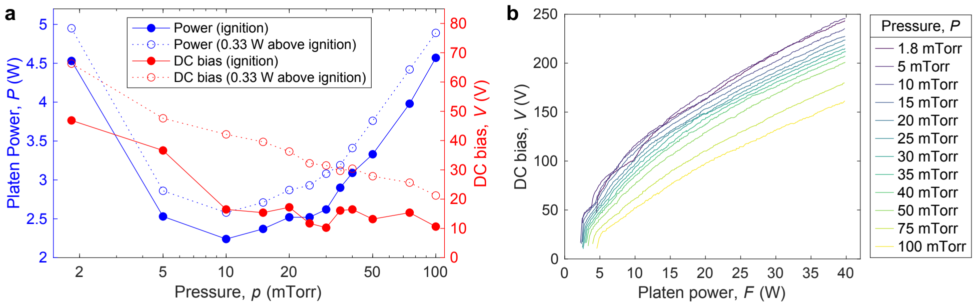

Figure 4.9. Paschen curves and measured DC bias for oxygen plasma. **a**, Measured Paschen curve at ignition and 0.33 W above it as well as the corresponding DC bias. The distance between the electrodes is 13.5 cm. **b**, The measured DC bias against the measured platen power dissipated in the plasma at different pressures 1.8–100 mTorr.

to manually reset its matching circuits between each cycle, as it is assumed that deposition and etching switches back and forth rapidly and without extinguishing the plasma as would be typical within an industrial Bosch process. However, the matching is very different for each of the O-, R-, and E-steps and in particular the E-step has very different configurations when helium is added. That is, ultra-short depositions might encounter problems to properly striking the plasma. However, if the ICP-coil with its separate matching system was used for the E-step, this problem would be alleviated somewhat. It must be noted that the software limitations of the etchers are unique to each brand and model, and many of the issues related to the software are resolved in some more modern etchers.

Due to the TDESC electrically isolating the sample from the point where the DC-bias is measured, the displayed DC-bias normally holds little value or meaning directly; however, it is possible to protrude the pins normally used during loading of the substrate to provide electrical contact to the carrier wafer and thereby measure the actual DC-bias of the process. This requires clamping—and thereby also substrate cooling—to be turned off, and therefore is only feasible for these processes since they are run at low power and at room temperature. When providing electrical contact the substrate is lifted $\sim 1\,\mathrm{mm}$ above the chuck. Then the Paschen curves [86] are measured to quantify the plasma system. This is done by running a series of processes at different pressures and ramping the power very slowly. It is then possible to see when the plasma is ignited by monitoring the forward, auxiliary and reflected powers as well as the DC bias, since the wafer is charged to a negative potential as soon as electrons are delivered to it. Figure 4.9**a** shows a measurement of the Paschen curve for oxygen plasma, i.e., the minimum platen power that can ignite and sustain the plasma at a given pressure as well as its corresponding DC-bias. It can be seen that already at $\sim 20\,\mathrm{mTorr}$ pressure (mean free path, $\lambda_e \approx 1.1\,\mathrm{cm}$) the DC bias drops to $\sim -10\,\mathrm{V}$ for the minimum power. Figure 4.9**b** shows the DC bias against the platen power for various pressures, which reveals that the DC bias is low for the $10\,\mathrm{W}$ used for both O- and E-steps and for pressures, $p > 20\,\mathrm{mTorr}$. The parameters of the fine-tuned process are displayed in Table 4.1.

Figure 4.10 shows cross-sections SEM-images at x500 thousand magnification of gratings with a 100 nm and 200 nm pitch in **a**–**e** and **f**–**j**, respectively. The images shows the developed patterns (**a**, **f**) as well as after each of the steps, i.e., continuous etch into the poly-crystalline silicon mask (**b**, **g**), resist strip (**c**, **h**), chromium etch (**d**, **i**), main etch silicon etch into the device layer (**e**, **j**). The dashed green lines track the outlines between the steps and coincides directly with the center of the scalebar for the 100 nm pitch grating, however, the 200 nm is overexposed during the lithography such that the void feature becomes wider. Nevertheless, this is not an etching issue as the offset dimension is still accurately transferred. It can be seen that the features grow slightly during the etch into the poly-crystalline silicon layer, which is intentional and in order to balance the small undercuts of the chromium etch and the main silicon etch to result in no overall change in the feature-size, however, it does put a lower limit on the achievable dimensions as they must be able to grow a few nanometers in order to be resolved by the poly-crystalline silicon etch step. The

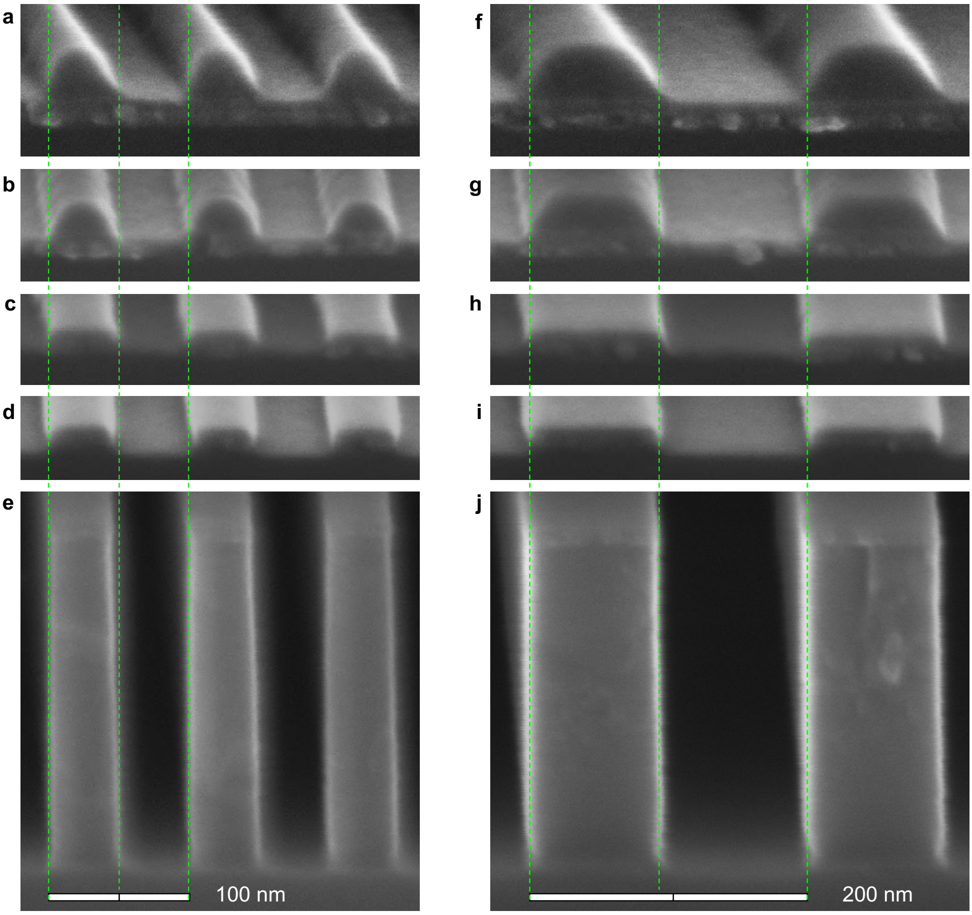

Figure 4.10. Cross-section images of the pressure-controlled CORE process with a double-layer hardmask. a–**e** (**f**–**j**), Gratings with a 100 nm (200 nm) pitch. The green dashed lines shows how the etching process maintains the dimensions of the original mask, and by comparing to the center of the scale bars it can be seen the 100 nm–pitch gratings maintains the designed dimensions, while the void parts of the wider 200 nm–pitch gratings grow slightly due to an overexposure during the electron-beam lithography step. It can be seen (**a**–**c** and **f**–**h**) that the chromium layer has substantially more roughness compared to the poly-crystalline silicon, due to the very poly-crystalline nature of chromium. Both layers are fairly smooth, however. Both gratings are fabricated on the same chips and so this figure shows samples from 5 different chips. The cross-section in the resist (**a** and **f**) are from a different piece than the other 4, and so the spin-coating as well as the hardmask deposition was run separately, albeit back to back and all chips were cleaved and imaged on the same day using the same scanning electron microscope.

Process	**Pressure**	**O_2 flow**	**SF_6 flow**	**He flow**	**Power**	**DC bias**
Poly Si	0.2 mTorr	5 sccm	5 sccm	0 sccm	20 W	160–170 V
Strip	50 mTorr	100 sccm	0 sccm	0 sccm	30 W	170–180 V
Cr etch	50 mTorr	100 sccm	5 sccm†	0 sccm	40 W	210 V
C step	2 mTorr	100 sccm	0 sccm	0 sccm	0 W	0 V
O step	25 mTorr	100 sccm	0 sccm	0 sccm	10 W	85 V
R step	0.1 mTorr	0 sccm	5 sccm	0 sccm	30 W	$\sim$ 205 V‡
E step	50 mTorr	0 sccm	20 sccm	100 sccm	10 W	28 V

Table 4.1. Parameters of pressure-controlled CORE-process with a double-layer hardmask. † The SF_6 flow is run for 1 s every 10 s. The DC bias for the Cr etch is given as the value after SF_6 enters the chamber; without it $V_{dc} = 190$ V. ‡ The DC bias is not perfectly stable during the R-step and fluctuates between 200-210 V, limited by fluctuations in the inlet gas flow. The VAT is kept fully open to achieve the minimum possible pressure with the reactor. The duration for the steps are 120 s (poly Si), 180 s (strip), 15×10 s $= 150$ s (Cr etch), and 25 ramped cycles (total 25 min 20 s) with the Deposition-phase: 4 s clear, 3 s to stabilize pressure for O-step, 5 s O-step and the Etch-phase: 5 s clear, 20 s R-step and 20–28 s E-step. The time for the full process incl. auxiliary steps (e.g., pump and stabilization times) is 36 min 36 s.

100 nm grating shows a minor faceting, which could be further reduced by increasing the passivation and balancing this with a longer R-time. Optionally, the pressure in the E-step could be further increased. It is also possible to decrease the R-power further and instead increase the R-time, however, this would make the process less stable to variations in aspect ratios, which is a prime feature of the process required for photonic and phononic components. Finally, it can be observed that the chromium mask remains almost intact after the 25 cycles employed here, indicating that there is still plenty of room to etch deeper. This is further corroborated by Fig. 4.5, where 75 cycles still did not erode the mask. Here, in the optimized process, the combined etch time is ramped from 45–53 s with the first 5 s spent without power to separate the chemistries, the next 20 s constitutes the R-step and the final 20–28 s is the E-step—while in the 75-cycle deep-etch it was increased to 60–84 s, the entire change to the E-step—both in order to obtain a straight side-wall, and the latter increased to improve the etched depth gained per cycle. The etch rate for AR$\sim$ 1 is about 10 nm per cycle in crystalline (100) silicon.

Figure 4.11 compares two chips etched 5 weeks apart. The hardmasks used throughout this chapter are all deposited on the same day using a batch-run on 10-by-10 cm shards, which are cleaved into 25-by-25 mm chips, which are then cleaned, spin-coated and exposed (see specific process flow in Appendix A). Chip 1 was exposed with EBL on April 26, 2022 and Chip 2 was exposed on September 29, 2022 with a 2 nm pitch and a current, $I \approx 0.8$ nA; both were developed immediately afterwards in amyl acetate (Zeon N-50) and cleaved into 8-by-12 mm pieces with a long grating-set

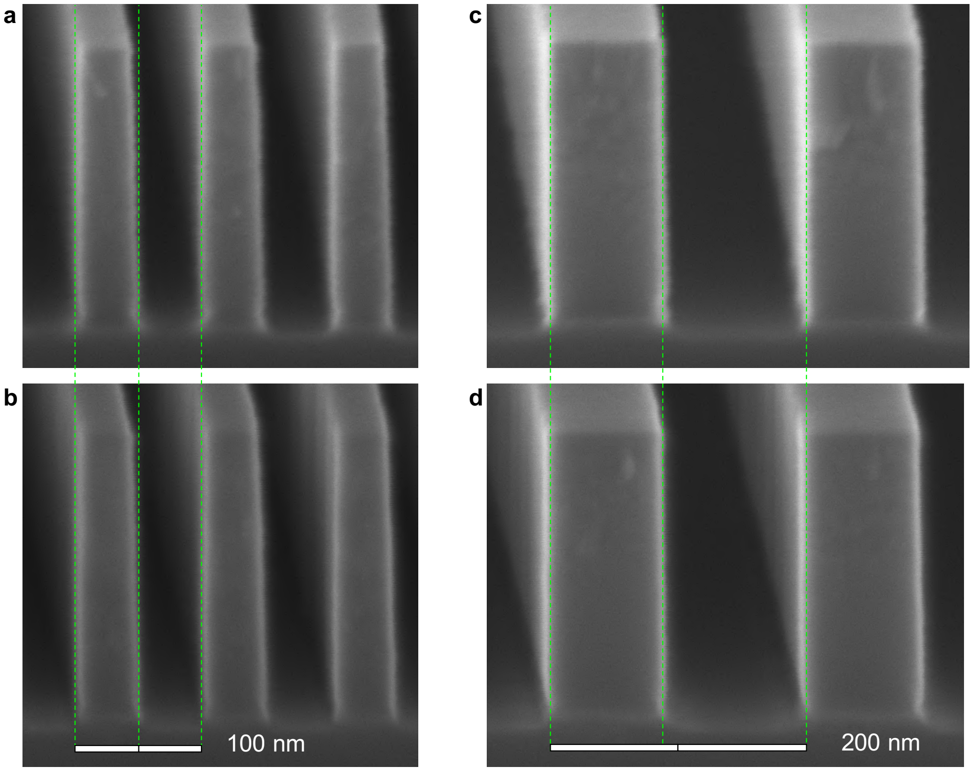

Figure 4.11. Comparison of two chips etched 5 weeks apart. **a** and **c**, 100 nm– and 200 nm–pitch gratings etched on chip 1, and **b** and **d**, the same on chip 2. The dashed green lines verifies that the processes are the same. Both images are shown after the final chromium strip-step, and chip 2 is from the same piece as was used in Fig. 4.10**a**, i.e., the process is highly reproducible.

on each piece. The electron-beam lithographic system underwent substantial service in between these exposures, including a change of its gun. Chip 1 (Figure 4.11**a**,**c**) is etched on September 2, 2022 with the pins down, i.e., the DC bias cannot be read accurately during it, however, clamping and cooling would be possible to apply if desired. It is inspected immediately afterwards. Chip 2 (Figure 4.11**b**,**d**) is etched on October 7, 2022, i.e., precisely 5 weeks later and together with the 4 other chips displayed in Fig. 4.10, and therefore run with the pins up. The reactor was not preconditioned for any of the processes, since the oxidation rather than the fluorocarbon-passivation maintains a clean and stable reactor. Despite the many small fluctuations during the process, it is clear that the results are highly reproducible and that the process does not drift, the hardmask across different shards, spin-coating of different chips, etching on different days and hours, as well as time between development and etching, all have no clear effect on the results. This may not be surprising, however, it is important to stress the importance of a stable and reproducible process, since this is required in order to tailor a process to pursue applications requiring the highest resolution down to the nanometer-scale deterministically.

Part II

Exploring novel physics

CHAPTER 5

Theory of light-matter interactions

The interaction between light and matter is crucial across a range of applications [102–105] such as conversion between electrical and optical signals by emission or detection of light [3, 106]. Emission, in particular, can be achieved with lasers and light-emitting diodes (LEDs), which are used to drive communications across the internet or for everyday use, while detection spans solar-cells to signal-processing [104, 107, 108]. Further applications of light-matter interactions are modulation and routing of optical signals as well as emerging quantum technologies [24, 109, 110]. However, light and matter interacts only weakly – often it is described with the platitude *feeble*. This weak interaction can be an advantage to build low-loss waveguides in dielectrics, which are electrically insulating materials where the band gap is larger than the energy of electric field. Silicon for example has a band gap, $E = 1.12\,\mathrm{eV} \sim 1100\,\mathrm{nm}$, which suppresses optical losses due to absorption at telecom wavelengths, $\lambda \sim 1550\,\mathrm{nm}$ [10]. Such optical waveguides are used both to transmit information across large distances through fibers, which are made by pulling glass, or on-chip by nanofabrication-processes on wafers [84, 111–113].

However, the weak interaction is also a problem for many other applications. To overcome this limitation, optical cavities can confine and store light, thereby enhancing its interaction with the material [16, 17, 114–116]. This chapter introduces light-matter interactions in optical nanocavities (Sec. 5.1) including the Purcell effect (Sec. 5.2) describing the enhancement of the decay-rate of an emitter place inside such a cavity. Additionally, references to the established theory are provided, with a special focus on the recent advances in spatial confinement in dielectric cavities using bowtie structures. These are introduced in Sec. 5.3 and a two-dimensional study on its optimal shape is presented [17]. Section 5.4 covers the differences between field enhancement in the bulk medium as opposed to lightning-rod effects at the surface [17]. These effects are discussed in the context of the well-known photonic crystal (PhC) cavity with 3 holes removed in a line (L3-PhC cavity) [114]. This leads to the experimental work presented in Ch. 6 on Ref. [16].

5.1 Enhancement of the light-matter interaction with optical cavities

Optical cavities can be used to enhance the light-matter interaction, and Fig. 5.1**a** and **b** show two ideal optical cavities of lengths, L and $2L$, respectively. They are constructed by a perfect conductor (i.e., mirror) [117] at both ends with reflectivity,

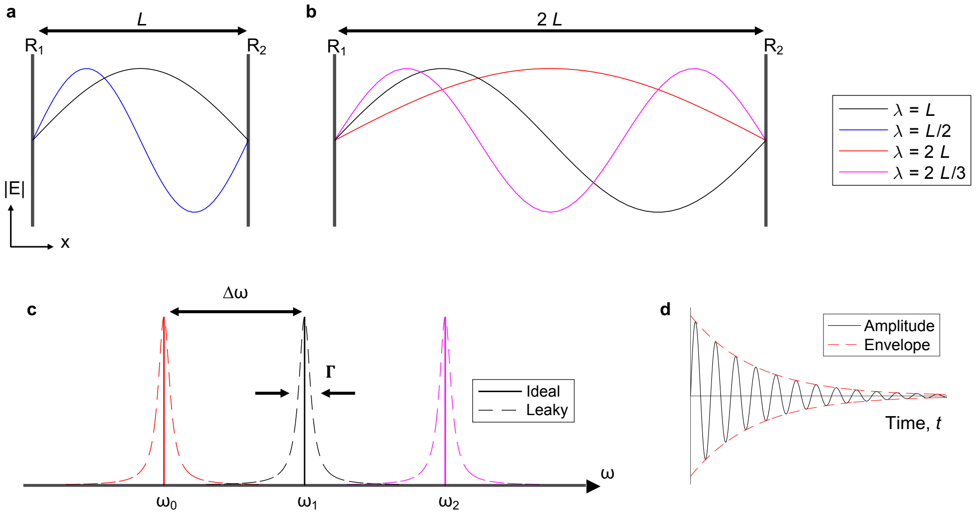

Figure 5.1. Principles of an optical cavity. **a**, Ideal Fabry-Pérot (FP) cavity with two perfect mirrors, $R_1 = R_2 = 1$, and the first two modes with $\lambda = \{L/2, L\}$. The amplitude of the electric field of a mode, $|E|$, has a spatial variation. **b**, FP cavity of twice the length as **a** with the first 3 modes. Its second mode has the same wavelength as the fundamental mode in **a**. **c**, Spectrum of modes in **b**, higher-order modes have a shorter wavelength and higher frequency indicated by the solid lines for ideal cavities. Imperfect cavities have losses, corresponding to a Lorentzian lineshape (dashed lines) with a full-width at half-maximum intensity (FWHM), $\Gamma = 2\gamma$. The distance between peaks in the spectrum is called the free-spectral range (FSR), $\Delta\omega$. **d**, Optical signal of a mode in the time-domain. An ideal cavity will oscillate forever, however, a real cavity have a loss, γ, which dampens the amplitude of the electric field over time, illustrated by the exponential envelope, $\exp(-\gamma t)$.

$R_1 = R_2 = R = 1$, which forms Fabry-Pérot (FP) cavities. Only light with a wavelength,

$$\lambda = 2L/q, \quad q \in \mathbb{N}, \tag{5.1}$$

will be zero at the conductors while other wavelengths will vanish away [116–119]. The discrete solutions to this problem are called modes, and the fundamental mode has $\lambda = L/2$ with higher-order modes having faster oscillations—or equivalently, shorter wavelengths—characterized by the angular frequency,

$$\omega = 2\pi f = \frac{2\pi c}{\lambda}, \tag{5.2}$$

with f the frequency and c the speed of light. The modes have an amplitude in the cavity that varies in space (x) and time (t) given as,

$$E(x,t) = A\mathrm{e}^{-i(kx-\omega_0 t)}, \tag{5.3}$$

where A is the maximum amplitude and ω_0 is a frequency of one mode shown in Fig. 5.1**a**. Figure 5.1**b** shows a cavity that is twice as long, and it can be seen that the fundamental mode of the shorter cavity (Fig. 5.1**a**) has the same wavelength as the second-order mode in Fig. 5.1**b**.

Figure 5.1**c** shows the angular frequencies of three lossless modes (solid lines) separated by a free spectral range (FSR), $\Delta\omega$, i.e., a series of equally spaced δ-peaks. In reality, a cavity will not be loss-less, i.e., the angular frequeny becomes loss-less [116]

$$\omega_0 \to \widetilde{\omega_0} = \omega_0 + i\gamma, \tag{5.4}$$

which affects the time-evolution of the amplitude of the mode,

$$E(t) = A(x)\mathrm{e}^{i\omega_0 t-\gamma t} \propto \mathrm{e}^{i\omega_0 t}\mathrm{e}^{-\gamma t}. \tag{5.5}$$

Here, the argument of the last exponential becomes real and therefore describes an exponential decay in the amplitude as energy leaks from the cavity with a decay rate, γ. This real part of the time-evolution of a leaky cavity mode is shown in Fig. 5.1**d**. The energy in the cavity is proportional to the absolute square of the electric field, and the ratio of the frequency and the decay rate of energy in the cavity defines the so-called quality factor [116],

$$Q = \frac{\omega_0}{2\gamma}, \tag{5.6}$$

which describes the localization in frequency—or equivalently the storage time in the cavity. It can further be interpreted as the number of optical cycles over which light is stored in the cavity [102, 114, 116, 118].

Assuming the field in the cavity is excited at time, $t = 0$, the Fourier transform of the lossy time-dependent amplitude of the electric field (Eq. (5.5)) yields its spectrum, i.e., the amplitude of different frequencies,

$$\begin{aligned} F(\omega) &= \int_0^\infty E(t)\mathrm{e}^{-i\omega t}dt && (5.7)\\ &= \int_0^\infty A(x)\mathrm{e}^{i\omega_0 t-\gamma t}\mathrm{e}^{-i\omega t}dt && (5.8)\\ &= A(x)\int_0^\infty \mathrm{e}^{i(\omega_0-\omega)t-\gamma t}dt && (5.9)\\ &\approx \frac{1}{\gamma - i(\omega_0-\omega)}. && (5.10) \end{aligned}$$

The spectrum can then be written as the real part,

$$\mathrm{Re}\{F(\omega)\} \propto \frac{\gamma}{(\omega_0-\omega)^2-\gamma^2}, \tag{5.11}$$

which is the canonical Lorentzian lineshape of a leaky optical cavity with a full-width at half-maximum intensity (FWHM), $\Gamma = 2\gamma$, displayed as the dashed lines in Fig. 5.1**c**.

Experimentally, high-Q has been achieved in dielectric nanocavities for decades [114, 120, 121], and more recently, multi-million quality factors have been demonstrated in nanocavities [122, 123]. The quality factor is limited by loss-mechanisms such as disorder (which will cause scattering) and loading of the cavity, e.g., by placing a waveguide in its vicinity such that light leaks away from it and into the desired waveguide rather than uncontrollably being lost. Another loss-channel is the absorption, e.g., two-photon absorption (TPA), which can occur if two photons have more energy than the band gap. In silicon it is $\sim 1100\,\mathrm{nm}$, and so this process can occur for wavelengths, $\lambda \leq 2300\,\mathrm{nm}$, such as telecom wavelengths. All these different loss-mechanisms stack together limiting the total quality factor [123, 124],

$$\frac{1}{Q} = \frac{1}{Q_i} + \frac{1}{Q_{\mathrm{wg}}} + \frac{1}{Q_{\mathrm{scat}}} + \frac{1}{Q_{\mathrm{abs}}} + ..., \tag{5.12}$$

Where Q_i is the intrinsic quality factor, Q_{wg} describes the controlled loss into a waveguide, Q_{scat} is the loss due to scattering and Q_{abs} is the absorption loss, which for telecommunication wavelengths is nonlinear in silicon. A measurement will probe the total Q, while a typical calculation will evaluate the intrinsic Q_i – and in case there is a waveguide the loading due to it, Q_{wg}. The absorption will depend on the power in the cavity as well as the material, and the scattering depends on the disorder, which is hard to calculate [19] and often disregarded. Cavities can be engineered to have high Q_i, so to achieve ever-higher optical quality factors, the challenge has been to fight structural disorder. It is in this context relevant to note that there is a difference between roughness and disorder. Scattering depends on a complex interplay between the polarization and the type of roughness, i.e., on whether it manifests as a protrusion or a re-entrant perturbation from the ideal system. The field can diverge, remain constant or go to zero around such a defect [119, 125, 126], with only the divergent points acting as antennas causing scattering. Appendix B includes some examples of these phenomena, where notably the slot-mode waveguides (discussed in Chs. 8 and 9) depends sensitively on protrusions – such as those created by the scallops from the cyclic dry-etching. However, the bowtie-based nanocavity with a solid center will have a constant field across scallops on its boundary, while the void version will diverge [16, 17].

5.2 Purcell enhancement and spatial confinement with bowtie structures

The previous section introduced optical cavities that can confine light temporally, i.e., increase the Q, to enhance its interaction with matter [105]. Cavities also enhance the interaction through spatial confinement as well as through the refractive index, n. The enhancement is more completely described with the projected local density of optical states (LDOS) [116, 127],

$$\rho_p(\mathbf{r}) = \frac{2\omega}{\pi c^2}\mathrm{Im}\{\hat{\mathbf{e}}^{\mathrm{T}} G(\mathbf{r}, \mathbf{r}, \omega)\hat{\mathbf{e}}\}, \tag{5.13}$$

where G is the Green function for a quasi-normal mode (QNM, $\tilde{\mathbf{f}}(\mathbf{r})$. For a single-mode system, and when the mode overlaps perfectly with the emitter [105], this can be written in terms of the QNM [116],

$$G_0(\mathbf{r},\mathbf{r}',\omega) \approx \frac{c^2}{2\omega}\frac{1}{(\omega_0 - i\gamma) - \omega}\frac{\tilde{\mathbf{f}}_0(\mathbf{r})\tilde{\mathbf{f}}_0(\mathbf{r}')}{\langle\langle\tilde{\mathbf{f}}|\tilde{\mathbf{f}}\rangle\rangle}. \tag{5.14}$$

On resonance ($\omega = \omega_0$) this becomes

$$G_0(\mathbf{r},\mathbf{r}',\omega) \approx \frac{c^2}{2\omega_0}\frac{1}{\gamma}\frac{i}{\varepsilon(\mathbf{r})v(\mathbf{r})}, \tag{5.15}$$

which is written in terms of the full, complex mode volume [128, 129],

$$\frac{1}{v(\mathbf{r})} = \frac{\varepsilon(\mathbf{r})\tilde{\mathbf{f}}_0(\mathbf{r})\tilde{\mathbf{f}}_0(\mathbf{r}')}{\langle\langle\tilde{\mathbf{f}}|\tilde{\mathbf{f}}\rangle\rangle}. \tag{5.16}$$

In a homogeneous medium the overlaps in Eq. (5.13) are unity, and the imaginary part of the Green function [127],

$$\mathrm{Im}\{G_B(\mathbf{r},\mathbf{r}',\omega)\} = \frac{n\omega}{6\pi c}. \tag{5.17}$$

The density of states (DOS) in a homogeneous medium is (using Eq. (5.13) with Eq. (5.17)),

$$\rho_{\mathrm{hom}} = \frac{2\omega}{\pi c^2}\frac{n\omega}{6\pi c} = \frac{n\omega^2}{3\pi^2 c^3}. \tag{5.18}$$

It is possible to write the projected LDOS in terms of the Green function [127], i.e.,

$$\mathrm{Im}\{G(\mathbf{r},\mathbf{r}',\omega)\} = \frac{c^2}{2n^2\omega_0\gamma V_{\mathrm{eff}}}, \tag{5.19}$$

where $1/V_{\mathrm{eff}}(\mathbf{r}) = \mathrm{Re}\{1/v(\mathbf{r})\}$ is the effective mode volume. Throughout this thesis, $V_{\mathrm{eff}}(\mathbf{r})$ is simply called V, and the spatial dependence is no longer written explicitly. Many other mode volumes exists [104, 115] but are not discussed further here. Thus, the projected LDOS for a QNM is

$$\rho_p^{\mathrm{QNM}} \approx \frac{1}{\pi n^2\gamma}\frac{1}{V}. \tag{5.20}$$

Normalizing the projected LDOS to the homogenous DOS yields the well-known Purcell factor [130],

$$F_P = \frac{\rho_p^{\mathrm{QNM}}}{\rho_0} = \frac{\mathrm{Im}\{G(\mathbf{r},\mathbf{r}',\omega)\}}{\mathrm{Im}\{G_B(\mathbf{r},\mathbf{r}',\omega)\}} \tag{5.21}$$

$$= \frac{6\pi c}{n\omega_0} \frac{c^2}{2n^2\omega_0\gamma V} \tag{5.22}$$

$$= \frac{6\pi c^3}{n^3\omega_0^3} \frac{\omega_0}{2\gamma} \frac{1}{V} \tag{5.23}$$

$$= \frac{6\pi c^3}{n^3\omega_0^3} \frac{Q}{V} \tag{5.24}$$

$$= \frac{3}{4\pi^2} \left(\frac{\lambda_0}{2n}\right)^3 \frac{Q}{V}, \tag{5.25}$$

where the definition of the quality factor is used as well as $\lambda_0 = 2\pi c/\omega_0$. The Purcell factor shows the canonical Q/V ratio, which is an indirect figure-of-merit for a nanocavity.

The quality factor is a global parameter of the cavity, however, the mode volume of the cavity, V, is—just as the LDOS—typically evaluated at single point, at the position of the emitter, which is normally placed at a point of maximum field strength. This assumes that the field varies slowly compared to the size of the emitter like an atom. However, if the field varies fast or the polarization of the field and the emitter does not overlap, this should be taken into account [105]. The mode volume for a point-source dipole in a real cavity is [16, 128, 129],

$$\frac{1}{V} = \mathrm{Re}\left[\frac{\epsilon_r(\mathbf{r}_0)\mathbf{E}(\mathbf{r}_0)\cdot\mathbf{E}(\mathbf{r}_0)}{\int_V \epsilon_r(\mathbf{r})\mathbf{E}(\mathbf{r})\cdot\mathbf{E}(\mathbf{r})\,dV + i\frac{c\sqrt{\epsilon_r}}{2\omega}\int_S \mathbf{E}(\mathbf{r})\cdot\mathbf{E}(\mathbf{r})\,dA}\right], \tag{5.26}$$

where $\mathbf{E}(\mathbf{r})$ is the full 3D vectorial electric field, and $\epsilon_r(\mathbf{r}) = n^2$ is the dielectric constant of the material, both at position, $\mathbf{r}$. The volume integral is over all space and diverges [128], however, the surface integral over the outer boundaries normalize it. For high-Q cavities ($Q \gg 10$), the surface term only contributes a minor correction. This is an excellent approximation for very high-Q cavities and correct for ideal systems [17]. For further details on the mode volume, the reader is referred to Ref. [129], and for additional discussions on its interpretation to Ref. [131]. The mode volume takes its name due to its units of volume, however, loosely one may consider it as the inverse energy density [17],

$$u(\mathbf{r}) = \frac{\epsilon_r(\mathbf{r})\mathbf{E}(\mathbf{r})\cdot\mathbf{E}(\mathbf{r})}{\int_{\mathbf{r}'} \epsilon_r(\mathbf{r}')\mathbf{E}(\mathbf{r}')\cdot\mathbf{E}(\mathbf{r}')\mathrm{d}\mathbf{r}'}, \tag{5.27}$$

with $u_0 = \mathbf{D}\cdot\mathbf{E} = \epsilon_0\epsilon_r\mathbf{E}\cdot\mathbf{E}$, and the total energy in the mode is $\int u_0 \mathrm{d}\mathbf{r}'$.

The mode volume considered in this work is the so-called effective mode volume, and a number of other figures of merits (FOMs) exists for other applications such as optical nonlinearities and two-photon absorption processes [104, 115]. Other FOMs may for example scale as Q^2, however, the focus in this thesis is on the enhancement of the decay-rate of a point-like emitter in the cavity, which is described by the Purcell factor and scaling as Q/V [105, 132]. Another important point to take into account is the bandwidth of operation, which is typically defined by the linewidth, $\Gamma = 2\gamma$, and thus the $Q = \omega_0/\Gamma$ (cf. Eq. 5.7). For example a laser pulse centered around $\lambda = 1550\,\mathrm{nm}$ (corresponding to the frequency, $f = 193.4\,\mathrm{THz}$, and period, $T = 5.17\,\mathrm{fs}$). This implies that a 1 ps-pulse matches the linewidth of a cavity with $Q \sim 5000$. This Q is moderate, however, it is important to achieve a high intrinsic Q_i by reducing the optical losses from scattering and absorption; then the Q is reduced by loading the cavity with a waveguide such that the light leaks in a controlled fashion through the engineered channel (cf. Eq. (5.12)). The light matter interaction is then increased by reducing the mode volume, i.e., by intensifying the optical field around the emitter.

The theory of diffraction states that it is not possible to focus light to an area smaller than the square of half-a-wavelength in a material, which is often taken to imply that light cannot be focused to a volume smaller than half-a-wavelength cubed, $[\lambda/(2n)]^3$ [117, 119, 133]. This limit applies for example to optical lithography methods where reducing the wavelength has increased the resolution of nanofabrication [7, 10] and it applies to conventional optical microscopes. The diffraction limit applies to the smallest spot-size of a Gaussian-shaped beam propagating in free space through a set of lenses. It is a far-field property and it is intrinsically related to the concept of refraction. However, beams can be shaped into multiple hotspots, thus bypassing the diffraction limit [134].

The name mode ”volume” makes it easy to think that it is also bounded by the diffraction limit, while in fact it describes the energy density in a single point point. The simple 1D cavities in Fig. 5.1 show that the the smallest mode is linked to the size of the cavity, since the mode must have nodes at the cavity ends. However, the electric field in 3D is a vector quantity that is only required to have nodes along two dimensions of a hypothetical box of perfect mirrors [117]. For the nanocavities shown Fig. 5.2**a**, the boundary conditions across the interface of a dielectric material. The tangential component of the electric field, $\mathbf{E}$, and the normal component of the displacement field, $\mathbf{D} = \epsilon\mathbf{E}$, must be continuous [17, 117]. The opposite configuration causes a discontinuity scaled by a factor of the dielectric constant, ϵ_r. Importantly, the potential, Φ, can change around a point – but its derivative, the field, changes rapidly when moving around a corner, which for an infinitely sharp corner implies a divergent field amplitude in that point [117, 119, 125, 126, 133], and further, implies a corresponding mode volume of 0. While infinitely sharp points often occur in numerical simulations due to convenience, in reality they do not exist, and instead a finite radius of curvature, R, should be applied to sharp vertices in a numerical model to adequately represent the physics [16, 17] and to control the transition. Often the mode volume is not calculated using Eq. (5.27) but rather as the maximum

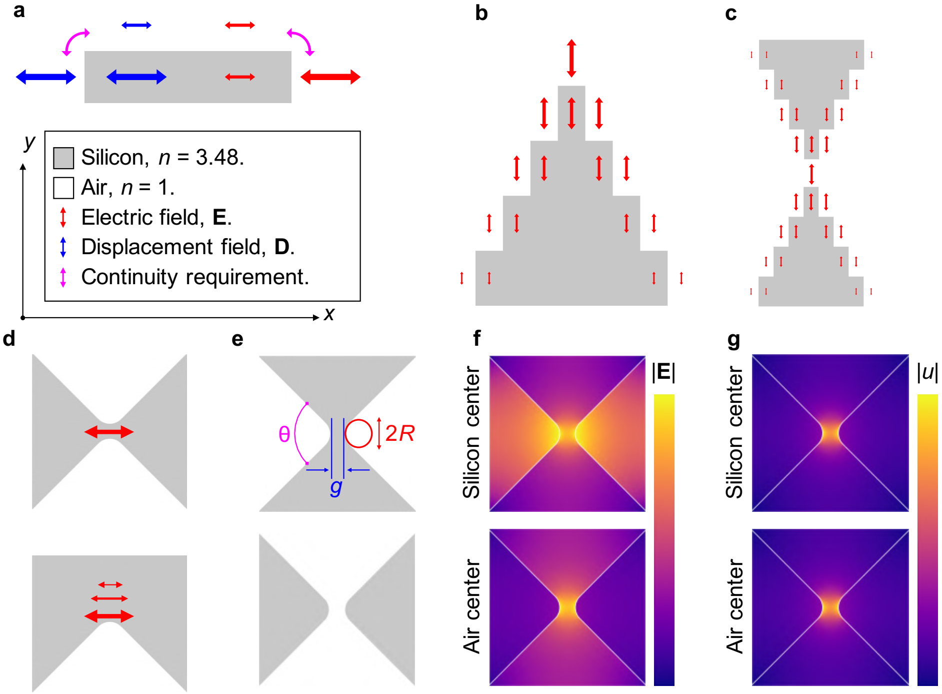

Figure 5.2. Minimizing the mode volume with bowtie features. **a**, Boundary conditions of the electric and displacement fields. **b**, Stacking the boundary conditions to obtain an extremum of $\mathbf{E}$ as a lightning-rod. **c**, Two facing lightning-rods forming a bowtie where the field is only enhanced very locally. **d**, Schematic of the bowtie (top) and lightning-rod (bottom) showing the field decay away from a lightning-rod compared to the localization due to supression of background field around the bowtie. **e**, Schematic of a bowtie in high-index (top) and low-index (bottom), e.g., air. The central design-figures of merit are detailed: The bowtie angle, θ, gap, g—i.e., the separation between two facing tips— and the radius of curvature of the bowtie, R. **f**, Amplitude of the electric field, $|\mathbf{E}|$, for solid (void) bowtie in top (bottom), and **g**, energy density, u. Notably the energy densities are identical since solid-center bowtie already is enhanced by n. Calculations solved as 2D electrostatic problem. **a**, **d**–**g** adapted from Ref. [17].

(normalized) energy density, which is prone to pick-up such numerical divergences. Figure 5.2**b** shows a series of material interfaces stacked to increase the field intensity manifold [17, 115, 135], and while the field could be larger at many of the corners, the engineered enhanced field at the tip apex is likely the important value of interest. Figure 5.2**c** shows how two such tips can be placed facing each other—forming a bowtie structure [136–139]—both enhancing the field locally and suppressing the field elsewhere. Intuitively, this enhancement can be interpreted as a reduction in V through changing the normalization integral. Instead of the stacked interfaces, the same effect can be obtained through smooth features (Fig. 5.2**d**), characterized by the radius of curvature of the tips, R, the angle of the bowtie structure, θ, and the gap, g, between the two tips (in this thesis considered a gap irrespective of the center being low- or high-index and whether it is void or solid. Figure 5.2**f** shows the amplitude of the electric field in a solid (void) center bowtie in the top (bottom) calculated using a 2D electrostatic finite element model (FEM), which is valid for a sub-wavelength volume [17, 115, 140]. The electric field amplitude is more localized in the structure with air in the center. However, the energy density (shown in Fig. 5.2**g**), $|u|$, illustrates that the energies obtained are identical, since the each obtain their field enhancement either through $\mathbf{D}$ and $\mathbf{E}$ for solid and void, respectively. Looking at the electric field only may misleadingly lead one to believe that a bowtie that confines the light in the low-index medium achieves a tighter field confinement. It can be practical to give a mode volume in units of $[\lambda/(2n)]^3$ such that the pre-factors of the Purcell effects cancels out and simply becomes, $P \approx 0.6\,Q/V$. This factor happens to be equivalent to the diffraction limit (or rather its fictitious volume-version), which further can create confusion as stating V in "units of the diffraction limit" is practical when talking about the quantities, while, in fact, the two concepts have nothing to do with one another. In this context it is worth noting that the Purcell factor includes a factor $1/n^3$ not from the LDOS but from the DOS, and it is well known that increasing the refractive index of the material also increases the light-matter interaction (e.g., by slow light [19, 105, 141]). The Purcell factor, and therefore V, therefore includes n^3 to avoid double-counting this effect. However, this should not be interpreted as cavities with low-index centers (and thus, smaller mode volumes and larger Purcell factors) leads to stronger light-matter interactions [139].

Starting with a valid motivation a hypothesis was proposed that dielectric nanocavities cannot confine light below the diffraction limit [142]. Although this is not the case, it has spurned a widespread misconception that it is [131, 140, 143]. It is often stated to motivate the use of plasmonics, which incur substantial losses due to Ohmic absorption, and thereby bounding the $Q < 100$ [144]. This is restrictive for some applications but not for others [110, 140, 145]. Sub–diffraction-limit mode volumes have been demonstrated over and over with new designs but due to the steep nanofabrication requirements to etch a small dielectric bowtie structure it has eluded experimental efforts until recently [16], and these results are presented and discussed further in Ch. 6. In this context, the author wishes to highlight the pioneering work of the Weiss group, reported in Hu *et al.* [146], which takes on the daunting task of fabricating such a structure to experimentally realize a dielectric bowtie nanobeam cavity, which achieves a mode volume on the order of the diffraction limit [17] and further employ a V-groove to make a sharp point that reduces the mode volume below it around the interface. However, the mode volume reported originates in a V-groove, which is a local perturbation of the system. The near-field measurements in Ref. [146] instead probes the ”bulk” mode volume, i.e., the larger envelopes that are not considerably modulated by these local ”lightning-rod” effects. These terms are discussed in Ref. [17] and will be discussed further in the following sections. In summary, corroborating experimentally a deep sub–diffraction-limit mode volume in a dielectric cavity has not been demonstrated until Ref. [16], and this will be presented in Ch. 6.

5.3 Numerical 2D electrostatic study of optimal shape

While the electric field is a 3D quantity, a lot of insight on the scalings can be gained from a simpler 2D-system [17, 115]. Figure 5.3**a** shows examples of lightning-rod effects using a 2D electrostatic FEM calculation. A lightning-rod effect is a local spike in the field at the tip apex [125, 126], which rapidly decays and plateaus – it can be thought of as a small perturbation of the mode. Notably, the 2D equivalent of the mode volume is simply the mode area and those can be interpreted identically [120] as the energy density in the respective dimension. On the other hand, Fig. 5.3**b** shows instead bowtie structures where the field is only locally enhanced between the tips. Figure 5.3**c** shows linescans through the four structures in Fig. 5.3**a**–**b**. The spikes at the material interface created by the lightning rods sensitively depend on the radius of curvature, R, but plateaus to a similar value over a similar distance, i.e., the

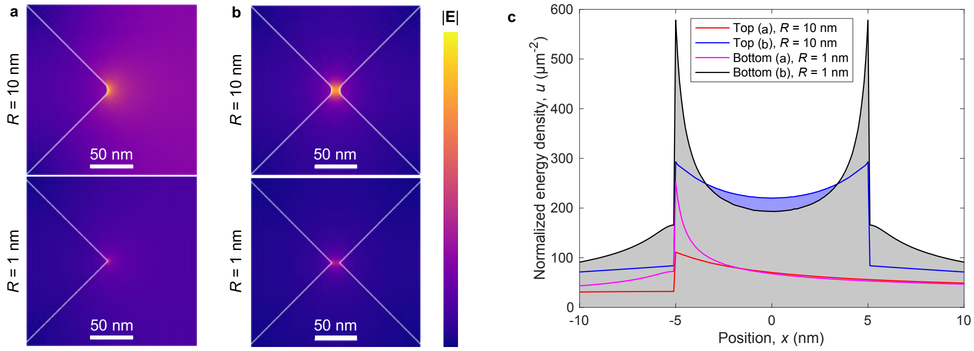

Figure 5.3. Lightning-rod versus bulk confinement. a, Lightning-rods for $R = 10\,\text{nm}$ ($R = 1\,\text{nm}$) in top (bottom), and **b**, corresponding bowtie, both with $g = 10\,\text{nm}$. It can be observed that the field spikes at the edges in the case where $R \ll g$. **c**, Line-scans along the center showing how the field spikes at the interface when $R < g$. Interestingly, when $R = g$ the field is more intense in the center (blue) – farther from surface effects. In both cases the center-values are local minima, not maxima. Calculations solved as 2D electrostatic problem. Adapted from Ref. [17].

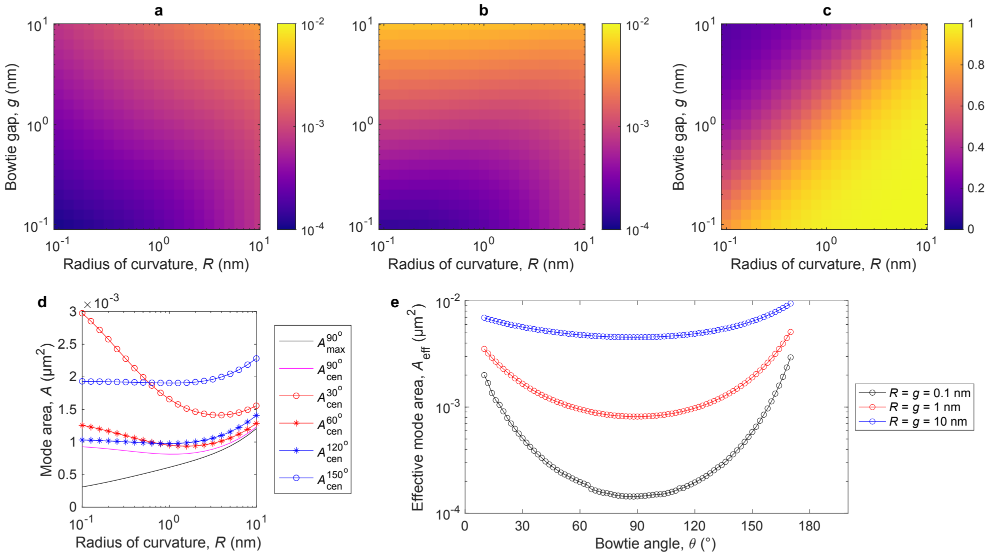

Figure 5.4. Optimization study of shape and form of dielectric nano-bowties. Mode-area minimum (field intensity maximum), $A_{\max}$ (**a**) and at the center, A_{cen}, between the tips (**b**) against the radius of curvature, R, and bowtie gap, g. **c**, Ratio, $A_{\max}/A_{\min}$, against R and g. **d**, Mode area in the center against radius of curvature for various bowtie angles, θ, as well as $A_{\max}$ for $\theta = 90°$. **e**, Sweep of bowtie angles for $R = g = \{0.1, 1, 10\}$ nm. **a**–**d** adapted from Ref. [17].

rate of decay also depends on the radius of curvature and a few nanometers away it is not possible to identify the tip nor its sharpness. The linescans through the bowtie show that the value in the center of the structure, is more intense for a less-sharp bowtie. This is interesting due to the symmetry it imposes [105] and the distance from surface-effects such as dephasing [105] and surface-states [123]. Moreover—and contrary to many conventional cavities with larger mode areas—the field enhancement in the center of a bowtie is a minimum, not a maximum, and optimizing the maximum in the structure will invariably seek to make the tips more sharp. This, in turn, will increase the mode area in the center, i.e., reduce the field strength.

To study this effect further, Fig. 5.4 shows a brute-force optimization study to map the optimal shape of a bowtie by sweeping the radius of curvature and the bowtie gap. Figure 5.4**a**, **b** and **c** maps $A(\mathbf{r}_0)$, $1/\max[1/A(\mathbf{r})]$ and $\max[1/A(\mathbf{r})]/A(\mathbf{r}_0)$, respectively, with $\mathbf{r}_0$ at the geometry center of the bowtie and the maximum consistently occurring at the tip apex. Figure 5.4**a** implies that reducing the gap always increases the mode area in the center, while this is not the case for a reduction in the radius of curvature, consistent with Fig. 5.3**c**. Figure 5.4**b** shows that reducing R always reduced the maximum mode area, and Fig. 5.4**c** shows a rapid deviation between the two values when $r < g$ (i.e., the color becomes less yellow/orange and more purple/blue). Figure 5.4**d** shows particular linescans with different angles of the bowtie. The value evaluated at the global maximum (black line) is always the smallest mode area. It deviates from the value evaluated in the center (purple line) when $R \to g$. Notably, the purple line, corresponding to $\theta = 90°$, has a minimum at $R = g$. Angles, $\theta \neq 90°$, consistently yield larger mode areas and Fig. 5.4**e** illustrates this explicitly by sweeping the bowtie angle for three values of $R = g$. To conclude, the optimal shape for an isolated bowtie is $\theta = 90°$, with $R = g$ – and then the gap should be as small as possible, limited by the fabrication for the experiment in mind. However, other figures of merit [147] or integrating with waveguides may change the optimal shape [139, 148], and in particular Ref. [148] provides a clear overview on the trade-offs between Q and V when optimizing the LDOS for different geometries and constraints.

5.4 Lightning-rod effects in nanocavities

The 2D study provided an understanding of the bowtie scaling. Next, the full 3D vectorial fields are solved to generalize the concepts of lightning-rod effects. Figure 5.5**a** shows a photonic crystal (PhC) cavity [114, 149] where a line-defect in the crystal is formed by removing three holes along a line, i.e., it is a so-called L3 cavity. The blue square highlights a defect (zoom-in in Fig. 5.5**b**) placed away from the center [17], and Fig. 5.5**c** (**d**) shows the amplitude of the electric field of the cavity eigenmode calculated with a full 3D FEM calculation in COMSOL Multiphysics without (with) a defect. Figure 5.5**d** further shows the field around the defect in the inset. The two calculations yield essentially identical modes, however, their profiles appear different due to the normalization of the colormap to the field at the defect in Fig. 5.5**d**. Figure 5.5**e** shows the resonant wavelength, λ_0, and quality factor, Q, without a defect and with a number of different defect radii of curvatures. Importantly, the defect far from the center has no effect on the cavity as it is only a minor perturbation. Similarly, Fig. 5.5**f** shows the mode volume in the center (blue circles) and at the defect (red circles); the value in the center is unaffected by the defect, while the maximum of the inverse mode volume would yield the value at the defect for small R. The diffraction limit is illustrated for clarity, to show that such a cavity can produce a mode volume well below it and by no means is bounded. However, this only occurs in a tiny volume at the surface, which for the purpose of Purcell enhancement likely will not have any real value unless an emitter is placed immediately next to it – and even then the presence of the surface should be taken into account. Of course, other applications such as sensing [150] may care about an enhanced field at the surface, see below. Figure 5.5**g** shows a linescan along y with the black line (blue shaded area) with (without) the defect. The modes are almost identical everywhere except around the defect, illustrating that it is only a minor perturbation. The motivation for the position of the defect is detailed in Appendix B.

In conclusion, bowties can cause tight spatial confinement of the electric field. They sensitively depend on the smallest feature size, and therefore, the optimal

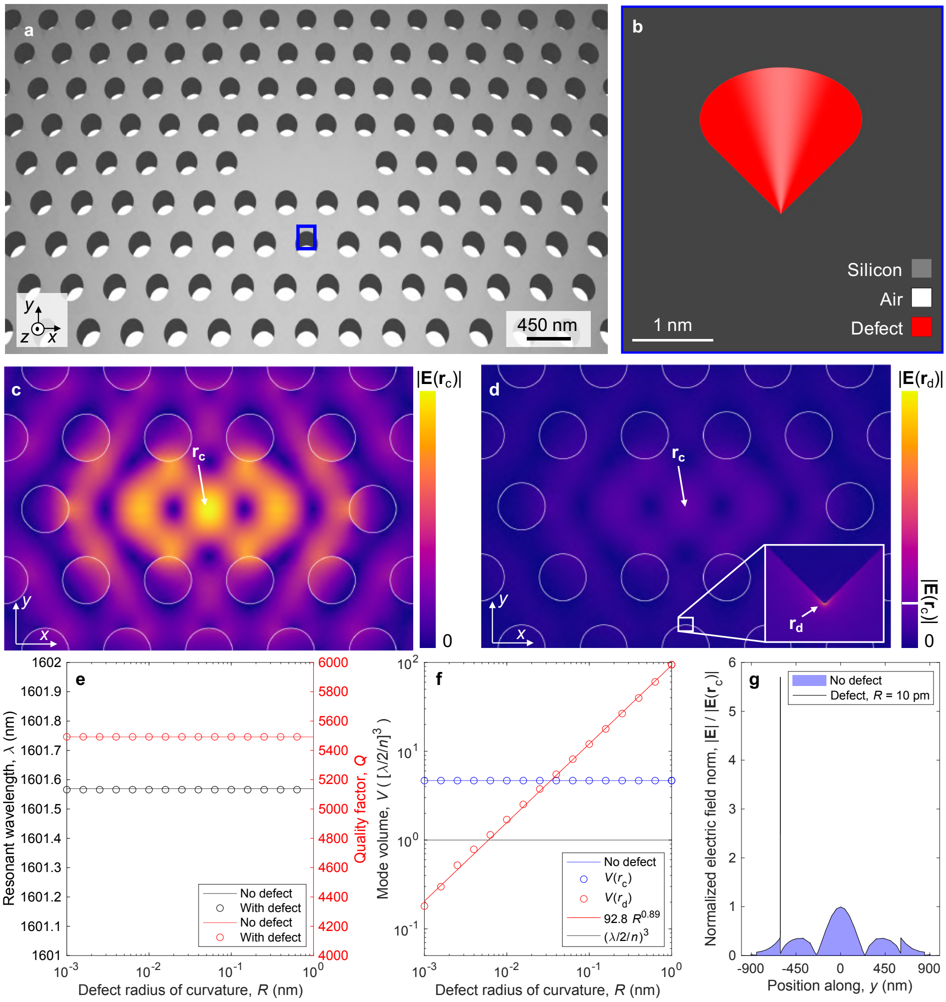

Figure 5.5. Mode volume below the diffraction limit in an L3 cavity due to lightning-rod effects at a cone far away from the cavity center. **a**, L3 cavity formed by removing 3 holes along a line in the photonic crystal. The blue square shows the position of a defect (solid protrusion at $\mathbf{r}_d = (y = -a\sqrt{3} - R, x = z = 0)$), enlarged in **b**. **c** (**d**), Mode calculated without (with) the defect, limited by a radius of curvature, $R = 10\,\mathrm{pm}$; they are essentially identical but appear different due to the colormap normalization to the field at $\mathbf{r}_d$. **e**, Resonant wavelength and quality factor with (without) a defect in circles (solid line) for multiple, R. The defect has no significant effect. **f**, Mode volume evaluated in the center, $V(\mathbf{r}_c)$, and at the defect tip, $V(\mathbf{r}_d)$. The red line is a power-law fit $V(\mathbf{r}_d, R)$ showing an almost linear dependence on R of the defect in this particular case. **g**, Norm of the electric field, $|\mathbf{E}(y, x = z = 0)|$. The black outline is for a defect with $R = 10\,\mathrm{pm}$ and the blue shaded area is the mode without a defect. They are identical everywhere except at $\mathbf{r}_d$ where the field has a local spike. Figure reproduced and caption adapted from Ref. [17].

bowtie-shape is intrinsically linked to the specific fabrication process used to realize them. The bowtie employs the field discontinuities of the boundary conditions and this is most efficiently obtained with two conical lightning-rods facing each other. Nevertheless, the sharpness of the tips must be taken into account explicitly or the results will simply reflect the numerical meshing used for the calculation. An example is to describe the finite sharpness using a radius of curvature, R, which enables well-behaved numerical convergence studies. Moreover, this analysis found that the optical bowtie shape for light-matter interaction in the center of the structure requires that $R \geq g$, with g the gap between the tips [17]. Sharper isolated tips on top of other cavities will work as a perturbation of the cavity mode. If interaction at the surfaces are desired, e.g., within sensing [150], such effects can be desirable – otherwise, it is indiscernible from disorder. In any case, the polarization of the cavity mode must be engineered to ensure that the lightning-rods cause a field enhancement where intended [125]. For example, outside the structure if sensing of a molecule is the application of interest.

CHAPTER 6

Experimental demonstration of sub-diffraction confinement in dielectrics

Multiple techniques exist to enhance the optical quality factor, including distributed Bragg reflection [104, 106, 114, 122, 151], total internal reflection [102], Fano resonances or bound states in the continuum [107] and topological confinement [152]. While order-of-magnitude improvements to the light-matter interaction have been achieved in this way, the other figure of merit, the mode volume, have so far not been experimentally demonstrated to achieve confinement of light below the so-called diffraction limit, $[\lambda/(2n)]^3$. This have been demonstrated using plasmons, but the absorption loss in metals limits the scope and applications [104, 140, 153].

Bowtie structures consist of two facing lightning-rods and have a long history – e.g., lightning-rods have received much attention in the context of the interaction between aeroplane tips and radio-frequency waves [125], and the same analysis is germane to dielectrics and metals. Bowtie structures have been fabricated in metals for a long time, made possible with lift-off techniques. However, lift-off of very small features tends to leave substantial line-edge roughness (LER), and it is further not trivial to deposit crystalline dielectrics, which instead must be grown and polished. Nevertheless, dielectric cavities with mode volumes deep below the diffraction limit have been proposed theoretically, starting with the pioneering work of the Lipson group with Robinson *et al.* [154] in 2005 using a narrow slot in a photonic crystal (PhC) nanobeam cavity following their development of the slot-mode waveguide in 2004 [155]. Next, they use an evolutionary algorithm in Gondarenko *et al.* [136] in 2006 to allow the bowtie-shape to emerge freely as the optimum – they further identify the bowtie shape and analyze this explicitly, and in 2008 they combine an engineered nanobeam cavity with a bowtie in the center in Gondarenko *et al.* [137]. Later work by other groups include the inverse design methods of Lu *et al.* [156] and Liang and Johnson [139]. And more recently the field has seen substantial attention [115, 132, 135]. However, it remains hard to fabricate the narrow bowtie structures generated with early attempts still achieving mode volumes on the order of the diffraction limit [146, 157].

This chapter reports on the experimental demonstration of a silicon nanocavity with a mode volume deep below the diffraction limit (which notably, is not a limit that applies to cavities and the reader is referred to Ch. 5 for a more complete discussion) reported in Ref. [16] and further details later developments using the hardmask-processes developed in Ch. 4. Recently, the field of dielectric cavities with small mode volumes have seen considerable interest, including theoretical contributions to understand the fundamental limits that govern the interaction between light and matter at the deep nanoscale. These topics are beyond the scope of this thesis but the reader is referred to Refs. [148, 158–160].

6.1 Maximizing light-matter interactions with fabrication-constrained topology optimization

Topology optimization [161] is a deterministic method for inverse design based on gradient descent [162]. Originally used in mechanical engineering but generic to problems from aeroplane wings [163] and suspension bridges [164] to solve nontrivial challenges nanophotonics [165–167]. It was originally developed at the Technical University of Denmark in the 1990's but is widely used today [139, 156, 168]. The process of using topology optimization is beyond the scope of this thesis and the interested reader is instead referred to the tutorials in Refs. [169, 170]. Topology optimization employs a material interpolation scheme [171] as well as filter functions [172] (such as the point-spread function of electron-beam lithography [73] as mentioned in Ch. 3). This enables taking into account manufacturing tolerances, i.e., fabrication constraints [173] ensuring realistic designs – and further ensuring that the optimizer does not exploit numerical artefacts (e.g., insufficient meshing) but rather designs only features limited by a radius of curvature (ROC) [16, 132, 173].

The interaction between light and matter is inherently weak, however, cavities enhance it. Different figures of merit exist [104, 115, 147], and here the decay rate of an emitter placed inside of a cavity is considered. The direct figure of merit is the local density of optical states (LDOS), and commonly the Purcell factor is discussed to compare across materials and platforms. The Purcell factor [130] describes the LDOS normalized to the density of states (DOS) for a homogenous material [105]. However, it is in fact faster to optimize the LDOS directly [139] by using a finite element method (FEM) [174] to solve Maxwell's equations in a finite volume of space, assuming time-harmonic field behavior, i.e., a finite element frequency-domain problem [16, 132]. The problem is solved by assuming a dipole emitter placed at the geometric center of the design domain, $\mathbf{r}_0$, the design-variables are linked out-of-plane, and 3-fold symmetry is applied to the computational domain [132].

The starting point is a state of the art nanofabrication process, and it is characterized by measuring the radii of curvatures for void, $R_v = 22\,\mathrm{nm}$ and solid, $R_s = 10\,\mathrm{nm}$ as shown in Fig. 6.1**a**. The radius of curvature is in principle independent of the feature size and can be measured consistently across most shapes. It is most conveniently measured using a triangle (positive or negative triangle in the mask to identify the void and solid ROC, respectively), and different sizes or corners yields the same results as shown in Fig. 6.1**b**. Moreover, previous theoretical work on strong light-matter interaction has found that the enhancement depends sensitively on the feature size close to the dipole, e.g., using bowtie structures. This insight originates from inverse design [132, 136, 139, 156] and has later been generalized and improved upon using insight and meticulous trial and error [115, 135, 137, 154]. Therefore, a

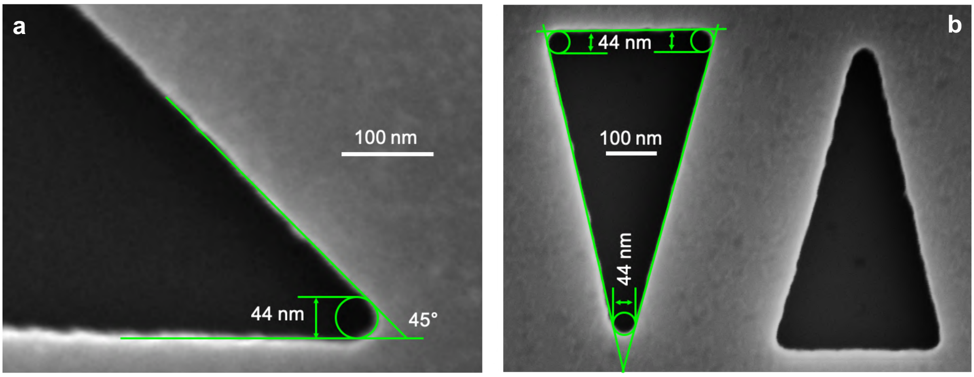

Figure 6.1. Measurement of the radius of curvature (ROC), R. a–b, The ROC for void features is measured for different angles to be $R = 22\,\mathrm{nm}$. Figure adapted from Ref. [16].

further critical radius of curvature, $r_c = 4\,\mathrm{nm}$, is identified as feasible through manual adjustments of the exposure mask and brute-force parameter sweeps of the fabricated structures; such schemes are not uncommon—albeit may be unsatisfying—to realize optimal structures within nanofabrication research (e.g., Refs. [65, 175]). This r_c is applied locally around the dipole, which is further required to be in a solid [16]. The thickness of the silicon-membrane in the SOI wafer is measured to be 240 nm, and the design is restricted to fit in a $(2\lambda)^2$ square region surrounded by air.

Figure 6.2**a** shows a render of the resulting cavity geometry [16], which is entirely emergent as an optimal distribution of material to maximize the LDOS given the fabrication constraints and the limited design domain. It is not possible to verify that it is a global optimum due to the amount of degrees of freedom [163, 164], but it is possible to compare with existing knowledge using physical intuition to understand what the optimizer has done with the various features. The outlines are extracted from the inverse design and the quasi-normal mode (QNM) [116] is calculated of the structure using a finite-element method (FEM, COMSOL Multiphysics). The norm of the electric field, $|\mathbf{E}|$, is projected onto the three symmetry-planes of the calculation [132], and Fig. 6.2**b** shows a zoom-in around the central feature to which the the light is primarily localized. This feature resembles a bowtie structure [136] with a tip-sharpness limited by the void radius of curvature, and notably $r_v > g$ so the structure achieves bulk confinement [17] consistent with the optimization targeting LDOS in the geometric center. The structure further features a number of circular (eliptical) rings, resembling a Bragg grating [106, 114] spaced by integer-multiples of the wavelength in the material. The electric field polarization is primarily along x, such that the material discontinuity around the bowtie causees a field enhancement [125, 126, 154, 155]. The small ”hairy” features are orthogonal, i.e., along y, and may be interpreted both to act as a sub-wavelength grating to smooth the material transition of the Bragg reflectors to avoid scattering (i.e., a reduction of the Q) and further to preferentially enhance

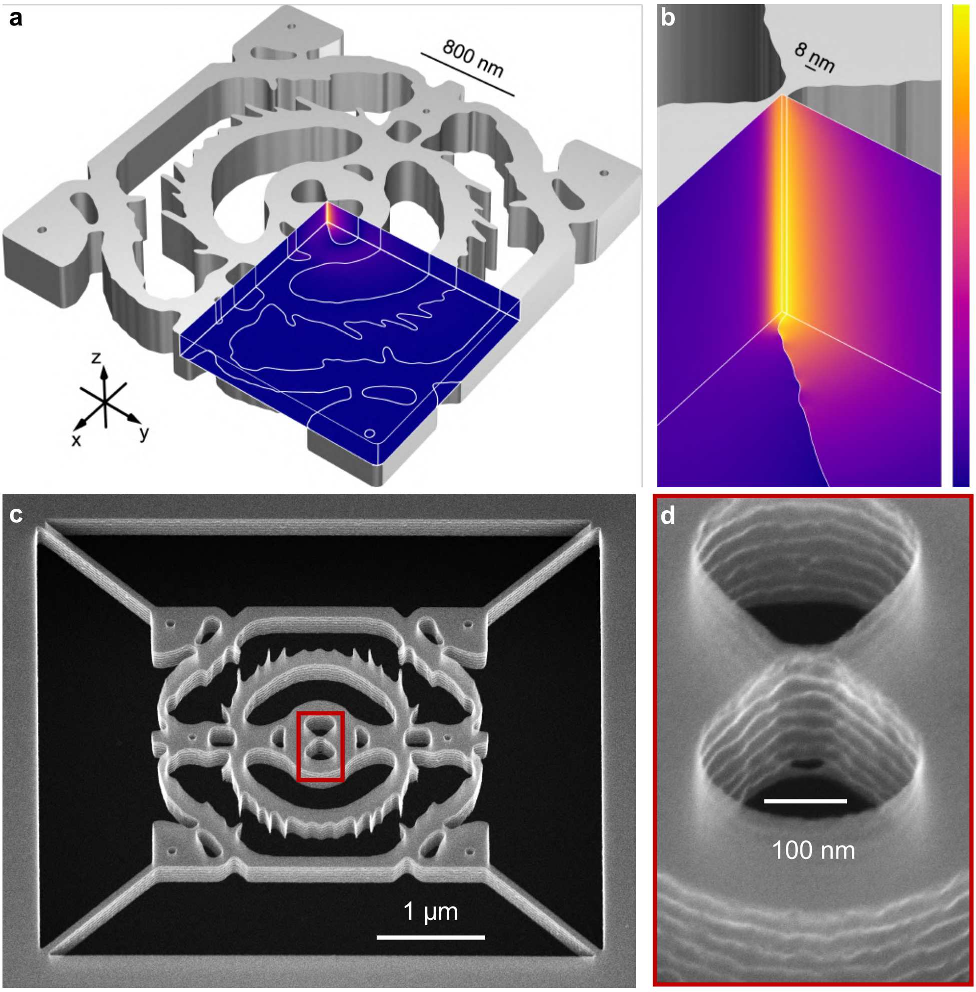

Figure 6.2. Dielectric bowtie cavity designed with fabrication-constrained topology-optimization. **a**, The inversely designed structure with the electric field, **E**, projected on the symmetry-planes used for the design. **b**, Zoom-in around the central 8 nm wide bowtie etched with an aspect-ratio of 30. The colorbar shows the normalized electric field amplitude. **c**, Scanning electron micrograph of a fabricated structure, which greatly resembles the design, and **d**, zoom-in of the bowtie. Figure adapted from Ref. [16].

polarization of the mode. It is in this context relevant to note that they only manifest for in-plane polarization (quasi–transverse electric (quasi-TE)), while the transverse magnetic mode results in circular rings [139, 159, 160]. During the design phase, and to avoid local minima, topology optimization considers a continuous gray-scale ε [171]. Here, the rings does not have a sharp transition while the bowtie immediately obtains a sharp transition [132, 139], further corroborating this intuition. In practice, surfaces are hard to characterize since a native oxide will form almost immediately – moreover, condensation of water will occur, forming surface states [123].

The resulting structure is clearly limited by the square design-domain and the choice of wavelength (in practice filtered close to a target center wavelength, $\lambda = 1550\,\text{nm}$, using the square of a Lorentzian to ensure convergence [139]), $\lambda_0 = 1551\,\text{nm}$. Increasing the domain results in better figures of merit in general [132]. However, a nontrivial trade-off between Q and V exists when optimizing LDOS directly [148], depending on the design constraints. Additionally, and as previously discussed, it is not desirable to increase Q for all applications [115], e.g., interaction with short pulses, and keeping a limited design domain forces the optimizer to improve the spatial confinement, here achieved through the bowtie structure. The cavity has a mode volume (evaluated using Eq. (5.27), cf. [16, 128, 129]), $V = (1/12)[\lambda/(2n)]^3$ and a calculated quality factor, $Q = 1120$, corresponding to a theoretical broadband (2 nm) Purcell factor of 8000. Figure 6.2**c** shows a tilted SEM image of a fabricated cavity with an inset of the narrow bowtie-feature in Fig. 6.2**d**. A 1 µm air-spacing is added around the cavity and mechanical supports are added to the corners. These are included in the numerical calculation of the post-processed design [16]. The fabricated structure resembles the design well, accurately reproducing both the bowtie but also all the other narrow, "hairy" features. From a fabrication point-of-view it is worth highlighting that all the small holes are etched as well. These have a high aspect-ratio in the void, which are hard to etch due to the microloading effects. The scallops resulting from the switch CORE-process are clearly visible in Fig. 6.2**d**, where some roughness can further be observed at the very top, likely caused by mask retraction/erosion of the softmask. Importantly, however, the bowtie is still substantially intact. A small sidewall angle, $\sim 1^\circ$, can be seen, which will be discussed later. This results in the scallops piercing through the bowtie in the bottom-most scallop.

It is efficient to compute the mode from the design pixels used during the topology optimization, but to preserve the fidelity of the design, the polygon-outline used for the render in Fig. 6.2**a** and **b** is extracted with a large number of points, forcing excessive meshing to ensure an accurate evaluation of the post-processed design [16]. Furthermore, trying to directly expose such an outline with electron-beam lithography is problematic due to the issues related to the required fracturing and shot-filling discussed in Ch. 3. Therefore, another outline is produced from the original topology optimized material distribution by projecting it on a 1 nm–grid, matching the shot-pitch to-be-used by the e-beam during the exposure. Then a Manhatten-outline (i.e., only 90° vertices allowed) is drawn around all features, which can be fractured deterministically and maintaining the design-symmetries in the exposure mask. This method avoids shot-filling errors but instead causes a large number of shapes. This can be a problem as the electron-beam is blanked between each shape, which is a slow (µs) process [64] that consequently can allow drift in the system to shear the structure. However, since the cavity is small and can be exposed within a second it is not a problem in this particular case. Nevertheless, to minimize this problem the mask is written in order, first of the original polygon-outlines of the final air-features and then of each slice within it, along y, i.e., minimizing the drift across the bowtie and the two sides of it is written within a few µs. A final point is that the e-beam writer uses a 4 µs subfield, and therefore stitches the mask 1.1 µm from the left and bottom sides in Fig. 6.2**c**; this does not cause any visible errors, however.

A recent study further optimized the design into smooth features [145] enabling a better-controlled meshing, as well as allows the features to extend beyond the original design domain, specifically the outer Bragg gratings, which clearly appears truncated in Fig. 6.2**a**. This confirms that the main features for the Purcell enhancement are the Bragg grating to enhance the temporal confinement and the bowtie to enhance the spatial confinement, while the small features only adds a minor contribution [132, 145]; in any case, since fabrication-tolerances are taken into account the features are realistic and contribution is real, so they should be included for optimality.

In conclusion, multiple version of the design exists, the gray-scale and differentiable material distribution obtained with topology optimization, a grid-style Manhattan-outline extracted for the nanofabrication process, a shape-optimized post-processed version with smooth curves that is ideal for numerical meshing and studies; and finally, the smooth outline used to visualize it. The first two can be merged by using the electron point-spread function as the filter in topology optimization and exposing the gray-scale mask by modulating the dose [73].

6.2 Fabrication of dielectric bowtie cavities

Figure 6.3**a** shows the grid-style Manhatten-outline of the electron-beam lithography mask where the black (air) is exposed. In acknowledging that the central bowtie feature is critical, it was allowed to be smaller than the generic radii of curvatures, which further requires manual modifications of the masks, specifically using the principles of over-dose–under-size (ODUS), see Ch. 3 for further discussions. The patterns are exposed with an area-dose to clear, $D = 300\,\mu\mathrm{C\,cm^{-2}}$, i.e., a $\sim 10\,\%$ overexposure. Then the mask-outline is retracted by not exposing the air-features–pixels inside a radial distance given by the local-mask correction (LMC) contours. Figure 6.3**b**–**i** shows the resulting top-view SEM images resulting from this exposure – and it can be seen that without the LMC the bowtie is etched through but for sufficient LMC it remains, corroborating this approach.

Figure 6.4**a** shows a global geometry-tuning in which the outline is grown or shrunk in 2 nm steps, while corners are preserved and overlapping polygons only are exposed once. This systematic variation of the outline enables a systematic evaluation of the realized dimensions from the frequency shift [16, 145]. The retraction from

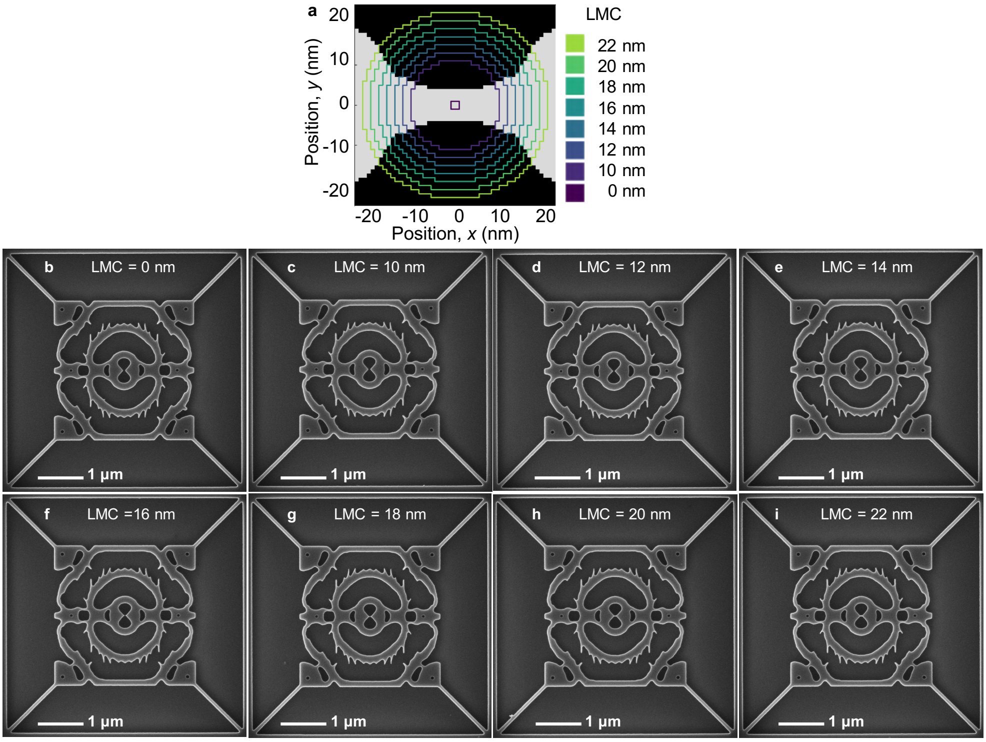

Figure 6.3. Local mask-corrections (LMCs) to resolve critical features beyond the general radii of curvature. a, The mask is defined by exposing the air-features (black) in positive-tone CSAR and subsequently etching through the openings, leaving the silicon (gray). The 8 outlines show LMCs where the black parts inside a given contour are not exposed, thereby implementing a manual under-sizing of the mask around the critical features. **b**–**i**, Corresponding top-view scanning electron micrographs etching in silicon—but not yet underetched—for the 8 LMCs, it can be seen that the structures remain unchanged except around the bowtie, which is etched away for the low LMCs and remains for the larger LMCs. Figure reproduced from Ref. [16].

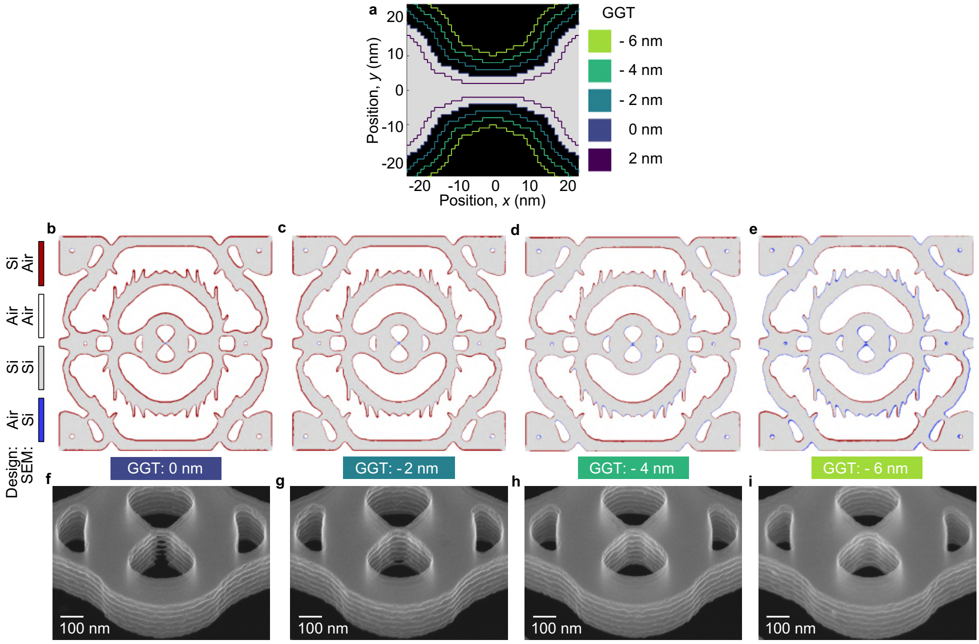

Figure 6.4. Global geometry-tunings (GGTs) to systematically adjust the entire mask dimensions. a, The mask (black) is exposed and the silicon (gray) is not. By shifting the contour of the mask across the entire geometry the size of the cavity can be tuned systematically and without introducing new shot-filling errors. **b**–**e**, Top-view scanning electron micrographs (SEMs) binarized by a gray-scale threshold and subtracted from the unchanged (binary) input mask pixel-for-pixel to show correct pixels in air/solid (gray/white) as well as overexposed (underexposed) pixels in red (blue) for four values of GGT. The result becomes less red along the outline—and even blue—for more negative GGT, i.e., by undersizing the exposure mask the resulting features becomes less over-exposed consistent with the over-dose–under-size (ODUS) principles. The SEMs are scaled and rotated to fit the centroids of the 4 holes in the corners. **f**–**i**, Tilted SEMs showing that top-view microscopy alone is insufficient to probe nanometer-scale dimensions in the presense of a sidewall angle; The bowtie in **b** appears too large, whereas **f** reveals that this is an SEM-artefact where edges are brighter (blooming). Figure reproduced from Ref. [16].

the blue print combined with the overexposure serves as a global ODUS-correction. Figure 6.4**b**–**e** shows the difference between a binarized top-view SEM image re-scaled to overlap with the mask by forcing the 4 corner-holes to overlap. It can be seen that the amount of red (i.e., overexposed silicon) is reduced along the entire contour with increased mask retraction. However, the main contribution to the frequency-shift comes from the bowtie [145].

Figure 6.4**f**–**i** shows corresponding tilted SEM images of the bowties where it can be seen that even though the bowties appeared to be well-resolved in the top-view inspection, they may not be etched all the way down. The SEM is an indirect measurement where an electron beam is directed towards a spot and the scattered electrons are collected during the same time-bin, i.e., features scattering more electrons will be brighter. For high-voltage SEM (i.e., $\geq 10\,\mathrm{kV}$) the incident electrons will propagate deep into silicon. Thus, the scattered low-energy electrons may not have enough energy to come back out and be detected, i.e., a very thin (partially etched) bowtie with scallops will very efficiently scatter electrons directed close to it, causing a wide region around it to brighten in the top-view inspection. This effect is called blooming. Low-voltage SEM can be used to reduce this effect, but this sacrifices penetration-depth of the imaging as well as a drop in depth-of-focus and a larger spot-size of the electron-beam, i.e., the measurement becomes more blurry. Finally, an SEM scale bar is only approximate [16] – it both depends on focus but typically it also takes tens to hundreds of seconds to obtain a high-resolution image during which the stage will drift several nanometers, thereby shearing the image. However, the e-beam stage is far superior with nanometer-scale drift per hour, and the structures are further written much faster. For example, the electron-beam lithography system employs a titanium sample-holder, which has a much lower thermal expansion coefficient compared to aluminium, and employs a laser-interferometer to compensate stage-drift by deflecting the beam accordingly. Nevertheless, it takes up to 6 h for the drift due to thermal effects to settle. There is also a key difference between chips and wafers due to the sample-holder configuration. Wafers are loaded in tightly-fitting slots, so when they expand they tend to bend out-out-plane, therefore changing the focus. Instead, chips are clamped onto a slit-opening and can therefore expand freely in-plane – they experience a shearing to the patterns in-plane. The most accurate scale is not a particular width of a feature since the fabrication can change this, but rather the distance between the centroid of far-apart features – a key reason to investigate gratings when doing process optimization as in Part I. Moreover, by scanning the SEM line-by-line multiple times it is possible to observe the direction of the drift, which will normally be caused by a combination of systematic effects, e.g., thermal expansion that stabilizes over time and random effects such as mechanical noise due to the environment. By rotating the scan-direction at which the SEM acquires the image and by averaging multiple images it is possible to compensate (at least in part) these two effects, respectively. Lastly, dynamic effects of SEM-imaging are important to keep in mind, since electrons charging up the sample surface will deflect incoming electrons thereby causing that pixel to be brighter. These considerations are the motivation for the re-scaling of the SEM images before comparing to the mask in Fig. 6.4**f**–**i**, in any case leaving the sample in the SEM-chamber for an hour or two before imaging can substantially improve the quality by reducing the drift. Furthermore, if images are taken in a multi-user facility it can be advantageous to take images in off-peak hours. SEM imaging in industry and technology imaging known patterns for, e.g., quality control can scan much faster to reduce these effects and errors, and then evaluate the lower-resolution images directly. This is in stark contrast to SEM-images commonly encountered in the scientific literature on applications.

Figure 6.5**a** (**b**) shows the electric energy density, $\varepsilon(\mathbf{r})|\mathbf{E}^2(\mathbf{r})|$, in a cross-section view of bowtie with a vertical (1° angled sidewall) illustrating that the side-wall angle does not create a lightning-rod effect, nor does it substantially affect the mode volume in the center of the structure. Figure 6.5**c** shows the calculated mode volume for all the structures, indicating a linear dependence [16]—further corroborated by [145]—and Fig. 6.5**d** (**e**) shows out-of-plane linescans of the mode volume through the centers of the vertical (angled) bowtie indicating that the volume in the center remains much lower than any previous experiment even for much wider gaps.

6.3 Optical characterization of the far- and near-field

Six nominally identical copies of the bowtie structures are fabricated and their optical properties are characterized first in the far-field using confocal cross-polarized microscopy (using optical setup 1 laid out in Appendix C). Here, a super-continuum pulsed laser is focused on the structure with linearly polarization (rotated 45° with respect to the cavity-polarization along x) and the light leaking from the cavity is collected with an orthogonal polarization (i.e., $-45°$ rotated) to suppress reflections. Figure 6.6**a** shows a a broadband spectrum of cavity 5 with GGT, $\delta = -6\,\text{nm}$, which shows a wide peak centrally and the on-set of two peaks at 1200 nm and 1700 nm. These peaks are at the limit of the optical spectrum analyzer (OSA). This results from a standing wave across the air-gap formed by the etched-away buried oxide under the cavity, i.e., a 3 µm gap. The peak-to-peak distance is called the free-spectral range (FSR),

$$\Delta\lambda = \frac{\lambda_0^2}{2nL}, \tag{6.1}$$

where λ_0 is the center of a peak, n is the refractive index of the cavity medium (i.e., $n = 1$ for air here) and L is the length of the cavity. For a $L = 3\,\mu\text{m}$ cavity around $\lambda_0 = 1450\,\text{nm}$, $\Delta\lambda = 350\,\text{nm}$, which corresponds well with the observation. Due to the interaction with the broad background mode, the cavity-mode of interest manifests as a Fano-resonance [176],

$$F(\omega) = A_0(\omega) + F_0\,\frac{[q + 2(\omega - \omega_0)/\Gamma]^2}{1 + [2(\omega - \omega_0)/\Gamma]^2}\ , \tag{6.2}$$

with $A_0(\omega)$ a linear function representing the background signal of the low-Q mode, q measures the relative amplitudes between them and F_0 is a constant scaling-factor,

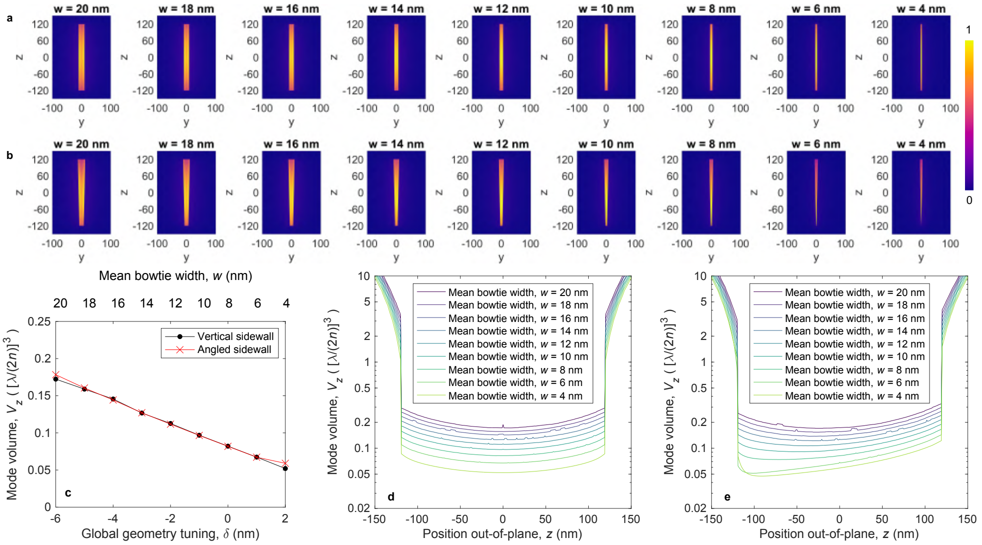

Figure 6.5. Numerical study of the effect of a sidewall angle. a (**b**), Cross-section view of the bowtie calculated with a finite element method for the entire geometry with a vertical (angled) side-wall. **c**, Mode volume, V, at the geometric center calculated for a range of global geometry-tunings (GGT), δ, for both angled and vertical sidewalls; the variations are small and linear. Deviations from linear is due to the change in physical volume of the bowtie not being linear for the angled side-wall when they co-incide. **d** (**e**) Mode volume, V, for vertical (angled) sidewall as a function of position along height of the cavity (along z). In all cases it remains well below the diffraction limit, and the precise value depends only weakly on the precise dimensions. The field is substantially less confined above and outside the structure where the s-SNOM measurement probes. Figure reproduced from Ref. [16].

i.e., the cavity is the sharp modulation highlighted by the red box, which shows a 40 nm band around the mode.

Figure 6.6**b**–**d** shows the 40 nm band around the main cavity modes of the 18 sepctra corresponding to the 6 nominal copies for $\delta = \{-2\,\text{nm}, -4\,\text{nm}, -6\,\text{nm}\}$, respectively. Each copy is offset by 0.25 nW nm^{-1} and colored consistently, i.e., one can trace the background mode across the figures. The red lines show a fit to Eq. (6.2) and the extracted Q and λ_0 are displayed in Fig. 6.6**e** for the mean and standard deviation across the 6 copies. The measured spectral shifts $\leq \Delta\lambda/10$, which implies that on average the cavities are identical to within $|\delta| \leq 0.2$ nm [16]. Moreover, and due to the comparatively low Q, the cavities are reproducible enough for their resonances to overlap, which is important for many applications relying on integration with emitters [105].

To investigate the spatial localization of the mode, the near-field is probed using scattering-type scanning near-field optical microscopy (s-SNOM) [16]. A monochromatic s-polarized laser (Santec TSL-710, $\lambda = 1480$–1640 nm) is split with a beam-

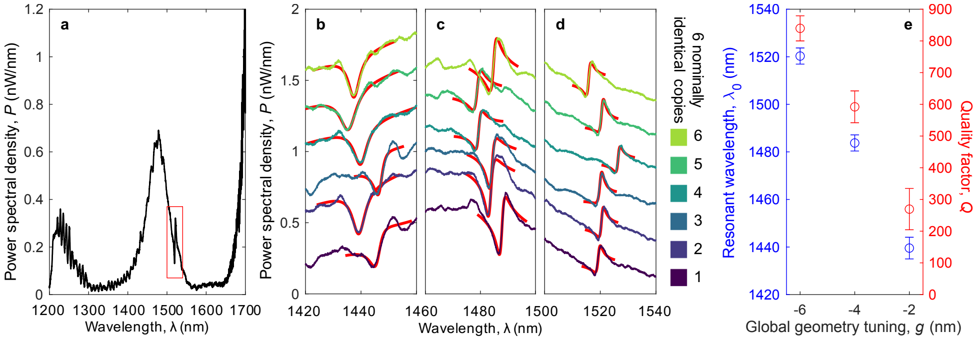

Figure 6.6. Optical characterization by confocal cross-polarized spectroscopy of the far-field. **a**, Broadband spectrum showing the cavity as a Fano-resonance on top of the standing wave between the device-layer and the bulk silicon (i.e., in the 3 µm air-gap defined by the underetched buried oxide). **b**–**d**, Characterization of 3 sets of each 6 nominally identical copies with different global geomtry-tuning (GGT); the background can be traced between the measurements corroborating that it is a feature independent of the cavity, and the high-Q modes manifests close to each other spectrally (relative to the linewidth). The red lines show fits to a Fano-lineshape with the mean and standard deviation of the extracted resonant wavelengths, λ_0, and quality factors, Q, shown in **e** for each value of GGT. The broadband spectrum in **a** corresponds to cavity 5 with GGT -6 nm (i.e., second from the top in **d**). Figure reproduced from Ref. [16].

splitter and one part is focused on an atomic-force microscope (AFM) silicon-tip (nominal radius of curvature 10 nm) in tapping mode ($f_0 = 280$ kHz, 60 nm amplitude) using a curved mirror. The sample is moved under the tapping tip and the AFM-signal is measured and demodulating at $4f_0$ with a lock-in amplifier yields the signal when the tip is ~ 5 nm away the silicon surface. This allows mapping the spatial structure of the cavity shown in Fig. 6.7**a**. The s-polarized light excites the cavity mode and the tip acts as a new loss-channel scattering the light to the far-field. The scattered light is measured with a pseudo-heterodyne interferometric scheme, which strongly suppresses interference with the far-field background [177]. Both excitation and scattering depends on the tip causing the amplitude of the electric field measured in the far field to depend on the square of the amplitude of the QNM at the position of the tip (or strictly, the integral of the QNM, $\mathbf{f}$, over the volume of the tip), i.e., $|E_{\text{scat}}(\mathbf{r}_{\text{tip}}, \omega)| \propto |(\mathbf{f}(\mathbf{r}_{\text{tip}}))^2|/[(\omega - \omega_0)^2 + \gamma^2]$, which further imply a Lorentzian lineshape of the amplitude rather than the intensity as is often assumed in optical experiments. Careful QNM-based calculations (unpublished as of the time of writing) corroborates this physical argumentation.

By keeping the sample still—and instead sweeping the laser wavelength—the spectrum is measured and the Lorentzian lineshape is confirmed as shown in Fig. 6.7**b**. From a fit the central wavelength, $\lambda_0 = (1489.4 \pm 0.1)$ nm, and an optical quality factor, $Q_{\text{NF}} = 370 \pm 40$. This reduction in Q from the far-field is due to the loading by the tip, which acts as a loss-channel. The rapid oscillations in the measurements cor-

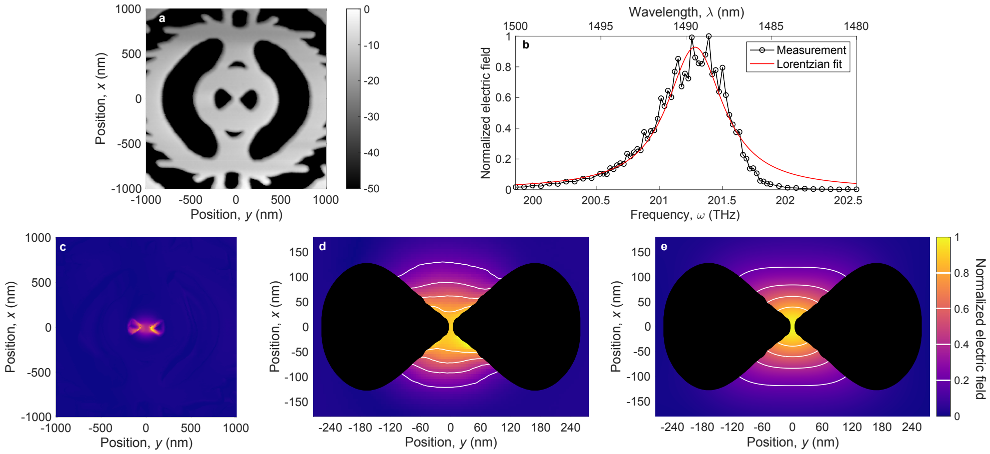

Figure 6.7. Scattering-type scanning near-field optical microscopy (s-SNOM). A continuous wave (CW) laser is focused on an oscillating atomic-force microscope (AFM) tip and the cavity is moved underneath it, thereby modulating the amplitude of the signal scattered to the far-field by the square of the quasi-normal mode (QNM) at the position of the tip. **a**, The AFM-trace of the scan. **b**, The frequency of the CW laser is swept while the tip is kept at a fixed-position, resulting in a Lorentzian modulation of the scattered amplitude and the quality factor and resonant wavelength is extracted. **c**, On-resonance amplitude of the electric field scattered to the far-field (i.e., a spatial map of the square of the QNM amplitude). The measurement is unclear when the AFM-tip falls into the holes in the cavity, and **d** shows the measurement only on top of the surface of the structure, where it can be more clearly interpreted. **e**, Convolution between the calculated square of the QNM and the instrument-response function, $f(\sigma)$, taken as a Gaussian. Figure reproduced from Ref. [16].

responds to a standing wave across the handle-wafer, i.e., with $n = 3.48$, $L = 675\,\mu\text{m}$ and $\lambda_0 = 1489.4\,\text{nm}$ the FSR is $\Delta\lambda = 0.47\,\text{nm}$. This is not seen in the far-field measurements, since a 2 nm wide slit is used with the OSA, therefore averaging these oscillations out. Importantly, the signal-to-noise ratio when the laser is off-resonance is excellent, clearly allowing the measurement of the mode. Figure 6.7**c** shows the spatial structure of the square of the mode when the laser is set to its resonance wavelength. This corroborates the field-localization to around the bowtie – but notably the second lope of the field around the first Bragg grating, which is visible in Fig. 6.2**a**, cannot be seen in the near-field. This observation was an additional motivation for the more rigorous QNM-mode investigation carried out to justify that the scattered field amplitude has a the square dependence of the cavity-QNM. Furthermore, the tip dips into the holes causing strong scattering so to compare the measured field structure to theory only the parts where the tip is above the silicon is included. Figure 6.7**d** shows a slow-scan ($(5\,\text{nm})^2$ pixels) with the holes blacked out and Fig. 6.7**e** shows the calculated mode profile convoluted with an instrument-response function,

$f(\sigma)$, assumed to take a Gaussian form [16].

The Bhattacharyya coefficient [178], $t = \sum \sqrt{|\mathbf{E}_s| \cdot (|\mathbf{E}_c|^2 * f(\sigma))}$, denotes the overlap between the normalized maps for the scattered and calculated fields. The maximum overlap, $t_{\delta=-4\,\mathrm{nm}} = 0.984$ and $t_{\delta=-6\,\mathrm{nm}} = 0.991$ for two different bowtie-dimensions [16] both occurs for $\sigma = 37\,\mathrm{nm}$, corroborating that this indeed is germane to the instrument and not the cavity. This number corresponds to a FWHM of $2\sqrt{2\log(2)}\sigma = 87\,\mathrm{nm}$, which is much larger than the mode but notably also substantially below half of the wavelength, $\lambda/(2n_{\mathrm{Si}}) \sim 200\,\mathrm{nm}$, which would correspond to the diffraction limit. It is difficult to measure such well-confined modes directly [179], and future work might rather investigate other physics, e.g., optical non-linearities in waveguide-coupled bowtie-structures [115, 148, 157]. To verify that the measured mode structure is limited by the resolution of the present s-SNOM configuration Fig. 6.8**a**–**b** shows the near-field measurements of the two structures measured, which appears different at first due to the normalization to the maximum, which occurs inside the holes. Figure 6.8**c**–**d** shows the same measurements but only considering the field above the surface, and the Bhattacharyya coefficient by overlapping these two measurements with each other is 99.1 %. Figure 6.8**e**–**f** shows corresponding high-resolution tilted SEM images of the structures where the bowties have a visibly different size, consistent with the $\sim 40\,\mathrm{nm}$ spectral shift of the optical resonance in both near- and far-field characterization. This difference corresponds to a $\sim 4\,\mathrm{nm}$ change in the mean bowtie width, consistent with the geometry-tuning and the dimensions extracted by SEM [16]. This change would cause the mode volume to increase by $\sim 50\,\%$ (cf. Fig. 6.5**c**), but almost exactly the same data is obtained.

6.4 Outlook

Resonant confinement is among the most important and studied applications in all of nanophotonics, critical to phenomena ranging from light-matter interactions to sensing and information processing. This chapter presented recent experiments to confine light within nanometer-scale dielectric bowtie cavities (DBCs) reported in Ref. [16]. This is achieved by intertwining design and fabricating directly using fabrication-constrained topology optimization to directly optimize the local density of optical states inside the geometric center of a silicon slab. This direct integration is demonstrated for the first time across any field of research or engineering using fabrication-tolerances measured for the state-of-the-art manufacturing process used to later fabricate the structures. The structures are fabricated, and scanning electron microscopy is used to qualitatively confirm that they are accurately reproduced. Furthermore, the structures are characterized quantitatively using far-field characterization which is in excellent agreement with the quasi-normal mode calculations of the cavity. This agreement may not be totally surprising—yet it is a remarkable demonstration that confirms the strategy—and holds further promise for strategies to integrate theory, technology and applications as directly as possible [73, 74]. The

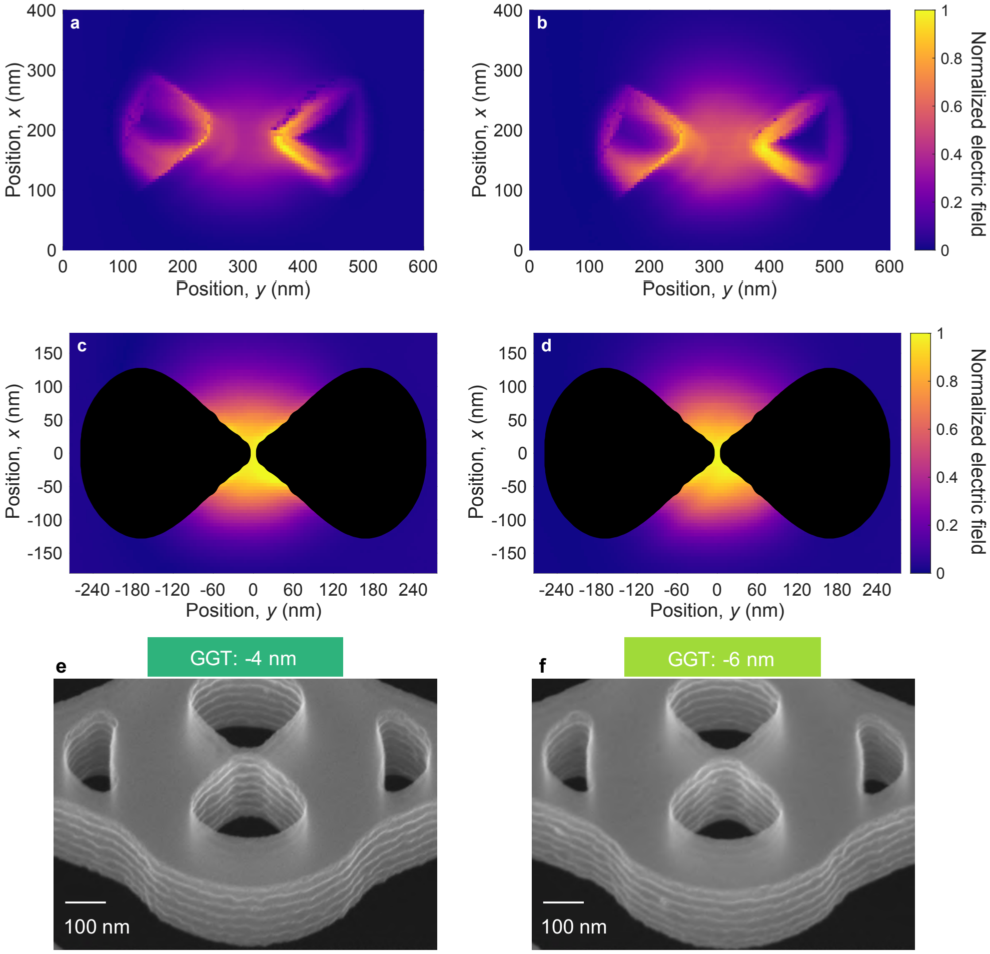

Figure 6.8. Comparison of near-field results for different bowtie dimensions. a (**b**), Scattering-type scanning near-field microscopy (s-SNOM) measurements to map the square of the electric field amplitude for global geometry-tuning (GGT) −4 nm (−6 nm). They appear different due to the normalization to the maximum, which occurs in the air-holes. **c**–**d**, Air-holes blocked out and the signal is shown above the silicon surface; the maps looks identical with an overlap of 99.1 %. **e**–**f**, Tilted scanning electron micrographs of the two specific bowties measured in **a**–**d**. Figure reproduced from Ref. [16].

near-field measurements provides an experimentally compelling demonstration of, for the first time, extreme dielectric confinement well below the diffraction limit in a dielectric bowtie nanocavity and it will be a daunting challenge for future research to accurately map the mode structure of such nanometer-scale structures [179].

So far, all structures reported in the chapter have been fabricated with the softmask-version of the CORE process reported in Sec. 4.2, resulting in an unprecedented spatial resolution and high aspect-ratio nanostructure, albeit with substantial surface roughness caused by the scattering. By exposing the very same electron-beam mask used in Ref. [16] but instead with a slightly lower dose to clear, $D = 290\,\mu\mathrm{C\,cm^{-2}}$, due to the hardmask stack, and subsequently fabricating it with the stable process developed in Sec. 4.4, scallop-free bowties nanocavities with narrow voids and solids is fabricated and shown in Fig. 6.9**a** and **b**. Specifically, the solid bowtie (Fig. 6.9**a**) results from the mask without any local mask-correction (LMC) and $\delta = -2\,\mathrm{nm}$, while the void bowtie ((Fig. 6.9**b**)) results from the first LMC (i.e., 10 nm) but no global geometry-tuning. Both structures are fabricated and achieves 6 nm bowtie gaps, which implies a critical radius of curvature, $r_c = 3\,\mathrm{nm}$, and further, the narrow slots etched for the optomechanical structures implies a void radius of curvature, $r_v \leq 10\,\mathrm{nm}$. This is promising for future work on nanometer-scale photon confinement with dielectric bowtie cavities to achieve unlocking new experimental regimes throughout most areas of semiconductor nanotechnology [180], including nanophotonics [110], cavity optomechanics [102], nanoelectromechanics [39], optical non-linearities without emitters and quantum photonics [105]; such as broadband Purcell-enhancement with nascent emitters in silicon [181, 182].

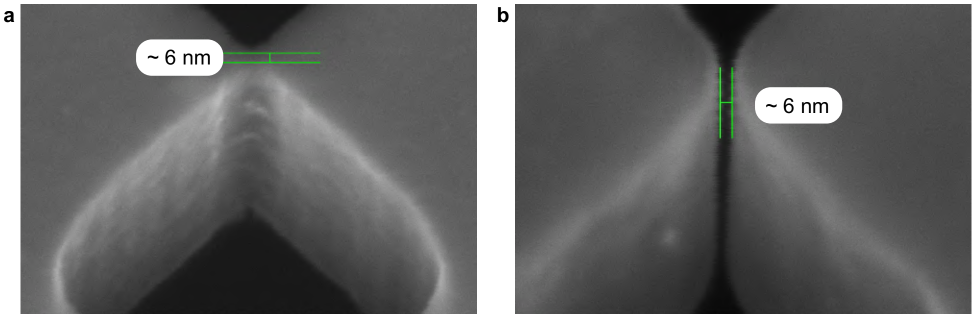

Figure 6.9. Fabrication of dielectric bowtie cavity with the hardmask process. **a**–**b**, A solid or void bowtie gap of 6 nm can be fabricated next to each other on the same chip, using the same fine-tuned pressure-controlled etching process developed in Ch. 4. To achieve it the LMC is simply adjusting to open the solid bowtie into a void one, i.e., exactly the same exposure mask is used for the electron-beam lithography.

CHAPTER 7

Phononics and optomechanics

Optomechanics (OM) has a wide range of applications and has seen substantial research interest, from fundamental physics to photonic devices, e.g., using cavities and nanostructures to enhance and engineer the interactions [102, 183–185]. The vacuum optomechanical coupling, g_0, determines the strength of the OM interaction in a cavity-OM system [186]. This chapter summarizes the findings on hypersonic phononics and gigahertz cavity optomechanics (OM) reported across 4 manuscripts [18–21] as well as during an external stay at the Phononic and Photonic Nanostructures group led by Prof. Clivia M. Sotomayor Torres at the Catalan Institute of Nanoscience and Nanotechnology (ICN2, UAB). The author of this thesis contributed primarily to the four manuscripts through nanofabrication of the structures characterized. Highlights from the papers are presented to logically build the foundation motivating the design, fabrication, and characterization of the engineered mechanical-optical-mechanical (MOM) systems investigated during the external stay – some recent results of which are presented in this chapter mainly focusing on the platform. In the context of this chapter, the author wish to highlight explicitly supervision by and insightful discussions with Guillermo Arregui, Guilhem Madiot and Omar Florez.

The structure of this chapter is as follows: First, the shamrock phononic crystal (PnC) is introduced, which opens a mechanical band gap with wide geometric tunability in the gigahertz [18]. Second, the shamrock crystal is flipped forming a line-defect (W1) multimode PnC waveguide (PnC-WG) in the interface [18]. Third, the slotted photonic crystal (sPhC) is introduced, which enables strong OM coupling using Anderson-localized modes [19]. Fourth, a slotted PnC-WG (sPnC-WG)—based on the shamrock structure and terminated with a phonon-shield crystal—is investigated. It supports an Anderson-localized mode with strong optomechanical coupling enabling self-sustained mechanical oscillations in the gigahertz driven by radiation-pressure forces (i.e., phonon lasing) [20], and moreover, this same structure can interact with the MHz–Fabry-Pérot (MHz-FP) standing wave between the mirror-termination to form a phonon frequency-comb [21]. Finally, the best features of all these structures are combined in Sec. 7.3 to design a MOM system that is engineered—i.e., it relies on an intentional optical cavity mode rather than on spontaneously occurring Anderson-localized modes—by tapering the lattice pitch in a sPnC-WG. Moreover, the super–unit-cell is modified by exchanging the shamrock closest to the slot with a circle, which greatly improves the optical quality factor, thereby leading to substantially higher OM coupling to the two plates on either side of the slot. By systematically varying the hole-radius of one side it is possible to accurately tune the relative frequencies of the mechanical modes. Lastly, the engineered nature of the cavity enables further systematic studies of the tapered fiber-loop setup used [19].

7.1 Shamrocks to engineer a GHz band-gap

Figure 7.1**a**–**c** (**d**–**f**) shows top-view (tilted) SEM images of large fabricated phononic crystals using a shamrock in a triangular lattice [18]. The shamrock is shown schematically in the inset in Fig. 7.1**c** and its outline is composed from 3 circles of radius, r, offset and rotated in 120° steps along an outline, $f = 2r/\sqrt{3}$. The crystals shown in Fig. 7.1**a**–**c** are formed as a triangular lattice of periodicity, $a = \{220, 330, 440\}\,\mathrm{nm}$, and a fixed radius-to-pitch ratio ($r = 0.22a$), which controls the mechanics. The shamrock phononic crystal (PnC) structure defines a range of blocks with large masses connected through thin junctions with three thin necks [187]. The band gap is a range of mechanical frequencies that are not possible within the crystal. The periodicity of the mass of the blocks combined with the elasticity of the junction, i.e., the thickness of the neck, defines the frequency range of the band gap, and therefore, scaling the pitch changes the center frequency of the band gap [18].

From a fabrication point-of-view the shamrock is an easy structure, since it relies on features with large radii of curvature easing high-resolution lithography, and moreover, inherently will have a low aspect ratio making etching tolerances more relaxed. Therefore, the system can be scaled down to push its band gap well into the gigahertz (i.e., hypersonic) regime [18]. Previous two-dimensional phononic structures relied on snow-flakes [187–189] or square-like platforms with four necks [190]. They include sharp corners that must be rounded to the limit of the fabrication process [189], and further features high aspect-ratios that restricts their scalability. Here, the smallest pitch considered (Fig. 7.1**a**) is $a = 220\,\mathrm{nm}$ and it is chosen as the band gap is limited by a band edge at $\sim 12\,\mathrm{GHz}$ and a smaller crystal will no longer open a substantial band gap. This pitch corresponds to the radius, $r = 0.22a = 48.4\,\mathrm{nm}$, (vertices in the mask are rounded to integer-precision), which is much larger than the void radius of curvature of the fabrication process discussed in Ch. 6 and Ref. [16], $r_v = 22\,\mathrm{nm}$. Consequently, the shamrock crystal can readily be fabricated. Since the resolution requirements are relaxed, a thicker resist is used (180 nm) and more cycles (14) are used to etch the structures. This reduces the roughness, i.e., the scallop size (Ch. 4). The necks are several tens of nanometers and so well within the solid radius of curvature (Sec. 4.2), $r_s = 10\,\mathrm{nm}$.

By flipping the crystal around a line and offsetting it by $w = 184\,\mathrm{nm}$ two mechanical modes are defined within the band gap that moves along the defect, i.e., a multi-mode PhC waveguide (PnC-WG) is formed. Figure 7.1**g**–**i** shows dark-field optical microscope images of waveguides along x fabricated in the 220 nm thick device layer with various number of mirror unit-cells along y. None of these images are false-color and so the line-defect in the vertical center of each waveguide is clearly visible with dark-field microscopy directly and further, the color gradients are caused by the variation in dimensions for the larger structures due to insufficient proximity-effect

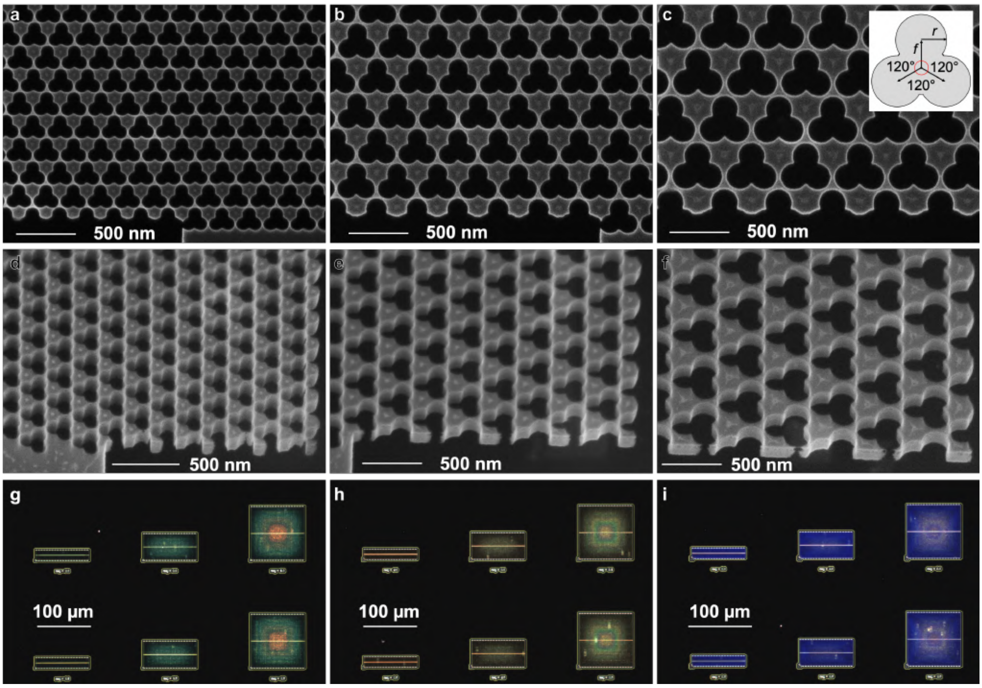

Figure 7.1. Phononic crystals with hypersonic band gaps. **a** (**b**–**c**) and **d**–**f**, Top-view and tilted-view scanning electron micrographs of large shamrock-structures that opens a mechanical band gap in the gigahertz tuned by the pitch, a = 220 nm, a = 330 nm and a = 440 nm for **a**–**c** and **d**–**f**, respectively. The inset in **c** shows a schematic of a shamrock unit-cell. **g**–**i**, Dark-field optical microscope image of phonon waveguides of different width and number of shield–unit cells, with a pitches corresponding to **a**–**c**. The color gradient is due to a feature-size variation caused by insufficient proximity-effect correction (PEC). Measurements on the structures are reported in Ref. [18].

correction (PEC), as indeed these membranes are large compared to the long-range scattering range β (see Ch. 3).

The mechanical bands are mapped using Brillouin light scattering (BLS) spectroscopy on 50-by-50 µm membranes where a laser is focused on the sample, which is rotated to expose the entire first Brillouin zone; due to the proximity errors the larger 100-by-100 µm crystals are disregarded. Moreover, BLS is used to confirm the existence of the two guided mechanical modes of the waveguide. These measurements are reported in Ref. [18].

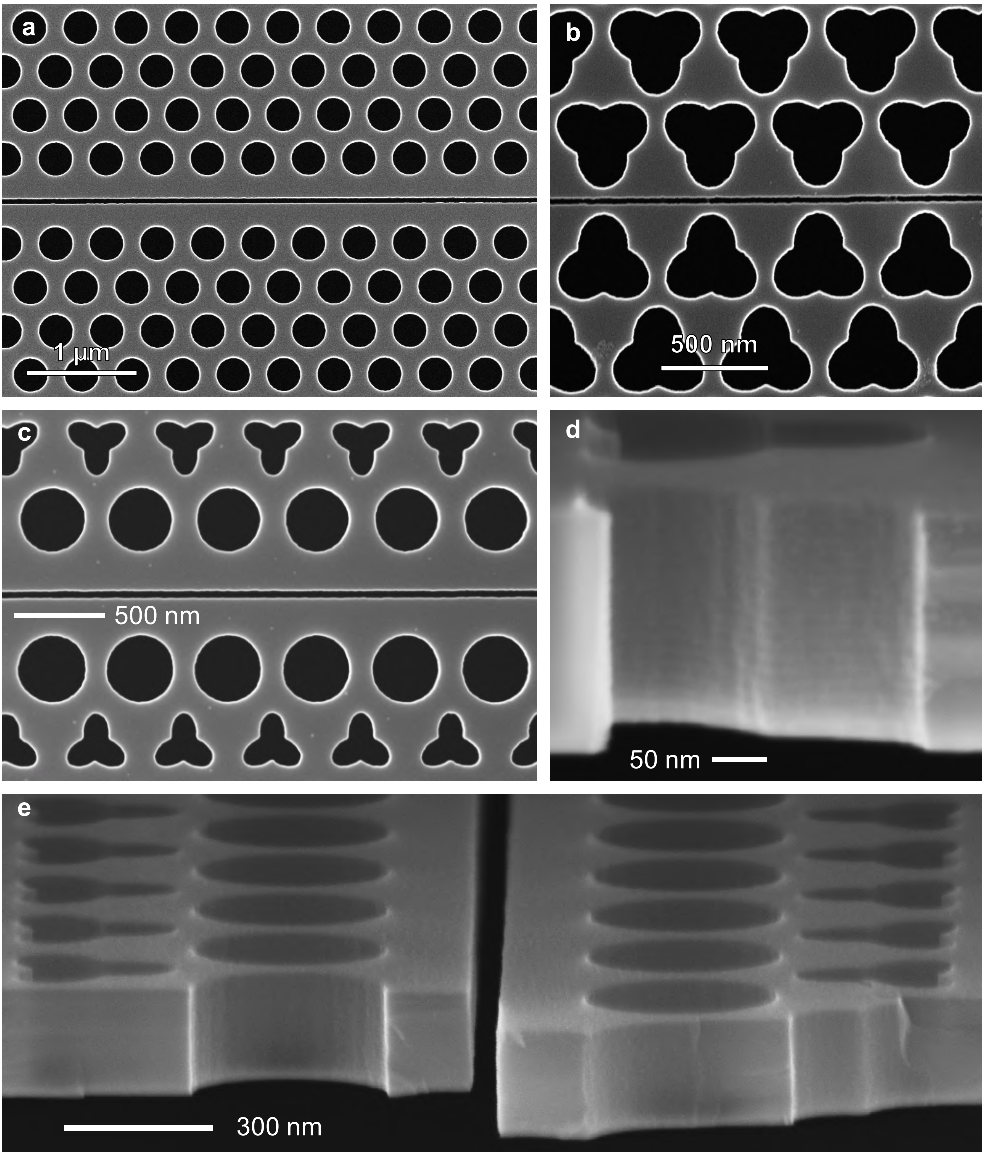

Figure 7.2. Development of optomechanical platforms. a (**b**), Slotted photonic (phononic) crystal waveguide [19] ([20, 21]) using circles (shamrocks [18]) to achieve high optical Q (shielding from mechanical modes leaking). **c**, Slotted mechanical-optical-mechanical (MOM) cavity where the first row of shamrocks is replaced with circles, improving the optical Q while keeping the mechanical shielding. The radius of the holes in the top-part is tuned to shift the mechanical resonance of that plate. **d**–**e**, Cross-section images of a single shamrock (**d**) and the MOM slotted interface (**e**).

7.2 Cavity optomechanics and phonon sources

The previous section demonstrated a phononic crystal that disallows the propagation of mechanical vibrations at certain frequencies as well as phonon waveguides, which can be engineered to route GHz-acoustic phonons. Such mechanical modes can be generated by a multitude of methods [191], e.g., by optomechanical coupling where a laser pumps the system and the optical fields drives mechanical modes. This effect is enhanced by a factor quantified as the vacuum optomechanical coupling [186], g_0, in addition to the previously introduced optical quality factor, Q, and mode volume, V. Figure 7.2**a** shows an SEM-image of a fabricated slotted [155] photonic crystal waveguide (sPhC-WG) reported in Ref. [19], which tightly confines the electric field and sensitively depends on the slot-width, s. For examples, any mechanical modes that are ”breathing”, i.e., mechanically deforms or modulates the slot, strongly couples to the optical field [192]. The surrounding photonic crystal protects the optical modes from in-plane leakage to the device-layer [106, 114] and light is coupled into the structure using a tapered fiber-loop [19, 193] directly in contact with it. The photonic crystal is engineered to achieve slow light which makes it more sensitive to disorder – creating so-called Anderson-localized modes [194–196], which are localized and can be excited at certain points along the waveguide by sliding the loop along it [19]. For example, one of these modes has a high optical quality factor, $Q = 5.31 \cdot 10^5$ leading to a strong vacuum optomechanical coupling, $g_0/(2\pi) = 228\,\text{kHz}$. This can drive self-sustained mechanical oscillations (i.e., phonon-lasing) at a mechanical frequency, $\Omega \gg 230\,\text{MHz}$. However, the photonic crystal does not support a mechanical band gap, and hence, the line-defect does not support any guided GHz mechanical modes. Instead, hypersonic mechanical vibrations disperse and fade away. These results are reported in Ref. [19].

Figure 7.2**b** shows an SEM image of a fabricated slotted PnC-WG where each end is terminated by a mechanical shield, i.e., by shifting the pitch and thereby the band gap. This structure enables exciting coherent GHz-phonons using Anderson-localized modes, i.e., phonon lasing around $\Omega = 6.8\,\text{GHz}$ with a vacuum optomechanical coupling, $g_0/(2\pi) = 135\,\text{kHz}$ is achieved, and these results are reported in Ref. [20]. Furthermore—and using the very same nanostructure—it is possible to coherently drive an in-plane membrane mode at a frequency, $\Omega_{\text{FP}} = 265\,\text{MHz}$, similarly to the OM-system in Fig. 7.2**a** and Ref. [19]. The mixing of these two tones leads to the formation of a mechanical frequency comb reported in Ref. [21]. However, the optical quality factor of the modes in these shamrock-systems are not very high ($Q = 18400$), leading to a weaker optomechanical coupling strength. To further improve the vacuum optomechanical coupling of the system for a hypersonic mode, a high optical Q is needed simultaneously with a GHz band gap with protected line-defect mode.

7.3 An engineered mechanical-optical-mechanical slotted system

The insight of the previously discussed systems is combined: The slot tightly localizes the electric field around it, while the mechanical modes extend farther into the crystal. Therefore, by replacing the first row of the crystal closest to the slot in a sPnC-WG with a circle, a reasonable and simultaneous protection for both optical and mechanical modes can be obtained to enhance g_0 for GHz phonons. Moreover, the PnC waveguide and shields works due to the differences in their pitches, and using a cubic interpolation-scheme between the waveguide and shield a cavity mode is engineered within the band gap. The structure is designed by Guillermo Arregui and Fig. 7.2**c** shows an SEM image of a fabricated device, which is characterized by the author of this thesis and in collaboration with Guilhem Madiot and Guillermo Arregui. Figure 7.2**d** and **e** shows cross-section images of a shamrock and the hybrid structure, respectively, illustrating the vertical sidewalls and low levels of roughness. The cross-section structures are fabricated using a higher current during the electron-beam lithography step, $I = 0.8\,\text{nA}$, and consequently a larger shot pitch, $p = 2\,\text{nm}$, must be used, which translates into additional line-edge roughness (LER) due to, e.g., shot-filling errors. This can be seen in Fig. 7.2**d** on the left side of the junction of the two circles forming the shamrock. Notably, this is not "disorder" [197] but rather "ordered roughness" as it is a systematic error in the lithography, which will be accurately reproduced on all the unit-cells. There is $\sim$ 22 scallops indicating a scallop-size (and corresponding etch rate) $\sim 10\,\text{nm}$.

Figure 7.3**a** shows a calculation using a finite element method of the mechanical eigenmodes of the system, which is a breathing mode following the envelope of the tapering of the engineered cavity. Figure 7.3**b** shows the optical mode profile of the

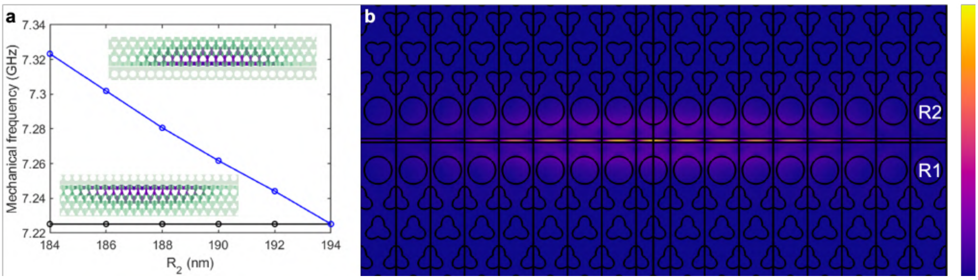

Figure 7.3. Numerical calculations of mechanical-optical-mechanical (MOM) system. **a**, The mechanical frequency calculated as a function of the radius of the top-plate, R_2, as it is changed from 184–194 nm, i.e., $\Delta R = -10$–$0\,\text{nm}$. The modes are breathing and confined around the cavity-structure as shown in the insets. **b**, Amplitude of the electric field of the optical mode of the system when $R_2 = R_1$. Calculation and figure courtesy of Guillermo Arregui.

eigenmode in the system. The circle in the engineered cavity has a radius, $R = 194\,\mathrm{nm}$. By adjusting the radius of the circle in the top plate, $R_2 = 184$–$194\,\mathrm{nm}$ in $1\,\mathrm{nm}$ steps. The mechanical frequency can be tuned by $\sim 10\,\mathrm{MHz/nm}$, thereby forming a mechanical-optical-mechanical interface where the frequencies of each plate can be tailored individually [40, 198, 199].

The sample is characterized using the fiber-loop setup in which a fiber is tapered down to be single-mode (diameter, $d \sim 1\,\mu\mathrm{m}$) using a furnace (Fig. 7.4**a**–**b**). It is then twisted 4π and pushed together until a loop is formed, and the ends are then slowly pulled apart to reduce the loop size to a slightly elliptical circle with a radius of a few tens of µm, forming a ring-like cavity albeit with an almost flat transmission (Fig. 7.4**c**). Figure 7.4**d** shows an image captured through the 100x microscope in the setup where the fiber-loop is brought into contact with the structure and a monochromatic laser is coupled to the device through the loop. Coupling manifests as a dip in the transmission curve or a peak in the reflection curve (measured with a fiber-circulator) [19]. The loop can be slided along the length of the slot and the polarization can be adjusted to maximize the cavity mode energy. Bringing the loop into contact perturbs the system, illustrated by Fig. 7.4**e**, where a sequence of transmission curves are plotted and the loop is moved a little along the slot using a micrometer-screw and the position is extracted using a 100x objective to visualize its position on the cavity. A Lorentzian fit is performed to each resonance and Fig. 7.4**f**–**h** shows the resulting λ_0, Q, and coupling fraction F—i.e., the extinction of the peak—respectively. This shows that when the loop is on top of the cavity mode, the mode is over-coupled and the resonance is red-shifted − by as much as $14\,\mathrm{nm}$, and Q degrades to $\sim 10^4$. Similarly, when the loop is moved far away ($> 4\,\mu\mathrm{m}$) the resonance comes back to the unperturbed, intrinsic value, and the quality factor increases. However, the coupling fraction also increases, and as can be seen in Fig. 7.4**e** almost no light is coupled into the cavity mode. Consequently, the optomechanical response is weak. In the range $3.5 - -4.5\,\mu\mathrm{m}$ from the center F and Q remains high, while λ_0 is almost not perturbed. Therefore, the best coupling strategy is identified by finding the mode at the center and then move away until λ_0 stabilized and the coupling is fine-tuned by adjusting the polarization. The final position is chosen to obtain $F \sim 0.5$. The numerical calculations yield $Q \gg 10^6$ but the experimentally obtained $Q \sim 10^5$, which is much lower. This is limited by fabrication-defects such as scattering (see Eq. (5.12) and discussion of Sec. 5.1). Finally, it should be noted that if the loop rests substantially on either plate rather than in the center it will dampens one mechanical mode over the other, however, when the loop is moved a little away this dampening effect is much less pronounced, and in this context it must be noted that the mechanical motion of interest is in-plane and localized to the center (cf. Fig. 7.3**a**).

Figure 7.5**a** shows optically transduced mechanical spectra for the 11 different structures with different R_2. Each spectrum is normalized to its peak value and the noise floor remain constant across all measurements; i.e., even though one mode is hard to see for, e.g., $R_2 = 189\,\mathrm{nm}$ this is due to the other mode being much more intense. Specifically, the first mode lases at the minimum power required to drive the

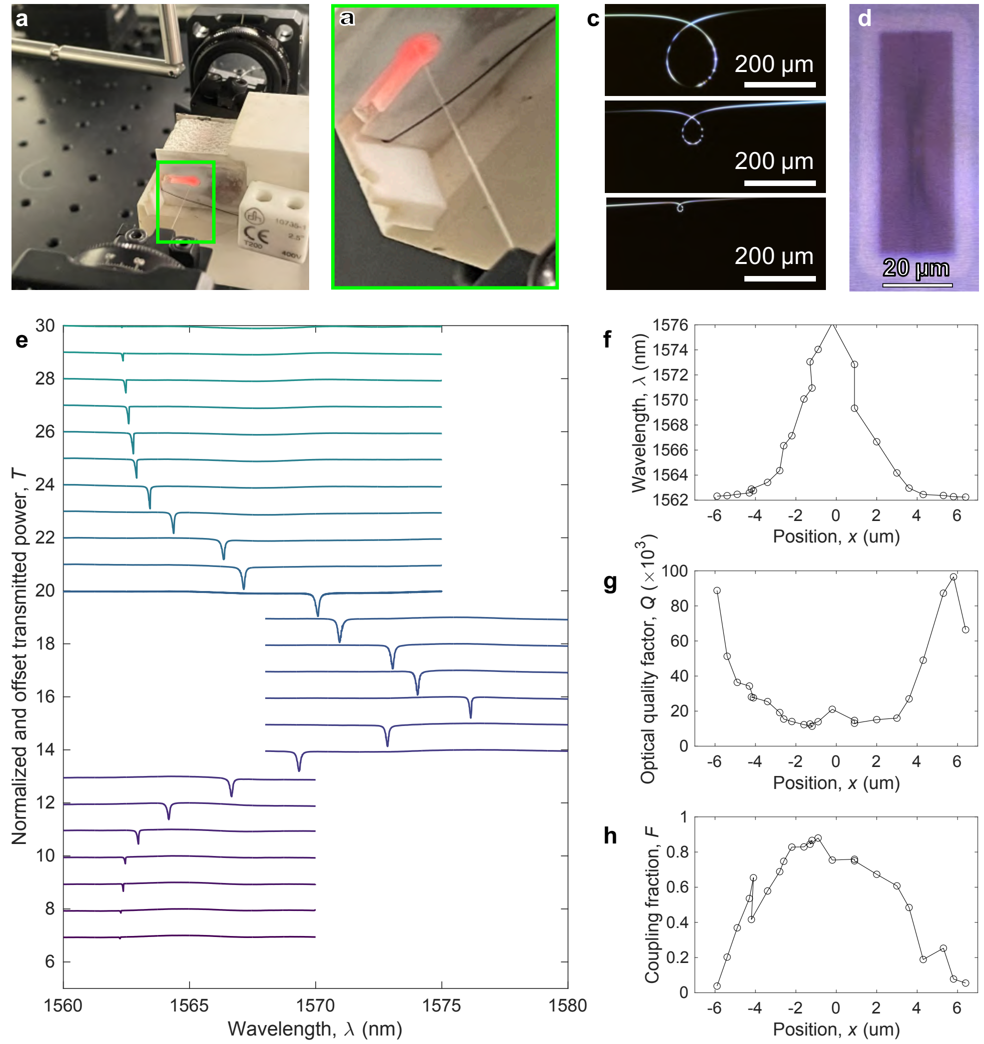

Figure 7.4. Fiber-loop–measurements. **a**, A fiber without cladding is heated and pulled to taper it down. **b**, Zoom-in where the fiber enters the free-space furnace. **c**, The fiber is twisted and pushed together forming a large loop and then pulled to reduce its. **d**, The loop is put in contact with the structure and the mechanical modulation of the transmitted or reflected signals is measured. **e**, The loop strongly perturbs the system; by sliding it along the structure and recording the spectra this can be illustrated. **f**–**h**, Optical center-wavelength, λ_0, quality factor, Q, and coupling fraction, F, against the absolute position along the slot-length (x) with the center of the cavity at $x = 0$. The coupling fraction is the extinction ratio of the dip in **e**. An optimal exists around 3–4 µm where the spectral shift, $\Delta\lambda_0$, remain low while F and Q both remain high.

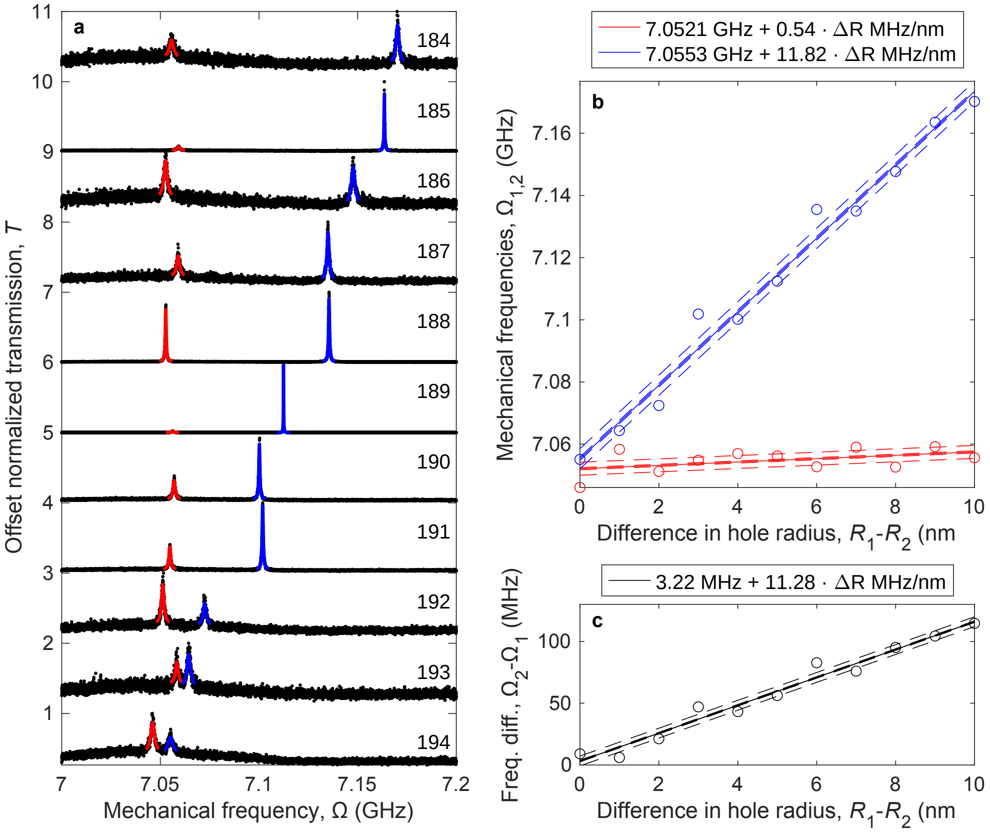

Figure 7.5. Measured mechanical frequencies as a function of R_2. a, 11 offset and normalized mechanical spectra for all the offsets. A Lorentzian fit is used to extract $\Omega_{1,2}$ for all the modes. It is hard to have both modes in the thermal regime with sufficient signal-to-noise ratio simultaneously, which is the reason for the variations in peak-height, however, even the smallest peaks have several dB extinction. **b**, Extracted R_1 (red) and R_2 (blue) with fit (solid line) and its corresponding uncertainty (dashed line). **c**, Frequency difference $R_2 - R_1$ with fit and uncertainty as in **b**.

second mechanical mode. From a Lorentzian fit to each resonance the mechanical frequencies are extracted and displayed in Fig. 7.5**b** and Fig. 7.5**c** further displays the difference between the two frequencies. Moreover, a linear fit is computed for each data set in Fig. 7.5**b**–**c** to obtain a shift of $\sim 11.28\,\mathrm{MHz/nm}$, which is in close agreement with the shift predicted from the FEM calculations..

Finally, the vacuum optomechanical coupling, g_0, is measured for the two modes using the method originally described in Ref. [186] and specifically in Refs. [19, 20]. The excitation laser is passed through an electro-optic phase-modulator before exciting the cavity and a vector-network analyzer (VNA) is used to supply a modulation-tone at $\Omega = 7.01\,\mathrm{GHz}$ to the phase-modulator with a power, $P_{\mathrm{dBm}} = -10\,\mathrm{dBm}$, corresponding to a voltage,

$$V_{\mathrm{VNA}} = \sqrt{R \cdot 10^{-3} \cdot 10^{P_{\mathrm{dBm}}/10}}, \tag{7.1}$$

where the resistance $R = 50\,\Omega$ and so $V_{\mathrm{VNA}} = 70.7\,\mathrm{mV}$, which should be compared with the half-wave voltage, $V_\pi(\Omega = 7\,\mathrm{GHz}) = 5.29\,\mathrm{V}$. Figure 7.6 shows a mechanical spectrum acquired with resolution band-width (RBW) 30 kHz where both modes exhibit only thermal motion, i.e., there is no dynamical back-action. The VNA-induced tone is visible as a narrow peak with a Gaussian line shape. Using Lorentzian fits, the mechanical frequencies $\Omega_1 = 7.043\,\mathrm{GHz}$ and $\Omega_2 = 7.064\,\mathrm{GHz}$ as well as the mechanical quality factors, $Q_m^{(1)} = \Omega_1/\Gamma_1 = 3500$ and $Q_m^{(2)} = 2900$ are extracted. This implies a phonon number in the cavity,

$$n = \frac{k_B T}{\hbar\Omega}, \tag{7.2}$$

with $T = 25\,^\circ\mathrm{C}$ measured in the lab – possibly the sample is a little warmer due to thermal heating as the laser power is dissipated, but this is not investigated further. The vacuum optomechanical coupling is,

$$\frac{g_0^{(i)}}{2\pi} = \left(\frac{\pi V_{\mathrm{VNA}}\Omega_i}{2V_\pi(\Omega_i)}\right)\sqrt{\frac{A_i/A_{\mathrm{VNA}}}{n}}, \tag{7.3}$$

with A_i the area under the i-th mechanical mode (strictly, this method is only valid for one isolated mode, however this is neglected [19]) measured with a Lorentzian fit and A_{VNA} is the area under the VNA-supplied tone in the spectrum (measured using a Gaussian fit). Equivalently, since the RBW is the same for the entire spectum, the ratio of the peak amplitudes can be used instead to yield the same results. The factor of 2 comes from the fact that the electronic spectrum analyzer (ESA) used to acquire the spectra only maps one half [186]. This method results in $g_0^{(1)}/(2\pi) = 2.33\,\mathrm{MHz}$ and $g_0^{(2)}/(2\pi) = 2.34\,\mathrm{MHz}$, which are an order of magnitude higher than the previously considered Anderson-localized modes, and among the highest values ever reported for hypersonic phononics in nanostructures. This confirms that the strategy of the hybrid phononic and photonic crystal to shield both the tightly confined slot-mode as well as the less localized mechanical breathing modes of the two plates.

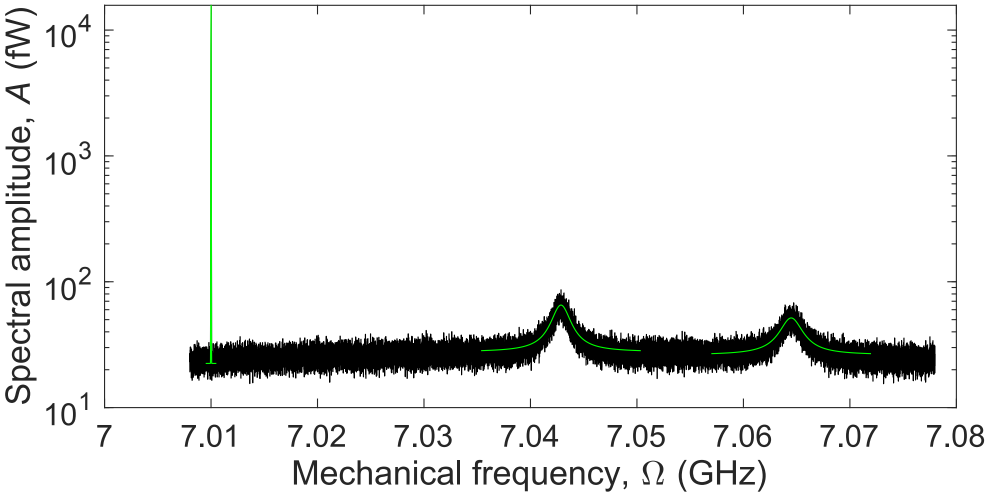

Figure 7.6. Measurement of the strong vacuum optomechanical coupling, g_0. a, The driving laser is modulated with a phase-shifter driven by a vector-network analyzer (VNA) at XX dBm and close to the two mechanical modes. The $V_\pi(7\,\mathrm{GHz}) = 5.29\,\mathrm{V}$, and both mechanical modes are in their thermal states. Lorentzian fits to the modes yields resonance at $\Omega_1 = 7.043\,\mathrm{GHz}$ and $\Omega_2 = 7.064\,\mathrm{GHz}$, linewidths $\Gamma_1 = 2.04\,\mathrm{MHz}$ and $\Gamma_2 = 2.42\,\mathrm{MHz}$, corresponding to mechanical $Q_m^{(1)} = \Omega_1/\Gamma_1 = 3500$ and $Q_m^{(2)} = 2900$. By comparing the areas to the VNA-tone the vacuum optomechanical coupling, $g_0^{(1)}/(2\pi) = 2.33\,\mathrm{MHz}$ and $g_0^{(2)}/(2\pi) = 2.34\,\mathrm{MHz}$.

Part III

Exploring novel applications

CHAPTER 8

Nano-electro-mechanical silicon photonics

Nano-electro-mechanical systems (NEMS) are the nanoscale versions of micro-electro-mechanical systems (MEMS). They employ electrostatic forces to cause mechanical deformations, for example a spring force, k, balanced by a stored capacitive energy, which in turn is tuned by applying a voltage, V [200–202]. For MEMS, such deformation can cause large mirrors [203, 204] or even objects [205] to move. Meanwhile, NEMS allow tuning systems with dimensions comparable to the wavelength of light, such as photonic waveguides, where the near-field can be affected to cause a change in the effective refractive index, n_{eff}, of a propagating mode. Thereby, the group velocity of the optical signal, $v_g = c/n_{\text{eff}}$, can be tuned. These photonic systems are called nano-opto-electro-mechanical systems (NOEMS) [39] and they offer a flexible platform to construct a number of systems such as optical phase shifters [206, 207], delay lines and switching [23, 24, 208–210]. They can further be combined to form complex integrated systems, e.g., within programmable photonics [25, 26], sensing, as well as classical [211] and quantum computing applications [109, 212].

These systems have an inherent low power-consumption since the deformation is tuned through a change in the voltage and, in principle, no current is dissipated. Instead, the energy is stored in the spring and can be recovered. In practice, the finite resistance of the nanostructures will cause a finite Ohmic loss [10, 213] but the power remains negligible [212]. In contrast to NEMS, thermal tuning is widely used [214, 215] due to, e.g., its mechanical robustness and direct CMOS-compliance and relative ease-of-packaging [26] – nano-mechanical systems are sensitive to impact and dirt, and must therefore be packaged in a protected environment [27]. Nevertheless, thermal systems consume considerable power limiting the scalability, and moreover, systems are prone to cross-talk [215]. Furthermore, they are incompatible with, e.g., cryogenic environments where instead NOEMS offers a promising platform [109, 212]. Alternative materials offer other tuning methods. For example, the electro-optic properties of lithium niobate ($LiNbO_3$) [216] and galium arsenide (GaAs) [217]. However, these material platforms are both more expensive and less developed compared to CMOS-silicon processing, which leads to other challenges. They are not considered further in this thesis.

A key figure of merit for most applications is the response time, i.e., the speed, of the system. For MEMS and NEMS this is in general limited by the mechanical frequency of the system [200],

$$\Omega = \sqrt{k/m}, \tag{8.1}$$

with k the spring constant and m the mass of the entire NEMS system. This implies that thin and compact NEMS can achieve high speeds and importantly fringing fields become important at the nanoscale [218], thereby ensuring that such light systems can continue to operate. In this thesis, NOEMS are formed using slot-mode waveguides in silicon—enabling large tunability—combined with comb-drive actuators [200], which allow large in-plane displacements. This chapter first introduces the slot-mode system, then documents the comb-drive actuator, and finally, provides an outlook on example implementations of the specific systems considered. Chapter 9 presents a specific application in more depth, namely the construction of a low-cost chip-scale nano-electro-mechanical spectrometer with a small footprint and power consumption.

8.1 Slot-mode waveguides

The slot-mode waveguide was invented in 2004 by Almeida *et al.* [155] and consists of a narrow slot with a low refractive index clad by two slabs of higher refractive index. The slot-mode waveguide is closely related to the even supermode formed when the evanescent tails of two waveguides overlaps, thereby hybridizing their modes into two coupled modes – an even and an odd supermode [39, 210]. In contrast, the slot-mode forms when the gap between the high-index claddings, g, is small compared to the length-scale of the evanescent tail and these overlap strongly, enhancing the field inside the narrow slot. This typically implies that each of the two high-index slabs are narrow such that the mode is less confined and the field is enhanced locally inside the slot. This effect is similar to the effect of the bowtie discussed in Ch. 5. In this thesis the low-index material is always air, i.e., $n_{\text{slot}} = n_{\text{air}} = 1$, while the high-index material is silicon, $n_{\text{Si}} = 3.48$.

Figure 8.1**a** shows a two-dimensional (2D) calculation of the quasi-transverse electric (quasi-TE) eigenmode of a rectangular waveguide using a frequency-domain finite-element method (FEM) at $\lambda = 1550\,\text{nm}$. The waveguide has a device-layer thickness, $h = 220\,\text{nm}$, it is $w_r = 508\,\text{nm}$ wide, and it can be seen that the mode is confined inside the silicon with considerable evanescent tails extending a few hundred nanometers. Figure 8.1**b** shows the corresponding calculation for a slot-mode system where the high-index claddings each have a width, $w_s = w_r/2 = 254\,\text{nm}$, and are separated by a gap, $g = 50\,\text{nm}$. The evanescent tails has a comparable extend to Fig. 8.1**a**, however, the norm of the electric field, $|\mathbf{E}|$, is substantially enhanced inside the slot due to the strong overlap. The system transforms adiabatically between the modes in Fig. 8.1**a** and **b**, and Fig. 8.1**c** shows the calculated n_{eff} against the waveguide width as well as a waveguide with twice its width. The mode becomes more confined as the width increases and in particular when it extends beyond $\lambda_0/(2n) \sim 223\,\text{nm}$. Figure 8.1**d** shows the difference between the two lines in Fig. 8.1**c**, i.e., it shows the change in n_{eff} as two far-apart slabs are moved closer together, thereby forming a slot-mode – and ultimately brought together to recover the quasi-TE mode of the rectangular waveguide. This change implies the available tunability of the system by mechanical deformation, and the maximum $\Delta n_{\text{eff}} \sim 1.25$ is achieved for a $w_s \sim 254\,\text{nm}$, and for symmetry reasons $w_s \sim 255\,\text{nm}$ is considered. This is huge compared to, e.g., the thermo-optic effect in silicon, which can only achieve $\Delta n_{\text{eff}} \sim 10^{-2}$ for $100\,\text{K}$ temper-

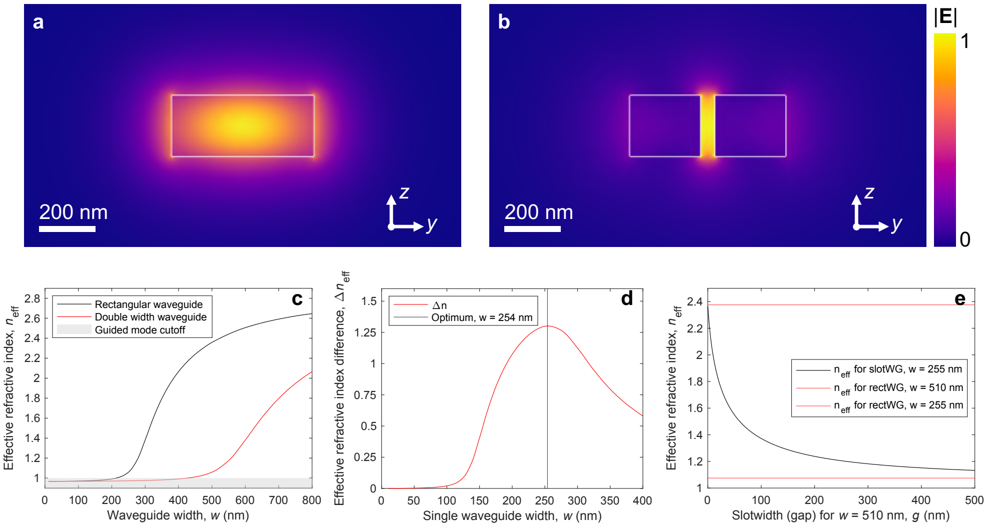

Figure 8.1. Transverse electric (TE) modes in a rectangular and slotted waveguide. a (**b**), Electric field norm, $|\mathbf{E}|$, in a rectangular (slot-mode) waveguide (rWG and sWG). The rWG is $w_r = 508\,\text{nm}$ wide and each of the two high-index parts forming the slot are $w_s = w_r/2 = 254\,\text{nm}$. The slot gap is $g = 50\,\text{nm}$ wide. Both waveguides are $h = 220\,\text{nm}$ tall following the thickness of the silicon device-layer. **c**, The effective refractive index, n_{eff}, of the rWG. This graph is repeated by scaling the width by a factor of two. When n_{eff} approach that of the cladding (i.e., $n_{\text{air}} = 1$) the mode is not well confined and instead leaks. **d**, Difference between the two graphs in **c** showing a maximum difference when two pieces 254 nm wide are joined, and therefore maximal tunability for $w_s = 254\,\text{nm}$. **e**, n_{eff} against the slot-width gap for a $w_s = 255\,\text{nm}$. It varies from the n_{eff} of the rectangular waveguide ($w_r = 2w_s$) when there is no gap, $g = 0\,\text{nm}$, to that of $w_r = w_s$ when they are far apart.

ature adjustments [214]. Figure 8.1**e** shows $n_{\text{eff}}(g)$, which starts at the value of the fundamental mode in the rectangular waveguide of with w_r and tends asymptotically towards the value of the isolated case, i.e., $w_s = w_r/2$. It can be observed that the majority of the change occurs over the first few hundred nanometers, and this range should therefore be targeted to achieve the most efficient tunability.

Almeida *et al.* [155] solved the case of the infinitely tall slot-mode waveguide (i.e., $h \to \infty$) and obtained, in essence, a bi-exponential spatial scaling of the electric field distribution. The effective refractive index is computed as the sum of the different material indices scaled by the fraction of the field energy inside that material. Therefore, a bi-exponential scaling is expected for $n_{\text{eff}}(g)$, and Fig. 8.2 confirms that this remains a good approximation even for the thin-film device layer, which is only $h = 220\,\text{nm}$ thick. The bi-exponential fit takes the form,

$$n_{\text{eff}}(g) = 1.14 + 0.55\,\mathrm{e}^{-0.0072g} + 0.63\,\mathrm{e}^{-0.05g}, \tag{8.2}$$

which imply that the effective index of the mode when the high-index claddings are

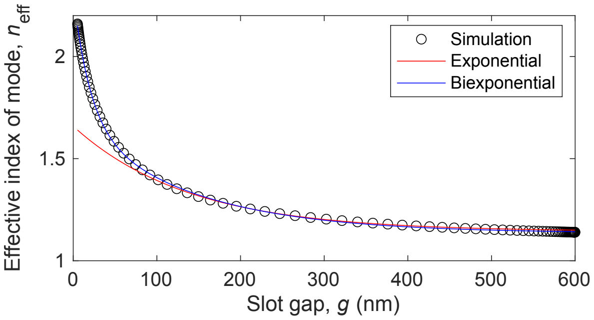

Figure 8.2. Bi-exponential scaling of the slot-mode system. Numerical calculation of the effective refractive index of a slot-mode waveguide with cladding width, $w_s = 255\,\mathrm{nm}$, as a function of the slot gap, g. An exponential and a bi-exponential fit are carried out and the latter is in excellent agreement despite the finite device-layer thickness, $h = 220\,\mathrm{nm}$.

far apart tend to 1.14. Moreover, it can be seen that the first exponential, which falls off slowly (1/e distance of 139 nm), contributes with 0.55 to the index change, while the second exponential contributes with 0.63 and falls off much faster (1/e distance of 20 nm).

8.2 Nano-electro-mechanical systems

The previous section introduced the slot-mode waveguide, where displacements of a few hundred nanometers can cause large changes in the effective refractive index of the propagating mode, $\Delta n_{\mathrm{eff}} \sim 1$. By applying a potential difference, V, to the two (suspended) high-index claddings, and attractive electrostatic force, $F \propto V^2$, is created, which is balanced by the Hookian spring force describing their rigidity [210, 219]. The capacitance of thick MEMS are well described by the parallel-plate approximation and such systems will collapse when the displacement exceeds 1/3 of the initial gap, g_0, while thin sheets are dominated by the fringing fields and collapse at $g_0/2$ [218]. NEMS falls in between but the problem can be all together alleviated using comb-drive actuators [200]. Here, an array of parallel fingers provides the electro-static actuation. They are connected to a rigid case, which again is connected to the rigid substrate using springs. In this way the actuation distance is limited by the length of the comb-drive fingers. This section presents and analyzes the nano-electro-mechanical systems considered in this thesis, specifically the comb-drive actuator, which can cause large displacements of a nanostructure without in-plane collapse [200].

Figure 8.3**a** shows an SEM image of NOEMS that is electrically contacted under the SEM using an Imina miBot-system. The two electrical probes can be seen in contact with the left and middle gold bonding-pad. The red square highlights a comb-drive actuator. Figure 8.3**b** shows a tilted scanning electron-microscope image

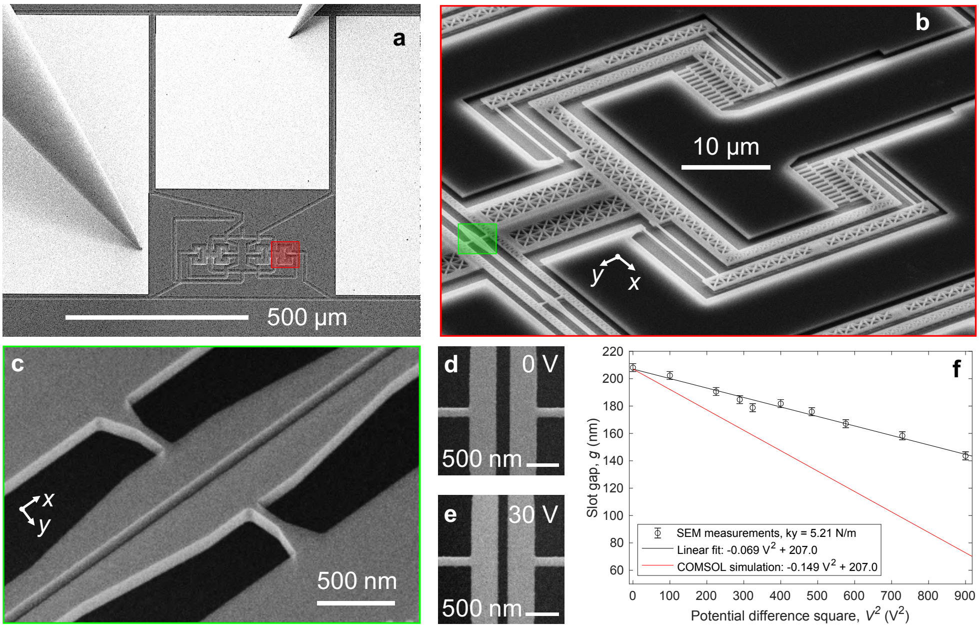

Figure 8.3. Characterization of nano-electro-mechanical system (NEMS). a, A photonic NEMS is electrically contacted using an Imina-system inside a scanning electron-microscope (SEM). **b**, Tilted zoom-in of the comb-drive actuator (red square in **a**) used to mechanically deform the NEMS. It has 4 double-folded springs with each beam 12 µm long and 500 nm wide. This yields a total in-plane spring constant, $k = 5.2\,\mathrm{N/m}$. **c**, Tilted zoom-in of the slotted waveguide (green square in **b**) where the optical mode is affected through electrostatic actuation of the comb-drive. **d** (**e**), Top-view SEM image of the gap, g, for 0 V (30 V) actuation. **f**, Experimentally measured gap versus the applied voltage and comparison to a full calculation of the actuator-force from the capacitance using a finite-element method that includes the effects of fringing fields reported in Ref. [218].

of a partially underetched (i.e., the release etch, but not the deep etch, is performed, cf. Sec. 2.4). This comb-drive [200, 201] body is skeletonized to reduce its mass (and thereby, its frequency) as well as to ease the release-etch process. The electro-static part consists of 42 finger-pair–overlaps and the structure is suspended using 4 double-folded springs, pair-wise joined through a truss, which makes the structure stable with respect to off-axis rotation [200]. The beams forming the springs have a length, $L = 12\,\mu\mathrm{m}$, and width, $w = 500\,\mathrm{nm}$. This structure is fabricated on wafer type 1 (i.e., the device-layer is $h = 240\,\mathrm{nm}$ thick, see Ch. 2). The total spring constant of the system is therefore [28, 200],

$$k_x = 2Ew\left(\frac{h}{L}\right) \tag{8.3}$$

$$k_y = 2Eh\left(\frac{w}{L}\right)^3 \tag{8.4}$$

$$k_z s = 2Ew\left(\frac{h}{L}\right)^3 , \tag{8.5}$$

where $E = 150\,\mathrm{GPa}$ is Young's modulus of silicon [201], and $k_y = 5.2\,\mathrm{N/m}$ is the spring constant in the direction of actuation, and k_z is the out-of-plane spring constant.

The NEMS is interfaced to a suspended slot-mode waveguide, highlighted by the green square, and Fig. 8.3**c** shows a tilted SEM of the slot-mode waveguide, which is tapered out such that tethers can be connected to it with a minimal optical loss to transfer the mechanical motion from the comb-drive [24, 28]. Figure 8.3**d** (**e**) shows top-view SEMs of the structure in Fig. 8.3**a** when a potential, $V = 0\,\mathrm{V}$ ($V = 30\,\mathrm{V}$), is applied and the slot-gap can be observed to change. Figure 8.3**f** shows a range of voltages and corresponding measurements of the resulting slot-gap, confirming that the electrostatic actuation-force has a square dependence on the applied voltage [218], i.e.,

$$g(V) = \frac{-0.069\,\mathrm{nm}}{\mathrm{V}^2}V^2 + 207.0\,\mathrm{nm}. \tag{8.6}$$

In this case, the designed initial gap is $g_0 = 200\,\mathrm{nm}$ in the mask and the features grows slightly. The system is symmetric with a comb-drive on both sides, and therefore, the displacement corresponding to 42 overlapping finger-pairs is only half of the gap-change. The red line shows the theoretically predicted displacement from a FEM calculation of the capacitance [218]. The difference is likely due to the edge-effects of the system, as the slot-mode waveguide is mechanically connected to the rest of the optical circuit, which increases the total spring-constant of the system.

To improve the performance of the comb-drive, more comb-fingers must be added. Figure 8.4**a** shows an optical miroscope image of four interfacing comb-drives using an improved battering-ram [220] design. This design features 140 finger-pair overlaps, up from 42, using only half the footprint. The green square highlights the mechanical-optical interface shown in the tilted SEM image in Fig. 8.4**b**. Here, the red (blue) square highlights the regions shown in the high-resolution SEM images in Fig. 8.4**c** (**d**) of the comb fingers (spring). The springs in this improved design have $L = 5.1\,\mu\mathrm{m}$ and $w = 200\,\mathrm{nm}$, corresponding to a spring constant of the full comb-drive, $k_y = 4.0\,\mathrm{N/m}$. This structure is fabricated in the SOI-wafer type 2 with a device-layer thickness, $h = 220\,\mathrm{nm}$. A key difference is that the width, $w < h$, and consequently, the out-of-plane spring constant, $k_z > k_y$. This means that out-of-plane collapse due to stress release (see discussion in Ch. 2) is less likely and the structural stability of the system improves.

Figure 8.5 shows a mask (black parts are exposed) with precise dimensions of a battering-ram comb-drive with three cross-beams. This device achieves a further enhancement of the electrostatic force per area, and optionally the hindmost parts (relative to the optical interface at the comb-drive front) can be exchanged with this component. Moreover, and if the optical interface already has considerable mechanical robustness, the springs at the front of the comb-drive (in Fig. 8.4**a**–**b**) can be

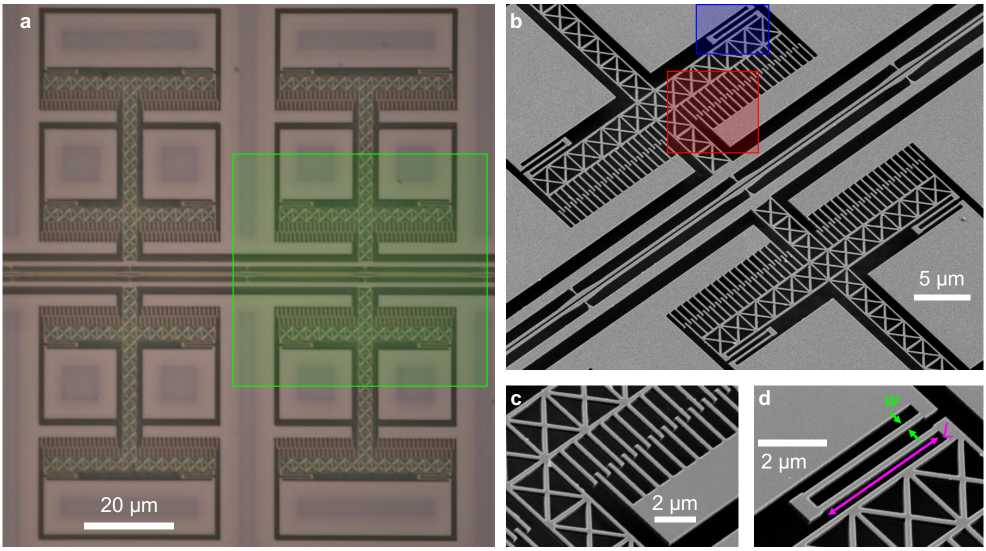

Figure 8.4. Next-generation battering-ram comb-drive actuator. **a**, Optical microscope image of four battering-ram comb-drive actuators facing a tunable slot-mode waveguide. It features 140 finger-pair overlaps, up from 42 in the previous version, i.e., a 233 % improvement in the actuation force. Moreover, the strong comb-drive has half the footprint (40-by-40 µm down from 60-by-55 µm). **b**, Tilted scanning electron micrograph of the comb-drive interface with a red (blue) square highlighting the comb-drive fingers (spring) in **c** (**d**). **c**, Zoom-in of comb-drive fingers connected to the skeletonized comb-drive body. **d**, Zoom-in of a spring with length, $L = 5.1\,\mu\text{m}$, and width, $w = 200\,\text{nm}$. The total spring constant of one comb-drive is, $k_y = 4.0\,\text{N/m}$.

disregarded. Importantly, this battering-ram comb-drive is less wide (along x) compared to the first generation shown in Fig. 8.3**b**, which means more actuation force per length of the optical waveguide (and hence, stiffer springs and operation at higher speeds). This reduction in width is, in part, also due to the springs not being connected pair-wise through a truss, which makes the system less stable to deformations along x, as well as to other detrimental effects such as shearing. Ultimately, the intrinsic mechanical robustness of the system that the comb is interfaced with—i.e., the slot-mode waveguide here—should be taken into account when pushing the performance. On the other hand, self-contained mechanical robustness of the comb drive should be prioritized when smaller or slower deformations are targeted, due to the ease of integration across a variety of applications.

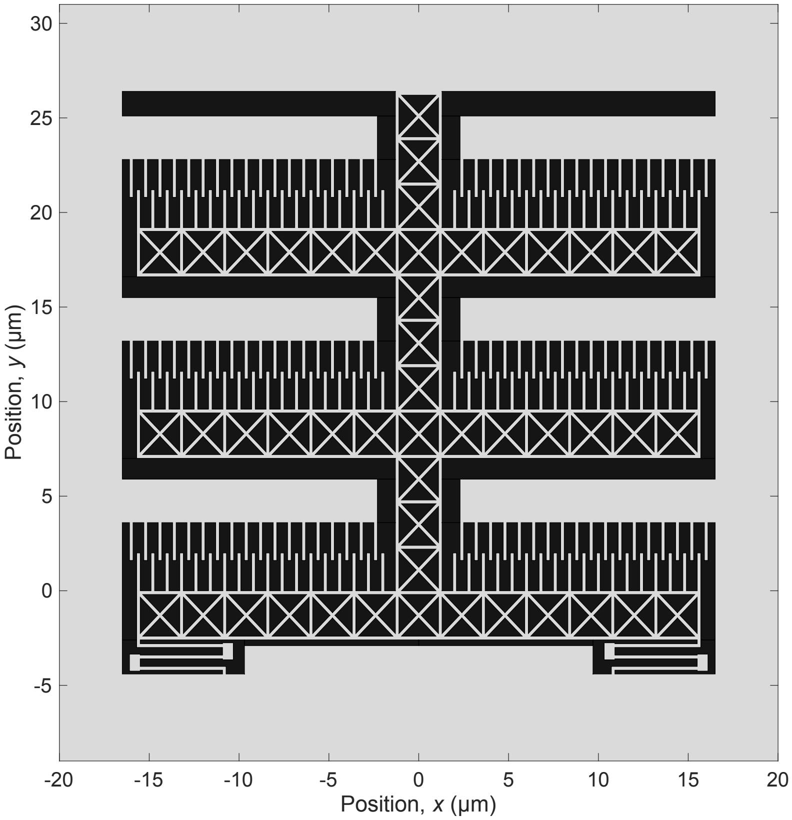

Figure 8.5. Battering-ram comb-drive actuator schematic. Multiple cross-bars with comb-arrays can be stacked to efficiently boost the actuator efficiency and reduce the voltage, either for low-voltage applications or to compensate higher spring constants, and thereby, a faster mechanical response.

8.3 Outlook

This chapter introduced the slot-mode waveguide as well as the comb-drive actuator. The former enables a nonlinear change in the effective refractive index of a single-mode waveguide-system on a chip. Specifically, it achieves a bi-exponential scaling with the width of the slot gap, i.e., the distance between the two high-index claddings. The actuator works by balancing an electrostatic force, $F_a \propto V^2$, with the spring force of a Hookian system, $F_k = kx$ [200, 218]. That is, $n_{\mathrm{eff}} \propto \exp(V^2)$, and this strong non-linearity translates to strict requirements on the voltage-control for applications. While this is rarely an issue in laboratories where a high-quality voltage-control is readily available, it does translate into a higher price-tag for a packaged device. It is possible to linearize the scaling (or rather make it less non-linear) [221] using pull-type

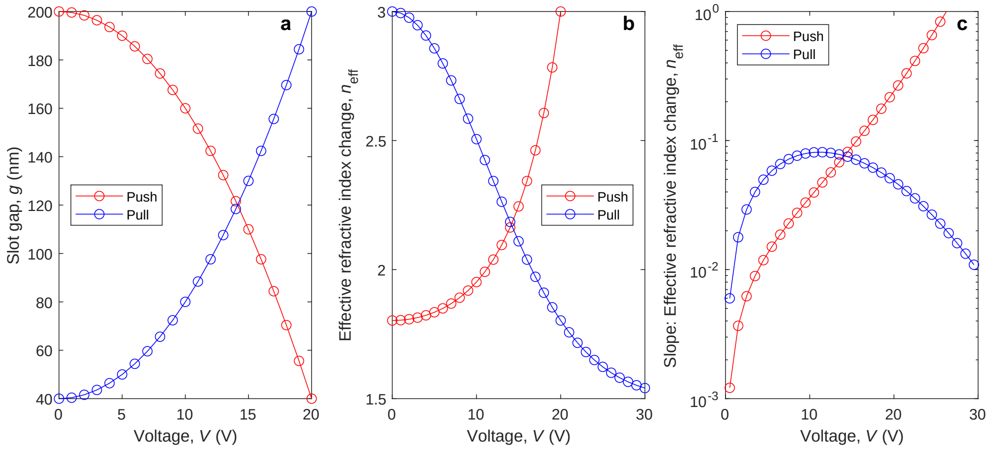

Figure 8.6. Push-type versus pull-type actuators. a (**b**), Voltage dependence of the slot gap, g, (calculated effective refractive index of a slot-mode waveguide, n_{eff}). **c**, the slope of **b** – all for a push- and pull-type actuator. The comb-drive displacement has a square dependence on the voltage, V, and the slot-mode waveguides a bi-exponential scaling on the gap resulting from the displacement. Therefore, the slope is much lower for a pull-type actuator, thereby relaxing the requirements on the voltage control. In addition it may be possible to recover structures with in-plane collapses using pull-type actuation.

actuation [222] instead, which achieves $n_{\text{eff}} \propto \exp(-V^2)$.

Figure 8.6**a** illustrates the square dependence of the slot gap with the voltage for both pull- and push-type actuation. Figure 8.6**b** combines this with the bi-exponential scaling of the slot-mode system ($h = 220\,\text{nm}$, $w_s = 255\,\text{nm}$), and Fig. 8.6**c** shows the slopes of the two curves. It is immediately clear that a pull-type system achieves a much stronger response for low-voltage, which is relevant for applications such as switching [24] where standard CMOS-only allows few volts. Furthermore, pull-type systems yield an almost linear scaling over many volts, and the maximum slope (Fig. 8.6**c**) is much lower. Another advantage of pull-type systems relates to a central risk for NEMS: the in-plane collapse when structures are moved to close [220]. The square voltage-response of push-type systems implies an increasing risk of collapse, while for pull-type systems the minimum gap is the starting point. That is, when a larger voltage is applied the structures are pulled apart, which may even allow recovering collapsed structures [220], thereby extending the lifetime of a system. Despite these many advantages of pull-type systems, push-type actuation is much more prevalent due to the ease of fabrication – specifically, a pull-type system requires a narrow slot to be fabricated, which is a high aspect-ratio structure that is hard to etch (see Ch. 4). On the other hand, a push-type system relaxes this fabrication challenge by allowing wider features to be etched, which can then be pushed together to benefit from the tight field-confinement inside a narrow slot with dimensions beyond the resolution of the fabrication process.

Finally, the two slot-mode waveguide and the comb-drive actuator discussed in this chapter must be integrated with a range of additional components to form integrated programmable photonic circuits. Scanning electron microscope images of a range of such components are shown in Fig. 8.7. Figure 8.7**a** shows an input grating coupler (top-view SEM image in the inset), along with a chip-scale beamsplitter and 3 tethers to mechanically suspended the single-mode rectangular waveguide. The point-scatter grating coupler [223–225] converts light focused on it using a microscope objective into in-plane motion, i.e., it rotates the wave vector. Appendix C presents the optical setups used, and it presents the propagation loss in the suspended optical waveguides including the tethers. This type of grating coupler is very broadband, which is useful for initial testing. However, this is at the price of a low optical transmission, $T \sim 1\,\%$, and a high reflection, causing standing waves between an input and output grating coupler. More complex grating couplers using apodized gratings [95, 226–236], including focusing grating couplers [237–240], have been investigated as part of this thesis, but is presently unpublished, and instead this circular grating coupler is considered exclusively. The interested reader is referred to the review by Marchetti *et al.* [241] and Klenk *et al.* [242] for further details on grating couplers. A range of complex applications and coupling schemes have been demonstrated to couple different polarizations into the same optical waveguide on-chip [243], to enable long working-distance grating couplers [244, 245]. Moreover, inverse design [246, 247] optimize for a range of figures-of-merits, and Sapra *et al.* [248] provides an overview of the trade-offs between bandwidth and peak transmission through inverse design of grating couplers. Finally, Li *et al.* [249] optimizes for lateral coupling required by the most stable photonic packaging strategies. In this context, it is worth highlighting the fiber-loop system used to study cavity optomechanics in Ch. 7, which achieves a transmission, $T \sim 100\,\%$ [19]. This approach, however, is not suited for packaging but remains excellent for characterization within fundamental research.

Figure 8.7**b** shows a mode-converter between a suspended and slot-mode waveguide system [251] where the slot-mode waveguide is connected to a lever, which is skeletonized to reduce its mass. This type of coupler impose substantial mechanical stiffness to short slot-mode waveguides [252, 253]. This may be the reason for the large discrepancy between theory and experiment in Fig. 8.3**f**, and the other coupling schemes reported in Refs. [251, 254] might be promising for fast and low-voltage optical switches. Figure 8.7**c** shows a slot-mode waveguide and its interface with a comb-drive actuator. Here, there lever is not skeletonized to increase its mechanical stiffness. Figure 8.7**d** shows an electronic-photonic circuit-crossing [24, 28, 250], which is designed using topology optimization (see Sec. 6) to transmit optical signals across an electrically insulating gap in a compact footprint of 3.1 µm long segment and enabled by a single lithography step. Other waveguide crossings exist [251, 255], however, to achieve low optical losses they require long tapering distances, which are not suited for compact and large photonic circuits. These optical components all achieve insertion losses, $\mathrm{IL} < 10\,\%$ [28] over a wide bandwidth, and the limiting factor for most smaller systems is the low optical transmission provided by the grating coupler. Ref. [24] further shows a design with transmission, $T = 99.8\,\%$, which could

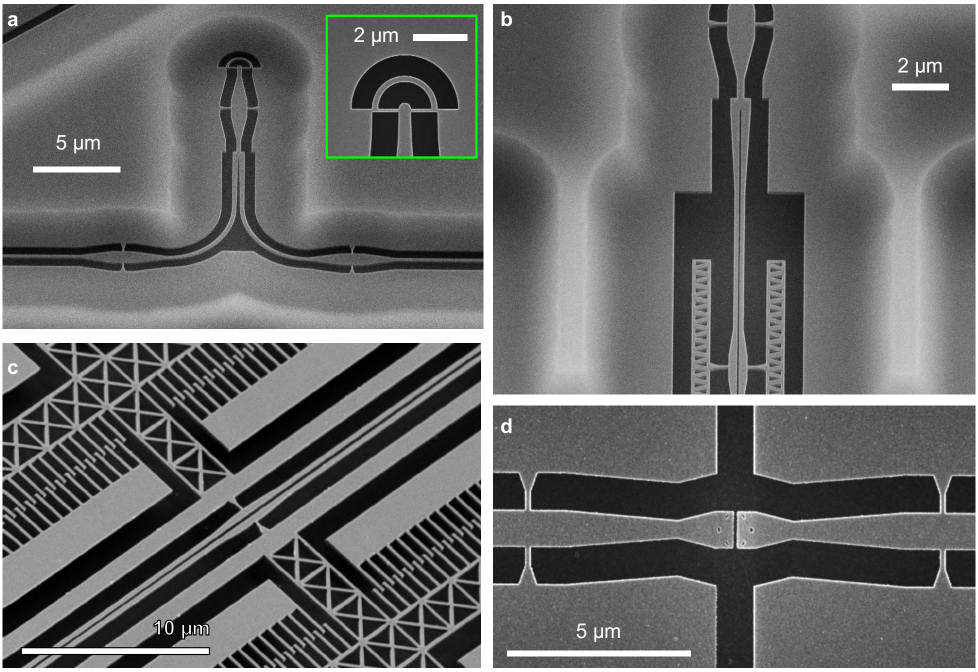

Figure 8.7. Tilted scanning electron microscope (SEM) images of photonic components for chip-scale nano-opto-electro-mechanical systems (NOEMS). a, Point-scatter grating coupler (top-view in inset), beam-splitter, and tethers used for suspension. **b**, Mode converter from suspended rectangular transverse electric mode to a slot-mode waveguide. **c**, Mechanical-optical interface using a slot-mode tether connected to a load-arm that distributes the deformation from the comb-drive actuators uniformly. **d**, Electronic-photonic circuit-crossing (EPCC) that enables crossing electrical and optical signals without cross-talk. All components have broadband ($> 100\,\mathrm{nm}$ around $1550\,\mathrm{nm}$) insertion losses [28], IL $< 10\,\%$. The EPCC is reported in Refs [24, 28, 250], and Ref. [24] further presents EPCC designs with transmission, $T > 99\,\%$, which are realistic using the high-resolution fabrication processes developed in this thesis.

be realized using the fabrication processes reported in this thesis and may enable a simplification of the electrical routing in large and complex chip-scale nanophotonic networks [24, 25, 209].

CHAPTER 9

Chip-scale nano-opto-electro-mechanical spectrometer

Different materials and substances absorb and scatter light differently, leaving a unique fingerprint in light that is transmitted through it or reflected off of it. A spectrometer measures the spectrum of light [22], which enables it to detect the fingerprint and thereby identify the material being analyzed. Existing table-top systems are bulky and expensive but can achieve excellent performance in terms of spectral resolution, bandwidth and signal-to-noise ratios. This chapter presents the early results of on-going efforts towards a low-cost chip-scale spectrometer [256]. It is based on the advantages of the nano-opto-electro-mechanical systems (NOEMS) discussed in Ch. 8. Here, the principles of the specific system are introduced, and early results are presented along with an analysis demonstrating the concepts. Then the emerging challenges related to the commercialization—and in particular the nascent field of packaging photonic integrated circuits (PICs) such as NOEMS [27, 257]—are briefly introduced. Finally, an outlook is presented in the form of a proposal for a next-generation design based on the knowledge developed within this chapter.

9.1 Chip-scale spectrometers

A range of technologies can be used to construct a spectrometer [22]: light can be dispersed [258], i.e., its wavelengths can be spread out spatially, either on an array of detectors or using a single detector combined with a slit that filters a part of the spectrum. This is the method used to record the spectra reported in Ch. 6 [16]. Another strategy uses reconstructive methods [259], and finally, the time-domain signal of the light can be measured and the Fourier transform (FT) of the signal yields its spectrum [22, 214, 215]. Infrared detectors are expensive, which rules out the multi-detector schemes [260–265] to keep costs low. Sweeping a slit enables high resolution with table-top designs but requires careful calibration and operation in a stable laboratory. This leaves the FT-based methods that require measuring the signal in the time-domain. Telecommunication photons have a wavelength, $\lambda \sim 1550\,\mathrm{nm}$, which corresponds to a frequency, $f = c/\lambda = 193.4\,\mathrm{THz}$, with $c = 299\,792\,458\,\mathrm{m/s}$ the speed of light in vacuum. A signal must be sampled at least twice per period of its fastest frequency component, i.e., the sampling rate, $F_s \geq 2f \sim 400\,\mathrm{THz}$, which is called the Nyquist criterion or sampling theorem [214, 266]. This corresponds to a detector that can sample the signal at least once per $\delta t = 2.5\,\mathrm{fs}$. Detectors are rarely fast enough for this, and certainly, compact and low-cost detectors are not;

for example the detector used in Ch. 7 used to measure the GHz phononics and optomechanical-transduction has a sampling rate of 40 GHz, which is considered fast. Moreover, fast detectors have poor signal-to-noise ratios, which makes the subsequent analysis harder and less certain.

Instead, FT-methods [266, 267] employ interferometers where light is split into two parts with variable optical path lengths (OPL), $L_o = nL$, before they are rejoined. The resulting signal is an interferogram and its intensity corresponds to that of the signal at the time, $\tau = nL/c$. Therefore, by tuning either the refractive index, n, or the path length, L, and measuring the resulting intensity on a single detector, the signal can be reconstructed. Now the signal-to-noise ratio is limited by the integration time at each step, and the time-steps, $\delta\tau$, should satisfy the sampling theorem. The spectral resolution,

$$\delta\lambda = \frac{\lambda_0^2}{c\Delta\tau}, \tag{9.1}$$

depends on the maximum time-delay, $\Delta\tau$, and for $\lambda_0 = 1550\,\mathrm{nm}$ it is $\delta\lambda \sim 8\,\mathrm{nm}(\mathrm{ps}/\Delta\tau)$. That is, 1600 optical cycles must be measured to obtain a 1 nm spectral resolution.

Figure 9.1 shows a concept-illustration of a FT-spectrometer. Multi-colored light is passed through a sample (e.g., blood) obtaining its fingerprint. An interferometer filters the light and the interferogram is measured using a single detector. The FT of the interferogram yields the spectrum (e.g., primarily red is transmitted through blood). Light-sources and detectors are readily available, and the FT is a post-processing step requiring only some computational power. The missing part is the interferometer, and Ch. 8 already discussed grating couplers and waveguides to get the light to, from and around the chip as well as beamsplitters required for the interferometer. The key component is therefore a tunable delay-line, which must have an accuracy to satisfy $\delta t \leq 1/Fs$, a maximum tuning-range to yield the required resolution and optical losses that are low enough for the detector to resolve the signal. Beyond this, reducing the price and footprint are the key figures of merit.

Technologies that rely on free-space propagation, such as table-top setups and micro-electro-mechanical systems (MEMS), normally use a Michelson–Morley inter-

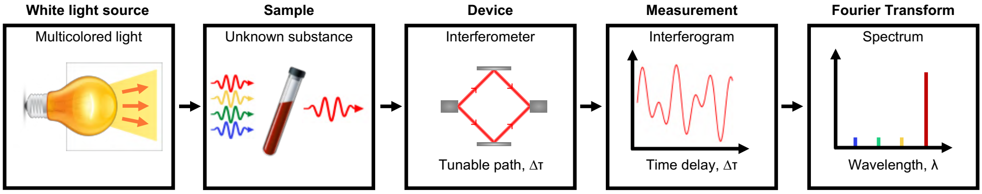

Figure 9.1. Concept-illustration of a Fourier transform spectrometer. White light is passed through a sample of unknown substance, e.g., blood, milk or oil, and this material leaves a fingerprint in the spectrum. An interferometer can measure the signal in the time-domain and a Fourier transform yields the spectrum from which the sample can be identified.

ferometer (MMI) [203, 204, 268–270] configuration where a mirror is physically moved to change the path length. Here, micrometer-scale precision suffice to satisfy the sampling theorem and millimeter-scale travel ranges ensures a high resolution. However, when aiming for miniaturization using single-mode waveguides the length cannot easily be changed. While MMI-configurations have been demonstrated [271] it is instead more convenient to use a Mach-Zehnder interferometer (MZI) as shown in Fig. 9.1 where the optical path length is tuned through and adjustment in the effective refractive index. This has been demonstrated using thermal tuning [214, 215, 272–274], carrier injection [275] as well as the electro-optic effect in for example GaAs [217] and $LiNbO_3$ [216, 276, 277].

Slot-mode waveguides combined with comb-drive actuators can also induce time delays [219, 256]. See Ch. 8 for a discussion of these systems and components. Such NOEMS achieve large changes in the refractive index, and short systems (sub millimeter-scale) therefore can achieve high spectral resolution compared to the centimeter-scale required for, e.g., thermally tuned delay-lines [214]. Figure 9.2**a** shows an optical microscope image of a fabricated interferometer. The mask is laid-out in collaboration with Mathias Korsgaard. Three potentials can be supplied to the bonding pads (gold), with the top (bottom) bonding pads applying a potential to the suspended parts in the two interferometer-arms, and the middle bonding pad supplies 0 V to the fixed parts. The input light is split into two paths, an electronic-photonic circuit-crossing (EPCC) [24] is employed to electrically isolate the two arms, while the semiconductor-waveguides conducts current to supply the voltage. This structure has 16 comb-drives–pairs in series on each delay-line, and since the signal is symmetric around $\tau = 0$ the two arms can be delayed sequentially to improve the resolution [214]. The output of the interferometer is routed back using a suspended waveguide to enable measuring it with confocal microscopy. See Appendix C for a detailed charaterization of the propagation losses as well as documentation on the optical setups used. Figure 9.2**b** shows a top-view SEM image of a short delay-line with only a single comb-drive actuator-pair. The mode converters between the suspended and slot-mode waveguides can be seen in each end, and these cause considerable stiffness to the waveguides, i.e., the spring-constants of the four double-folded springs are insufficient on their own. This is corroborated by the direct characterization of the comb-drive actuators in Ch. 8 (Fig. 8.3). Figure 9.2**c** shows a tilted SEM image of an 8-comb spectrometer where the parts connected to the central bonding pad charges up, therefore causing an increase in the SEM-signal due to scattering of incident electrons. Meanwhile, the suspended parts remain dark verifying the good electrical isolation provided by the EPCCs [24].

High spectral resolution is required for many applications, and in particular within research where stable laboratories are available. However, for many applications these requirements are greatly relaxed [22] and instead the key figure of merit is to reduce the cost. One example is the continuous validation required of hydraulic oil, which is used to lubricate the moving parts (e.g., gears) in machines – from factories-tools and lawn mowers to tanks, aeroplanes and aircraft carriers. As the oil gets older it lubricates insufficiently due to contamination with dirt or a too-high water

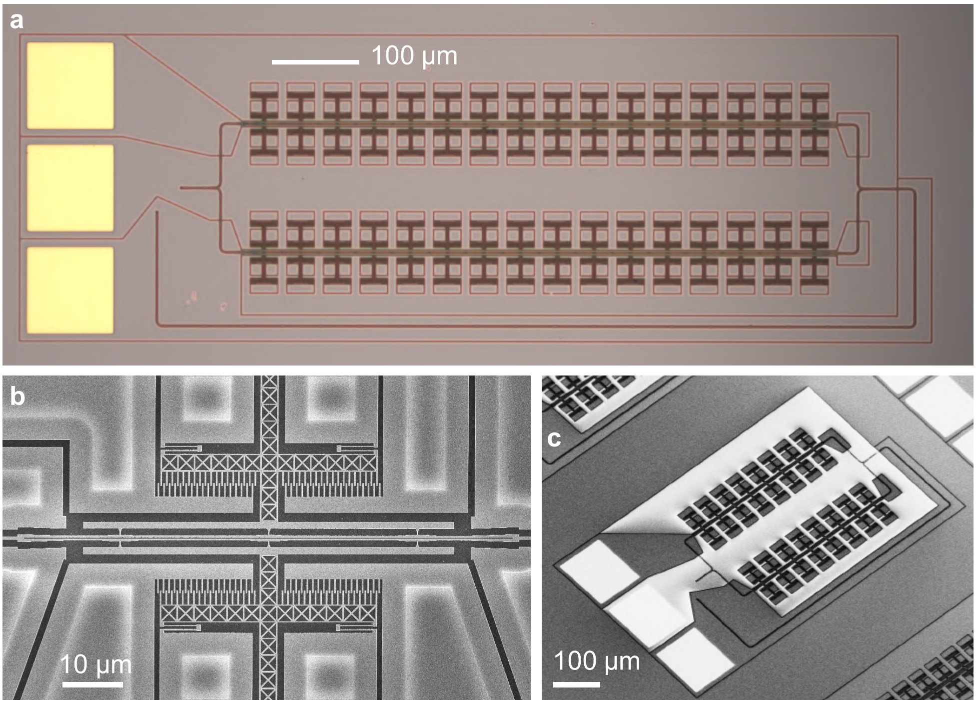

Figure 9.2. Fabricated chip-scale nanoelectromechanical spectrometers. **a**, Optical micrograph of 1 mm wide spectrometer MZI-design with two arms, each with 16 pairs of comb-drive actuators. The output waveguide is routed back to the input to measure it with a confocal microscopy setup. The three 100-by-100 µm bonding pads can be seen on the left and electrical isolation trenches are routed around them. **b**, Top-view scanning electron micrograph of a short single–comb-drive actuator delay-line. The mode converters from suspended to slot-mode waveguide are visible at each end. **c**, Tilted scanning electron microscope (SEM) image of an 8-comb interferometer. By changing the scanning-configurations on the SEM the central bonding-pad (at 0 V) is charged up along with the parts of the spectrometer connected to it, while the parts electrically isolated by the electronic-photonic circuit-crossings remain dark. This image is not false-color.

concentration [278]. Critical systems (e.g., fighter jets) therefore exchanges the oil more regularly than needed due to an overly-cautious mind-set, or they can afford the high price-tag of high-performance characterization-systems. Large machines (e.g., ships) can afford the space and price to test the oil, while smaller systems (such as cars) are allowed occasional failure, but nevertheless still exchange the oil on a regular basis causing waste. Another example is the continuous quality-control in production-lines within the food-industry. If the contents are not monitored, larger safety-margins are required to ensure certain specifications. However, by monitoring, e.g., fat, protein and moisture in the dairy industry (e.g., milk and butter production), it is possible to reduce costs, improve quality and lower the food waste. Typically, only a single point is monitored in large dairies due to the price-tag of such systems, but future internet-of-things (IoT) intelligent production lines require numerous low-cost sensors. Here, the precision-tolerances can be lower but critically the cost must also be lower.

The list of applications goes on, but interestingly a study by Jesper Sand available in Ref. [278] demonstrated that a spectral resolution of only $\delta\lambda \sim 10\,\mathrm{nm}$ over a well-chosen bandwidth of only $\Delta\lambda \sim 60\,\mathrm{nm}$ is in fact sufficient for the detection of moisture in the hydraulic oil case – and therefore, it can detect water in milk-production as well. To a large extend, this is because liquids broaden the resonances to $\sim 10\,\mathrm{nm}$. Beyond these specifications, it is required that the signal-to-noise ratio is low enough for the detector to detect the signal. Since essentially no current is consumed, NOEMS offer low power – and since the mechanical deformation achieves a strong tunability—further enabling a small footprint—the price-tag becomes the central consideration.

9.2 Fourier transform infrared (FTIR) spectroscopy

The structures in Fig. 9.2**a** and **b** can achieve the required resolution $\delta\lambda \sim 10\,\mathrm{nm}$ in principle. This section reports the characterization and analysis of a structure with eight combs in series (Fig. 9.2**b**) and a delay-line length, $L \sim 350\,\mu\mathrm{m}$. The specific data set analysed in this section has been acquired by Jesper Sand [38].

The structure characterized has an initial slot-mode gap, $g_0 = 175\,\mathrm{nm}$. The input port is excited with a monochromatic laser at $\lambda = 1520\,\mathrm{nm}$ with $P = 3\,\mathrm{dBm} = 2\,\mathrm{mW}$ (the laser wavelength is chose for compatibility with a legacy-camera used in the optical setup, which primarily could detect infrared light at this wavelength [279]). Following $g \propto V^2$, the voltage steps probed are, $\sqrt{0 : 0.05 : 10}$, following `MATLAB` syntax. Figure 9.3**a** shows the resulting transmitted power in nanowatts – the huge drop in power is primarily caused by the poor (yet broadband) grating couplers, see Appendix C. The first peak does not occur until $V = 1.6\,\mathrm{V}$, while the step-size in the end is $< 3\,\mathrm{mV}$ to sufficiently capture the oscillations, which immediately corroborate the intuition developed around Fig. 8.6 to use a pull-type rather than a push-type system with a smaller initial slot. By measuring the delay in both arms, the envelope for low voltages could be obtained as well, but here the first partial oscillation is ignored for clarity. At high voltages the system becomes unstable due to

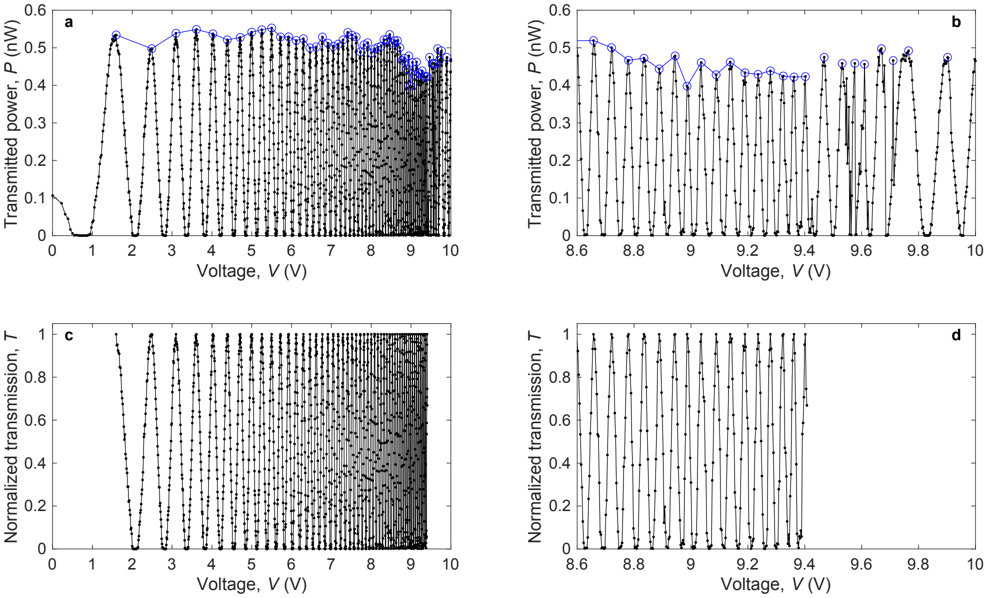

Figure 9.3. Optical measurements of a spectrometer with a 350 µm long tunable slot-mode waveguide. a, Transmitted power in nW against the applied voltage. The blue dots highlight the peaks to yield the envelope. Only data after the first peak ($V > 1.6\,\mathrm{V}$) is considered as it can be normalized. **b**, Zoom-in of **a** for $V = 8.6$–$10\,\mathrm{V}$. The data beyond $V > 9.41\,\mathrm{V}$ is noisy and also not considered in the analysis. **c**–**d**, Normalized transmission of the data considered using the envelope and zoom-in **d**.

two reasons. First, a poor-design choice was made in which the voltage is applied to the suspended part, relative to the substrate, which is at a floating potential (albeit $\sim 0\,\mathrm{V}$). This means that a considerable out-of-plane force is applied, rendering the system unstable. Instead, the variable voltage should be applied to the fixed parts, which enables operation at much higher voltages [24]. In the following analysis, this part of the data set is also excluded for clarity. Second, at small slot-mode gaps the system becomes unstable due to ubiquitous surface forces (e.g., the Casimir force) [280, 281] as well as the increased optical forces. This would be alleviated somewhat by using more stiff springs, and further, the lower slope of actuation at low voltages of the pull-type approach would enable a separation of these two issues. The smallest viable gap could then be investigated, and measurements imply that care must be taken already when using a gap on the order of 30–50 nm [280].

The peaks are identified, the envelope computed and the data normalized using `MATLAB`,

```
[Ppk, Vpk] = findpeaks(P_nW, V, 'MinPeakProminence', 0.2);
P_env = interp1(Vpk, Ppk, V, 'linear','extrap');
P_norm = P_nW ./ P_env;
```

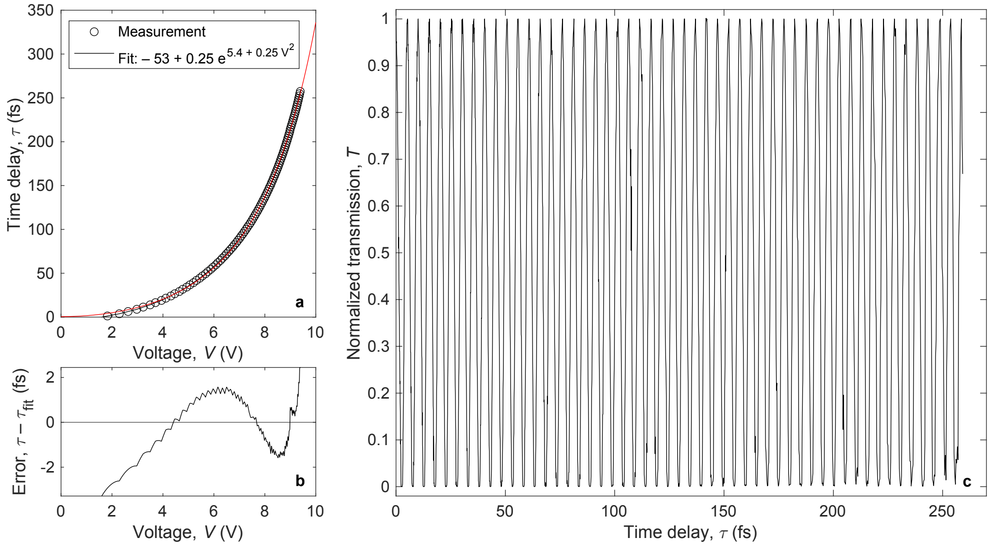

Figure 9.4. Calibration of FTIR-interferometer. **a**, Measured time delay, τ, corresponding to an applied voltage, V, as well as an exponential fit to the square of the voltage. **b**, Error between the measurement and the fit. The error is small compared to the optical period imposed but this will nevertheless cause a spectral error. A key future challenge is to investigate the reproducibility of the $\tau(V)$ dependence. **c**, The measured transmission against the time-delay, i.e., a measurement of the signal corresponding to a monochromatic input at $\lambda_0 = 1520\,\mathrm{nm}$.

The normalized transmitted power in the well-behaved region is shown in Fig. 9.3**c**–**d**. Next, to obtain the corresponding time for each applied voltage, all intersects between the measured normalized powers and the midpoint-value are identified (`xi`), which are known to be separated by $f = 197.2\,\mathrm{THz} = 5.071\,\mathrm{fs}$ due to the known laser-wavelength, $\lambda = 1520\,\mathrm{nm}$, such that the measured time can be extrapolated,

```
xi = polyxpoly(V,P_norm, V([1 end]), 0.5*[1 1]);
time_fs = (period_fs/2) * (0.5 + (0:length(xi)-1));
meas_t_fs = interp1(xi,time_fs, V, 'linear','extrap');
```

Where `period_fs = 1e15/frq0;` and `frq0 = c/lam0;`. This conversion is shown in Fig. 9.4**a** along with a fit, $\tau(V) \propto \exp(V^2)$, where a single exponential—rather than a bi-exponential—scaling for the refractive index with the slot gap is assumed due to the large slot-gaps. Figure 9.4**b** shows the deviation from the fit, which is generally low (compared to the period, $T \sim 5\,\mathrm{fs}$) but cannot be neglected, and a linear interpolation between the measurements in Fig. 9.4**a** is employed to re-scale the data and the normalized transmission as a function of the time-delay is shown in Fig. 9.4**c**. The fit is carried out as follows (the fit-result is used as the starting-guess here),

```
fittype = @(p,x) p(1) + p(2) .* exp(p(3) .* x.^2 + p(4));
fitres = nlinfit(xi', time_fs, fittype, [-53, 0.25,  0.02 5.37]);
```

The maximum time delay difference measured is $\Delta\tau = 259\,\mathrm{fs} = 51.1$ periods, i.e., the OPL is increased by $\Delta L = 51.1\lambda_0 = 77.7\,\mu\mathrm{m}$. This corresponds to an increase in the length of $\Delta L/L = 22.2\,\%$. At an initial gap, $g_0 = 175\,\mathrm{nm}$, the effective index of the slot-mode waveguide, $n_{\mathrm{eff}} = 1.26$. This is increased by $22.2\,\%$ to $n_{\mathrm{eff}} = 1.54$, which in turn occurs at the gap, $g \sim 50\,\mathrm{nm}$. Hence, the $\sim 10\,\mathrm{V}$ cause a gap-change from $\sim 175\,\mathrm{nm}$ to $\sim 50\,\mathrm{nm}$, consistent with the hypothesis that the instabilities at higher voltages are related to the small gaps.

Using a FT the spectrum is recovered from the signal. First, however, the data must be uniformly sampled. This is done using a linear interpolation (`u_t_s` and `u_P_norm` for the time and signal, respectively). From the calibration curve in Fig. 9.4**a** it is possible to define the voltages at which the intensity should be measured such that it is uniformly sampled.

```
Fs_THz = frq0 * 100;
u_t_s = meas_t_fs(1)*1e-15:1/Fs_THz:meas_t_fs(end)*1e-15;
u_P_norm = interp1(meas_t_fs*1e-15, P_norm, u_t_s, 'linear');

L = length(u_t_s);
N = ceil(L/2);
frq = (0:N) .* (Fs_THz/L); % frequency in Hz
lam = c ./ frq; % wavelength in meter
```

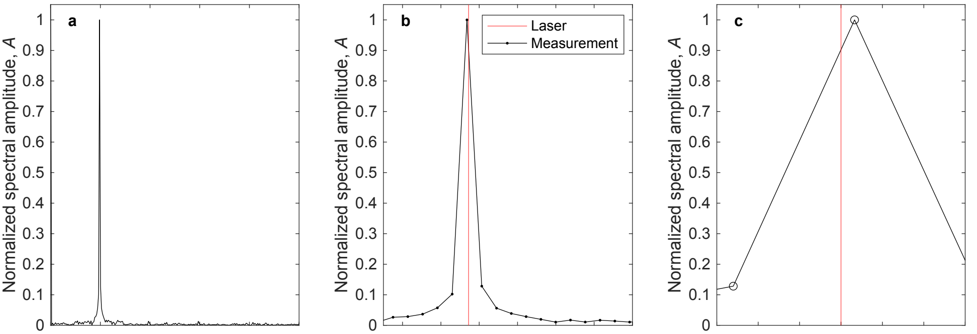

Figure 9.5. Fourier transform (FT) of the measured signal. **a**, FT of the signal with uniform bins on frequency. The monochromatic laser at $\lambda = 1520\,\mathrm{nm}$ yields a single peak as expected. **b**, Zoom-in around the laser frequency, $f = 197.2\,\mathrm{THz}$. **c**, Zoom-in in wavelength-domain, where the data points are unevenly spaced. The peak-value is offset from the laser (red), due to the length of the original signal. The resolution (i.e., distance between the points in the FT), $\delta\lambda \sim 32\,\mathrm{nm}$. The spectra are normalized to $0.459\,\mathrm{THz}^{-1}$.

Here, `L` (`N`) is (half) the length of the signal; since the FT is symmetric and only the one side is used these are needed to obtain the correct power spectral densities of the resulting spectrum. `frq` and `lam` are the corresponding frequency and wavelengths corresponding to the spectral amplitudes recovered using a fast FT (FFT).

```
spectrum_frq = abs(real(fft(u_P_norm))./L);
spectrum_frq = spectrum_frq(1:N+1);
spectrum_frq(2:end-1) = 2 * spectrum_frq(2:end-1);
```

The resulting spectra are shown in Fig. 9.5**a** with an inset in **b**. The bins are uniformly sampled in frequency. Figure 9.5**c** shows the spectrum for the wavelengths where an offset can be observed due to the bin-centers produced by the FT.

To determine the center of the peak more accurately, the original signal can be zero-padded, i.e., artificial zeros can be added to the signal before the FFT, which adds fast oscillations to the spectrum but also evaluates it at many more points. This is illustrated in Fig. 9.6**a** with a zoom-in in **b** and in wavelength-domain in Fig. 9.6**c**. It is carried out by inserting the following three lines of code after the definition of `u_t_s` and `u_P_norm` and before computing the lengths of the signal.

```
t_zeroPadding = u_t_s(end) + (1/Fs_THz:1/Fs_THz:10e-12);
u_t_s = [u_t_s, t_zeroPadding];
u_P_norm = [u_P_norm, zeros(1,length(t_zeroPadding))];
```

To analyse a spectrum, the voltage-to-time conversion must be obtained across all wavelengths, and further, the transmission as a function of wavelength and slot-width (i.e., applied voltage) should be obtained. This is known as the transfer function and should be implemented in the FT-scheme as detailed in Ref. [214].

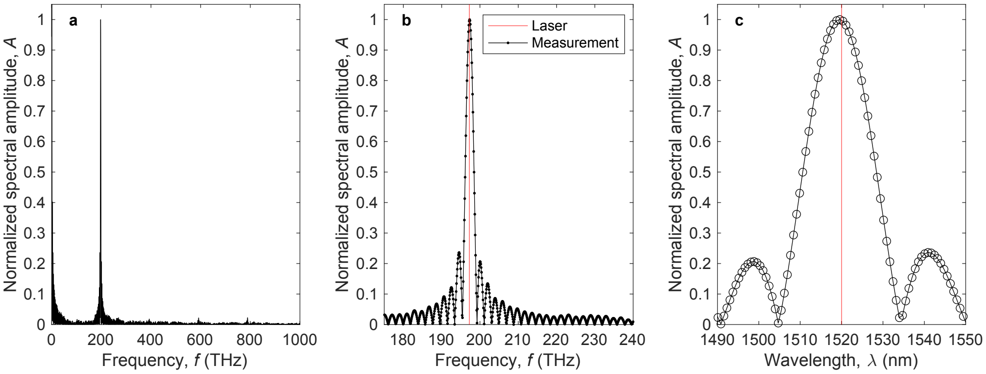

Figure 9.6. Effects of zero-padding the measured signal with 10 ps. a–b (c), FT of the signal where 10 ps of zeros are added to the signal before the FFT and zoom-in in frequency (wavelength). This reproduces the peak-location more accurately but introduces artificial oscillations around the peak. The full-width half-maximum intensity now manifests as a resolution, $\delta\lambda \sim 20\,\text{nm}$. The spectra are normalized to $0.0129\,\text{THz}^{-1}$.

9.3 Emerging challenges for commercialization: Packaging of photonic integrated circuits

A number of technological challenges remain to be solved to achieve a low-cost and compact spectrometer, such as a chip-scale nanoelectromechanical spectrometer. The main challenge is packaging – electronic signals can be routed as long as two wires touch. However, photonic signals are vectors where both position and direction are key. Getting light to and from a chip is already a challenge in a laboratory, but to achieve it in a packaged solution is hard [282]. On top of this, electrical signals can be transferred in a sub-micron wire and immediately connected to a large bonding pad to create an interface, while a single-mode silicon waveguide is a few hundred nanometers wide, while the core of a fiber is $\sim 10\,\mu$m. Today, fiber-arrays are considered a standard [25, 282], low-cost packaging option, that can be used with specially designed grating couplers [249]. The problem is that a single fiber-array readily costs $\sim 100\,\$$, which is prohibitively expensive for low-cost ($\sim 10\,\$$) photonics applications, required for a wide market penetration such as IoT- and smartphone-integration. Further to this point, a central packaging-challenge for NOEMS is that, while they are light and therefore mechanically robust to vibrations or gravity, they remain fragile nanostructures that must be suspended. This means that even a single dust-particle or direct impact can completely destroy the chip, and therefore, the NOEMS components must be hermetically sealed during packaging. Hermetic sealing is even more expensive than the fiber-arrays, which has not been a problem for low- and intermediate-volume applications within the price-range is 1000-10000 \$. Nevertheless, recent work has demonstrated wafer-scale hermetic sealing of NOEMS components [27, 257], which can be a low-cost and scalable solution. Here, a lid is bonded on top of the sample using a metal interface-layer. Moreover, placing a buried metal-layer between the buried oxide and handle wafer has been used to considerably improve the performance of grating couplers [228], since it alleviates the $\sim 1/3$ loss of light, which normally leaks into the substrate [240].

Finally, in this context it is worth highlighting the difference between pre- and post-dispersive FTIR-spectrometers. Figure 9.1 shows the intuitive flow of conventional table-top systems in which light is passed through a sample, then to the interferometer with an integrated detector, and then the signal is analyzed. This is called post-dispersive, since the light becomes disperse and diffuse as it passes through the sample. This is not a problem for free-space methods, but it is challenging to couple such disordered light into a single-mode waveguide on a chip without massive losses. Instead, a pre-dispersive configuration can be used where the light-source is integrated with the interferometer, and the filtered output from the interferometer is passed through the sample and onto an area-detector, which readily can measure the diffuse light. While it remains active research, the author again wish to highlight the advances in Refs. [27, 257]. They show a path towards realistic solutions to one of the most—if not the most—substantial challenges to the applications of nano-opto-electro-mechanical systems.

9.4 The next-generation spectrometer design

This chapter introduced a chip-scale nanoelectromechanical spectrometer based on a Fourier transform (FT) in the infrared (FTIR) technology. Specifically, nanoelectromechanical actuators are used to modulate the gap of a slot-mode waveguide, thereby tuning the optical path length. This delay-line is integrated with suspended silicon-photonic components to form an interferometer. It is experimentally demonstrated to accurately recover the sinusoidal oscillations of a monochromatic light-source. Furthermore, the FT-analysis, which can be used for a general spectrum, is detailed and demonstrated. A spectral resolution, $\delta\lambda \sim 20\,\text{nm}$, is demonstrated using zero-padding of the measured signal in a $L = 350\,\mu\text{m}$ long delay line – and using only the delay obtained from applying a voltage to one arm. By applying the delay to both arms this resolution could be doubled to match the $\sim 10\,\text{nm}$ required for many high-volume low-cost applications.

Despite this, a number of challenges remain. Packaging remains the most challenging in terms of commercialization of a realistically-priced device. However, a number of technological improvements to the system could further enhance the performance through increased robustness or less strict demands on, e.g., the control-electronics. Figure 9.4 shows a schematic of a next-generation spectrometer where a number of challenges of the current technology are resolved.

First, the beamsplitter in the current version employs a multi-mode interference-scheme to split the light with an insertion loss (IL) of around 6 %. To some extend this has resonant features, e.g., the distance between the expansion into multi-moded propagation and until the bifurcation into two beams. The slight taper of the splitter alleviates this problem enabling a bandwidth $> 100\,\text{nm}$. A more significant problem is that it electrically connects the two arms of the interferometer forcing them to be on the same potential – and combined with the output beamsplitter in the same configuration it creates an island in the center at a floating potential. While experiments could probe a bonding pad on such an island [23], packaging demands bonding pads only at the edges, which in turn demands complex multi-layer stacks to electrically access the isolated island out-of-plane. This was resolved using an electronic-photonic circuit-crossing (EPCC) [24], but can be resolved as well using other established beamsplitter configurations. A nanotaper [283] will expand the mode independent of wavelength and has been demonstrated to achieve almost unity broadband transmission, and furthermore, the same configuration can be used for the slot-mode waveguides [254]. Ref. [251] shows alternative configurations of electrically isolated taper-based coupling schemes. As noted in Ref. [254] such a coupling scheme depends sensitively on the sharpness of the tip of the taper, as this will determine the amount by which the light is expanded. Here it should be remembered that high-resolution silicon nanofabrication-methods developed in Part I enables unprecedented small feature-sizes reproducibly and deterministically. While this should not be expected with present-day foundry-technology it is reasonable to expect in the coming years [7]. Consequently, it is a justifiable approach within research.

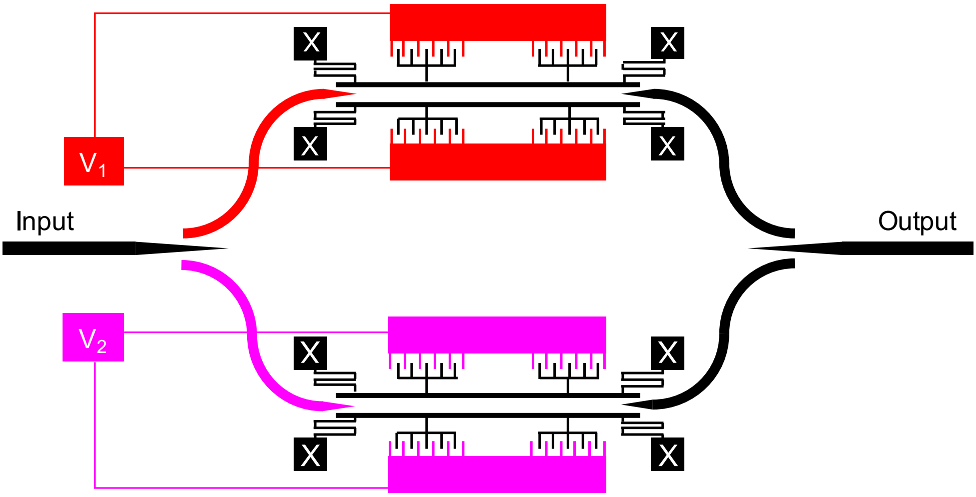

Figure 9.7. Schematic of next-generation chip-scale nanoelectromechanical spectrometer. First, the input beamsplitter and suspended-to-slot mode-converter should both be based on inverse tapers to increase bandwidth and to reduce insertion loss. In the beamsplitter-case it further provides electrical isolation of the two arms. In the slot-mode case it provides mechanical isolation of the two high-index claddings forming the slot, thereby, enabling better control and improved robustness of the delay-line. Second, all black parts are connected to the device-layer and should be at 0 V. The variable voltages, V_1 and V_2, for the two arms are supplied to the red and magenta parts, respectively. They are not suspended to avoid instability. Third, the nanoelectromechanical parts should employ pull-type actuation to linearize the actuation curve.

For the slot-mode waveguide, this further enables electrical isolation, which in turn substantially simplifies the electrical routing (i.e., drawing and connecting the electrical isolation trenches). This both reduces the time required to produce a mask as well as the risk of errors. Moreover, it mechanically isolates the two high-index claddings, such that the mechanical actuation can become uniform along the length of the slot. In this context, it is reasonable to assume that at least part of the deviation from the predicted scaling, $n_{\text{eff}} \propto \exp(V^2)$, in experiment is caused by non-uniform slot-mode gaps along the length of the waveguide. The electrical isolation of the high-index claddings from the suspended waveguides also enables setting their potential to common ground with with substrate to avoid out-of-plane forces. The free mechanical boundary conditions of such a slot-mode system also ease the prediction of deformation caused by stress-release, which will expand the device-layer causing a reduction in the slot-mode gap [40]. A reduction in the gap is not desirable for a push-type comb-drive actuation scheme, but it is germane for a pull-type actuator where the challenge is to fabricate the narrow slot with a minimum of sidewall roughness in order to keep the propagation losses low [284]. If a larger slot can be fabricated enabling lower roughness, and the slot is then allowed to decrease, or self-assemble, due to stress-release [40] this is advantageous. In this context, speed-bums to avoid a pull-in collapse of the gap might be desirable [201]. This should be chosen such that a reasonable voltage can pull the waveguides apart [220]. Additionally, the pull-type actuator (Fig. 9.4) has the advantage of linearizing the actuation curve, which reduces the requirements of the precision of the actuation-voltage (see Fig. 8.6) [221].

While most of the components enjoy low insertion losses, the slot-mode tether is a problem since a large number of them are placed in series causing considerable losses. It has an insertion loss 5–10 % depending on the gap and with 17 tethers in series, this corresponds to a 83–58 % loss, which is considerable. Instead, a sub-wavelength grating [255, 284–286] can be used. Such a grating offers mechanical support and avoids the continuous back-and-forth mode-conversion to otherwise enable tethering [285]. This would also exploit the mechanical stability of the lever-arm, which should ideally be locally doped to ensure that the applied potential is uniform along the propagation-length of the slot. In the present configuration the undoped silicon causes an immense resistance, and likely a voltage-slope along the propagation length of the system can be expected. This would cause an additional instability to the system and the slot-width might become non-uniform.

CHAPTER 10

Conclusions

This chapter summarizes and concludes the findings presented in this thesis, which covers the exploration of novel physics and applications using high-resolution silicon nanofabrication. Next, an outlook is provided [287], highlighting results of additional on-going studies of fundamental interest that have been a considerable part of this thesis. All these topics share the fact that they have been enabled by the high performance of the novel fabrication methods developed.

10.1 Summary

Part I introduced the high-resolution silicon nanofabrication process, with Ch. 2 introducing the general principles, methods and nomenclature of nanofabrication. It further provided a specific fabrication-process to realize local diffusion-doping as well as presented work on the process to release suspended silicon membranes by underetching the buried silicon dioxide (BOX) using hydrofluoric acid in vapor phase. Chapter 3 covered high-resolution patterning with electron-beam lithography, detailing processes to measure a consistent dose to clear, the point-spread function (PSF) of electron-scattering through stratified media, and lastly, the importance of the shot-filling processes and how to combine it with the PSF to enhance the resolution. Chapter 4 introduced plasma etching and the Reinberg reactor—from continuous dry-etching and the Bosch process that benefits from inductively-coupled plasma (ICP)—to the recently developed clear-oxidize-remove-etch (CORE) processes that can be carried out in standard reactive-ion etching (RIE) systems. The advantages of the self-limited oxidation process were discussed and a multi-layer hardmask scheme was introduced to circumvent the downsides, leaving a highly flexible and tunable process. Lastly, the remaining challenges were discussed, and techniques to stabilize the process by tuning it to employ the self-adjusting mechanisms available in the reactor yielded a robust process. This was demonstrated to be stable across > 1 month in a multi-user facility and without the need for preconditioning, consistently able to etch simultaneous high and low aspect-ratio features with low roughness and microloading.

Part II covered selected novel physics explored as part of this thesis. Chapter 5 introduced the theory of light-mater interactions and discussed dielectric bowties structures to enhance the electric field, following the principles derived in Ref. [17]. Chapter 6 reported the experimental demonstration of deep sub-diffraction confinement in a dielectric bowtie cavity structure, which was designed using fabrication-constrained topology optimization. This is a state-of-the-art method for deterministic inverse design, and the target of the optimization was to maximize the local density of optical states (LDOS) in the geometric center of a silicon structure. The fabrication-constraints used were that of a measured fabrication-process reported in Part I, and their direct inclusion ensured that the resulting design was realistic. The structure was evaluated using scanning electron microscope (SEM) imaging to verify that the structure appeared as-designed qualitatively. Then a set of nominally identical structures were characterized in the far-field using confocal cross-polarized spectroscopy to verify the yield and reproducibility. Lastly, it was characterized in the near-field using scattering-type scanning near-field optical microscopy (s-SNOM) to confirm the tight spatial localization of the optical mode. The results of this chapter were reported in Ref. [16], but this chapter further provided additional details, placing the results into the context of this thesis. Chapter 7 introduced the field of hypersonic phononics and cavity optomechanics, i.e., mechanical vibrations in the gigahertz. The nanofabrication process demonstrated in Part I has enabled a series of novel structures and samples, which have been characterized and published in Refs. [18–21]. The insights gained from these systems were combined to construct a novel mechanical-optical-mechanical system, which was characterized as part of an external stay. Some highlights from these on-going measurements were presented, demonstrating a vacuum optomechanical coupling, $g_0/(2\pi) = 2.34\,\mathrm{MHz}$, for mechanical vibrations at a frequency $\Omega \sim 7\,\mathrm{GHz}$ and a quality factors as high as $Q_m = 3500$. Notably, the structures combined a so-called shamrock-structure to open a mechanical band gap, a circle to achieve high optical quality factors, and a narrow slot to enhance the electric field intensity to strongly couple the electric field with the breathing mechanical mode modulating the slot. The simultaneous etching of a high–aspect-ratio slot with the low–aspect-ratio shamrocks and circles is an excellent demonstration of the performance of the nanofabrication methods developed in Part I.

Part III focused on novel applications enabled by the nanofabrication methods developed in Part I. Specifically, Ch. 8 introduced the slot-mode waveguide properly, which had already been used to strongly couple the optical field with the mechanical modes in Ch. 7. The slot-mode is based on many of the same theoretical principles of the bowtie structures introduced in Ch. 5, and in fact a bowtie with an angle of 180° becomes a slot (see Fig. 5.4**e**). Moreover, nano-electro-mechanical systems (NEMS) were introduced through comb-drive actuators. They can mechanically deform nanostructures by applying a voltage, and thereby an electrostatic force, which is balanced by an engineered spring constant. Slot-mode waveguides, as well as parallel rectangular-mode waveguides, sensitively depends on their separation, which can be accurately controlled with the NEMS to achieve nano-opto-electro-mechanical systems (NOEMS). Such systems were shown to achieve a strong nonlinear response of the effective refractive index of a propagating mode, and example applications include switch-networks based on directional couplers [24] and phase shifters [252], as well as photonic computing and quantum networks. Chapter 9 used the slot-mode waveguide to construct a long optical delay-line in Mach-Zehnder interferometer (MZI) to build a scalable on-chip nanoelectromechanical spectrometer for volume applications [256].

Here, the price-tag and power consumption are key figures of merit, while adequate spectral resolution and bandwidth can be tolerated [278]. A spectrometer was characterized optically, and the Fourier transform in the infrared (FTIR) analysis was presented and discussed.

10.2 Outlook

The nanofabrication methods reported in this thesis achieve unprecedented nanostructures, but relies on electron-beam lithographic processes, which are slow due to its serial nature. Electron-beam lithography has been predicted for some low-volume applications or to define a single unique low-density layer on each chip for encryption purposes [7]. However, it will be important for silicon photonics foundry-processes to continue its advance to enable applications of the cavities for nanometer-scale photon confinement and optomechanics presented within this thesis.

A key challenge for applications of NOEMS is the total loss in the optical structures, where the electric field is intense at the material boundary. Reducing the loss relates to reducing structural disorder rather than the feature-sizes, and in particular the narrow slots are sensitive to roughness such as the scallops left by the cyclic dry-etching. Future work on surface passivation as well as annealing to smooth the surfaces could be promising. Nevertheless, the strong nonlinear response offered by NOEMS [39] enables compact devices, and combined with the low power-consumption of NEMS—compared to, e.g., thermal tuning [214]—imply a powerful platform for integrated programmable photonics applications [25], ranging from photonic computing [282] and quantum networks [109]. Packaging remains a central challenge, but recent times have seen substantial advances and progress to resolve this with scalable methods [27]. Consequently, NOEMS remain more promising than ever for widespread integration in fundamental research and new applications – ranging from healthcare and diagnostics to internet-of-things (IoT).

Photonic topological insulators (PTIs) [152] have been proposed as a promising platform to protect optical modes from losses induced by back-scattering due to structural disorder. However, recent experimental efforts by Rosiek *et al.* [84] brings this strategy into question, showing that PTIs effectively have indiscernible propagation losses to normal photonic crystal waveguides – albeit, the propagation losses demonstrated are among the lowest in the world, owing to the exceptional performance of the nanofabrication processes developed as part of this thesis. This study is yet another example of the applications and novel fundamental physics that can be explored using high-resolution silicon nanofabrication.

The CORE-processes developed achieve very low etch rates, in part due to the self-limited nature of the oxygen passivation, compared to industry-standards. However, it also allows considerably simpler reactor specifications, which begs the question: could a high-speed etcher be replaced by multiple cheaper and low-speed tools? Already, the partial abatement of the potent greenhouse gas (GHG) C_4F_8 is a step towards sustainable etching. Even more to this point, with access to the toxic, yet sustainable, fluorine source F_2 instead of the potent SF_6 a GHG-free high-performance silicon dry-etching process can be envisioned. Finally, it is relevant to highlight that research and industry often diverge when it comes to cleanroom processes, due to the accelerating costs of state-of-the-art nanofabrication tools. However, if industry instead were to employ multiple lower-cost tools where researchers can afford a single version of it, it can enable researchers to further contribute to the development of industrial nanofabrication. This is for example the case with the HF vapor phase etcher, where processes can be developed on low-cost single-wafer tools and remain compatible with foup (25 wafer-batch) foundry processing.

The nanometer-scale photon confinement in dielectric cavities [16] demonstrated in this thesis (Ch. 6) holds promise for a variety of applications enabled by its small modal volume, but from a fundamental point of view a question arises if there is a fundamental limit to the interaction strength of light and matter [158, 160, 288]. Additionally, it will be interesting to study the field profiles of such cavities either directly using alternative spatially-resolved optical spectroscopy methods [179] or indirectly using, e.g., optical nonlinearities [157].

Finally, constructive self-assembly of suspended nanoscale systems [40, 289] can realize structures with dimensions well below the resolution of the nanofabrication processes. In particular, measurements of the surface forces at the deep nanoscale, such as the vacuum fluctuation forces (i.e., the Casimir and van der Waals forces) have been carried out [280, 281] during the span of this thesis. These measurements hold promise for further exploration at the nanometer-scale – and may even pave a realistic way for the quest to study novel physics and applications at the fundamental atomic scale.

Appendices

APPENDIX A

Optimized process flow

This appendix includes the precise steps followed to fabricate a suspened silicon nanostructure using the processes developed in this thesis. The "DeDam" step [11] listed as part of the etch-protocol is not described in the main text, since it is auxiliary with little real value for the actual process and could be deleted for speed; rather their purpose is to verify that the etching tool can strike the plasmas a required such that the tool can be left to complete the etch automatically. It consists of two steps, DeDam strike and DeDam etch.

The DeDam strike step has 30 sccm SF_6 gas-flow and uses a fixed VAT-position of 100 % (i.e., fully open), which results in a pressure of 0.9 mTorr, which is allowed to stabilize for 15 s and then the power is ramped from 0–20 W over 10 s. The plasma typically ignites around 10 W, and this step serves to verify that the plasma ignites correctly with proper matching conditions converging fast. It also allows verification that the measured gas flow matches the set-point and that the pressure reaches $<$ 1 mTorr, i.e., that the pump works as is intended.

The DeDam etch step 15 sccm SF_6 and a fixed VAT-position of 100 %, which results in a pressure of 0.4–0.5 mTorr. After 15 s time to stabilize the pressure, the plasma is ignited with 10 W and run for 15 s. This step is tuned to etch away the native oxide on the silicon surface, and to a large extend is similar to the poly-silicon etch. However, lower power and higher pressure is used and for much shorter time.

Process flow: Suspended photonics in SOI chips

Contact: Marcus Albrechtsen (maralb@dtu.dk)
Content revised on February 17, 2023.
Compiled on February 17, 2023.

1 Sample name Note the full sample name and understand what it means (see separate documentation). In "C01A21", C01 means wafer `01` from batch `C` (Soitec "G12P-194-01", 300 mm wafers), cleaved into shards (size ≤ 75-by-100 mm) labelled by a letter, here `A`. Chips 25-by-25 mm are cleaved with row (column) given by `2` (`1`), respectively.

2 Stack information Note (use blue/black pen only) any additions to the stack on the chip box (and in the logbook), writing the material abbreviation and thickness in nm. E.g., the SOI stack could be written: `box3000si220`.

3 E-beam lithography hardmask (cr10si10csar50) Sample assumed to have hardmask stack: cr10si10.

3.1 Spin-coating Prepare/fetch bowlset, space, pipettes, and resist (AR 6200.09 (CSAR) diluted 1:1 in anisole).
3.1.1 Safety Treat CSAR as anisole (i.e., use 4H/barrier-gloves). Do not agitate (leave 24 h after mixing).
3.1.2 Cleaning Clean chip with DI-water gun, IPA, acetone, IPA; blow dry with dry nitrogen.
3.1.3 Dehydrate sample Prebake the chip on a hotplate (≥ 100 °C) for ≥ 5 min.
3.1.4 Clean pipette Blow with dry N_2 for at least 30 s.
3.1.5 Spin-coat Place chip in bowlset and confirm vacuum (run process for a few seconds). Take ~ 2.5 mL of resist form the center of the resist container and deposit the first 2-3 drops away from the chip. Then cover the entire chip and discard remaining resist in the pipette into the bowlset and discard the pipette in the bin.
3.1.6 Parameters Immediately start with preset time: 60 s, speed: 6000 rpm, acceleration: 4000 rpm/s.
3.1.7 Softbake Immediately move chip to hotplate (setpoint: 200 °C, actual: 180 °C) for 5–10 min (aim for 5).

3.2 E-beam exposure Prepare files at least 1 day before an exposure. Ensure a colleague has validated the design.
3.2.1 Pattern preparation Perform proximity effect correction in Beamfox Proximity ($\alpha = 5$ nm, $\beta = 30$ µm, and $\eta = 0.5$) and export as layered GDS II.
3.2.2 Calibration Select condition-file and run `RESTOR` followed by batch daily short. Note current from first `CURRNT` and gain shift in x and y from averaged `PDEFBE`. Setup and run `HEIMAP` and `SAVE`, then start the exposure.

3.3 Development Use N-50 (amyl acetate) in semi-automatic developer for 60 s SP (single puddle).

4 Dry etch on Pegasus 2 with hardmask (cr10si10) Verified baseline process.

4.1 Carrier wafer and sample mounting Multiple chips can be etched simultaneously; each is placed within 50 mm of center of an 6" SSP silicon wafer.
4.1.1 Log carrier usage Note `Wafer ID` of the carrier wafer in LabManager log (comment field).
4.1.2 Replace dirty carrier wafer If carrier is dirty after processing: Discard it and fetch a new. Never leave the box with new carriers with fewer than 3 carrier wafers.

4.2 Dry-etching steps Process-name of combined process: `CORE maralb 2.0`, which executes the following steps: DeDam (10 s), Cont-si (120 s), resist strip (3 min), Cr etch (15 cycles, 150 s, 1 nm/s), main Si, 25 cycles (~ 20 min), Cr etch (15 cycles).
4.2.1 Solvent clean Clean chip with DI-water, IPA, acetone, IPA; blow dry with dry nitrogen.

5 Release-etch with vapor-phase HF etcher After the release the structures will be fragile, so the sample must be clean before starting and extra care should be taken in this step.

5.1 Pre-bake (≥ 200 °C, ideally 250 °C) for 2 min. Then place sample on carrier wafer; pump down using meter valve.

5.2 Select and setup etch recipe(s) Release the structures using 2 cycles of 12.5 min = 750 s with `RECIPE 3`, which has a nominal etch rate of 150 nm/min.
5.2.1 Release etch for fragile structures Some suspended structures has a spring constant, $k < 1$ N/m, and can be released using a milder process, followed by a reduced deep etch. A milder etch is often `RECIPE1` with a nominal etch rate of 17 nm/min at 131 mTorr. All cycles of all recipes should last ≥ 10 min and ≤ 20 min.

APPENDIX B
Roughness, disorder and scattering around scallops

Figures B.1 and B.2 illustrates scattering in a slotted waveguide system, calculated using a two-dimensional finite element method (FEM) in COMSOL. Small defects are added to highlight where scattering occurs. The slot-mode is a quasi-TE (transverse electric) mode, i.e., the main polarization of the electric field is horizontal (in-plane). Therefore, scattering occurs at sharp protrusion from the silicon, while slowly-varying intrusions does not cause scattering. The top rows show that some scattering occurs also at the two vertices with $> 90^\circ$ angle leading to the sharp intrusion.

This is interesting in the context of scallops resulting from a cyclic dry-etching process. Here, the scallops themselves will be large/wide and are formed by a chemical etch, which tends to result in smooth features, however, the interface between scallops will be sharp. One may imagine two overlapping circles – while the circles themselves are smooth the interface between them is a discontinuous point. Consequently, one should expect high optical losses from slotted optical waveguides if the scallops are substantial, however, this will generally not be a problem for, e.g., a bowtie nanocavity with a solid central bridge. Several of the optomechanical structures considered in this thesis, employ Anderson localization to achieve a strong opto-mechanical coupling, and this may benefit from the disorder from the scallops. This is not investigated further, however. It is worth highlighting also that the scallops will ideally be periodic and so can be taken into account in the engineering of an optical structure – to, e.g., form 3D bowties by etching through the device-layer locally using only two cycles. Such a 3D-bowtie could even be ”grown back” using ALD techniques to place an interesting nonlinear material at the epicenter of the bowtie [115], and the size of the bowtie gap could be controlled with atomic-layer precision.

Finally, Fig. B.3 shows a roughness sensitivity map leading to the placement of the defect in the L3-cavity explored in Ref. [17] and in ch. 5. Around the outline of each circle (forming an air-hole through the membrane) the polarization of the electric field is computed and combined with the angle of the interface; the size of the blue (red) circles shows the magnitude of the maximum field at its position inside (outside) of the silicon, i.e., as a intrusion (protrusion) of the hole [125]. Based on this, and combined with the visual clarity of the point, the defect considered is a protrusion at $(x = 0, y = 600\,\mathrm{nm})$, which enables making the smallest possible perturbation of the system that produces a substantial lightning-rod effect. Such a map could further be used to optimize the cavity by shifting the holes to make it less sensitive to disorder [124, 151].

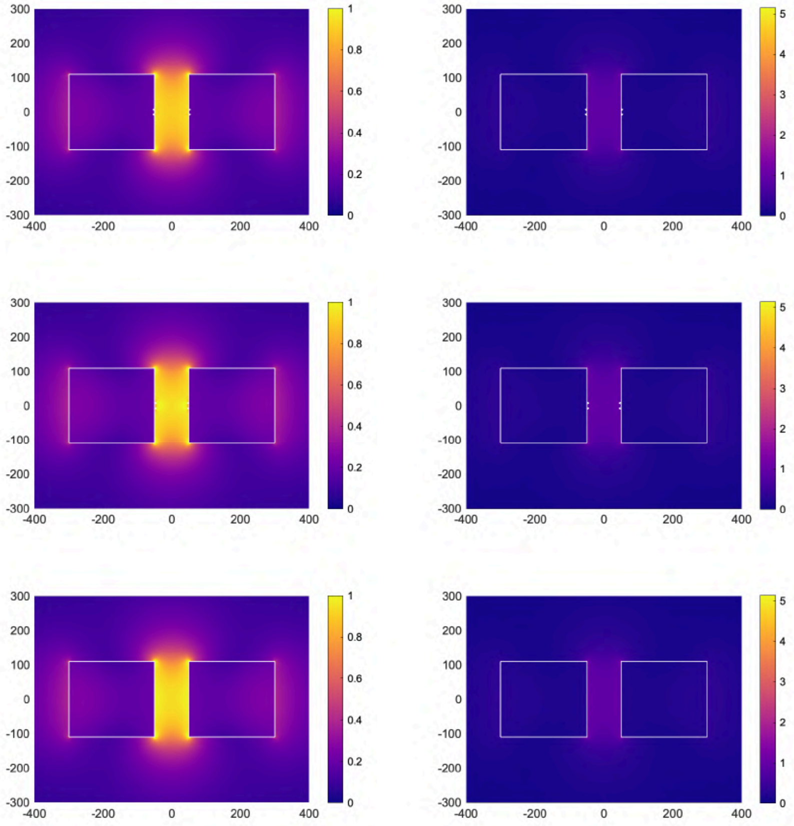

Figure B.1. Scattering in a slot-mode waveguide. Two-dimensional FEM-calculation (COMSOL) of the eigenmode of a slot-waveguide system. The colormap is truncated at 1 (5) in the left (right) column to illustrate the unpertubed (local divergences) of the mode. The top (middle) row shows an intrusion (protrusion) and the bottom row shows the unperturbed system. The axis shows position in nanometers and the colormap shows $|E|$.

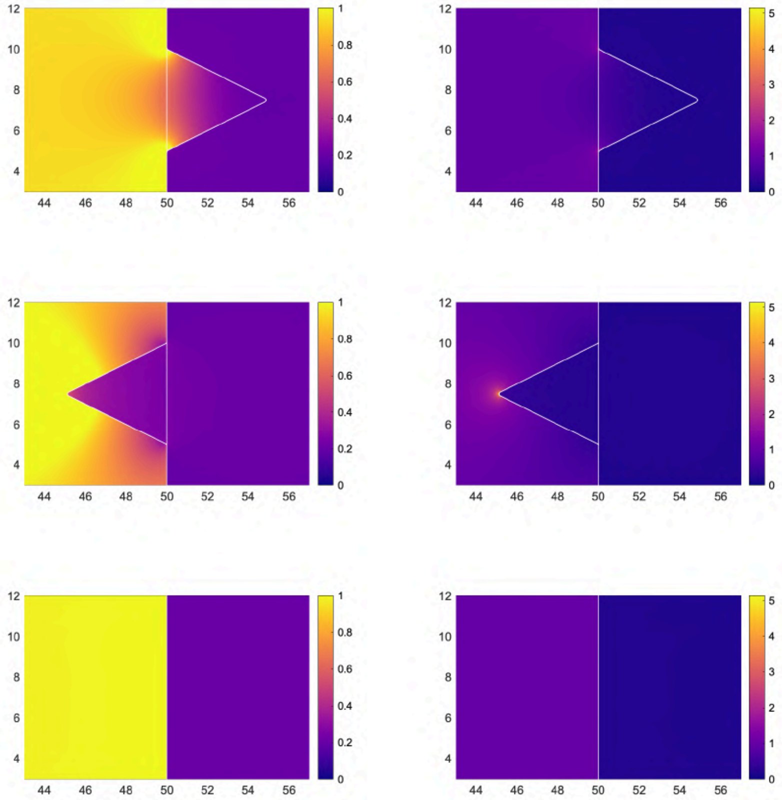

Figure B.2. Zoom-in of scattering in a slot-mode waveguide. Two-dimensional FEM-calculation (COMSOL) of the eigenmode of a slot-waveguide system. The colormap is truncated at 1 (5) in the left (right) column to illustrate the unpertubed (local divergences) of the mode. The top (middle) row shows an intrusion (protrusion) and the bottom row shows the unperturbed system. The axis shows position in nanometers and the colormap shows $|E|$. Scattering be observed only at sharp protrusions from silicon.

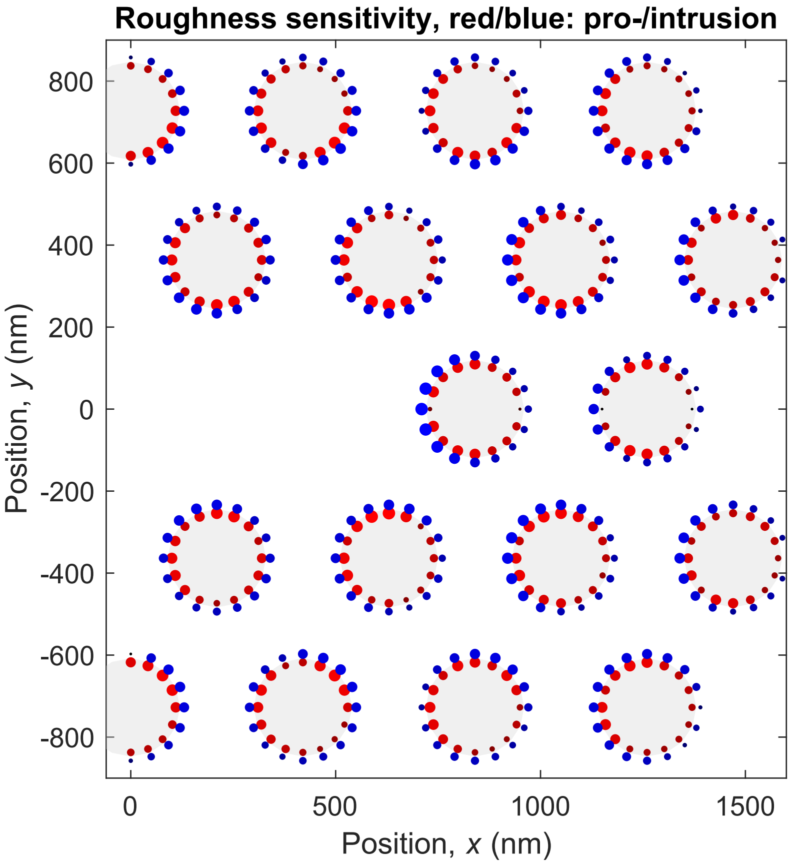

Figure B.3. Map of sensitivety to roughness in an L3 cavity. The size of blue (red) circles shows the relative magnitudes of a divergence caused by a lightning-rod placed as an intrusion (protrusion) from the silicon-air interface at the given point.

APPENDIX C

Optical setups used in this thesis

This appendix introduces the two optical setups used in this thesis, Optical setup 1 [279, 290], shown schematically in Fig. C.1, and Optical setup 2 shown schematically in Fig. C.3 (figure courtesy of Jesper Sand [38]). Figure C.2 shows an example of how a sample looks on the camera. The sample is mounted vertically in setup 1, which makes electrical contact difficult, however, the setup is mechanically very stable. Moreover, it offers flexibility with the detection where the collection-polarization can be changed independently of the excitation. The second half-wave plate (HWP) can further be removed and the output fiber replaced with an area-detector to measure unpolarized light.

Optical setup 2 is designed and build to enable more robust characterization of the nano-electro-mechanical systems, i.e., convenient electrical access is given priority and the optical setup is mounted vertically on the microscope tower of an electrical probe station inside a dark enclosure. Keeping the weight low is important and so the path is simplified using a configuration similar to Ref. [143]. This only allows measuring cross-polarized in- and output paths. By avoiding the multiple passes through 50:50 BS the overall transmission is substantially improved. The objectives can be changed but is typically a 20x objective with NA= .4.

Figures C.4 and C.5 report the propagation loss of the suspended waveguides considered in this thesis. The circuits consists of 6 waveguides with the in- and output ports placed at the same relative distances such that optical alignment can be preserved between measurements. The two smallest structures can be seen directly in Fig. C.2. Figure C.4 reports measurements by the author of this thesis during process optimization and Figure C.5 is adapted with permission from data acquired during systematic measurements by Jesper Sand [38] in comparing the optical setups and considered a sample fabricate with the less-stable hardmask-process reported in Sec. 4.3, which is also the reason for the odd waveguide widths, which are due to a systematic offset (i.e., loss of critical dimension (CD)).

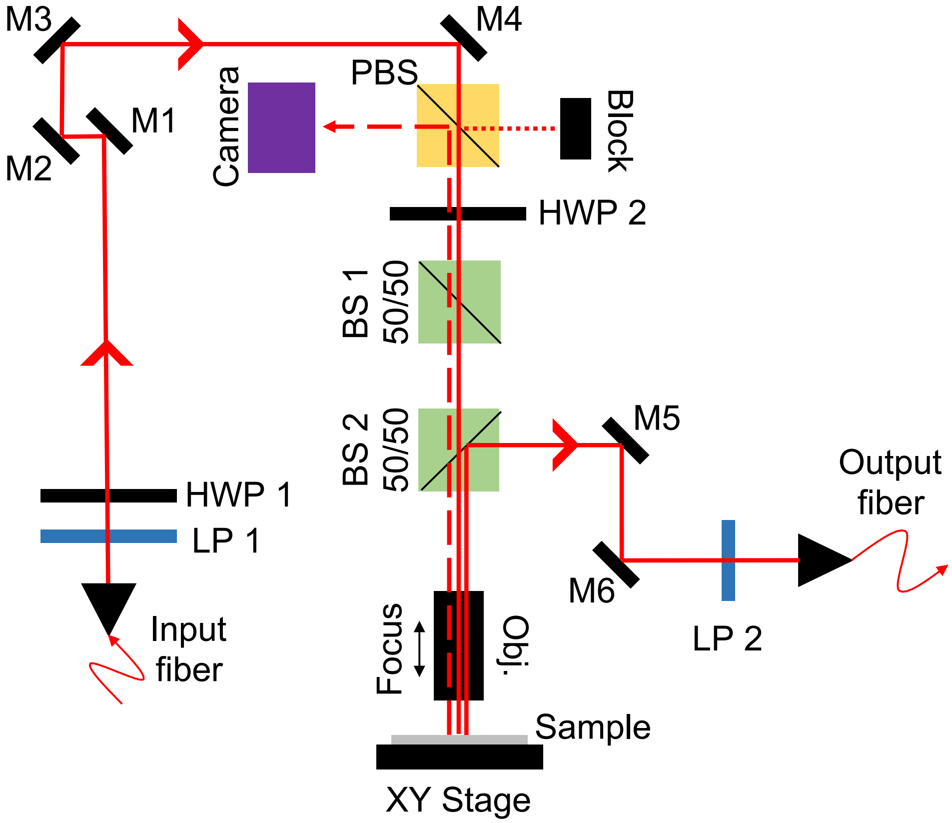

Figure C.1. Schematic of optical setup 1. The sample is mounted vertically and light is input to a fiber collimator and filtered with a linear polarizer (LP 1) to ensure the light is linearly polarized. The polarization angle is controlled with a half-wave plate (HWP 1), such that the subsequent polarizing beamsplitter (PBS) acts as a power-control; typically HWP 1 is adjusted to maximize the transmission, but it can be used to adjust the power without affecting the light source; the transmitted light therefore has a known polarization after this point. The excitation polarization is controlled with HWP 2: 0° (45°) to excite a TE-mode in a horizontal (vertical) waveguide as-displayed on the camera. The light passes two 50:50 beam-splitters (BS); BS 1 allows adding infra red sample illumination with an LED and the transmitted light is measured through BS 2. The collection-polarization is controlled with LP 2. The stage can move along x (horizontal) and y (vertical) with respect to the camera, and the objective is moved to adjust the focus (i.e., along z). The camera images the samples through the reflection path (dashed line), which naturally filters direct reflections thereby making a weak transmitted signal manifest with comparable intensity as the reflected signal. The input path is aligned with mirrors M1 and M2 while the output path is aligned with mirrors M5 and M6.

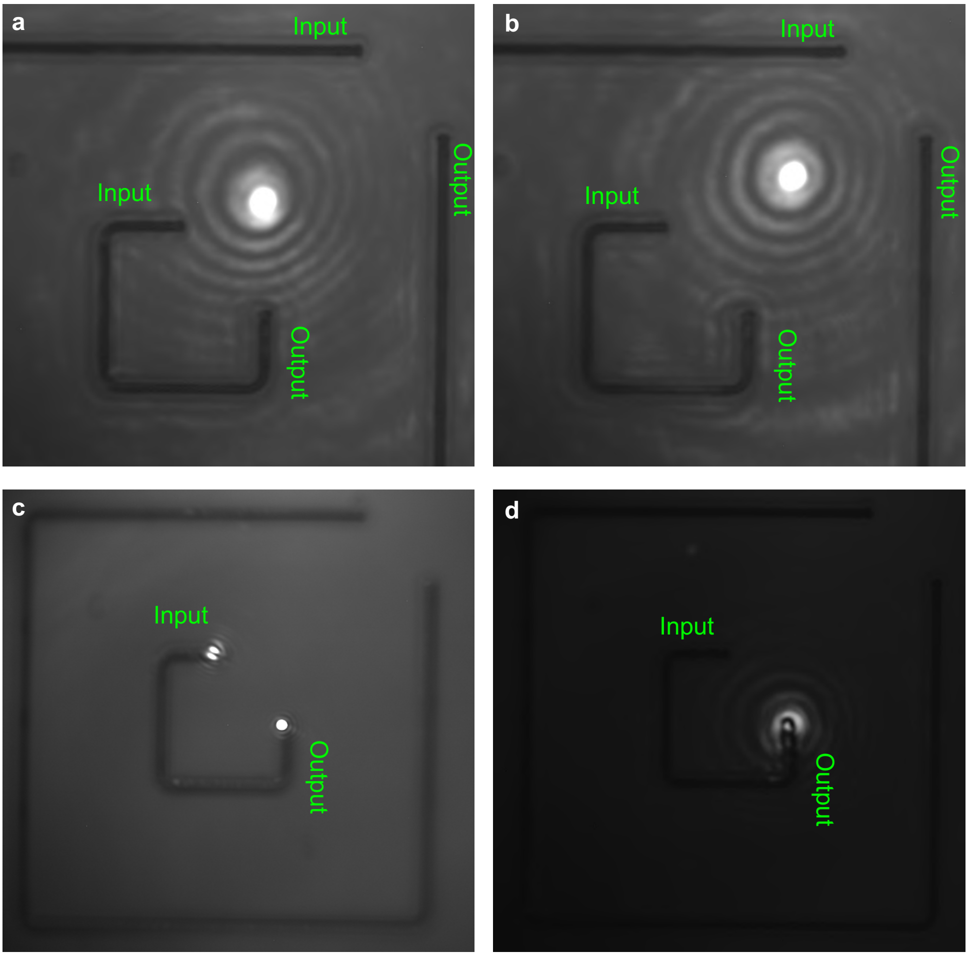

Figure C.2. Camera images captured during different stages of a transmission experiment. **a–b**, Direct reflection by focusing a laser on the silicon surface showing the spot resulting from a misaligned (**a**) and aligned (**b**) path, which can be identified due to the lack of symmetry for the concentric rings in **a**. **c**, Transmission through a short waveguide for a cutback measurement (the next length in this test-circuit is visible along the edges). The concentric rings are faintly visible around the bright spot at the output port, while the direct reflections from the input light appears less clean; the alignment is optimized for the transmission by adjusting the 4 mirrors and the objective focus. **d**, The output-port is excited and the concentric rings showing symmetry of the point-scattering grating coupler; however, transmission to the input port is not visible due to the camera being filtered by a polarizing beamsplitter.

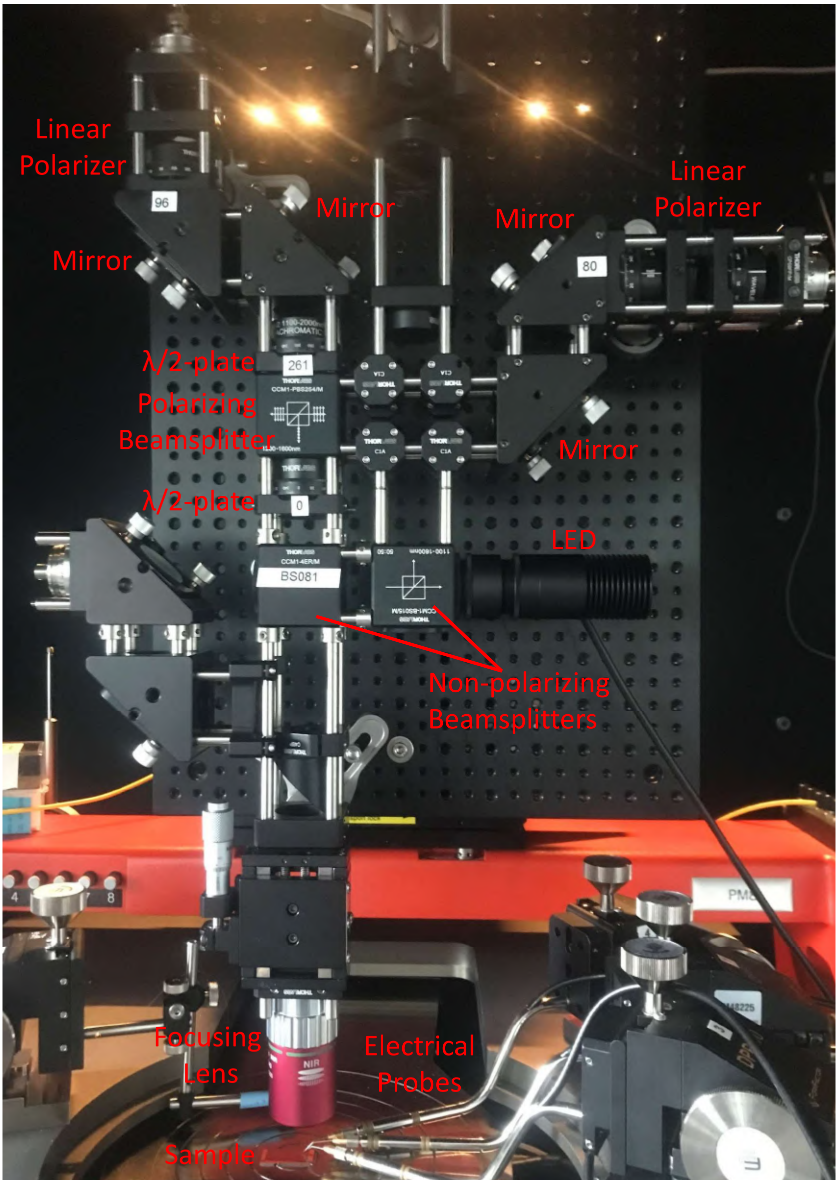

Figure C.3. Optical setup 2 (electro-optic setup). Image of the optical setup, which is mounted vertically on the microscope-tower of an electric probe station. 3 electrical probes (right) are used to contact the sample under the objective. Both in- and output paths go through the polarizing beamsplitter (similarly to the camera path in setup 1), thus only enabling cross-polarized measurements. However, when cross-polarized experiments are desired this configuration is preferable. Figure reproduced from Ref. [38] with permission.

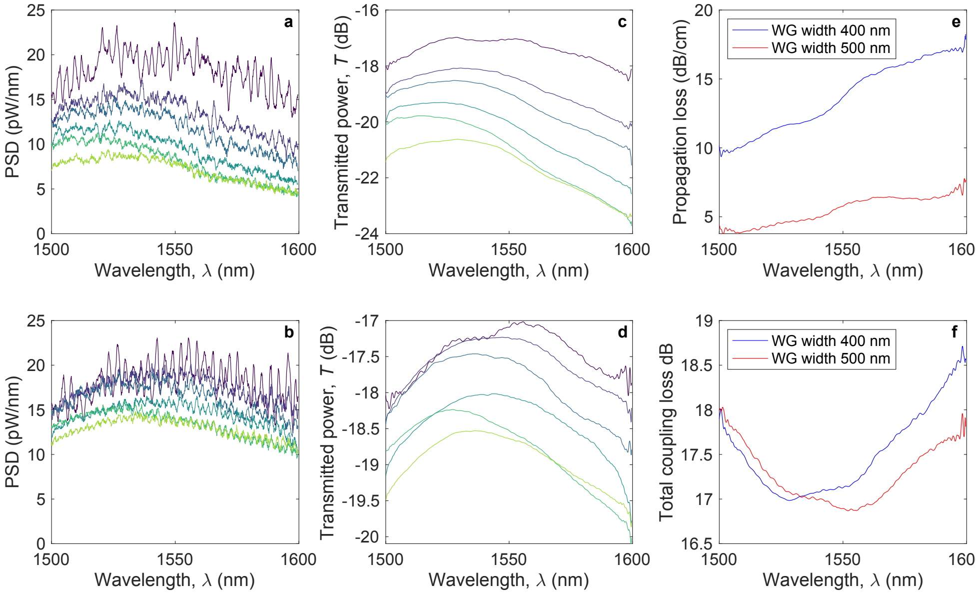

Figure C.4. Optical losses measured with a cutback-method. a (b), A broadband spectrum is acquired for six different circuit-lengths with suspended waveguides that are 400 nm (500 nm) nm wide. **c (d)**, Corresponding smoothed transmission-curves to supress the strong reflections from the point-scatter–type grating couplers [223]. **e** and **f**, Propagation loss and coupling loss as a function of wavelength showing losses as low as 4 dB/cm. The coupling loss includes all losses in the setups, coupling in and out of the chip as well as the 3 bends, the propagation loss includes the loss of the tethers used for mechanical support and spaced every at least 30 µm—as well as before and after each bend—to ensure the thinnest waveguides have sufficient mechanical stability. These structure is fabricated with an intermediate hardmask-process similar to Sec. 4.3 modified as described in Ref. [20].

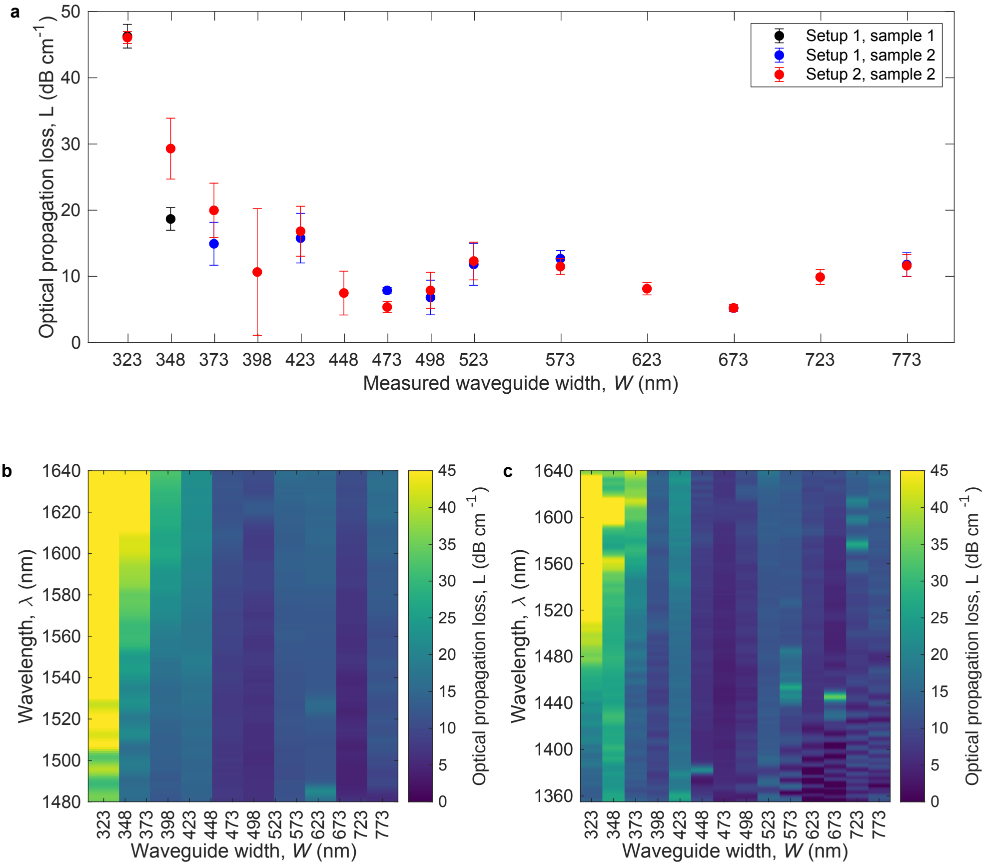

Figure C.5. Broadband propagation-loss in suspended silicon waveguides of various widths. a, Extracted propagation loss at $\lambda = 1520\,\text{nm}$ on two different samples with Optical setup 1 and reproduced for the second sample on Optical setup 2. The widths indicated are measured using scanning-electron microscopy, which verified a 27 nm reduction from the designed dimension. The oscillatory nature might be due to scattering into a leaky second order mode, but the measurements indicates that a wider waveguide (e.g., 673 nm) is not substantially more lossy and due its higher mechanical stability and tighter confinement of the fundamental mode, fewer tethers and sharper bends can be used, which may further reduce losses, thus making a wider waveguide preferable. **b** (**c**), Map of propagation loss against waveguide width and wavelength for optical setup 1 (2). The measurements are performed by sweeping a CW laser (Santec TSL-710, $\lambda = 1480$–$1640\,\text{nm}$). The measurements in **c** are performed with an additional Santec laser ($\lambda = 1355$–$1480\,\text{nm}$) combined with a switch to sweep the entire range without affecting the setup. Figure adapted with permission from data by Jesper Sand in Ref. [38].

Bibliography

[1] J. Bardeen and W. H. Brattain, “The transistor, a semi-conductor triode”, Phys. Rev. **74**, 230–231 (1948).

[2] T. H. Maiman, “Stimulated optical radiation in ruby”, Nature **187**, 493–494 (1960).

[3] P. A. Franken, A. E. Hill, C. W. Peters, and G. Weinreich, “Generation of optical harmonics”, Phys. Rev. Lett. **7**, 118–119 (1961).

[4] G. E. Moore, “Cramming more components onto integrated circuits”, Electronics **38** (1965).

[5] V. M. Donnelly and A. Kornblit, “Plasma etching: yesterday, today, and tomorrow”, J. Vac. Sci. Technol. A **31**, 050825 (2013).

[6] G. Hills, C. Lau, A. Wright, S. Fuller, M. D. Bishop, T. Srimani, P. Kanhaiya, R. Ho, A. Amer, Y. Stein, D. Murphy, Arvind, A. Chandrakasan, and M. M. Shulaker, “Modern microprocessor built from complementary carbon nanotube transistors”, Nature **572**, 595–602 (2019).

[7] H. Aoyama, M. Badaroglu, T. Fedynyshyn, D. Fried, R. Garreis, N. Hayashi, C. Higgins, E. Hosler, H. Ishiuchi, D. Kyser, M. Lercel, H. J. Levinson, K. Macwilliams, T. Nakamura, M. Neisser, S. Okazaki, G. Orji, M. Preil, D. Resnick, R. Tiron, W. Trybula, T. Watanabe, J. Wiley, and S. Wurm, *International roadmap for devices and systems IRDS: lithography* (IEEE, 2022).

[8] S. K. Moore, “The node is nonsense”, IEEE Spectr. **57**, 24–30 (2020).

[9] B. Murmann and B. Hoefflinger, eds., *Nano-chips 2030*, 1st ed., The Frontiers Collection (Springer, Cham, Switzerland, 2020).

[10] S. M. Sze and M. K. Lee, *Semiconductor devices, physics and technology*, 3rd ed (Wiley, Hoboken, N.J, 2012).

[11] V. T. H. Nguyen, C. Silvestre, P. Shi, R. Cork, F. Jensen, J. Hubner, K. Ma, P. Leussink, M. de Boer, and H. Jansen, “The CORE sequence: a nanoscale fluorocarbon-free silicon plasma etch process based on SF_6/O_2 cycles with excellent 3D profile control at room temperature”, ECS J. Solid State Sci. Technol. **9**, 024002 (2020).

[12] M. Bruel, “Process for the production of thin semiconductor material films”, US5374564A (Sept. 15, 1992).

[13] B. Geh, “EUVL: the natural evolution of optical microlithography”, in Extreme ultraviolet (EUV) lithography x, Vol. 10957 (Oct. 18, 2019), p. 1095705.

[14] S. Y. Chou, P. R. Krauss, and P. J. Renstrom, "Nanoimprint lithography", J. Vac. Sci. Technol. B **14**, 4129–4133 (1996).

[15] D. Resnick, "Nanoimprint lithography", in *Nanolithography*, edited by M. Feldman (Woodhead Publishing, Jan. 1, 2014), pp. 315–347.

[16] M. Albrechtsen, B. Vosoughi Lahijani, R. E. Christiansen, V. T. H. Nguyen, L. N. Casses, S. E. Hansen, N. Stenger, O. Sigmund, H. Jansen, J. Mørk, and S. Stobbe, "Nanometer-scale photon confinement in topology-optimized dielectric cavities", Nat. Commun. **13**, 6281 (2022).

[17] M. Albrechtsen, B. Vosoughi Lahijani, and S. Stobbe, "Two regimes of confinement in photonic nanocavities: bulk confinement versus lightning rods", Opt. Express **30**, 15458–15469 (2022).

[18] O. Florez, G. Arregui, M. Albrechtsen, R. C. Ng, J. Gomis-Bresco, S. Stobbe, C. M. Sotomayor-Torres, and P. D. García, "Engineering nanoscale hypersonic phonon transport", Nat. Nanotechnol. **17**, 947–951 (2022).

[19] G. Arregui, R. C. Ng, M. Albrechtsen, S. Stobbe, C. M. Sotomayor-Torres, and P. D. García, "Cavity optomechanics with anderson-localized optical modes", Phys. Rev. Lett. **130**, 043802 (2023).

[20] G. Madiot, R. C. Ng, G. Arregui, O. Florez, M. Albrechtsen, S. Stobbe, P. D. Garcia, and C. M. Sotomayor-Torres, *Optomechanical generation of coherent GHz vibrations in a phononic waveguide*, June 14, 2022, arXiv:`2206.06913`.

[21] R. C. Ng, P. Nizet, D. Navarro-Urrios, G. Arregui, M. Albrechtsen, P. D. García, S. Stobbe, C. M. Sotomayor-Torres, and G. Madiot, *Frequency comb modulation in bimodal optomechanical phonon laser*, Oct. 28, 2022, arXiv:`2210.16370[cond-mat,physics:physics]`.

[22] Z. Yang, T. Albrow-Owen, W. Cai, and T. Hasan, "Miniaturization of optical spectrometers", Science **371** (2021).

[23] T. J. Seok, N. Quack, S. Han, R. S. Muller, and M. C. Wu, "Large-scale broadband digital silicon photonic switches with vertical adiabatic couplers", Optica **3**, 64 (2016).

[24] B. Vosoughi Lahijani, M. Albrechtsen, R. Christiansen, C. Rosiek, K. Tsoukalas, M. Sutherland, and S. Stobbe, "Electronic-photonic circuit crossings", (2022), arXiv:`2204.14257`.

[25] W. Bogaerts, D. Pérez, J. Capmany, D. A. B. Miller, J. Poon, D. Englund, F. Morichetti, and A. Melloni, "Programmable photonic circuits", Nature **586**, 207–216 (2020).

[26] J. Capmany, I. Gasulla, and D. Pérez, "The programmable processor", Nat. Photon. **10**, 6–8 (2016).

[27] G. Jo, P. Edinger, S. J. Bleiker, X. Wang, A. Y. Takabayashi, H. Sattari, N. Quack, M. Jezzini, J. S. Lee, P. Verheyen, I. Zand, U. Khan, W. Bogaerts, G. Stemme, K. B. Gylfason, and F. Niklaus, "Wafer-level hermetically sealed silicon photonic MEMS", Photon. Res. **10**, A14–A21 (2022).

[28] M. Albrechtsen, "Nano-electro-mechanical silicon photonics: design, fabrication, and characterization", MSc. thesis (University of Copenhagen, Nov. 2019).

[29] W. I. Jang, C. A. Choi, J. H. Lee, C. H. Jun, H. Yang, and Y. T. Kim, "Characterization of residues on anhydrous HF gas-phase etching of sacrificial oxides for surface micromachining", Jpn. J. Appl. Phys. **39**, 337–342 (2000).

[30] J. Valle, D. Fernández, and J. Madrenas, "Experimental analysis of vapor HF etch rate and its wafer level uniformity on a CMOS-MEMS process", J. Microelectromech. Syst. **25**, 401–412 (2016).

[31] Y. Fukuta, H. Fujita, and H. Toshiyoshi, "Vapor hydrofluoric acid sacrificial release technique for micro electro mechanical systems using labware", Jpn. J. Appl. Phys. **42**, 3690–3694 (2003).

[32] B. Du Bois, G. Vereecke, A. Witvrouw, P. De Moor, C. Van Hoof, A. De Caussemaeker, and A. Verbist, "HF etching of si-oxides and si-nitrides for surface micromachining", in *Sensor technology 2001*, edited by M. Elwenspoek (Springer Netherlands, Dordrecht, 2001), pp. 131–136.

[33] A. S. Gangnaik, Y. M. Georgiev, and J. D. Holmes, "New generation electron beam resists: a review", Chem. Mater. **29**, 1898–1917 (2017).

[34] M. KGaA, *AZ nLOF 2000 series*, Darmstadt, Germany, 2021, `https://www.microchemicals.com/micro/tds_az_nlof2000_series.pdf`.

[35] M. T. Sutherland, "Fabrication and characterization of locally doped silicon electronic-photonic devices", BSc. thesis (Technical University of Denmark, Jan. 2021).

[36] K. Williams, K. Gupta, and M. Wasilik, "Etch rates for micromachining processing-part II", J. Microelectromech. Syst. **12**, 761–778 (2003).

[37] T. Tsuchizawa, K. Yamada, H. Fukuda, T. Watanabe, J.-i. Takahashi, M. Takahashi, T. Shoji, E. Tamechika, S. Itabashi, and H. Morita, "Microphotonics devices based on silicon microfabrication technology", IEEE J. Sel. Top. Quantum Electron. **11**, 232–240 (2005).

[38] J. Sand, "Characterization of nano-electro-mechanical systems", Special course report (Technical University of Denmark, June 2022).

[39] L. Midolo, A. Schliesser, and A. Fiore, "Nano-opto-electro-mechanical systems", Nat. Nanotechnol. **13**, 11–18 (2018).

[40] K. E. Grutter, M. I. Davanço, and K. Srinivasan, "Slot-mode optomechanical crystals: a versatile platform for multimode optomechanics", Optica **2**, 994–1001 (2015).

[41] D. M. Tennant, R. Fullowan, H. Takemura, M. Isobe, and Y. Nakagawa, "Evaluation of a 100 kV thermal field emission electron-beam nanolithography system", J. Vac. Sci. Technol. B **18**, 3089–3094 (2000).

[42] M. A. Mohammad, M. Muhammad, S. K. Dew, and M. Stepanova, "Fundamentals of electron beam exposure and development", in *Nanofabrication*, edited by M. Stepanova and S. Dew (Springer, Vienna, 2012), pp. 11–41.

[43] N. Saitou, C. Munakata, and Y. Honda, "Change of apparent sensitivity of an electron resist due to backing materials", Jpn. J. Appl. Phys. **11**, 1061–1062 (1972).

[44] R. J. Hawryluk, A. M. Hawryluk, and H. I. Smith, "Energy dissipation in a thin polymer film by electron beam scattering", J. Appl. Phys. **45**, 2551–2566 (1974).

[45] L. V. Spencer and U. Fano, "Energy spectrum resulting from electron slowing down", Phys. Rev. **93**, 1172–1181 (1954).

[46] N. Saitou, "Monte carlo simulation for the energy dissipation profiles of 5–20 keV electrons in layered structures", Jpn. J. Appl. Phys. **12**, 941–942 (1973).

[47] T. H. P. Chang, "Proximity effect in electron-beam lithography", J. Vac. Sci. Technol. **12**, 1271–1275 (1975).

[48] S. A. Rishton, "Point exposure distribution measurements for proximity correction in electron beam lithography on a sub-100 nm scale", J. Vac. Sci. Technol. B **5**, 135 (1987).

[49] H. Duan, D. Winston, J. K. W. Yang, B. M. Cord, V. R. Manfrinato, and K. K. Berggren, "Sub-10-nm half-pitch electron-beam lithography by using poly(methyl methacrylate) as a negative resist", J. Vac. Sci. Technol. B **28**, C6C58–C6C62 (2010).

[50] V. R. Manfrinato, J. Wen, L. Zhang, Y. Yang, R. G. Hobbs, B. Baker, D. Su, D. Zakharov, N. J. Zaluzec, D. J. Miller, E. A. Stach, and K. K. Berggren, "Determining the resolution limits of electron-beam lithography: direct measurement of the point-spread function", Nano Lett. **14**, 4406–4412 (2014).

[51] M. Parikh, "Self-consistent proximity effect correction technique for resist exposure (SPECTRE)", J. Vac. Sci. Technol. **15**, 931–933 (1978).

[52] E. Nomura, K. Murata, and K. Nagami, "Fundamental studies of the interproximity effect in electron-beam lithography", Jpn. J. Appl. Phys. **18**, 1353–1360 (1979).

[53] M. Parikh, "Corrections to proximity effects in electron beam lithography. i. theory", J. Appl. Phys. **50**, 4371–4377 (1979).

[54] G. Owen and P. Rissman, "Proximity effect correction for electron beam lithography by equalization of background dose", J. Appl. Phys. **54**, 3573–3581 (1983).

[55] S. Johnson and N. C. MacDonald, "A program for monte carlo simulation of electron energy loss in nanostructures", J. Vac. Sci. Technol. B **7**, 1513–1518 (1989).

[56] F. Murai, H. Yoda, S. Okazaki, N. Saitou, and Y. Sakitani, "Fast proximity effect correction method using a pattern area density map", J. Vac. Sci. Technol. B **10**, 3072–3076 (1992).

[57] H. Eisenmann, "PROXECCO—proximity effect correction by convolution", J. Vac. Sci. Technol. B **11**, 2741 (1993).

[58] C. A. Mack, "Electron-beam lithography simulation for mask making: VI. comparison of 10- and 50-kV GHOST proximity effect correction", in Photomask and next-generation lithography mask technology VIII, Vol. 4409 (Sept. 5, 2001), pp. 194–203.

[59] D. F. Kyser and C. H. Ting, "Voltage dependence of proximity effects in electron beam lithography", J. Vac. Sci. Technol. **16**, 1759–1763 (1979).

[60] R. E. Howard, H. G. Craighead, L. D. Jackel, P. M. Mankiewich, and M. Feldman, "Electron beam lithography from 20 to 120 keV with a high quality beam", J. Vac. Sci. Technol. B **1**, 1101–1104 (1983).

[61] M. Albrechtsen, B. Vosoughi Lahijani, R. E. Christiansen, V. T. H. Nguyen, L. N. Casses, S. E. Hansen, N. Stenger, O. Sigmund, H. Jansen, J. Mørk, and S. Stobbe, "Shot-filling effects in nanometer-scale electron-beam lithography", in 47th international conference on micro & nano engineering, Turin, Italy (2021), A5–127.

[62] D. M. Tennant, "Progress and issues in e-beam and other top down nanolithography", J. Vac. Sci. Technol. A **31**, 050813 (2013).

[63] M. M. Greve and B. Holst, "Optimization of an electron beam lithography instrument for fast, large area writing at 10 kV acceleration voltage", J. Vac. Sci. Technol. B **31**, 043202 (2013).

[64] E. Højlund-Nielsen, T. Greibe, N. A. Mortensen, and A. Kristensen, "Single-spot e-beam lithography for defining large arrays of nano-holes", Microelectron. Eng. **121**, 104–107 (2014).

[65] P. B. Deotare, M. W. McCutcheon, I. W. Frank, M. Khan, and M. Lončar, "High quality factor photonic crystal nanobeam cavities", Appl. Phys. Lett. **94**, 121106 (2009).

[66] L. Midolo, T. Pregnolato, G. Kiršanskė, and S. Stobbe, "Soft-mask fabrication of gallium arsenide nanomembranes for integrated quantum photonics", Nanotechnology **26**, 484002 (2015).

[67] M. E. Peskin and D. V. Schroeder, *An introduction to quantum field theory*, 1st ed. (Westview Press, United States of America, 1995).

[68] M. Albrechtsen and S. Stobbe, “Power-law short range point-spread function in electron-beam lithography”, in 45th international conference on micro & nano engineering, Rhodos, Greece (2019), PA21.

[69] J. R. Bickford, G. Lopez, N. Belic, and U. Hofmann, “Hydrogen silsesquioxane on SOI proximity and microloading effects correction from a single 1d characterization sample”, J. Vac. Sci. Technol. B **32**, 06F511 (2014).

[70] G. Owen, “Methods for proximity effect correction in electron lithography”, J. Vac. Sci. Technol. B **8**, 1889 (1990).

[71] A. Kaganskiy, T. Heuser, R. Schmidt, S. Rodt, and S. Reitzenstein, “CSAR 62 as negative-tone resist for high-contrast e-beam lithography at temperatures between 4 k and room temperature”, J. Vac. Sci. Technol. B **34**, 061603 (2016).

[72] M. Schirmer, B. Büttner, F. Syrowatka, G. Schmidt, T. Köpnick, and C. Kaiser, “Chemical semi-amplified positive e-beam resist (CSAR 62) for highest resolution”, in 29th european mask and lithography conference, edited by U. F. W. Behringer and W. Maurer, Dresden, Germany (Oct. 1, 2013), p. 88860D.

[73] M. Jansen, B. S. Lazarov, M. Schevenels, and O. Sigmund, “On the similarities between micro/nano lithography and topology optimization projection methods”, Struct. Multidisc. Optim. **48**, 717–730 (2013).

[74] E. H. Eriksen, A. Nazir, P. Balling, J. Vester-Petersen, R. E. Christiansen, O. Sigmund, and S. P. Madsen, “Dose regularization via filtering and projection: an open-source code for optimization-based proximity-effect-correction for nanoscale lithography”, Microelectron. Eng. **199**, 52–57 (2018).

[75] S. J. Wind, “Proximity correction for electron beam lithography using a three-gaussian model of the electron energy distribution”, J. Vac. Sci. Technol. B **7**, 1507 (1989).

[76] M. Kotera and T. Maekawa, “Simulation of fogging electrons in electron beam lithography”, Jpn. J. Appl. Phys. **48**, 06FB05 (2009).

[77] A. Clauset, C. R. Shalizi, and M. E. J. Newman, “Power-law distributions in empirical data”, SIAM Rev. **51**, 661–703 (2009).

[78] V. R. Manfrinato, “Electron-beam lithography towards the atomic scale and applications to nano-optics”, Ph.D. thesis (Massachusetts Institute of Technology, Sept. 2015).

[79] S. Yasin, D. G. Hasko, and H. Ahmed, “Comparison of MIBK/IPA and water/IPA as PMMA developers for electron beam nanolithography”, Microelectron. Eng., Micro- and Nano-Engineering 2001 **61-62**, 745–753 (2002).

[80] J. K. W. Yang, B. Cord, H. Duan, K. K. Berggren, J. Klingfus, S.-W. Nam, K.-B. Kim, and M. J. Rooks, “Understanding of hydrogen silsesquioxane electron resist for sub-5-nm-half-pitch lithography”, J. Vac. Sci. Technol. B **27**, 2622–2627 (2009).

[81] V. T. H. Nguyen, F. Jensen, J. Hübner, P. Leussink, and H. Jansen, "On the formation of black silicon in SF6-o2 plasma: the clear, oxidize, remove, and etch (CORE) sequence and black silicon on demand", J. Vac. Sci. Technol. A **38**, 043004 (2020).

[82] V. T. H. Nguyen, E. Shkondin, F. Jensen, J. Hübner, P. Leussink, and H. Jansen, "Ultrahigh aspect ratio etching of silicon in SF_6-o_2 plasma: the clear-oxidize-remove-etch (CORE) sequence and chromium mask", J. Vac. Sci. Technol. A **38**, 053002 (2020).

[83] V. T. H. Nguyen, F. Jensen, J. Hübner, E. Shkondin, R. Cork, K. Ma, P. Leussink, W. De Malsche, and H. Jansen, "Cr and CrO_x etching using SF_6 and o_2 plasma", J. Vac. Sci. Technol. B **39**, 032201 (2021).

[84] C. A. Rosiek, G. Arregui, A. Vladimirova, M. Albrechtsen, B. V. Lahijani, R. E. Christiansen, and S. Stobbe, *Observation of strong backscattering in valley-hall topological interface modes*, Number: arXiv:2206.11741, June 23, 2022, arXiv:`2206.11741[physics]`.

[85] A. Reinberg, "Radial flow reactor", U.S. pat. 3757733A (T. I. Inc, Sept. 11, 1973).

[86] M. A. Lieberman and A. J. Lichtenberg, *Principles of plasma discharges and materials processing: lieberman/plasma 2e* (John Wiley & Sons, Inc., Hoboken, NJ, USA, Apr. 8, 2005).

[87] V. T. H. Nguyen, "Directional nanoscale silicon etching using SF_6 and O_2 plasma", Ph.D. thesis (Technical University of Denmark, Nov. 2020).

[88] H. V. Jansen, M. J. d. Boer, S. Unnikrishnan, M. C. Louwerse, and M. C. Elwenspoek, "Black silicon method: x. a review on high speed and selective plasma etching of silicon with profile control: an in-depth comparison between bosch and cryostat DRIE processes as a roadmap to next generation equipment", J. Micromech. Microeng. **19**, 033001 (2009).

[89] H. Jansen, M. d. Boer, R. Legtenberg, and M. Elwenspoek, "The black silicon method: a universal method for determining the parameter setting of a fluorine-based reactive ion etcher in deep silicon trench etching with profile control", J. Micromech. Microeng. **5**, 115–120 (1995).

[90] F. Laermer and A. Schilp, "Method of anisotropically etching silicon", U.S. pat. 5501893 (R. B. GmbH, Mar. 26, 1996).

[91] H. Jansen, M. de Boer, R. Wiegerink, N. Tas, E. Smulders, C. Neagu, and M. Elwenspoek, "BSM 7: RIE lag in high aspect ratio trench etching of silicon", Microelectron. Eng. **35**, 45–50 (1997).

[92] B. Chang, P. Leussink, F. Jensen, J. Hübner, and H. Jansen, "DREM: infinite etch selectivity and optimized scallop size distribution with conventional photoresists in an adapted multiplexed bosch DRIE process", Microelectron. Eng. **191**, 77–83 (2018).

[93] B. Chang, F. Jensen, J. Hübner, and H. Jansen, “DREM2: a facile fabrication strategy for freestanding three dimensional silicon micro- and nanostructures by a modified bosch etch process”, J. Micromech. Microeng. **28**, 105012 (2018).

[94] M. De Marchi, D. Sacchetto, J. Zhang, S. Frache, P.-E. Gaillardon, Y. Leblebici, and G. De Micheli, “Top–down fabrication of gate-all-around vertically stacked silicon nanowire FETs with controllable polarity”, IEEE Trans. Nanotechnol. **13**, 1029–1038 (2014).

[95] Y. Tang, Z. Wang, L. Wosinski, U. Westergren, and S. He, “Highly efficient nonuniform grating coupler for silicon-on-insulator nanophotonic circuits”, Opt. Lett. **35**, 1290 (2010).

[96] M. Albrechtsen, A. N. Babar, B. Vosoughi Lahijani, E. Shkondin, G. Arregui, J. Sand, H. Jansen, and S. Stobbe, “Tailoring a nanometer-scale fabrication process for silicon photonics”, in 48th international conference on micro & nano engineering, Leuven, Belgium (2022), T1A18.

[97] G. S. Hwang and K. P. Giapis, “On the origin of the notching effect during etching in uniform high density plasmas”, J. Vac. Sci. Technol. B **15**, 70–87 (1997).

[98] M. Meinshausen, S. J. Smith, K. Calvin, J. S. Daniel, M. L. T. Kainuma, J.-F. Lamarque, K. Matsumoto, S. A. Montzka, S. C. B. Raper, K. Riahi, A. Thomson, G. J. M. Velders, and D. P. van Vuuren, “The RCP greenhouse gas concentrations and their extensions from 1765 to 2300”, Climatic Change **109**, 213–241 (2011).

[99] F. Illuzzi and H. Thewissen, “Perfluorocompounds emission reduction by the semiconductor industry”, J. Integr. Environ. Sci. **7**, 201–210 (2010).

[100] P. Frankwicz, L. Gardner, and T. Moutinho, “Reduction of greenhouse gas emissions by metal interconnect etch process optimization”, in 220th ECS meeting, Boston, MA (2012), pp. 1–7.

[101] T. Kovács, W. Feng, A. Totterdill, J. M. C. Plane, S. Dhomse, J. C. Gómez-Martín, G. P. Stiller, F. J. Haenel, C. Smith, P. M. Forster, R. R. García, D. R. Marsh, and M. P. Chipperfield, “Determination of the atmospheric lifetime and global warming potential of sulfur hexafluoride using a three-dimensional model”, Atmospheric Chem. Phys. **17**, 883–898 (2017).

[102] M. Aspelmeyer, T. J. Kippenberg, and F. Marquardt, “Cavity optomechanics”, Rev. Mod. Phys. **86**, 1391–1452 (2014).

[103] K. J. Vahala, “Optical microcavities”, Nature **424**, 839–846 (2003).

[104] M. Notomi, “Manipulating light with strongly modulated photonic crystals”, Rep. Prog. Phys. **73**, 096501 (2010).

[105] P. Lodahl, S. Mahmoodian, and S. Stobbe, “Interfacing single photons and single quantum dots with photonic nanostructures”, Rev. Mod. Phys. **87**, 347–400 (2015).

[106] O. Painter, R. K. Lee, A. Scherer, A. Yariv, J. D. O'Brien, P. D. Dapkus, and I. Kim, "Two-dimensional photonic band-gap defect mode laser", Science **284**, 1819–1821 (1999).

[107] Y. Yu, W. Xue, E. Semenova, K. Yvind, and J. Mork, "Demonstration of a self-pulsing photonic crystal fano laser", Nat. Photonics **11**, 81–84 (2017).

[108] A. A. Jørgensen, D. Kong, M. R. Henriksen, F. Klejs, Z. Ye, Ò. B. Helgason, H. E. Hansen, H. Hu, M. Yankov, S. Forchhammer, P. Andrekson, A. Larsson, M. Karlsson, J. Schröder, Y. Sasaki, K. Aikawa, J. W. Thomsen, T. Morioka, M. Galili, V. Torres-Company, and L. K. Oxenløwe, "Petabit-per-second data transmission using a chip-scale microcomb ring resonator source", Nat. Photon. **16**, 798–802 (2022).

[109] C. Papon, Y. Wang, R. Uppu, S. Scholz, A. D. Wieck, A. Ludwig, P. Lodahl, and L. Midolo, *Independent operation of two waveguide-integrated single-photon sources*, Oct. 18, 2022, arXiv:`2210.09826`.

[110] A. F. Koenderink, A. Alu, and A. Polman, "Nanophotonics: shrinking light-based technology", Science **348**, 516–521 (2015).

[111] T. A. Birks, J. C. Knight, and P. S. J. Russell, "Endlessly single-mode photonic crystal fiber", Opt. Lett. **22**, 961–963 (1997).

[112] X. Ji, F. A. S. Barbosa, S. P. Roberts, A. Dutt, J. Cardenas, Y. Okawachi, A. Bryant, A. L. Gaeta, and M. Lipson, "Ultra-low-loss on-chip resonators with sub-milliwatt parametric oscillation threshold", Optica **4**, 619 (2017).

[113] S. Y. Siew, B. Li, F. Gao, H. Y. Zheng, W. Zhang, P. Guo, S. W. Xie, A. Song, B. Dong, L. W. Luo, C. Li, X. Luo, and G.-Q. Lo, "Review of silicon photonics technology and platform development", J. Light. Technol. **39**, 4374–4389 (2021).

[114] Y. Akahane, T. Asano, B.-S. Song, and S. Noda, "High-Q photonic nanocavity in a two-dimensional photonic crystal", Nature **425**, 944–947 (2003).

[115] H. Choi, M. Heuck, and D. Englund, "Self-similar nanocavity design with ultrasmall mode volume for single-photon nonlinearities", Phys. Rev. Lett. **118**, 223605 (2017).

[116] P. T. Kristensen, K. Herrmann, F. Intravaia, and K. Busch, "Modeling electromagnetic resonators using quasinormal modes", Adv. Opt. Photon. **12**, 612–708 (2020).

[117] J. D. Jackson, *Classical electrodynamics*, 3rd (Wiley, N.J., 1999).

[118] L. Novotny and B. Hecht, *Principles of nano-optics*, 2nd ed. (Cambridge Univ. Press, 2012).

[119] L. D. Landau, E. M. Lifshitz, and L. P. Pitaevskii, *Electrodynamics of continuous media*, 2nd ed., Translated by J. B. Sykes, J. S. Bell, M. J. Kearsley. (Pergamon, Oxford, 1984), (Original work published 1982).

[120] T. J. Kippenberg, S. M. Spillane, and K. J. Vahala, “Demonstration of ultra-high-Q small mode volume toroid microcavities on a chip”, Appl. Phys. Lett. **85**, 6113 (2004).

[121] B.-S. Song, S. Noda, T. Asano, and Y. Akahane, “Ultra-high-q photonic double-heterostructure nanocavity”, Nat. Mater. **4**, 207–210 (2005).

[122] T. Asano, Y. Ochi, Y. Takahashi, K. Kishimoto, and S. Noda, “Photonic crystal nanocavity with a Q factor exceeding eleven million”, Opt. Express **25**, 1769–1777 (2017).

[123] H. Sekoguchi, Y. Takahashi, T. Asano, and S. Noda, “Photonic crystal nanocavity with a Q-factor of ~9 million”, Opt. Express **22**, 916–924 (2014).

[124] M. Minkov and V. Savona, “Automated optimization of photonic crystal slab cavities”, Sci. Rep. **4**, 5124 (2014).

[125] J. Andersen and V. Solodukhov, “Field behavior near a dielectric wedge”, IEEE Trans. Antennas Propag. **26**, 598–602 (1978).

[126] J. Van Bladel, “Field singularities at the tip of a dielectric cone”, IEEE Trans. Antennas Propag. **33**, 893–895 (1985).

[127] P. T. Kristensen, “Light-matter interaction in nanostructured materials”, Ph.D. thesis (Technical University of Denmark, Dec. 2009).

[128] P. T. Kristensen, C. Van Vlack, and S. Hughes, “Generalized effective mode volume for leaky optical cavities”, Opt. Lett. **37**, 1649–1651 (2012).

[129] P. T. Kristensen, R.-C. Ge, and S. Hughes, “Normalization of quasinormal modes in leaky optical cavities and plasmonic resonators”, Phys. Rev. A **92**, 053810 (2015).

[130] E. M. Purcell, “Spontaneous emission probabilities at radio frequencies”, Phys. Rev. **69**, 681 (1946).

[131] T. Wu, M. Gurioli, and P. Lalanne, “Nanoscale light confinement: the Q’s and V’s”, ACS Photonics **8**, 1522–1538 (2021).

[132] F. Wang, R. E. Christiansen, Y. Yu, J. Mørk, and O. Sigmund, “Maximizing the quality factor to mode volume ratio for ultra-small photonic crystal cavities”, Appl. Phys. Lett. **113**, 241101 (2018).

[133] A. Sommerfeld, *Mathematical theory of diffraction*, 1st ed., Translated by R. J. Nagem, M. Zampolli, G. Sandri. (Original work published Math. Ann. **47**, 317–374 (1896).) (Birkhäuser Boston, Boston, MA, 2004).

[134] N. I. Zheludev, “What diffraction limit?”, Nature Mater **7**, 420–422 (2008).

[135] S. Hu and S. M. Weiss, “Design of photonic crystal cavities for extreme light concentration”, ACS Photonics **3**, 1647–1653 (2016).

[136] A. Gondarenko, S. Preble, J. Robinson, L. Chen, H. Lipson, and M. Lipson, “Spontaneous emergence of periodic patterns in a biologically inspired simulation of photonic structures”, Phys. Rev. Lett. **96**, 143904 (2006).

[137] A. Gondarenko and M. Lipson, “Low modal volume dipole-like dielectric slab resonator”, Opt. Express **16**, 17689–17694 (2008).

[138] Q. Lu, F.-J. Shu, and C.-L. Zou, “Dielectric bow-tie nanocavity”, Opt. Lett. **38**, 5311–5314 (2013).

[139] X. Liang and S. G. Johnson, “Formulation for scalable optimization of microcavities via the frequency-averaged local density of states”, Opt. Express **21**, 30812–30841 (2013).

[140] J. B. Khurgin, “How to deal with the loss in plasmonics and metamaterials”, Nat. Nanotechnol. **10**, 2–6 (2015).

[141] P. Lodahl, S. Mahmoodian, S. Stobbe, A. Rauschenbeutel, P. Schneeweiss, J. Volz, H. Pichler, and P. Zoller, “Chiral quantum optics”, Nature **541**, 473–480 (2017).

[142] R. Coccioli, M. Boroditsky, K. Kim, Y. Rahmat-Samii, and E. Yablonovitch, “Smallest possible electromagnetic mode volume in a dielectric cavity”, IEE Proc., Optoelectron. **145**, 391–397 (1998).

[143] P. B. Deotare, M. W. McCutcheon, I. W. Frank, M. Khan, and M. Lončar, “Coupled photonic crystal nanobeam cavities”, Appl. Phys. Lett. **95**, 031102 (2009).

[144] F. Wang and Y. R. Shen, “General properties of local plasmons in metal nanostructures”, Phys. Rev. Lett. **97**, 206806 (2006).

[145] G. Kountouris, J. Mørk, E. V. Denning, and P. T. Kristensen, “Modal properties of dielectric bowtie cavities with deep sub-wavelength confinement”, Opt. Express **30**, 40367–40378 (2022).

[146] S. Hu, M. Khater, R. Salas-Montiel, E. Kratschmer, S. Engelmann, W. M. J. Green, and S. M. Weiss, “Experimental realization of deep-subwavelength confinement in dielectric optical resonators”, Sci. Adv. **4**, eaat2355 (2018).

[147] R. E. Christiansen, P. T. Kristensen, J. Mørk, and O. Sigmund, “Impact of figures of merit in photonic inverse design”, Opt. Express **31**, 8363–8374 (2023).

[148] G. Işiklar, P. T. Kristensen, J. Mørk, O. Sigmund, and R. E. Christiansen, “On the trade-off between mode volume and quality factor in dielectric nanocavities optimized for purcell enhancement”, Opt. Express **30**, 47304–47314 (2022).

[149] Y. Akahane, T. Asano, B.-S. Song, and S. Noda, “Fine-tuned high-q photonic-crystal nanocavity”, Opt. Express **13**, 1202 (2005).

[150] Y. Ma, B. Dong, and C. Lee, “Progress of infrared guided-wave nanophotonic sensors and devices”, Nano Convergence **7**, 12 (2020).

[151] M. Minkov, V. Savona, and D. Gerace, “Photonic crystal slab cavity simultaneously optimized for ultra-high Q / V and vertical radiation coupling”, Appl. Phys. Lett. **111**, 131104 (2017).

[152] M. A. Bandres, S. Wittek, G. Harari, M. Parto, J. Ren, M. Segev, D. N. Christodoulides, and M. Khajavikhan, “Topological insulator laser: experiments”, Science **359**, eaar4005 (2018).

[153] N. A. Mortensen, S. Raza, M. Wubs, T. Søndergaard, and S. I. Bozhevolnyi, “A generalized non-local optical response theory for plasmonic nanostructures”, Nat. Commun. **5**, 3809 (2014).

[154] J. T. Robinson, C. Manolatou, L. Chen, and M. Lipson, “Ultrasmall mode volumes in dielectric optical microcavities”, Phys. Rev. Lett. **95**, 143901 (2005).

[155] V. R. Almeida, Q. Xu, C. A. Barrios, and M. Lipson, “Guiding and confining light in void nanostructure”, Opt. Lett. **29**, 1209–1211 (2004).

[156] J. Lu, S. Boyd, and J. Vučković, “Inverse design of a three-dimensional nanophotonic resonator”, Opt. Express **19**, 10563 (2011).

[157] J. Zhou, J. Zheng, Z. Fang, P. Xu, and A. Majumdar, “Ultra-low mode volume on-substrate silicon nanobeam cavity”, Opt. Express **27**, 30692–30699 (2019).

[158] S. Mignuzzi, S. Vezzoli, S. A. R. Horsley, W. L. Barnes, S. A. Maier, and R. Sapienza, “Nanoscale design of the local density of optical states”, Nano Lett. **19**, 1613–1617 (2019).

[159] H. Shim, L. Fan, S. G. Johnson, and O. D. Miller, “Fundamental limits to near-field optical response over any bandwidth”, Phys. Rev. X **9**, 011043 (2019).

[160] P. Chao, B. Strekha, R. Kuate Defo, S. Molesky, and A. W. Rodriguez, “Physical limits in electromagnetism”, Nat. Rev. Phys., 1–17 (2022).

[161] M. P. Bendsoe and O. Sigmund, *Topology optimization: theory, methods, and applications* (Springer Science & Business Media, Apr. 17, 2013).

[162] K. Svanberg, “A class of globally convergent optimization methods based on conservative convex separable approximations”, SIAM J. Optim. **12**, 555–573 (2002).

[163] N. Aage, E. Andreassen, B. S. Lazarov, and O. Sigmund, “Giga-voxel computational morphogenesis for structural design”, Nature **550**, 84–86 (2017).

[164] M. Baandrup, O. Sigmund, H. Polk, and N. Aage, “Closing the gap towards super-long suspension bridges using computational morphogenesis”, Nat. Commun. **11**, 2735 (2020).

[165] P. I. Borel, A. Harpøth, L. H. Frandsen, M. Kristensen, P. Shi, J. S. Jensen, and O. Sigmund, “Topology optimization and fabrication of photonic crystal structures”, Opt. Express **12**, 1996–2001 (2004).

[166] J. S. Jensen and O. Sigmund, “Topology optimization for nano-photonics”, Laser Photonics Rev. **5**, 308–321 (2011).

[167] R. E. Christiansen and O. Sigmund, “Inverse design in photonics by topology optimization: tutorial”, J. Opt. Soc. Am. B **38**, 496–509 (2021).

[168] S. Molesky, Z. Lin, A. Y. Piggott, W. Jin, J. Vučković, and A. W. Rodriguez, “Inverse design in nanophotonics”, Nat. Photonics **12**, 659–670 (2018).

[169] R. E. Christiansen and O. Sigmund, “A 200 line MATLAB code for inverse design in photonics by topology optimization”, arXiv:2009.14276 [physics] (2020).

[170] O. Sigmund, “A 99 line topology optimization code written in matlab”, Struct. Multidisc. Optim. **21**, 120–127 (2001).

[171] R. E. Christiansen, J. Vester-Petersen, S. P. Madsen, and O. Sigmund, “A nonlinear material interpolation for design of metallic nano-particles using topology optimization”, Comput. Methods. Appl. Mech. Eng. **343**, 23–39 (2019).

[172] F. Wang, B. S. Lazarov, and O. Sigmund, “On projection methods, convergence and robust formulations in topology optimization”, Struct. Multidisc. Optim. **43**, 767–784 (2011).

[173] M. Zhou, B. S. Lazarov, F. Wang, and O. Sigmund, “Minimum length scale in topology optimization by geometric constraints”, Comput. Methods Appl. Mech. Eng. **293**, 266–282 (2015).

[174] J.-M. Jin, *The finite element method in electromagnetics*, 3rd ed. (Wiley, N.J., 2015).

[175] T. Yoshie, A. Scherer, J. Hendrickson, G. Khitrova, H. M. Gibbs, G. Rupper, C. Ell, O. B. Shchekin, and D. G. Deppe, “Vacuum rabi splitting with a single quantum dot in a photonic crystal nanocavity”, Nature **432**, 200–203 (2004).

[176] M. Galli, S. L. Portalupi, M. Belotti, L. C. Andreani, L. O’Faolain, and T. F. Krauss, “Light scattering and fano resonances in high-Q photonic crystal nanocavities”, Appl. Phys. Lett. **94**, 071101 (2009).

[177] N. Ocelic, A. Huber, and R. Hillenbrand, “Pseudoheterodyne detection for background-free near-field spectroscopy”, Appl. Phys. Lett. **89**, 101124 (2006).

[178] A. Bhattacharyya, “On a measure of divergence between two statistical populations defined by their probability distributions”, Bull. Calcutta Math. Soc. **35**, 99–109 (1943).

[179] F. J. García de Abajo, “Optical excitations in electron microscopy”, Rev. Mod. Phys. **82**, 209–275 (2010).

[180] J. A. Rogers, M. G. Lagally, and R. G. Nuzzo, “Synthesis, assembly and applications of semiconductor nanomembranes”, Nature **477**, 45–53 (2011).

[181] A. Gritsch, A. Ulanowski, and A. Reiserer, *Purcell enhancement of single photon emitters in silicon*, Jan. 18, 2023, arXiv:`2301.07753[quant-ph]`.

[182] V. Saggio, C. Errando-Herranz, S. Gyger, C. Panuski, M. Prabhu, L. De Santis, I. Christen, D. Ornelas-Huerta, H. Raniwala, C. Gerlach, M. Colangelo, and D. Englund, *Cavity-enhanced single artificial atoms in silicon*, Feb. 20, 2023.

[183] T. J. Kippenberg and K. J. Vahala, “Cavity optomechanics: back-action at the mesoscale”, Science **321**, 1172–1176 (2008).

[184] M. Eichenfield, J. Chan, R. M. Camacho, K. J. Vahala, and O. Painter, "Optomechanical crystals", Nature **462**, 78–82 (2009).

[185] M. Eichenfield, R. Camacho, J. Chan, K. J. Vahala, and O. Painter, "A picogram- and nanometre-scale photonic-crystal optomechanical cavity", Nature **459**, 550–555 (2009).

[186] M. L. Gorodetksy, A. Schliesser, G. Anetsberger, S. Deleglise, and T. J. Kippenberg, "Determination of the vacuum optomechanical coupling rate using frequency noise calibration", Opt. Express **18**, 23236–23246 (2010).

[187] A. H. Safavi-Naeini and O. Painter, "Design of optomechanical cavities and waveguides on a simultaneous bandgap phononic-photonic crystal slab", Opt. Express **18**, 14926–14943 (2010).

[188] A. H. Safavi-Naeini, J. T. Hill, S. Meenehan, J. Chan, S. Gröblacher, and O. Painter, "Two-dimensional phononic-photonic band gap optomechanical crystal cavity", Phys. Rev. Lett. **112**, 153603 (2014).

[189] H. Ren, M. H. Matheny, G. S. MacCabe, J. Luo, H. Pfeifer, M. Mirhosseini, and O. Painter, "Two-dimensional optomechanical crystal cavity with high quantum cooperativity", Nat. Commun. **11**, 3373 (2020).

[190] B. Gurlek, V. Sandoghdar, and D. Martin-Cano, "Engineering long-lived vibrational states for an organic molecule", Phys. Rev. Lett. **127**, 123603 (2021), arXiv:`2104.01254`.

[191] R. C. Ng, A. E. Sachat, F. Cespedes, M. Poblet, G. Madiot, J. Jaramillo-Fernandez, O. Florez, P. Xiao, M. Sledzinska, C. M. Sotomayor-Torres, and E. Chavez-Angel, "Excitation and detection of acoustic phonons in nanoscale systems", Nanoscale **14**, 13428–13451 (2022).

[192] A. H. Safavi-Naeini, T. P. M. Alegre, M. Winger, and O. Painter, "Optomechanics in an ultrahigh-q two-dimensional photonic crystal cavity", Appl. Phys. Lett. **97**, 181106 (2010).

[193] D. Navarro-Urrios, M. F. Colombano, G. Arregui, G. Madiot, A. Pitanti, A. Griol, T. Makkonen, J. Ahopelto, C. M. Sotomayor-Torres, and A. Martínez, "Room-temperature silicon platform for GHz-frequency nanoelectro-opto-mechanical systems", ACS Photonics (2022).

[194] L. Sapienza, H. Thyrrestrup, S. Stobbe, P. D. Garcia, S. Smolka, and P. Lodahl, "Cavity quantum electrodynamics with anderson-localized modes", Science **327**, 1352–1355 (2010).

[195] P. D. García, R. Bericat-Vadell, G. Arregui, D. Navarro-Urrios, M. Colombano, F. Alzina, and C. M. Sotomayor-Torres, "Optomechanical coupling in the anderson-localization regime", Phys. Rev. B **95**, 115129 (2017).

[196] H. H. Sheinfux, Y. Lumer, G. Ankonina, A. Z. Genack, G. Bartal, and M. Segev, "Observation of anderson localization in disordered nanophotonic structures", Science **356**, 953–956 (2017).

[197] J. Topolancik, F. Vollmer, and B. Ilic, “Random high-q cavities in disordered photonic crystal waveguides”, Appl. Phys. Lett. **91**, 201102 (2007).

[198] R. Leijssen, G. R. La Gala, L. Freisem, J. T. Muhonen, and E. Verhagen, “Nonlinear cavity optomechanics with nanomechanical thermal fluctuations”, Nat. Commun. **8**, ncomms16024 (2017).

[199] L. Mercadé, K. Pelka, R. Burgwal, A. Xuereb, A. Martínez, and E. Verhagen, “Floquet phonon lasing in multimode optomechanical systems”, Phys. Rev. Lett. **127**, 073601 (2021).

[200] R. Legtenberg, A. W. Groeneveld, and M. Elwenspoek, “Comb-drive actuators for large displacements”, J. Micromech. Microeng. **6**, 320–329 (1996).

[201] K. Takahashi, E. Bulgan, Y. Kanamori, and K. Hane, “Submicrometer comb-drive actuators fabricated on thin single crystalline silicon layer”, IEEE Trans. Ind. Electron. **56**, 991–995 (2009).

[202] S. Abe, M. H. Chu, T. Sasaki, and K. Hane, “Time response of a microelectromechanical silicon photonic waveguide coupler switch”, IEEE Photon. Technol. Lett. **26**, 1553–1556 (2014).

[203] Y. M. Sabry, D. Khalil, and T. Bourouina, “Monolithic silicon-micromachined free-space optical interferometers onchip”, Laser & Photonics Rev. **9**, 1–24 (2015).

[204] A. Fathy, Y. M. Sabry, S. Nazeer, T. Bourouina, and D. A. Khalil, “On-chip parallel fourier transform spectrometer for broadband selective infrared spectral sensing”, Microsyst. Nanoeng. **6**, 10 (2020).

[205] P. H. Pham, L. B. Dang, and H. N. Vu, “Micro robot system with moving micro-car driven by electrostatic comb-drive actuators”, Microsyst. Technol. **16**, 505–510 (2010).

[206] T. Grottke, W. Hartmann, C. Schuck, and W. H. P. Pernice, “Optoelectromechanical phase shifter with low insertion loss and a 13 tuning range”, Opt. Express **29**, 5525–5537 (2021).

[207] R. Baghdadi, M. Gould, S. Gupta, M. Tymchenko, D. Bunandar, C. Ramey, and N. C. Harris, “Dual slot-mode NOEM phase shifter”, Opt. Express **29**, 19113 (2021).

[208] S. Han, T. J. Seok, C.-K. Kim, R. S. Muller, and M. C. Wu, “Multicast silicon photonic MEMS switches with gap-adjustable directional couplers”, Opt. Express **27**, 17561 (2019).

[209] S. Han, J. Beguelin, L. Ochikubo, J. Jacobs, T. J. Seok, K. Yu, N. Quack, C.-K. Kim, R. S. Muller, and M. C. Wu, “32 × 32 silicon photonic MEMS switch with gap-adjustable directional couplers fabricated in commercial CMOS foundry”, JOM **1**, 024003 (2021).

[210] C. Papon, X. Zhou, H. Thyrrestrup, Z. Liu, S. Stobbe, R. Schott, A. D. Wieck, A. Ludwig, P. Lodahl, and L. Midolo, “Nanomechanical single-photon routing”, Optica **6**, 524 (2019).

[211] Y. Shen, N. C. Harris, S. Skirlo, M. Prabhu, T. Baehr-Jones, M. Hochberg, X. Sun, S. Zhao, H. Larochelle, D. Englund, and M. Soljačić, “Deep learning with coherent nanophotonic circuits”, Nat. Photonics **11**, 441–446 (2017).

[212] S. Gyger, J. Zichi, L. Schweickert, A. W. Elshaari, S. Steinhauer, S. F. Covre da Silva, A. Rastelli, V. Zwiller, K. D. Jöns, and C. Errando-Herranz, “Reconfigurable photonics with on-chip single-photon detectors”, Nat. Commun. **12**, 1408 (2021).

[213] S. Oda and D. Ferry, *Silicon nanoelectronics* (CRC Press, Dec. 19, 2017).

[214] M. C. M. M. Souza, A. Grieco, N. C. Frateschi, and Y. Fainman, “Fourier transform spectrometer on silicon with thermo-optic non-linearity and dispersion correction”, Nat. Commun. **9**, 665–672 (2018).

[215] S. N. Zheng, J. Zou, H. Cai, J. F. Song, L. K. Chin, P. Y. Liu, Z. P. Lin, D. L. Kwong, and A. Q. Liu, “Microring resonator-assisted fourier transform spectrometer with enhanced resolution and large bandwidth in single chip solution”, Nat. Commun. **10**, 2349–2356 (2019).

[216] D. Pohl, M. Reig Escalé, M. Madi, F. Kaufmann, P. Brotzer, A. Sergeyev, B. Guldimann, P. Giaccari, E. Alberti, U. Meier, and R. Grange, “An integrated broadband spectrometer on thin-film lithium niobate”, Nat. Photonics **14**, 24–29 (2019).

[217] L. Midolo, S. L. Hansen, W. Zhang, C. Papon, R. Schott, A. Ludwig, A. D. Wieck, P. Lodahl, and S. Stobbe, “Electro-optic routing of photons from single quantum dots in photonic integrated circuits”, Opt. Express **25**, 33514 (2017).

[218] K. Tsoukalas, B. Vosoughi Lahijani, and S. Stobbe, “Impact of transduction scaling laws on nanoelectromechanical systems”, Phys. Rev. Lett. **124**, 223902–7 (2020).

[219] K. Van Acoleyen, J. Roels, P. Mechet, T. Claes, D. Van Thourhout, and R. Baets, “Ultracompact phase modulator based on a cascade of NEMS-operated slot waveguides fabricated in silicon-on-insulator”, IEEE Photonics J. **4**, 779–788 (2012).

[220] W. M. v. Spengen, E. Bakker, and J. W. M. Frenken, “A ‘nano-battering ram’ for measuring surface forces: obtaining force–distance curves and sidewall stiction data with a MEMS device”, J. Micromech. Microeng. **17**, S91–S97 (2007).

[221] C. Errando-Herranz, A. Y. Takabayashi, P. Edinger, H. Sattari, K. B. Gylfason, and N. Quack, “MEMS for photonic integrated circuits”, IEEE J. Select. Topics Quantum Electron. **26**, 1–16 (2020).

[222] X. Chew, G. Zhou, H. Yu, F. S. Chau, J. Deng, Y. C. Loke, and X. Tang, "An in-plane nano-mechanics approach to achieve reversible resonance control of photonic crystal nanocavities", Opt. Express **18**, 22232 (2010).

[223] A. Faraon, I. Fushman, D. Englund, N. Stoltz, P. Petroff, and J. Vučković, "Dipole induced transparency in waveguide coupled photonic crystal cavities", Opt. Express **16**, 12154–12162 (2008).

[224] R. J. Coles, D. M. Price, J. E. Dixon, B. Royall, E. Clarke, P. Kok, M. S. Skolnick, A. M. Fox, and M. N. Makhonin, "Chirality of nanophotonic waveguide with embedded quantum emitter for unidirectional spin transfer", Nat. Commun. **7**, 11183 (2016).

[225] Z. K. Bishop, A. P. Foster, B. Royall, C. Bentham, E. Clarke, M. S. Skolnick, and L. R. Wilson, "Electro-mechanical control of an on-chip optical beam splitter containing an embedded quantum emitter", Opt. Lett. **43**, 2142–2145 (2018).

[226] X. Chen, C. Li, C. K. Y. Fung, S. M. G. Lo, and H. K. Tsang, "Apodized waveguide grating couplers for efficient coupling to optical fibers", IEEE Photon. Technol. Lett. **22**, 1156–1158 (2010).

[227] A. Bozzola, L. Carroll, D. Gerace, I. Cristiani, and L. C. Andreani, "Optimising apodized grating couplers in a pure SOI platform to -0.5 dB coupling efficiency", Opt. Express **23**, 16289 (2015).

[228] Y. Ding, F. Ye, C. Peucheret, H. Ou, Y. Miyamoto, and T. Morioka, "On-chip grating coupler array on the SOI platform for fan-in/fan-out of MCFs with low insertion loss and crosstalk", Opt. Express **23**, 3292 (2015).

[229] R. Marchetti, C. Lacava, A. Khokhar, X. Chen, I. Cristiani, D. J. Richardson, G. T. Reed, P. Petropoulos, and P. Minzioni, "High-efficiency grating-couplers: demonstration of a new design strategy", Sci. Rep. **7**, 16670 (2017).

[230] D. Vermeulen, S. Selvaraja, P. Verheyen, G. Lepage, W. Bogaerts, P. Absil, D. Van Thourhout, and G. Roelkens, "High-efficiency fiber-to-chip grating couplers realized using an advanced CMOS-compatible silicon-on-insulator platform", Opt. Express **18**, 18278 (2010).

[231] K. Yvind and J. M. Hvam, "High-efficiency, large-bandwidth silicon-on-insulator grating coupler based on a fully-etched photonic crystal structure", Appl. Phys. Lett. **96**, 051126 (2010).

[232] X. Xu, H. Subbaraman, J. Covey, D. Kwong, A. Hosseini, and R. T. Chen, "Complementary metal–oxide–semiconductor compatible high efficiency subwavelength grating couplers for silicon integrated photonics", Appl. Phys. Lett. **101**, 031109 (2012).

[233] Y. Ding, H. Ou, and C. Peucheret, "Ultrahigh-efficiency apodized grating coupler using fully etched photonic crystals", Opt. Lett. **38**, 2732 (2013).

[234] C. Li, H. Zhang, M. Yu, and G. Q. Lo, "CMOS-compatible high efficiency double-etched apodized waveguide grating coupler", Opt. Express **21**, 7868 (2013).

[235] W. S. Zaoui, A. Kunze, W. Vogel, M. Berroth, J. Butschke, F. Letzkus, and J. Burghartz, "Bridging the gap between optical fibers and silicon photonic integrated circuits", Opt. Express **22**, 1277 (2014).

[236] D. Benedikovic, C. Alonso-Ramos, P. Cheben, J. H. Schmid, S. Wang, D.-X. Xu, J. Lapointe, S. Janz, R. Halir, A. Ortega-Moñux, J. G. Wangüemert-Pérez, I. Molina-Fernández, J.-M. Fédéli, L. Vivien, and M. Dado, "High-directionality fiber-chip grating coupler with interleaved trenches and subwavelength index-matching structure", Opt. Lett. **40**, 4190 (2015).

[237] Z. Cheng, X. Chen, C. Y. Wong, K. Xu, and H. K. Tsang, "Apodized focusing subwavelength grating couplers for suspended membrane waveguides", Appl. Phys. Lett. **101**, 101104 (2012).

[238] Q. Zhong, V. Veerasubramanian, Y. Wang, W. Shi, D. Patel, S. Ghosh, A. Samani, L. Chrostowski, R. Bojko, and D. V. Plant, "Focusing-curved subwavelength grating couplers for ultra-broadband silicon photonics optical interfaces", Opt. Express **22**, 18224 (2014).

[239] Y. Wang, X. Wang, J. Flueckiger, H. Yun, W. Shi, R. Bojko, N. A. F. Jaeger, and L. Chrostowski, "Focusing sub-wavelength grating couplers with low back reflections for rapid prototyping of silicon photonic circuits", Opt. Express **22**, 20652 (2014).

[240] X. Zhou, I. Kulkova, T. Lund-Hansen, S. L. Hansen, P. Lodahl, and L. Midolo, "High-efficiency shallow-etched grating on GaAs membranes for quantum photonic applications", Appl. Phys. Lett. **113**, 251103 (2018).

[241] R. Marchetti, C. Lacava, L. Carroll, K. Gradkowski, and P. Minzioni, "Coupling strategies for silicon photonics integrated chips [invited]", Photon. Res. **7**, 201 (2019).

[242] R. H. Klenk, C. Schweikert, N. Hoppe, L. Nagy, R. Elster, W. Vogel, and M. Berroth, "Integrated dispersive structures for bandwidth-enhancement of silicon grating couplers", Opt. Quant. Electron. **52**, 119 (2020).

[243] C. R. Doerr and L. L. Buhl, "Circular grating coupler for creating focused azimuthally and radially polarized beams", Opt. Lett. **36**, 1209 (2011).

[244] C. J. Oton, "Long-working-distance grating coupler for integrated optical devices", IEEE Photonics J. **8**, 1–8 (2016).

[245] K. K. Mehta and R. J. Ram, "Precise and diffraction-limited waveguide-to-free-space focusing gratings", Sci. Rep. **7**, 2019 (2017).

[246] C. Dory, D. Vercruysse, K. Y. Yang, N. V. Sapra, A. E. Rugar, S. Sun, D. M. Lukin, A. Y. Piggott, J. L. Zhang, M. Radulaski, K. G. Lagoudakis, L. Su, and J. Vučković, "Inverse-designed diamond photonics", Nat. Commun. **10**, 3309 (2019).

[247] D. Vercruysse, N. V. Sapra, L. Su, and J. Vučković, “Dispersion engineering with photonic inverse design”, IEEE J. Sel. Top. Quantum Electron. **26**, 1–6 (2020).

[248] N. V. Sapra, D. Vercruysse, L. Su, K. Y. Yang, J. Skarda, A. Y. Piggott, and J. Vučković, “Inverse design and demonstration of broadband grating couplers”, IEEE J. Sel. Top. Quantum Electron. (2019).

[249] C. Li, K. S. Chee, J. Tao, H. Zhang, M. Yu, and G. Q. Lo, “Silicon photonics packaging with lateral fiber coupling to apodized grating coupler embedded circuit”, Opt. Express **22**, 24235 (2014).

[250] M. Albrechtsen, B. Vosoughi Lahijani, S. Stobbe, and R. E. Christiansen, “In-plane chip-scale photonic device”, pat. WO2021099392A1 (Sept. 8, 2022).

[251] H. S. Dutta, A. K. Goyal, V. Srivastava, and S. Pal, “Coupling light in photonic crystal waveguides: a review”, Photonics Nanostruct. **20**, 41–58 (2016).

[252] B. A. Frederiksen, B. Vosoughi Lahijani, M. Albrechtsen, C. A. Rosiek, K. Tsoukalas, T. A. S. Weis, and S. Stobbe, “Compact nanoeletromechanical optical phase shifters”, in 48th international conference on micro & nano engineering, Leuven, Belgium (2022), T3A24.

[253] B. A. Frederiksen, “Chip-scale phase shifters for programmable nanoelectromechanical photonic mesh networks”, BSc. thesis (Technical University of Denmark, June 2022).

[254] Z. Wang, N. Zhu, Y. Tang, L. Wosinski, D. Dai, and S. He, “Ultracompact low-loss coupler between strip and slot waveguides”, Opt. Lett. **34**, 1498–1500 (2009).

[255] S. Wu, X. Mu, L. Cheng, S. Mao, and H. Y. Fu, “State-of-the-art and perspectives on silicon waveguide crossings: a review”, Micromachines **11**, 326 (2020).

[256] M. Albrechtsen, B. Vosoughi Lahijani, S. Stobbe, and K. Tsoukalas, “Nanoelectromechanical interferometer for visible to infrared wavelengths”, pat. WO2021099398A1 (May 27, 2021).

[257] P. Edinger, G. Jo, C. P. V. Nguyen, A. Y. Takabayashi, C. Errando-Herranz, C. Antony, G. Talli, P. Verheyen, U. Khan, S. J. Bleiker, W. Bogaerts, N. Quack, F. Niklaus, and K. B. Gylfason, “Vacuum-sealed silicon photonic MEMS tunable ring resonator with an independent control over coupling and phase”, Opt. Express **31**, 6540–6551 (2023).

[258] L. Li, Q. Qiao, G. Zhou, Y. Qi, Z. H. Lim, F. S. Chau, and G. Zhou, “Design of an on-chip fourier transform spectrometer based on waveguide mach–zehnder interferometer and fluidics”, Opt. Commun. **460**, 125103 (2020).

[259] Z. Yang, T. Albrow-Owen, H. Cui, J. Alexander-Webber, F. Gu, X. Wang, T.-C. Wu, M. Zhuge, C. Williams, P. Wang, A. V. Zayats, W. Cai, L. Dai, S. Hofmann, M. Overend, L. Tong, Q. Yang, Z. Sun, and T. Hasan, “Single-nanowire spectrometers”, Science **365**, 1017–1020 (2019).

[260] A. V. Velasco, P. Cheben, P. J. Bock, A. Delâge, J. H. Schmid, J. Lapointe, S. Janz, M. L. Calvo, D.-X. Xu, M. Florjańczyk, and M. Vachon, "High-resolution fourier-transform spectrometer chip with microphotonic silicon spiral waveguides", Opt. Lett. **38**, 706–708 (2013).

[261] X. Nie, E. Ryckeboer, G. Roelkens, and R. Baets, "CMOS-compatible broadband co-propagative stationary fourier transform spectrometer integrated on a silicon nitride photonics platform", Opt. Express **25**, A409–A418 (2017).

[262] B. Hong, F. Monifi, and Y. Fainman, "Channel dispersed fourier transform spectrometer", Commun. Phys. **1**, 1–8 (2018).

[263] R. Cheng, C.-L. Zou, X. Guo, S. Wang, X. Han, and H. X. Tang, "Broadband on-chip single-photon spectrometer", Nat. Commun. **10**, 4104 (2019).

[264] A. Li and Y. Fainman, "On-chip spectrometers using stratified waveguide filters", Nat. Commun. **12**, 2704 (2021).

[265] H. Wang, Q. Li, and W. Shi, "On-chip polarization-insensitive fourier transform spectrometer", Opt. Lett. **45**, 1479–1482 (2020).

[266] J. Cohen, *Introduction to fourier transform spectroscopy* (U.S. Department of Commerce, National Bureau of Standards, Gaithersburg, MD 20899, Mar. 1, 1986).

[267] A. Barducci, D. Guzzi, C. Lastri, P. Marcoionni, V. Nardino, and I. Pippi, "Theoretical aspects of fourier transform spectrometry and common path triangular interferometers", Opt. Express **18**, 11622 (2010).

[268] O. Manzardo, H. P. Herzig, C. R. Marxer, and N. F. d. Rooij, "Miniaturized time-scanning fourier transform spectrometer based on silicon technology", Opt. Lett. **24**, 1705–1707 (1999).

[269] R. Voelkel, "Wafer-scale micro-optics fabrication", Adv. Opt. Technol. **1** (2012).

[270] Y. M. Eltagoury, Y. M. Sabry, and D. A. Khalil, "All-silicon double-cavity fourier-transform infrared spectrometer on-chip", Adv. Opt. Technol. **4**, 1900441 (2019).

[271] D. Patel, V. Veerasubramanian, S. Ghosh, A. Samani, Q. Zhong, and D. V. Plant, "High-speed compact silicon photonic michelson interferometric modulator", Opt. Express **22**, 26788 (2014).

[272] Y. A. Vlasov, M. O'Boyle, H. F. Hamann, and S. J. McNab, "Active control of slow light on a chip with photonic crystal waveguides", Nature **438**, 65–69 (2005).

[273] M. Montesinos-Ballester, Q. Liu, V. Vakarin, J. M. Ramirez, C. Alonso-Ramos, X. L. Roux, J. Frigerio, A. Ballabio, E. Talamas, L. Vivien, G. Isella, and D. Marris-Morini, "On-chip fourier-transform spectrometer based on spatial heterodyning tuned by thermo-optic effect", Sci. Rep. **9**, 14633 (2019).

[274] A. Li, J. Davis, A. Grieco, N. Alshamrani, and Y. Fainman, "Fabrication-tolerant fourier transform spectrometer on silicon with broad bandwidth and high resolution", Photon. Res. **8**, 219 (2020).

[275] M. Burla, D. Marpaung, L. Zhuang, C. Roeloffzen, M. R. Khan, A. Leinse, M. Hoekman, and R. Heideman, "On-chip CMOS compatible reconfigurable optical delay line with separate carrier tuning for microwave photonic signal processing", Opt. Express **19**, 21475 (2011).

[276] X.-L. Huang, C.-T. Zheng, C.-L. Sun, C.-T. Li, Y.-D. Wang, and D.-M. Zhang, "Investigation on an ultra-compact mach–zehnder interferometer electro-optic switch using poled-polymer/silicon slot waveguide", Opt. Quant. Electron. **47**, 3783–3803 (2015).

[277] J. Loridat, S. Heidmann, F. Thomas, G. Ulliac, N. Courjal, A. Morand, and G. Martin, "All integrated lithium niobate standing wave fourier transform electro-optic spectrometer", J. Lightwave Technol., JLT **36**, 4900–4907 (2018).

[278] J. Sand, "Near-infrared spectroscopy for continuous quality control of oil", BSc. thesis (Technical University of Denmark, June 2021).

[279] M. Herskind, "Experimental characterization of silicon photonic crystal waveguides with glide-plane symmetry", MSc. thesis (University of Copenhagen, Apr. 2018).

[280] T. A. S. Weis, M. Albrechtsen, K. Tsoukalas, A. N. Babar, and S. Stobbe, "Measurements of attracting surface forces in nanoelectromechanical systems", in 47th international conference on micro & nano engineering, Turin, Italy (2021), PA30.

[281] T. A. S. Weis, "Design and fabrication of silicon nanostructures using quantum vacuum forces", MSc. thesis (Technical University of Denmark, Feb. 2021).

[282] D. Pérez, I. Gasulla, L. Crudgington, D. J. Thomson, A. Z. Khokhar, K. Li, W. Cao, G. Z. Mashanovich, and J. Capmany, "Multipurpose silicon photonics signal processor core", Nat. Commun. **8**, 636 (2017).

[283] V. R. Almeida, R. R. Panepucci, and M. Lipson, "Nanotaper for compact mode conversion", Opt. Lett. **28**, 1302 (2003).

[284] D. M. Kita, J. Michon, S. G. Johnson, and J. Hu, "Are slot and sub-wavelength grating waveguides better than strip waveguides for sensing?", Optica **5**, 1046–1054 (2018).

[285] Q. Qiao, H. Sun, X. Liu, B. Dong, J. Xia, C. Lee, and G. Zhou, "Suspended silicon waveguide with sub-wavelength grating cladding for optical MEMS in mid-infrared", Micromachines **12**, 1311 (2021).

[286] P. Cheben, R. Halir, J. H. Schmid, H. A. Atwater, and D. R. Smith, "Subwavelength integrated photonics", Nature **560**, 565–572 (2018).

[287] Editorial, "Elements of style", Nat. Phys. **3** (2007).

[288] H. Shim, H. Chung, and O. D. Miller, “Maximal free-space concentration of electromagnetic waves”, Phys. Rev. Appl. **14**, 014007 (2020).

[289] F. Capasso, J. N. Munday, D. Iannuzzi, and H. B. Chan, “Casimir forces and quantum electrodynamical torques: physics and nanomechanics”, IEEE J. Select. Topics Quantum Electron. **13**, 400–414 (2007).

[290] C. M. Patil, “Experiments on glide-symmetric photonic-crystal waveguides”, Ph.D. thesis (University of Copenhagen, 2020).